Freehand Three Dimensional Ultrasound for Imaging Components of the Musculoskeletal System

Erin Ross

PhD

University of Edinburgh

2009

Abstract

There have been reports on the use of Ultrasound (US) for monitoring fracture repair and for measuring muscle volume. Change in muscle mass is a useful bio-marker for monitoring the use and disuse of muscle, and the affects of age, disease and injury.

The main modality for imaging bone is X-ray and for muscle volume Magnetic Resonance (MR). Previous studies have shown US to have advantages over X-ray and MR. US can image all stages of the fracture repair process and can detect signs of healing 4-6 weeks before X-ray allowing earlier detection of possible complications. Compared to MR, US is less resource intensive, easier to access and also has fewer exclusion criteria for patients.

Despite these advantages, the limited field of view that US can provide results in high operator dependency for scan interpretation and also for length and volume measurements.

Three-dimensional Ultrasound (3D US) has been developed to overcome these limitations and has been used to provide extended field of view images of the foetus and the heart and to obtain accurate volume measurements for organs.

In this thesis it is hypothesized that 3D US can provide a more comprehensive method of imaging fracture repair than X-ray and is also a viable alternative to MR for determining muscle volumes *in vivo*.

Initially, an electromagnetically (EM) tracked 3D US system was evaluated for clinical use using phantom-based experiments. It was found that the presence of metal objects in or near the EM field caused distortion and resulted in errors in the volume measurements of phantoms of up to ±20%. An optically tracked system was also evaluated and it was found that length measurements of a phantom could be made to within ±1.3%.

Fracture repair was monitored in five patients with lower limb fractures. Signs of healing were visible earlier on 3D US with a notable, although variable, lag between callus development on X-ray compared to 3D US. 3D US provided a clearer view of callus formation and the changes in density of the callus as it matured. Additional information gained by applying image processing methods to the 3D US data was

used to develop a measure of callus density and to identify the frequency dependent appearance of the callus.

Volume measurements of the rectus femoris quadricep muscle were obtained using 3DUS from eleven healthy volunteers and were validated against volume measurements derived using MR. The mean difference between muscle volume measurements obtained using 3D US and MR was 0.53 cm^3 with a standard deviation of 1.09 cm^3 and 95% confidence intervals of 0.20 - 1.27 cm^3

In conclusion, 3D US demonstrates great potential as a tool for imaging components of the musculoskeletal system and as means of measuring callus density.

Declaration

I hereby declare that this thesis was composed by myself and that the work described within is my own, except where explicitly stated otherwise.

Erin Ross

June 2009

Acknowledgements

I would like to take this opportunity to acknowledge and thank those who have provided me with guidance, expertise and support during this research.

Firstly, I would like to thank my supervisors Prof Simpson head of the Orthopaedic Engineering Collaboration, Dr Tom MacGillivary Image Core Analyst at the Wellcome Trust, Mr Andrew Muir of the Orthopaedic Engineering Collaberation and Dr Will Hossack of the Physics Department. Prof Simpson, thank you for the initial inspiration for the work on monitoring fracture repair and for your guidance in assessing the X-rays and outcomes from the clinical study. Dr MacGillivray, thank you for your fantastic support, guidance and image analysis expertise. Also, thank you for involving me in your work with Dr Carolyn Greig and providing me with the opportunity to broaden the applications of three dimensional Ultrasound. To Mr Muir and Dr Hossack thank you for letting me sound out my ideas and providing me with additional equipment to carry out my research.

For the long term loan of equipment, thank you to the Medical Physics Department. Special thanks goes to Dr Carmel Moran for asking me to present at the BMUS conference in 2007 and for nominating me for the Mercia Award in 2008.

Thank you to all the staff of Out Patients Department 6 and to the healthy volunteers and patients involved in each of the clinical studies.

To all my colleagues in the Edinburgh Orthopaedic Engineering Collaboration and the other fantastic ladies who share our office, many thanks for making me very welcome and listening at those difficult times. In particular, a huge thank you to Deborah MacDonald for all her expert help with the ethics applications for each study.

Acknowledgements

Finally, to all my family and friends thank you for your endless support and encouragement I could not have done this without you. A special thanks goes to my parents for all the long hours they spent proof reading the final drafts of my thesis.

Contents

Figures

The original X-ray images and the annotated X-ray images used in chapter 5 have been included on a DVD at the end of the thesis for reference if required.

1. Introduction and Outline of Thesis

1.1. Musculoskeletal Imaging

The musculoskeletal system accounts for over 75% of the mass of the human body (1). As well as giving the body structure and the ability to move, the musculoskeletal system provides protection for vital organs. Throughout life it is inevitable that a person will suffer numerous musculoskeletal injuries from minor cuts, bruises and stained muscles to traumatic injuries resulting in broken bones and torn muscles. Disease can also have a detrimental effect on the musculoskeletal system, arthritis and osteoporosis can damage joints and weaken the load bearing capacity of bones whilst multiple sclerosis and muscular dystrophy can cause muscle wastage and loss of function.

When injury or disease affects the musculoskeletal system it is important to determine to what extent in order to plan the best course of treatment. Medical imaging techniques provide vital information to aid diagnosis and are frequently used to monitor the rehabilitation process during treatment to ensure the best possible outcome for the patient. In the field of musculoskeletal research imaging can be used to evaluate the effectiveness of treatment regimes as well as to monitor the progression of disease and to aid understanding of the ageing process.

The most commonly used imaging modalities are X-ray, Computerised Tomography (CT), Magnetic Resonance (MR) and two-dimensional Ultrasound (2D US). For musculoskeletal imaging, X-ray is primarily used to image broken bones. CT is used to gain more comprehensive views of complex fractures i.e. fractures of the pelvis or skull as well as to look for tumours. MR provides images of both bone and soft tissues and is particularly useful for imaging suspected damage to the spine and

joints. 2D US can image soft tissue damage such as muscle and tendon tears as well as be used to check for changes in the vascularisation of the musculoskeletal system resulting from injury or disease.

Significant work has been carried out in the field of 2D US imaging since the 1970's to develop three dimensional Ultrasound (3D US) which would widen the abilities and potential applications of US imaging (2-4). The basic concept of 3D US is to track the motion of the US probe during scanning and use this information to stack a series of parallel 2D US images together to create a continuous volume of image data. Over the last 15 years advancements in computing and technology have lead to a variety of 3D US systems being created, a number of which have been trialled successfully in the fields of Cardiology, Obstetrics and Gynaecology (5-8). There have been a very limited number of studies into the use of 3D US for musculoskeletal imaging and it has not been adopted as an imaging technique in the field of Orthopaedics remaining overshadowed by MR, CT and X-ray. When the imagining abilities of 3D US are given full consideration this new modality could play an important role in the field of musculoskeletal imaging. Most importantly is its potential to provide a more effective and comprehensive means of imaging the fracture repair process than X-ray. Furthermore, in the field of musculoskeletal research, 3D US could provide an inexpensive and accessible alternative to CT and MR for monitoring changes in the skeletal muscles which can be used as indicators of disease progression or the success of treatment and rehabilitation regimes.

1.1.1. Monitoring Fracture Repair

More than one million fractures occur each year in the UK alone as a result of diverse causes from high energy road accidents and sports injuries to low energy osteoporotic fractures (9). Surgically induced divisions of the bone (osteotomies) are a necessary intervention to treat adults and children with conditions such as limb length discrepancy and hip dysplasia. 5-10% of these fractures/osteotomies have healing problems, thus, many thousands of patients each year suffer from

complications during fracture repair. This causes considerable morbidity to the patient resulting in a burden to society due to the large number of working days lost as well as costing the NHS millions of pounds each year

X-ray is the standard method used to image the fracture repair process, however, it is by no means ideal. Despite giving a good outline of a patient's healthy bone the forming fracture callus cannot be detected on X-ray until it has become sufficiently dense with calcium. Even then, the variation in density of the callus makes an accurate outline of its volume hard to depict. For a simple fracture of the tibia the callus is not expected to be visible on X-ray until around 6-8 weeks post fracture. Earlier signs of the healing process cannot be detected which means if complications occur before the callus becomes visible then these may go undetected for weeks. The occurrence of such complications will only be indicated by a delay in the appearance of callus and will lead to an increased rehabilitation time for the patient. The decision on the state of healing lies with the clinical interpretation of X-rays and physical examination of the injury site. Both of these procedures are dependent on the physician making the assessment and both methods are subject to a degree of error (10).

Previous studies into the use of 2D US for monitoring fracture repair, have found that it could detect the earliest stages of the healing process 1-2 weeks after fracture and that complications could also be identified earlier (11). Ultrasound has been promoted as a useful adjunct to X-ray for monitoring fracture healing, however, despite its advantages 2D US has not been used in this role to any great extent. The high operator dependency in scan interpretation and the problems of obtaining the same views to make repeat measurements over time have limited its use for this purpose.

3D US overcomes these limitations by providing a volume dataset of images for scanned objects. These datasets make it easier to interpret the scanned anatomy and to identify points between which to make repeated length measurements over time. It is possible to make 3D models of features of interest which could potentially

provide a physician with more information about the state of a fracture than either 2D US images or X-rays. Building up a series of models charting a patient's progress from as early as one week post injury means that signs of healing as well as possible complications could be detected at the earliest stages. It is hypothesised that 3D US could provide an alternative method to X-ray for monitoring fracture repair.

1.1.2. Muscle volume measurements

Skeletal muscle provides the means to move the body, so if injury or disease effects a muscle it can reduce its ability to contribute effectively to the movement of the body. Understanding the effects of muscle disuse and the rate at which muscle strength diminishes over time is important when considering the rehabilitation of patients recovering from injury or disease. In lower limb fracture patients it is common to see muscle wasting of the effected limb as a result of non-weight bearing during the healing process (12). Conversely, if a specific physical training regime is undertaken this can enhance the size and strength of a muscle.

Change in skeletal muscle due to use, disuse, injury or disease is reflected by muscle volume. The ageing process also causes a gradual reduction in muscle volume over time. With a growing number of people living beyond 75 years of age there is an increased need to establish the effects of ageing after this point and determine efficient ways of maintaining muscle function. It has been shown that physical exercise at any stage in life can improve muscle strength and increase muscle volume (13).

Change in muscle volume can be used as an indicator in the field of medicine to monitor patient progress and determine the effectiveness of set treatment and rehabilitation regimes. It can also be used to monitor the progression of a disease and to assess whether a specific treatment is useful for slowing down or reversing the effects. The key to the success of such studies is a means of accurately measuring muscle volumes. Current methods include the use of MR, CT and US imaging as

well as the use of physical measurements such as limb girth and length measurements to estimate the cross-sectional area (CSA) and then volume of a group of muscles (1, 14, 15). Each method has its benefits and its disadvantages. MR is the favoured method for attaining muscle volume measurements as it can provide clear images of the different tissues found within the musculoskeletal system (16). However, it is resource intensive, waiting times for non urgent cases are long and there are a number of exclusion criteria for scanning. CT has been used in cadaver studies but the dose of ionising radiation that would be delivered during scanning makes it difficult to justify its use in studies where healthy volunteers are involved. Physical measurements are quick and low in cost to carry out, however, the accuracy of estimated muscle volume from these measurements is poor due to the approximation required in the calculation (17). Although US provides images of the musculoskeletal system at a much lower cost than MR and CT, it can only provide a limited field of view. Volume measurements made from 2D US scans involve the use of approximations similar to those used with anthropometric measurements meaning this method would not be accurate enough to monitor small changes in muscle volumes.

A further imaging technique is required that can provide images comparable to those of MR but without the limitations. The accurate volume measurements and additional imaging facilities offered by 3D US make it a potential alternative imaging method for measuring muscle volumes. 3D US is not location restricted unlike MR, is suitable for use with healthy volunteers and is relatively inexpensive. It is hypothesised that 3D US could provide a flexible and non invasive means of obtaining accurate muscle volume measurements *in vivo*.

1.2. Scope

This thesis looks at the development of 3D US and its applications in order to identify a suitable 3D US system for musculoskeletal imaging. The chosen system

will then be evaluated to ensure it is suitability for use before being trialled for the proposed applications of monitoring fracture repair and for determining muscle volume. Novel image analysis is carried out on the US image data in order to develop a new means of determining the state of healing fracture callus.

1.3. Outline of thesis

Four research questions have been formulated to test the hypotheses that 3D US could provide a suitable alternative to X-ray for monitoring the fracture repair process and a viable alternative to MR for determining muscle volume measurements *in vivo*.

1. Does an optically tracked or a magnetically tracked 3D US system offer the most accurate and reliable means of imaging the musculoskeletal system in a clinical environment?
2. Can 3D US provide a more comprehensive means of monitoring fracture repair than X-ray?
3. Can image data obtained from a 3D US scan of a fracture be used to determine a density measure of callus to provide a reliable and accurate means of identifying how healed a fracture is and at what stage full weight bearing can be safely resumed?
4. Can 3D US provide a suitably accurate and reliable alternative to MR for determining muscle volume measurements *in vivo*?

The background to the fracture repair process and the need for an accurate means of determining muscle volumes in vivo are introduced in Chapter 2. The advantages and also the limitations of current methods used to image fracture repair and measure muscle volumes are discussed along with the available alternative imaging techniques, in particular Ultrasound.

Chapter 3 covers the development of 3D US and the setup and assessment of an electromagnetically tracked 3D US system using a series of phantoms experiments. The assessment of an alternative, optically tracked 3D US system, using a further series of phantom, is covered in Chapter 4.

In Chapter 5, the abilities of the Optical 3D US system to monitor the fracture repair process are compared to the abilities of X-ray in a pilot clinical study of patients with lower limb fractures. In Chapter 6, image processing is used to extract additional information from the 3D US scan data and develop a means of assessing the change in callus density during the fracture repair process. A pre-clinical study is used to validate the callus density measure and determine its suitability for use on patient data.

The ability of the 3D US system to measure muscle volumes *in vivo* is investigated in Chapter 7. In a pilot healthy volunteer study, muscle volumes derived from 3D US scans are compared to volumes obtained using MR.

The conclusions of this thesis work are drawn together in Chapter 8 and areas for future research are presented.

2. Ultrasound and Musculoskeletal Imaging

2.1. Introduction

In this Chapter the principles of fracture repair, muscle volume measurement and 2D US are introduced. The current methods used to image fracture repair and obtain muscle volume measurements are covered highlighting the areas where 3D US could provide a more suitable alternative means of imaging.

2.2. Fracture

Fractures are a common occurrence and are caused by bones being loaded or strained beyond their normal biomechanical limits. This may result from direct violence due to impact, indirect violence due to twisting of the bone, fatigue from repeated use or due to pathological causes such as osteoporosis, tumours and cysts (12).

Fractures are classified as either open or closed. Closed fractures, sometimes referred to as simple fractures, are where the broken bone has not broken the skin and has no contact with the external environment. Open fractures, also referred to as compound fractures, are where the bone is exposed to the external environment i.e. the bone has either broken through the skin or significant laceration has occurred over the fracture site. Further classifications of fracture type can relate to the cause, e.g. a pathological fracture, or may be representative of the resulting pattern of the broken bone as shown in figure 2-1 (18). Fractures 1, 2, and 3 are simple fractures where the use of 'simple' relates to the fact that there are only two bone fragments and that the fracture runs around the full circumference of the bone: 1 simple

transverse; 2 simple oblique; 3 simple spiral. Fractures 4–9 in figure 2-1 are multi-fragmented fractures.

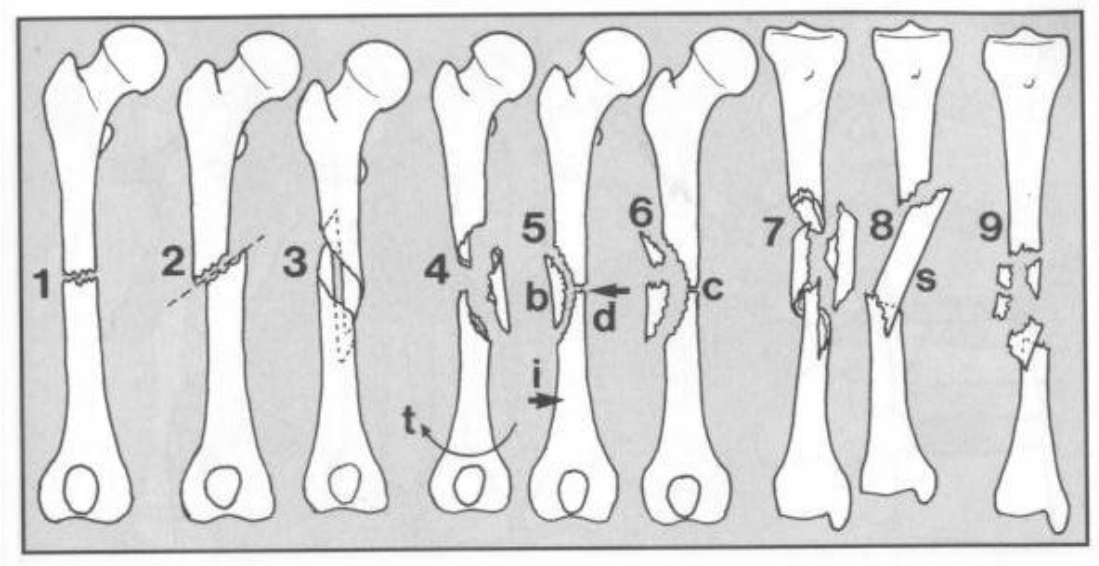

Figure 2-1: Common fracture patterns, (1) simple traverse, (2) simple oblique, (3) simple spiral, (4-9) multi-fragmentary fractures (18).

A fracture may be diagnosed from the patient's history or physical examination of the injury site on admission to hospital. If a fracture is suspected X-rays will be taken to confirm the diagnosis (18, 19). When taking an X-ray of a fracture the standard procedure requires two projections through the injury site to be obtained, the antero-posterior (AP) and lateral views. Both X-rays should include a reasonable length of the patient's healthy bone above and below the fracture site (20). In cases where fractures are known to be difficult to detect additional X-ray images at other orientations may be required (21). On occasion more specialist imaging techniques may be used to gain an understanding of the full extent of a fracture. With spinal and pelvic fractures or suspected bony lesions CT and MR may provide a more complete picture. Furthermore, radioisotope scanning can be used as a method of diagnosing the presence of a stress fracture.

2.2.1. The Healing Process

As soon as a fracture occurs the body responds by initiating the healing process. Despite this immediate response fracture repair is a lengthy process. In a normal healthy adult it will take around 6 weeks for a fracture of the cancellous bone, found at the ends of a long bone, to unite. A fracture of the cortical bone which makes up the shaft of a long bone can take 3 months to heal (22). One of the proposed applications of 3D US is for the monitoring of fractures of the shaft of the tibia and femur, thus, it is the healing process of cortical bone which is of relevance. Fractures of the shaft of the tibia often require surgical intervention to reduce and stabilise the fracture, this intervention can disrupt the healing process and lead to complications arising (9).

The repair process for a cortical bone fracture is described as occurring in five stages, however, there are no definite transition points between these healing phases and it is possible that two or more healing processes can be underway at different sites of the same injury (12, 20-23). The five stages of fracture healing are shown in figure 2-2.

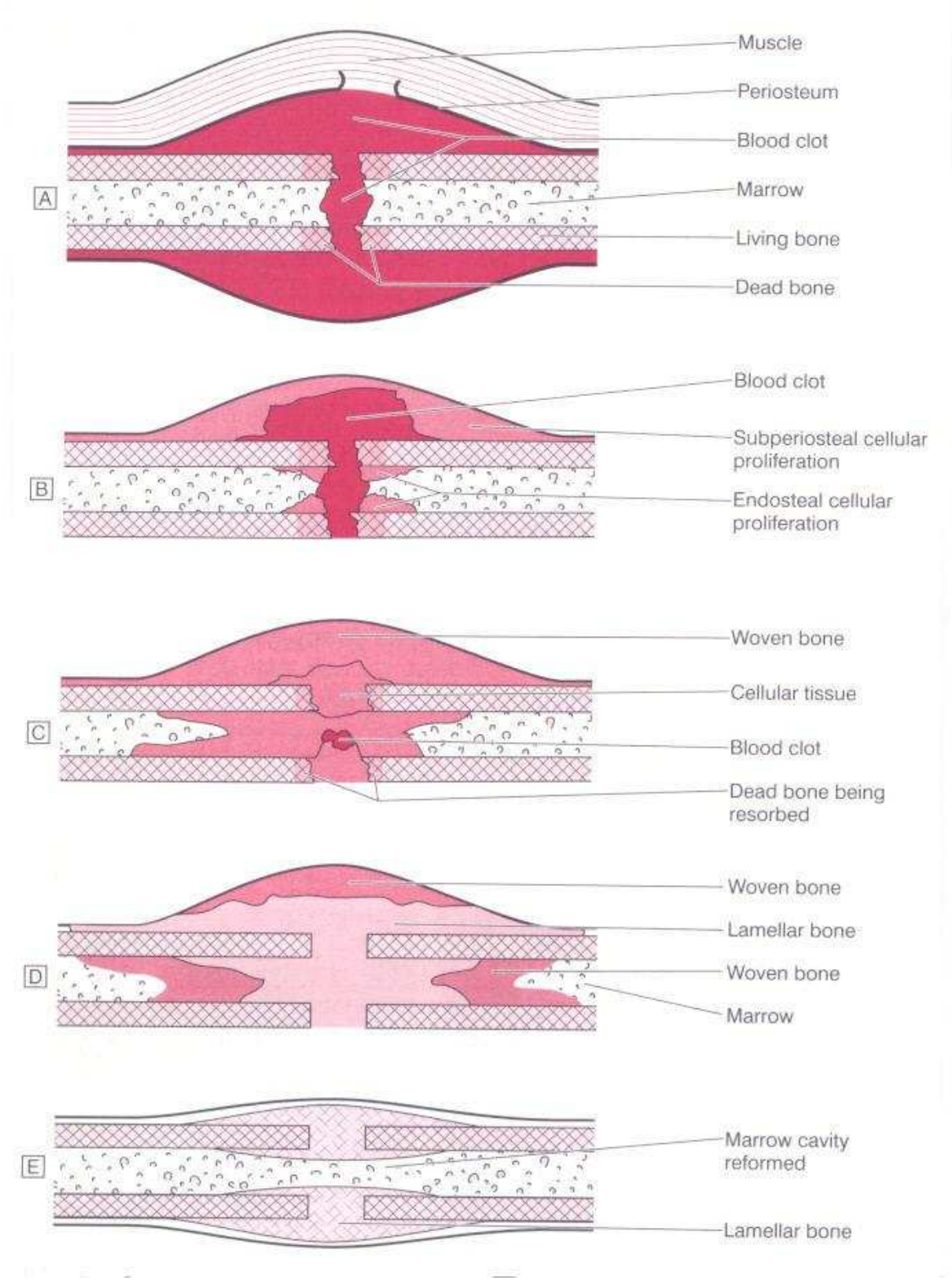

Figure 2-2: Stages of fracture healing. (A) Formation of the haematoma. (B) Subperiosteal and endosteal cellular proliferation. (C) Callus formation. (D) Consolidation. (E) Remodelling (21).

Long bones are covered by a thin fibrous membrane called the periosteum which contains a network of nerves and blood vessels that supply nutrients and minerals to the bone. There is also a blood supply running through the central medullary canal. When a bone breaks the blood vessels running through it and along its surface can be damaged along with the surrounding soft tissue. Blood from these vessels will seep into the fracture site forming a haematoma which may be contained by the periosteum if it remains undamaged during fracture. Usually however, the periosteum is lifted or stripped away from the bone surface and blood will seep into the surrounding soft tissues eventually becoming restricted by muscle, fascia and skin. Formation of this haematoma is the first stage in the healing process. The clotting of the torn blood vessels deprives regions of bone adjacent to the fracture site of a blood supply causing the bone to die back a few millimetres or more (20).

Within hours of the injury the second stage of the repair process, known as cellular proliferation, commences. The death of the bone ends attracts cells called macrophages and osteoclasts into the fracture gap which start removing the regions of dead bone. Osteoblast cells which are responsible for the production of new bones are also attracted into the area (12). Proliferation of other cells which are the precursors to osteoblasts occurs below the periosteum and within the medullary canal at the site of fracture (21). These cells surround the broken bone ends and begin to bridge the gap and stabilise the fracture. New blood vessels rapidly form and start to repair the vascular damage. Revascularisation of the fracture site continues throughout the healing process and the haematoma is gradually re-absorbed.

Cellular proliferation in the sub periosteal and medullary regions advances across the fracture gap to reunite the bone ends filling in the gap and enveloping any bone fragments lying in between. These cells then mature into osteoblasts and begin to lay collagen fibres across the fracture gap. The fibres are then gradually impregnated with calcium deposits to form immature woven bone which is called callus, see figure 2-2(C) (20). Callus provides rigidity and stability across the fracture site often taking on a bulbous form which may be felt as a hard mass below the skin.

Formation of callus is the third stage in the healing process and is the point at which signs of healing become visible on X-ray (22).

Consolidation is the fourth phase in fracture healing. The regions of woven bone have now expanded to fill the whole of the fracture gap as can be seen in figure 2-2 (D). Further ossification of the woven bone occurs and the activity of both osteoclasts and osteoblasts transforms the structure into stronger more substantial bone, known as lamellar bone, which bridges the fracture site (21).

In the final stage the bulbous shape of the lamellar bone callus is remodelled, see figure 2-2(E). The lamellar bone filling the fracture gap often obscures the medullary canal and remodelling works to carve out and reform it. Remodelling can take months or even years. Regions of the bone under low stress will be carved away and at regions of high stress extra layers of lamellar bone will be laid down to improve the strength of the bone (20). In children the process of remodelling is often so efficient that eventually signs of the site of fracture are no longer visible on X-ray whilst in adults remodelling is not so efficient and the site of fracture is often marked by an area of thickened bone (21).

Fracture union describes the callus formation stage of the healing process. Although the bone ends have united and calcification of the callus can been seen on X-ray the repair process is not yet complete. The mechanical strength of the bone is often insufficient to cope with the demands placed upon it, particularly weight bearing in the lower limb bones (12). There is no set method of determining how long it will take for a fracture to unite and consolidate. Estimated timelines have been published, however, it is very much patient specific and is dependent on a variety of different factors (12, 21, 22). To reach the consolidation stage of the healing process can take 4 - 6 weeks in children whereas in adults it can take up to 12-14 weeks (20). In adults, age is not such a major factor, whereas, good health, sufficient immobilisation of the bone fragments and a good blood supply to the fracture site are more influential in terms of an improved rate of healing (24).

Successful bony union and consolidation is determined by physical assessment of the fracture, which involves testing the mobility of the fracture, and should be supported by radiological findings (19). If consolidation has occurred there should be no mobility at the point of fracture and the patient should experience no pain or discomfort when the affected site is stressed or when gentle pressure is applied to the site of injury (21). If union has occurred but consolidation is only just underway the fracture site will still be tender, particularly when angulation across the injury is attempted (20, 25).

A small minority of fractures will not proceed to union and consolidation as expected and complications may arise. Complications may be directly related to the bony injury itself or may be a result of an associated injury such as nerve or blood vessel damage, compartment syndrome or tendon injury (9, 21). Directly related complications are those linked to the healing process of the bone and include delayed union, mal-union, non-union, shortening and bone infection. Bone infection can occur in the early stages of healing while delayed union, non-union and mal-union occur in the later stages (20). The bones of interest in this study are the long bones of the leg: the tibia, fibula and femur. The following discussion of complications is based on fractures relating to these particular bones.

Infection can occur in the early stages of repair, particularly in open fractures. In closed fractures infection is unlikely unless introduced during an operation to apply internal fixation (26). Deep infection may require the fracture to be re-stabilised after the removal of necrotic bone and soft tissue at the fracture site (21).

Slow healing is not uncommon as the time line given for fracture repair is very general and patient specific factors such as smoking, alcohol intake, physical health and mobility have an affect on the rate of repair (12, 21, 27). Delayed union is a delay beyond the normal time it takes for the fracture to reach bony union (28). There can be many reasons for this: poor revascularisation, too much mobility at the fracture site due to insufficient support of the injury and also biological and patient factors (20). In some cases of delayed union there is a small region visible on X-ray

where very poor quality callus has formed. Absorption of the bone at the fracture site then amplifies the appearance of the fracture gap on the radiograph. Initial treatment is to wait and see if union occurs after a prolonged period of up to 6 months, after which surgical intervention may be sought.

If a fracture fails to heal it is termed a non-union. Non-union becomes apparent on X-ray due to changes in the appearance of the broken ends of the bone. Non-unions are frequently classified into two types *hypertrophoic* and *atrophi*c. In *hypertrophic* non-union the bone ends appear flared out increasing the diameter of the bone beyond its normal width at the fracture site. This flaring of the bone ends defines and highlights the fracture gap on X-ray. In *atrophic* non-union the broken ends of the bone appear sclerotic on X-ray and are rounded in shape causing the fracture gap to be clearly visibly. Once a fracture has been determined to be a non-union various therapeutic interventions can be utilised such as bone grafting, Ultrasound and electromagnetic fields to stimulate healing (20, 28).

Mal-union is a term that describes fractures where the bone ends have become angulated or rotated with respect to one another as the repair process has progressed. This can cause deformity of the limb resulting in shortening of the bone. In the case of severe angulation the bone ends may be overlapping after fracture and heal along the edge of the opposite bone fragment rather than end on end as expected (18).

Limb lengthening procedures are carried out as a result of mal-union and bone loss and are also performed to correct for growth defects resulting from diverse causes (11). Lengthening of a bone is initiated by surgically inducing a fracture, a process known as osteotomy, in the effected bone(s). An external fixation device such as an Ilizarov frame or unilateral fixator, see figure 2-3(A), is fitted in order to stabilise the fracture site and provide a means of correcting the deformity of the bone by a process of gradual distraction (21). Alternatively, an internal fixation device such as an ISKD (Intramedullary Skeletal Kinetic Distractor) nail may be used, see figure 2-3(B).

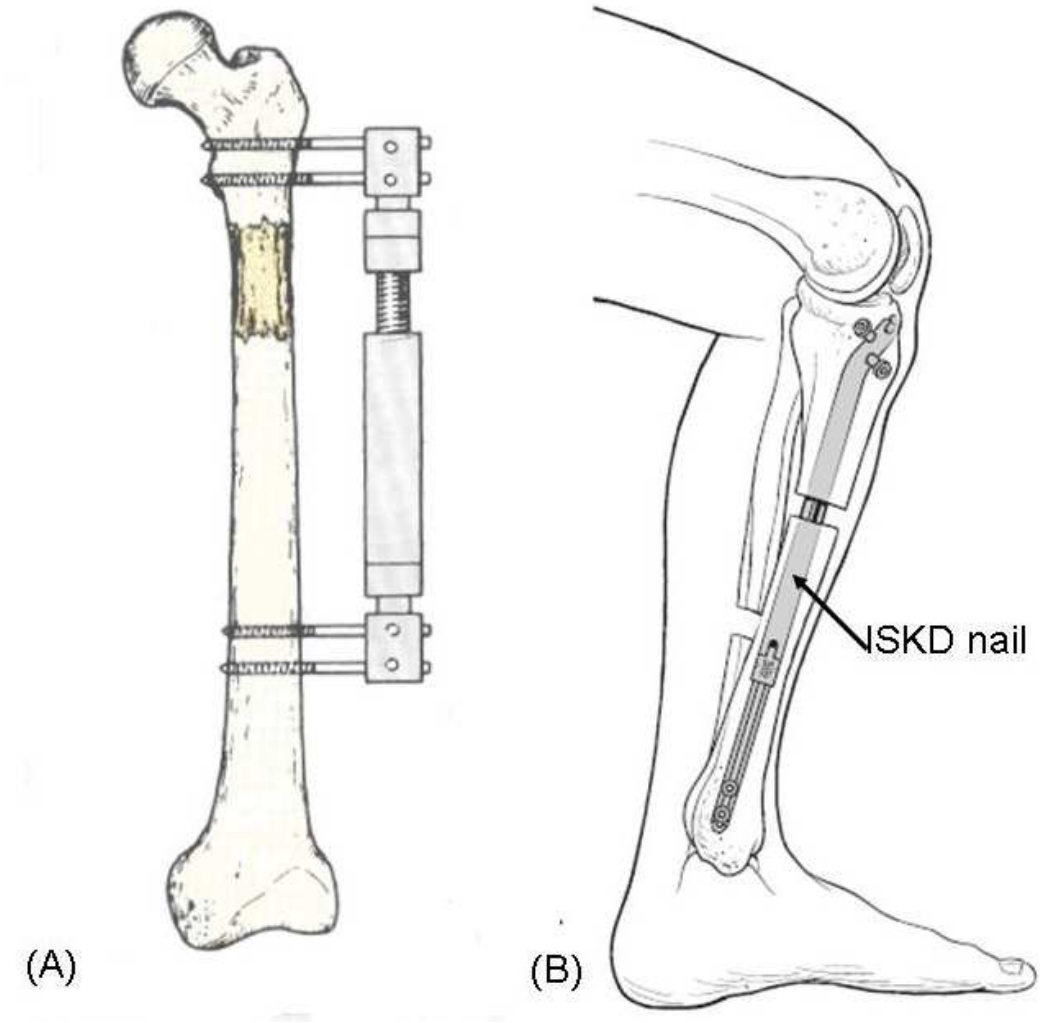

Figure 2-3: (A) Unilateral external fixation device used to stabilise a fracture (20) and (B) an ISKD nail[1] used to carryout lengthening.

The response of bone to osteotomy is the same as the healing process described previously for factures. It is during the second stage of fracture repair, when cellular proliferation is occurring, that lengthening is carried out. The length of the external fixation devices or ISKD nail is increased daily at a predetermined rate until the required additional length between the bone ends has been achieved. Typically, the rate of lengthening is usually around 1mm per day (12). It is important to establish the correct rate of lengthening; if the bone ends are pulled apart to quickly callus will

[1] www.ISKD.com

stop forming. Callus at the osteotomy site may bridge the gap if the lengthening rate is too slow in which case the bone cannot be lengthened further unless it is re-broken. Once the correct length is reached the healing process is allowed to progress to the final stages. As with fracture repair the progress of limb lengthening is monitored using X-ray and by physical assessment.

2.2.2. Imaging Fracture Repair

X-ray is the standard method used to image fractures from the point where a fracture is suspected until consolidation of the callus is reached. It is the calcium present in bone which gives the bright white appearance on radiographs (12). Healthy mature bone appears in clear detail on X-ray and any disruptions to the smooth surface of a bone or breaks can be detected relatively easily by visual inspection. X-ray is cost effective and relatively quick to use with digital X-rays taking only a matter of minutes to be developed.

Despite the clear images that X-ray generates there are drawbacks to using radiographs to detect fractures as well as to monitor the healing process. X-ray provides a 2D projection of the bone meaning details of depth and the surface features of the bone are lost. When confirming the presence of a fracture and assessing its severity it is vital to gain two orthogonal radiographs. This is because what looks like a simple fracture in one plane may in fact be a severely displaced fracture when viewed in the orthogonal plane, see figure 2-4.

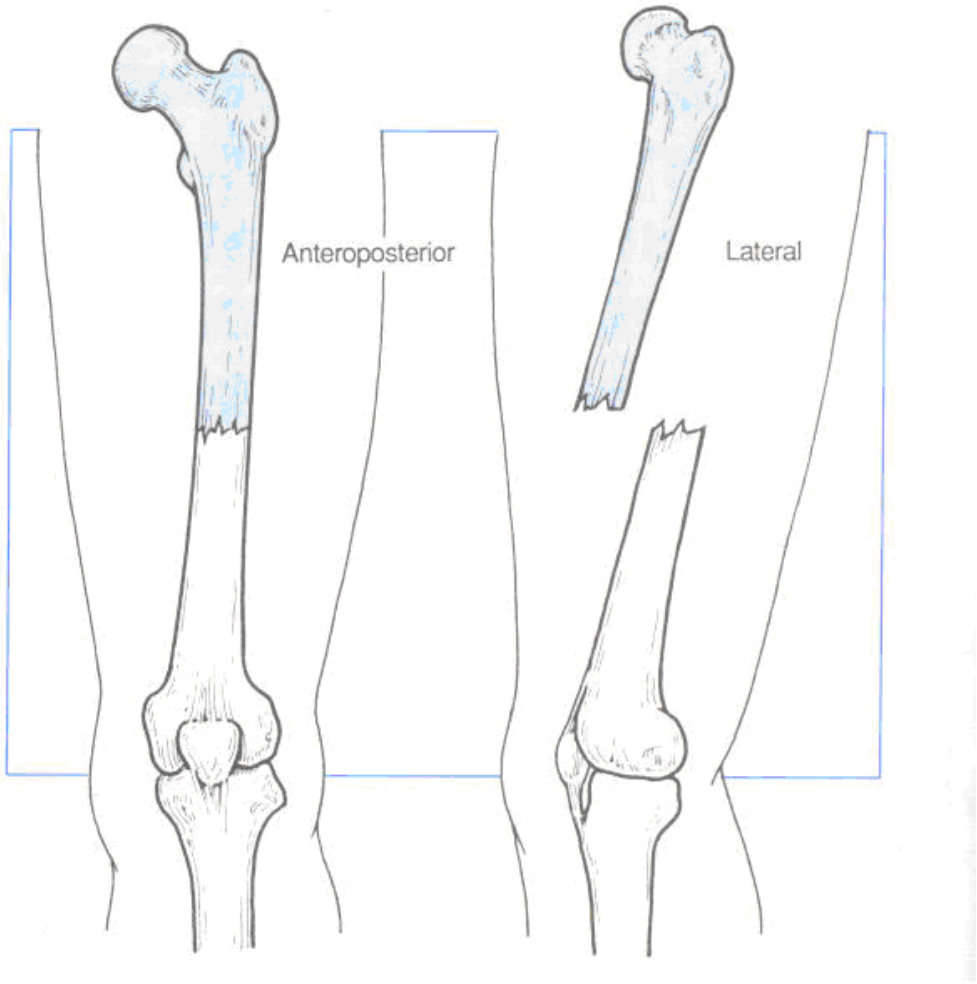

Figure 2-4: Two X-ray views of the same femoral fracture (12).

In some cases the haematoma present at the first stage of fracture healing may be detected on X-ray, however, it is far from being clearly visible. In addition, X-ray is unable to image the changes within the haematoma that occur during the second stage of healing. If complications have arisen which delay the second stage or halt it altogether it can be a number of weeks before this is confirmed by lack of callus on an X-ray.

As the fracture callus matures the visible fracture line on X-ray will begin to be obscured. The bridging callus has to be sufficiently dense with calcium to become visible on X-ray and for an adult this can take around 6-8 weeks. Due to the projection nature of X-ray images and the variability in the amount of calcification

throughout the callus it can be difficult to estimate the true callus volume accurately. Callus will appear as a "fluffy" region extending across and bridging the fracture gap and then blending with the bone ends when union has occurred (20). When a rigid internal fixation device such as a plate is used to stabilise a fracture the amount of callus generated is less because the callus is not required to provide stability (28). When the consolidation phase of the repair process is reached the fracture line will be almost invisible on X-ray concealed by the presence of a well defined callus surrounding the fracture site.

The stability and mechanical strength of a healing fracture cannot be judged from X-ray. When consolidation of the fracture is visible on radiographs the repair process is deemed to be complete and normal use of the limb is usually prescribed (20, 29). If the decision to remove the cast or fixation device is made and sound bony union has not been achieved the bone may re-fracture. There are no validated methods or marker scales against which the appearance of fracture repair on X-ray can be graded. The decision to remove a cast or fixation device is down to the individual clinician. It has been found that there is wide variation in the methods used to assess fracture healing on X-ray and the conclusions drawn about the state of healing (30, 31). This is discussed further in Chapter 6.

Patients undergoing limb lengthening are followed up regularly during the lengthening phase of treatment and require more X-rays than a simple tibial fracture patient, thus, they are exposed to greater hazard from an increased dose of radiation. Cysts can form within the distraction site during the healing process and these can be difficult to detect using X-ray. There are additional soft tissue complications which can arise during limb lengthening such as infection which can sets in around the tensioned wires and pins of the external fixation device which pass through the bone.

As previously mentioned complications may be indicated by the change in shape of the bone ends at the fracture sites, however, not all complications can be imaged sufficiently using X-ray. US can be used to image the surrounding soft tissues and to check for damage to the vascular network as well as provide images of the

surface of the bone. It is widely available in hospitals and is comparable to X-ray in terms of both cost and imaging time. There is minimal hazard to the patient from US, therefore, regular imaging of the fracture site can be undertaken without additional risk to the patient.

2.3. 2D Ultrasound

The term US refers to sounds which have a frequency above the audible range of human hearing, i.e. above 20 kHz (32). For diagnostic medical applications US frequencies within the range of 2-15 MHz are most commonly used, however, there are no naturally occurring sources of US (33). US waves are produced through the use of piezoelectric transducers which convert electrical wave energy into mechanical energy and vice versa. In other words, the transducer material is excited by the applied electrical signal causing it to expand and contract, thus, producing pressure waves within the medium which is in contact with the transducer; this is the inverse piezoelectric effect. The piezoelectric effect is the converse of this where a pressure wave impinging on the transducer causes an electrical signal to be produced see figure 2-5. A deformable elastic medium such as air or water is required to allow the pressure waves to propagate (34).

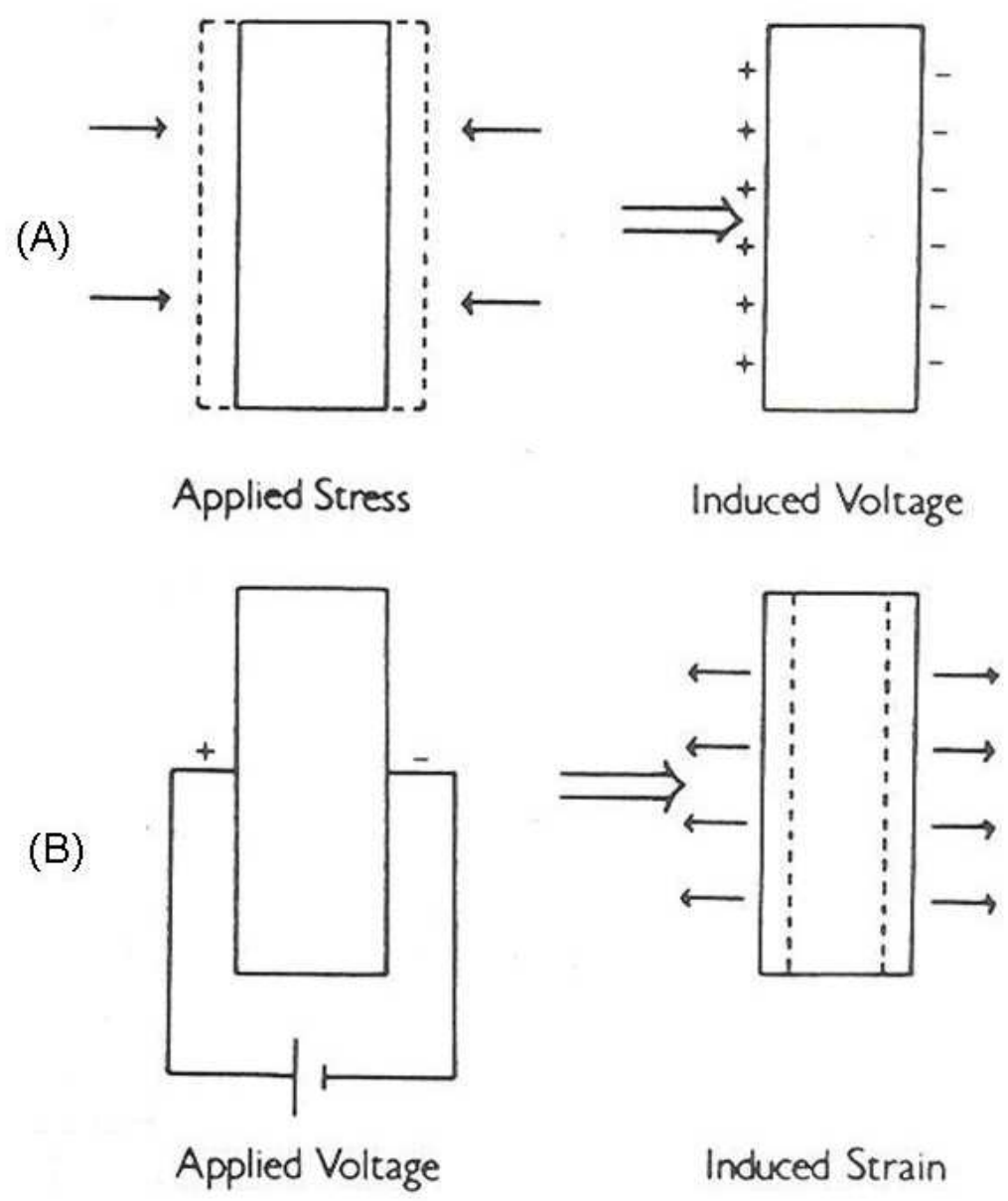

Figure 2-5: (A) the piezoelectric effect and (B) the reverse piezoelectric effect (33).

Both the piezoelectric effect and the reverse piezoelectric effect are used in US imaging. There are naturally occurring piezoelectric crystalline materials such as quartz, however, these are not very efficient (35). Lead-zicrconate-titanium (PZT) is a purpose grown piezoelectric crystal specifically conditioned for use in US probes (36). Figure 2-6 shows the basic construction of a single transducer US probe where a narrow rectangular piece of piezoelectric crystal is housed within a plastic casing.

The backing material behind the crystal is designed to dampen the oscillation of the crystal in order to produce the short pulses of waves required for US imaging. The chosen material will be impedance matched closely to the properties of the crystal so that the pulse length is restricted to only 2 or 3 wavelengths (32). The large difference in impedance between the crystal and patient tissue is overcome by placing a series of very thin matching layers of epoxy resin in front of the crystal to decrease the difference in impedance gradually (37).

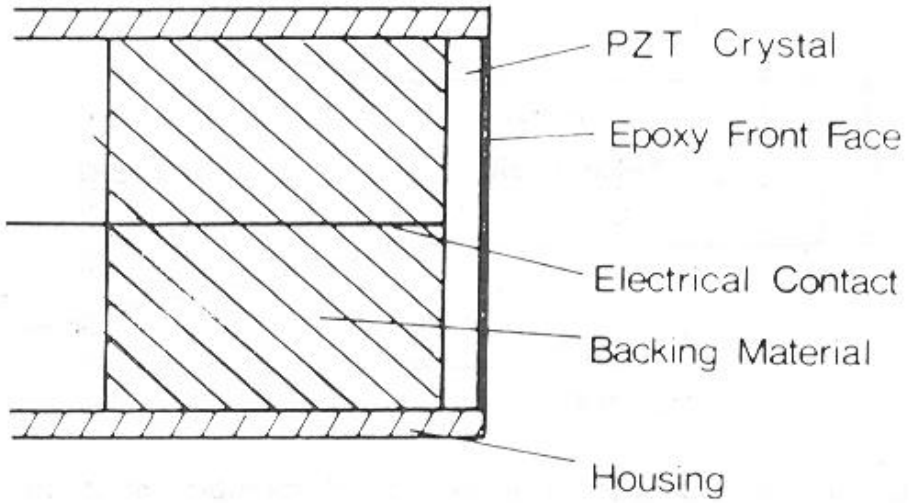

Figure 2-6: Basic internal structure of a pulse-echo single element transducer (33).

There are a variety of US probe types: linear, curvilinear, phased and mechanical (38). Their names relate to the arrangement of the transducer material within the probe housing. Only linear probes are considered here as this was the only type of probe used during the study. The term transducer specifically refers to the piece of piezoelectric material; though is also commonly used to refer to the probe as a whole.

A linear probe contains an array of narrow rectangular pieces of piezoelectric crystals acting as individual transducers where an array can contain between 64-600 elements and may be 3-20 cm in width depending on the intended application (32-34). The individual transducers in the array are fired in groups to produce a series of

small US beams. There is a short delay after firing to allow the reflected US pulses to be detected by the transducers before the next US pulse is fired.

The 2D greyscale images widely used in medical imaging are produced using B-mode imaging where the B refers to brightness in reference to how the images are displayed in varying brightness of greyscale. The images are often referred to as B-scan images. Figure 2-7 shows a B-scan image through the calf muscle; the different anatomical structures are labelled. There are three other types of US imaging: A-mode, M-mode and Doppler, the following references contain details of these (32, 35, 36, 38, 39).

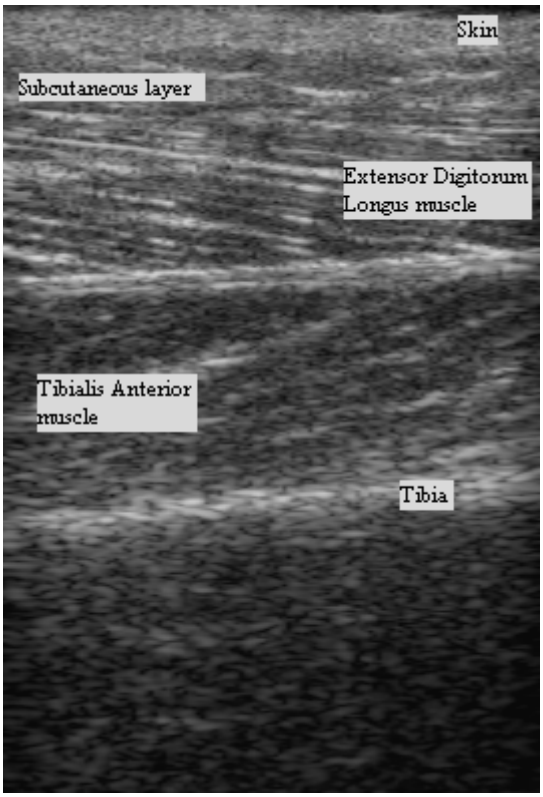

Figure 2-7: A B-scan image through the calf muscle where the different tissue layers have been labelled.

B-mode images are produced as a result of interactions of the US pulses with each of the tissues the US beam encounters. The transmission of an US pulse through a

medium is dependent on the acoustic impedance (Z) of that material where acoustic impedance is determined by the density (ρ) and speed of sound (υ),

$$Z = \rho\upsilon. \tag{2.1}$$

When the US pulse reaches a boundary between tissue types it is the difference in the acoustic impedance between the tissues which gives rise to the echoes visible on the image. The percentage of the US pulse which is reflected (R) from a tissue boundary is dependent upon the acoustic impedances (Z_1 and Z_2) of the two tissues at the boundary as given by,

$$R = \left(\frac{Z_2 - Z_1}{Z_2 + Z_1} \right)^2 \times 100 \tag{2.2}$$

The bigger the difference in the acoustic impedance between the two materials less of the US pulse will be transmitted and more will be reflected (39). An US pulse travels through human tissue at an average speed of approximately 1540 m/s. The speed of sound in blood, fat and water are all quite close to the average speed in tissue, however, for bone the speed of sound is much higher at 3500 m/s resulting in high reflection at the soft tissue-bone boundary (32). At each boundary part of the US beam will be transmitted and part of the beam will be reflected. Using the average speed of sound in tissue and the time between transmission and detection of the reflected pulse, the depth of the object causing the reflection can be calculated allowing it to be displayed at the appropriate position in the image.

Equation (2.2) used to determine the percentage of the US beam which is reflected assumes that the US pulse has a 90° angle of incidence at the tissue boundary (34). If the US pulse is incident at an angle of more that ±3º from the perpendicular very little of the reflected US pulse will be detected at the transducer (35).

As the US pulse travels through the body it is attenuated due to reflection, refraction, scattering and absorption (33). The random interference of returning reflections causes the background speckle present in the image (35). Attenuation increases as the frequency of the US pulse increases resulting in less depth penetration at higher frequencies. This has lead to the production of US probes at different frequencies (or frequency ranges) for imaging specific body parts dependent on their depth within the body.

As a result of attenuation the returning US pulse received by the transducer array is considerably weaker than the original transmitted pulse and the electrical signals generated by the transducer array have a wide range of amplitudes dependent on the intensity of the reflections (32, 33, 36, 38). The electrical signals are of Radio Frequency (RF) and are referred to as the RF signal. A set amount of gain is applied to amplify the RF signal this is termed the Received Gain (Rx) and is controlled by the scanner operator. The signals originating from deeper in the body are considerably weaker than those received at the surface. To allow reflections of equal intensity originating from different depths in the body to be displayed on the US image using the same intensity scale different amounts of amplification have to be applied to the signals. This is achieved using Time Gain Compensation (TGC) where the gain applied is dependent on the time taken for the signal to return to the transducer from inside the body. TGC is set by the scanner operator using a series of slider controls that relate to different depths as the amount of gain required is often dependent on the type of tissue being imaged. Next, the RF signal is demodulated, undergoing rectification and envelope detection to produce a video signal. Figure 2-8 shows this process. During analogue to digital conversion the amplitude of the video signal is sampled at regular intervals and values are assigned to a digital memory matrix according to their position in the original signal. Each amplitude value is assigned a corresponding greyscale intensity for display on the US image. After digital to analogue conversion the image information is displayed on the monitor of the US machine.

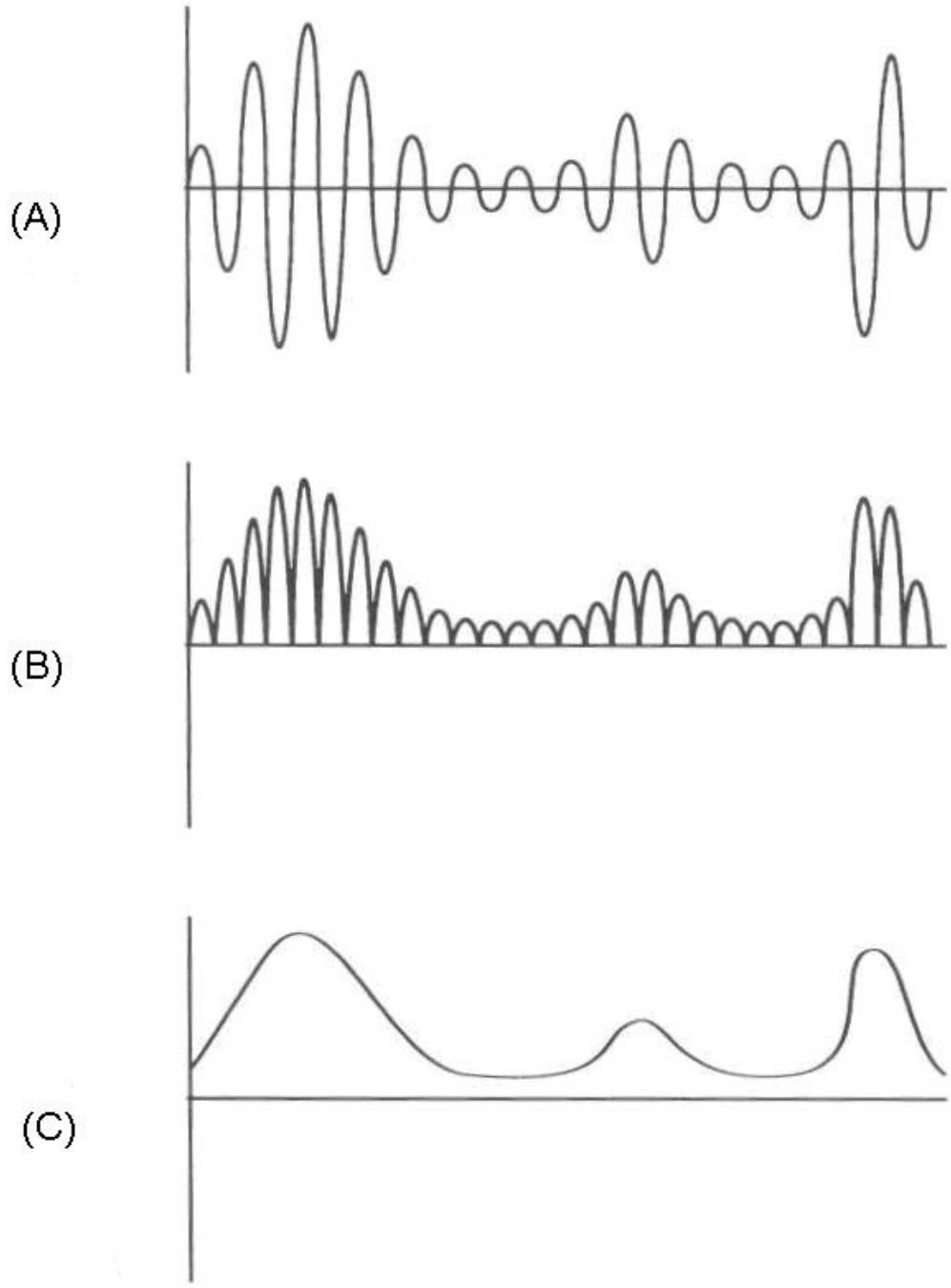

Figure 2-8: Demodulation process for the RF signal. (A) the RF signal. (B) RF signal after rectification. (C) RF signal component is removed leaving the signal envelope (32).

2.4. Musculoskeletal Imaging

A review article by Kaplan et al. described details of all aspects of musculoskeletal imaging, from the different US scanners used, to the various injuries and disorders that could be examined (40). In their paper it was stated that MR may provide images that are easier to interpret, however, this should not necessarily mean it is instantly the first choice of imaging modality. The least invasive and least expensive imaging technique should be considered, whenever possible, to confirm a diagnosis before requesting further detailed and often more resource intensive imaging studies.

Sonography has been employed to evaluate complications that have occurred with orthopaedic implants as well as to investigate the causes of anterior knee pain (41). Lin et al. imaged soft tissues defects and disease using 2D US (42). The imaging of bone and bone related disease using Sonography has been considered by Cho et al (43). Comparative X-ray, MR and US images are shown for a number of musculoskeletal complaints with US being promoted as the best modality for musculoskeletal imaging. The highly reflective nature of bone made US ideal for evaluating the bone surface which can be advantageous when investigating the presence of a fracture. Disruption to the smooth contour of the bone and the presence of a haematoma are clearly visible on US and are indicative of a fracture.

US has been compared with X-ray, CT and MR for the detection of fractures of the ribs and sternum (44-46). It was found that US could differentiate between old and fresh fractures from the presence of a haematoma; signs of fracture healing and bone remodelling could also be detected with US. Furthermore, the costal cartilage can be checked for signs of trauma. Despite these advantages it was concluded that X-ray was still the preferred method as the extent of the injury was indicated by the depth of dislocation and this was not as clearly visible on US. Also, scanning can be time consuming as well as difficult in obese, unconscious or uncooperative patients.

One of the main limitations of US is the need for the operator to interpret the series of 2D images viewed during scanning to form a diagnosis. There can be inter-operator dependency in the interpretation of the images which could lead to differences in patient management (3). Additionally, in cases that require follow up

with repeated measurements to be made of a specific part of the anatomy, it is almost impossible to find the same angle and transducer position that will provide the exact same view as in subsequent scans. Anatomical volume measurements are similarly very operator dependent. Two measurements are made with the transducer in one plane before it is moved to a perpendicular plane to obtain the third measurement in order to calculate a volume. The development of 3D US has helped address a number of the limitations of conventional 2D US in particular, obtaining accurate length and volume measurements, this is discussed further in Chapter 3.

2.4.1. Ultrasound for Monitoring Fracture Repair

The limitations of X-ray imaging and clinical assessment for monitoring facture healing are a long held concern. In 1958 Siegel et al. stated that the use of X-ray and physical assessment to monitor fracture repair was subject to error and that the volume of callus observed on X-ray did not correlate well with the true state of healing nor the clinical estimate of bony union (47). In a bid to reduce the error margins involved in callus assessment, investigations were carried out to measure how the change in speed of an US pulse passed across a fracture site related to the state of fracture healing. This technique was based upon long established methods for material testing. The aim was to provide an accurate method of assessing the degree of healing at any stage in the repair process as well as providing a means of identifying delayed healing or non-union earlier. Their method used separate transmitter and receiver probes placed above the bone to either side of the fracture site. A short sound pulse was transmitted and the time it took for the pulse to travel from transmitter to receiver was used to calculate the velocity of the sound across the fracture site. Velocity of sound travelling through a material is a property of its density and elasticity. By observing the change in velocity of the pulse as it travelled through the damaged bone the change in elasticity of the callus could be monitored. The tibia was studied in both human and animals as its close proximity to the skin and the flattened bone surface presented at the shin provided good testing conditions for the technique. The transmission of the sound pulse through the layers of skin and subcutaneous tissue were found to have no effect on the velocity of the sound pulse. In the animal study, changes were noted in the velocity

of sound and these were later identified, from the excised bones, as corresponding to different stages of the healing process. When calcification of the callus was underway the velocity of sound across the fracture began to increase and return towards that of normal bone. In the study monitoring healing in human tibial fractures, decreased sound velocity across the site indicated a non healed fracture.

The B-mode of US provides a method of imaging the changes occurring within the fracture site and at the bone ends as well as damage to the surrounding soft tissues. One of the first US imaging studies to investigate fracture healing, carried out by Riccardi et al., was designed to determine whether US could image the presence of periosteal callus before it became visible on X-ray (48). US was used to follow-up patients who had sustained a long bone fracture that had been stabilised using a mono-lateral external fixation device. At 7-11 days, the US images showed the fracture gap in detail, in particular, the sharp edges of the bone and the haematoma which was seen to extend over the edges of the gap. Two hyperechogenic collars of material became visible at 10-16 days post op extending from the periosteal region of the bone ends. The formation of collars starting to bridge the fracture gap coincided with the second stage of fracture healing as described in section 2.2.1. No signs of healing were yet visible on X-ray. Initial calcification of the hyperechogenic collars was signalled at 20-35 days by an increased brightness of echo. Small regions of callus started to become visible on X-ray at this stage. The appearance and echo of the bridging material became more uniform as calcification continued. US could no longer penetrate into the fracture gap at 35-50 days, and the bridging callus was now clearly visible on X-ray. At 50-90 days, the appearance of the callus on X-ray remained unchanged, however, on US the callus became sharper and the surface more clearly defined. The volume of the bridging callus was seen to reduce between 90 and 140 days as remodelling started to take place. No obvious change in the appearance of the callus was evident on X-ray.

A similar study comparing X-ray with US was carried out monitoring patients with long bone fractures for up to 1 year after discharge from hospital (49). The results of this study confirmed the observations of Ricciardi et al. and agreed with the accepted histology of fracture healing. Results of an MR study of fracture repair were

mentioned as detecting a similar healing pattern to US but no images or descriptions were included for direct comparison.

Two studies that have investigated the use of MR for monitoring fracture healing both identified a similar pattern of events during healing, which showed agreement with histology and US (50, 51). In addition, early signs of calcification of the callus were visible on MR before X-ray. However, no mention was made of the limiting factors of this imaging modality such as patient exclusion criteria (i.e. pacemakers), long waiting times for scans and also cost.

There are a number of papers discussing the role of US in limb lengthening procedures (11, 52-56). All agreed that US was superior to X-ray when looking for the first indications of bone re-growth, however, in terms of clinical use it was only a complimentary measure to X-ray and not a suitable replacement.

Maffulli et al. provided a thorough description of what can be seen on the US image between 0 and 8 weeks after the osteotomy operation (55). The value of US during the early stage of healing was recognised; more regular imaging of the lengthening site can be carried out without increased risk to the patient. The rate of growth and quality of ossification of the callus can be monitored effectively.

US has been used to evaluate the rate of new bone production during lengthening which has direct bearing on the rate at which the distraction process is carried out (11). Twelve patients were examined weekly using US along with standard X-ray starting at either 7 or 14 days post-surgery. In every case US detected new bone growth weeks before X-ray, bone formation was not visible on X-ray until 2-5 months after surgery. Signs of new bone formation on the sonograms were observed at 1-3 weeks in ten of the patients and in the remaining two patients it was 16 weeks before new bone formation was detected. Cysts of 1.5-2 cm were identified within the distraction sites for two of the patients using US but were not visible on X-ray. A disadvantage when using US for Ilizarov procedures was that during the initial stages of lengthening the rings on the frame may be very close together and it can be difficult, sometimes impossible, to scan the distraction site.

In a further study examining limb lengthening the size of the distraction gap measured on US images was compared with that measured from X-ray (52). In the early stages of bone re-growth the difference in width between the distraction gap visible on US compared to X-ray was taken to indicate the amount of new bone formation. Serial US examinations provided a quick and relatively accurate method of measuring the quantity and quality of mature callus laid down during the early stages of healing. US was found to complement radiography by reducing the number of X-rays required. It also provided a method of detecting cysts forming in the osteotomy gap and allowed the rate of callus growth to be monitored during the early stages of lengthening. In a similar study by Malde et al., US was found to be better than X-ray for detecting new bone growth, however, measurements of actual length gained during a limb lengthening process were found to be more accurate on X-ray (53).

US has also been employed to monitor the progress of fractures repaired by interlocking tibial nails (57). It was concluded that good fracture healing was underway when the nail was no longer visible on the US image due to substantial callus formation. Healing was still verified by radiograph, where 50% bridging callus visible on both the AP and Lateral X-rays was taken to be indicative of successful healing. Further work by the same group involved a pre-clinical study to determine the histological composition of the tissue, presumed to be callus on the US images, by using US guided needle biopsies (58). 100% correlation was found between the appearance of hyperechogenic regions on the US images and the presence of fibrous callus material in the biopsies. A clinical trial based upon this finding looked at forty-seven patients who had sustained a tibial shaft fracture which was stabilised using an interlocking tibial nail, the patients were followed up using both X-ray and US (59). Fractures were imaged at six weeks and nine weeks post op. The fracture site was imaged through three portals cut into the supporting cast which were equally spaced around the 270° visible surface of the tibia. The indication that healing was underway was that the nail was no longer visible through one of the three imaging portals. Bridging callus visible in at least two of the four views imaged by radiographs was taken to indicate fracture healing. US was found to have a positive predictor value of 97%; the average time to healing determined by US was 6.5 weeks compared with 19 weeks when using radiographs. It was recommended that US be used at six and nine weeks post fracture to assess the state of healing and to identify any

complications that may require surgical intervention. US examinations could identify when there was enough callus present around the implant to allow weight bearing and this was often weeks before signs of healing were evident on X-ray. However, the drawback that only 270° of the surface of the tibia was visible using US.

Additional advantages of US over other modalities include the ability to image the soft tissues surrounding metalware which is used to stabilise fractures (60). Both CT scanning and MR are affected by the presence of metal. In a CT scan metal will cause localised scattering of the X-rays producing streaks in the scan data. For MR, metal implants will cause distortion of the image around the implant and localised heating of the tissue and not all implants are suitable for scanning (36). Twenty one patients who suffered persistent symptoms following long bone fracture repaired using an internal fixation device were examined in the study using US and X-ray. Complications such as screw loosening, adjacent tissue infection, muscle impingement by metalware, and metalware loosening could all be identified on the US images as well as the radiographs. In the case of infection, US could be further employed to provide an accurate method of needle guidance for aspiration. Despite describing all these advantages, US was still only recommended as a useful adjunct to clinical assessment and radiology.

3D US has the potential to overcome the limitations of 2D US which have caused it to be relegated to a useful additional imaging tool to X-ray rather than a viable alternative. With 3D US the position of the probe is tracked and all the images viewed during the scan are recorded. By matching up positions and images a 3D dataset can be constructed which can be reviewed at any future date. Different imaging tools can be applied to the 3D dataset to make it easier to interpret the anatomy and also allow accurate volume and repeated length measurements to be made. To date no papers have been found that report on the use of 3D US for monitoring and assessing the process of fracture healing.

2.5. Imaging Muscle Volumes

The accurate volume measurements and extended field of view that 3D US can provide have potential application for measuring changes in skeletal muscle volumes. Change in muscle volume is an important biomarker in medical research, it can indicate progression of disease, signal response to treatment, and help predict recovery of muscle function after surgical repair. Furthermore, it can be used to measure the effects of specific physical training regimes and to quantify the changes in muscle due to the ageing process. Detailed and comprehensive studies of skeletal muscle are becoming more widespread in particular for studying the age related changes to muscles. With an increasing over seventy fives population more information about the changes to skeletal muscle after this age needs to be obtained (61). For example, we need to increase knowledge about the effects of training regimes to help maintain muscle function as we get older. Damage to muscles due to trauma or disease and wasting due to disuse will affect function and thus the ability to contribute effectively to the movement of the body.

The key to research in these areas is the ability to measure muscle volumes accurately and precisely. Muscle volume relates to muscle mass, strength, cross-sectional area (CSA), and power output as described by equation (2.3). Any change in the volume of the muscle will affect the strength and power as well as its overall mass. The power output of a muscle is a measure of the force that can be exerted when it is recruited for use, the greater a force a muscle can generate over a finite time interval the more powerful it is,

$$Mass = \frac{Strength}{CSA} = \frac{Power}{Volume}. \tag{2.3}$$

2.5.1. Skeletal Muscle

Skeletal muscles are attached to bones, either directly or via tendons, and are the only type of muscle which is voluntarily controlled through the nervous system. Groups of muscles work together in different arrangements in order to move the bones and joints of the skeleton to facilitate motion such as walking or rising from a chair (62).

Muscles only have the ability to pull by means of a contractile process. Muscular contraction occurs on a macroscopic scale, however, it originates from microscopic motion which is controlled by events at a molecular level (63). Scaling up the affect of multiple microscopic contractions to the macroscopic level throughout the whole volume of the muscle gives rise to a strong overall contraction. The volume of the muscle remains the same during contraction while the girth of the muscle increases to compensate (64). The pulling force, i.e. strength, which can be generated, is in proportion to the CSA of that muscle. However, the power output of a muscle is a product of both its length and CSA, i.e. its volume. The quicker the muscle fibre contractions can be engaged and the more fibres a muscle has the more power it will be able to generate when recruited for use. As power is dependent on volume a short fat muscle will have the same power output as a long lean muscle if both muscles have the same overall volume (65).

The quality and quantity of an individual's skeletal muscle changes considerably throughout their life time and this is a reflection of the type and volume of physical activity which is undertaken. Skeletal muscle is composed of two main types of fibres: type I and type II (1, 62, 66). Type I fibres are slow acting and recruited predominantly for endurance tasks where long lasting muscle contraction is required such as maintaining an upright posture. Type II fibres are fast acting and are involved in rapid contractions such as those in the muscles of the leg which control the foot and ankle during walking and running. Peak muscle strength is reached between the ages of twenty and thirty years after which muscle mass and strength begins to decline slowly at a rate of 1% per annum. After the age of fifty a more marked decrease in the strength and mass of muscle occurs (65). The consequences

of the menopause mean that these changes are more notable in woman than men. By the age of ninety years both men and women may have lost approximately 30% of their peak muscle mass. Specific training techniques can be employed by an individual to enhance the performance of the different muscle fibres which will lead to an increase in the size of that type of fibre. This is known as hypertrophy. Sprint training will increase the size of the type II fibres whereas marathon training will increase the size of the type I fibres. Previous studies have shown that muscle training undertaken by adults at any stage in life can increase the volume and performance of muscle (13, 67). Muscle fibres can be increased in size by regular exercise, however, they will decrease in size and waste away when no longer used, this is known as muscle atrophy. Fast type II fibres diminish rapidly after the age of seventy compared to the gradual decline of slow type I fibres. Muscles require a good network of blood capillaries and nerves to maintain muscle health, but, the progression of ageing results in denervation of the muscle which leads to atrophy and a permanent degeneration of muscle fibres. (1).

2.5.2. Methods of Determining Muscle Volume

Muscle volume can be measured directly or estimated from measurements of CSA. MR, CT and US imaging along with anthropometric measurements techniques have been used to obtain muscle volumes and CSA measurements. There are many forms of anthropometric measurements including limb girth, biometric impedance and skin fold pinch measurements used to estimate body fat percentage and muscle volume (1).

Despite having different methods of determining muscle volume there was no agreed validated standard against which each technique could be compared. The need for a validated ‘gold standard’ was recognised by Mitsiopoulos et al. (14) who used two phantoms to evaluate the accuracy of volume measurement obtained from MR. Volume measurements derived from MR were found to be within ±3% of the measured volume of the phantoms. In further investigations CT and MR imaging

were performed on a cadaver arm and leg, both limbs were then frozen and cross-sectioned at their mid point to provide comparative cross-sections. Both MR and CT were found to differ by ±1.3% from the actual muscle of volumes of the cadaver limbs calculated from the CSA measurements (14). It was concluded that MR and CT provided results which were a suitable standard against which other body composition measures could be calibrated. However, CT was not quantified using phantoms and was also found to underestimate absolute skeletal muscle area in the lower leg when the muscle CSA was less than 15cm².

A similar study of five healthy volunteers was carried out using MR and CT to measure the volumes of adipose tissue, muscle, skin, and bone (68). Compared to CT, MR was found to overestimate the volume of muscle, skin and also adipose tissue but underestimate the volume of bone. It was concluded that MR was suitable for making measurements of adipose tissue as the variation from CT was only 1-8%. However, it was not stated why CT was used as the reference measure nor if it was validated.

Validation studies frequently involve cadavers to compare volume measurements derived from MR with the measured volume of dissected muscles (69, 70). Using 10 cadaver shoulders, MR derived volume measurements were validated against water displacement volumes for a number of different muscles(70). This study was carried out on the basis that atrophy is a common occurrence after rotator cuff tears and will have a direct impact on patient recovery. MR was investigated as a means of providing pre-operative information to predict post-operative outcome and was validated using cadavers as a reference method against which anthropometric measurements could be compared. Significant correlation of $r^2=0.98$ was found between the water displacement derived volumes and MR for all rotator cuff muscles. None of the anthropometric measurements were found to be suitable predictors of post-operative outcome. It was concluded that MR could provide accurate information about muscle volumes pre-operative, however, cost and time were limitations of this technique.

MR is often used as the 'gold standard' reference when investigating anthropometric measurements. Change in muscle volume of the thigh is often taken as an indication of functional fitness, however, determining muscle volume requires an accurate estimation of the adipose tissue present (71). MR was the reference method for a validation study of anthropometric measurements used to predict the volumes of both the muscle and adipose tissue present in the thighs of nineteen healthy volunteers. It was assumed that the thigh could be modelled as a set of concentric circles representing bone, muscle, adipose tissue and skin. Anthropometric measurements of ten of the leanest volunteers were used to predict muscle and adipose tissue volumes. The assumed concentric circular model of the thigh was found to be valid, however, skin fold measurements used to predict volume of adipose tissue showed poor agreement with MR results. Predicted values of muscle volumes using anthropometric measures were found to be overestimated by 30% in the leanest volunteers compared to volume measurements from MR.

Anthropometric estimations of CSA have been used to quantify muscle mass in healthy volunteers and patients suffering from chronic obstructive pulmonary disease (COPD) (17). The ability to determine the extent of muscle atrophy is an essential part of a physical therapy assessment of these patients. Anthropometric measurements were found to overestimate the CSA at the mid thigh level in the COPD patients compared to MR. For the healthy volunteers, the anthropometric techniques were found to be insufficiently sensitive to distinguish between patients who were healthy and those suffering from COPD.

MR is described as being the most useful and safest non invasive imaging device to estimate human muscle volumes *in vivo*; the observable contrast between fat, muscle and bone gives clear distinction between tissue types (16). Eng et al. carried out a study to determine suitability of MR for accurately measuring the volume and size of specific muscles (72). Measurements of individual muscle dimensions would improve the predictive power of biomechanical models of the musculoskeletal system and aid understanding of muscle recovery after trauma and muscle atrophy due to aging and disease. Eng et al. criticised previously published MR validation

studies for not establishing the accuracy of serial volumetric measurements under realistic conditions. Their criticisms included grouping muscles without well defined bony compartments into a single set for volume measurement (69). Potential sources of error when measuring volumes from MR data are the field of view (FOV) chosen for scanning, spatial distortions caused by inhomogeneities in the magnetic field, and limitations of resolution and segmentation. Scans of phantom objects revealed that errors on linear measurements made in the acquisition plane were small, approximately 4%, however, out of the image plane these errors were significantly larger at approximately 25%. Seventeen cadaver forearms were scanned using MR before dissection to determine actual muscle volume. The large errors found to effect out of plane linear measurements were not considered to have as great an effect on the individual muscles of the forearm as they spanned a range of horizontal distances within the FOV. When comparing specific muscles, good agreement was found between the MR measured volumes and the volumes of the dissected muscles. There was a range of agreement, with a difference of 7-21% between MR and dissection measurements. Muscles with a high surface area to volume ratio were concluded to be effected to a greater extent by errors in segmentation resulting in the larger differences in volume.

Despite the variations in the MR findings for obtaining muscle volumes and CSA's, it is considered one of the best available imaging methods. There is no dose of radiation involved unlike with CT, muscle boundaries are clearly identifiable, and adipose tissue and bone can also be clearly seen. Muscle volume and CSA's derived from MR scans have been shown to be far more accurate than conventional anthropometric measurements. However, there are disadvantages to the use of MR: it is not possible to scan patients fitted with pace makers, metal surgical clips or some orthopaedic implants. During an MR scan patients are required to lay still for a prolonged period of time and some patients may find it an uncomfortable or claustrophobic experience. Post scan image processing required to remove motion artefacts can sometimes be time consuming and means results are not real time.

Access to both MR and CT scanners for research purposes can often be limited. Further to this it can be difficult to justify exposing healthy volunteers to the ionising radiation used to conduct a CT scan. With the increasing number of investigations into the effects of training, disuse and aging on muscle there is an increasing need to find an alternative imaging method. US has been proposed as it has the advantages of being portable, widely available, relatively inexpensive and there are few exclusion criteria for patients. There is good definition between muscle boundaries on US and it is possible to differentiate between bone, muscle, fat, tendons and connective tissue (15, 73).

US has been used to measure the volume of the tibialis anterior muscle *in vivo* in healthy volunteers (73). The measurements derived from US were validated against MR. Using a standard US machine, 11 axial scan images were recorded at equally spaced intervals along the length of the tibialis anterior muscle belly. The CSA of the muscle was measured on each axial scan and the volume of each scan section was calculated by treating the muscle as a series of truncated cones. By summing the volumes of each section the full muscle volume was determined. Comparison with muscle volumes determined from MR showed a difference in volume measurements of 0.20-6.86cm³. Concerns were raised about how errors in the positioning of the probe would effect volume measurement. It was found that if the transducer was held at an angle of between 10-20º to the skin, instead of perpendicular to the surface, this could introduce an error in the volume measurement of between 2-6.5%. Further concerns included the time it took to undertake the US scan (45 minutes as apposed to 20 minutes for MR) as well as the limited field of view. Finally, US was restricted to imaging only superficial muscles where delineation of muscle boundaries was clearest. Taking these factors into consideration US was still concluded to be a valid and reproducible method for measuring muscle volumes *in vivo*.

An alternative method of obtaining CSA from 2D US scans was developed be Reeves et al. whereby a series of overlapping panoramic US images of the vastus lateralis muscle were acquired (15). The US transducer was placed on the anterior

surface of the mid thigh perpendicular to the length of the muscle and moved slowly round to the posterior of the thigh. US images were captured at 30 mm intervals on the sweep round the thigh. Contour matching was used to line up and overlay the series of US images and produce a panoramic cross-sectional view of the muscle. The CSA was determined from the US images and compared to MR. A mean difference of ±1.7% was found. US was deemed to be a reliable and valid method for determining the CSA of the large muscles of the human body. However, the process of capturing the US images took more than three times longer than the MR scan. Concern was also raised about the contact pressure with which the transducer was held against the skin. Minimal pressure should be used to maintain contact so as to limit deformation of the underlying tissue which could cause errors in CSA measurements (15).

2D US has shown potential for acquiring muscle volume and CSA measurements. However, the approximations used to measure the volume of the tibialis anterior muscle would not give good enough accuracy to monitor the changes in muscle volume. The method developed by Reeves et al. to overcome the limited field of view of 2D US and obtain accurate CSA measurements was effectively a crude form of 3D US, however, it was time consuming to carry out. 3D US could potentially provide a means of obtaining accurate CSA's much quicker with less post scan processing and provide accurate volume measurements without the need for approximations.

2.6. Summary

Imaging of the musculoskeletal system has been shown to be an important means of assessing injury, the affects of disease and ageing as well as the progress of rehabilitation. The process of fracture repair and how to determine muscle volume measurements have been described further highlighting the need for an imaging technique that is easily accessible, suitable for imaging both bone and soft tissue, and which is not resource intensive. The currently available techniques of MR, CT, X-

ray and US have all been shown to have advantages in set fields as well as disadvantages which limit their usefulness.

MR and US showed the most promise as both could provide images of bone and soft tissue and could detect earlier signs of fracture repair than X-ray and CT. Despite being well suited for both roles MR has a number of disadvantages which limit its use: cost, scanning time, location restricted (i.e. not portable) and waiting times for non urgent cases can be long. Further to this patients with pace-makers and certain types of metal implants are not suitable for scanning. These disadvantages make MR impractical for the frequent monitoring required for fracture repair and mean it is costly method for assessing changes in muscle volume.

When used for monitoring fracture repair 2D US was found to be able to image the haematoma formed during the first stage of repair and could detect the first signs of callus development during the second stage of the healing process. As this is a non-invasive and non-ionising modality, monitoring of fracture repair could be carried out frequently with no risk to patients. US also offers a non-invasive, relatively inexpensive and flexible method of imaging muscle CSA and volume which had fewer exclusion criteria than MR.

Unfortunately the high operator dependency that occurs in scan interpretation, repeated length measurements and volume measurements has limited the use of 2D US. For monitoring fracture repair it has only ever been concluded to be a useful additional imaging tool to X-ray not a suitable alternative. The approximations required when making volume measurements mean it cannot provide highly accurate volume measurements. However, the development of 3D US has overcome many of the limitations of 2D US.

The focus of this work is to establish a 3D US system which is suitable for musculoskeletal imaging and trial this system in a clinical setting for monitoring fracture repair and measuring muscle volumes *in vivo*. The next Chapter introduces the field of 3D US and its development.

3. Electromagnetically Tracked Freehand Three-Dimensional Ultrasound

3.1. Introduction

Freehand 3D US has greatly reduced the operator dependency limitations of 2D US and has potential for imaging the musculoskeletal system. In this Chapter the development of 3D US is outlined with specific emphasis on the *StradX* software based sequential freehand 3D US system. This system is used in conjunction with an electromagnetic tracking system to investigate its potential for musculoskeletal imaging. It is referred to as the electromagnetic freehand 3D US (EM 3D US) system. An evaluation of this system using a series of phantom experiments and a healthy volunteer study is presented.

3.2. Development of 3D Ultrasound

3D US has the potential to overcome a number of the limitations of 2D US as well as the ability to expand and promote the use of US as an imaging tool in a variety of fields (4, 74, 75). The concept of 3D US is to record and "stack up" all the 2D US B-scan images viewed during a scan to build a 3D dataset which can then be manipulated and reviewed. The 3D aspect comes from knowing the position and orientation of the US probe during the scan and using this information to arrange the B-scan images into 3D space. There are a number of ways that this information can be obtained; these involve the use of tracking systems for the probe, specialist volume scanning probes, and also mechanical scanning arms. Advancements in technology over the past two decades have lead to the construction of a variety of 3D US systems.

The main components of a 3D US system are an US machine, a tracking system and specialised software. There are US machines such as the GE Voluson 730[2] that have 3D US software installed and use specialist motorised 3D US probes to record a volume of images, thus negating the need for external tracking. Other 3D US systems require the main components to be brought together separately. Freehand 3D US covers systems which use external tracking devices to monitor the position of the US probe. The key to freehand 3D US is that the motion of the US probe is not restricted, allowing a series of images to be obtained in any scan pattern. The use of a volume probe or a mechanical scanning arm is not freehand as the motion of the probe is restricted. Volume probes and mechanical scanning arms are suitable for scanning objects below a flat surface but would not be practical for scanning around a limb or across a shoulder. Freehand scanning allows the operator maximum flexibility in dictating the motion of the probe.

The review papers written by Fenster and Downey provide a comprehensive introduction to the field of 3D US (3, 4, 74, 76, 77). One of the main issues in freehand 3D US is the process by which the recorded image and position data is reconstructed into a 3D dataset. The most common method is to use a voxel array, similar to the process used to handle CT and MR images (78). The position data obtained during the scan is used to orientate the series of B-scan images into a 3D voxel array while the greyscale intensities from those images are used to assign voxel intensities, see figures 3-1and 3-2 (79). Not all of the voxels will be intersected by an US image and conversely some voxels may be intersected by more than one image. An interpolation algorithm is used determine voxel intensities once the US data has been placed in the array. This helps to offsets the effects of more than one US image intersecting a single voxel and also provides good approximations for filling in empty voxel array elements (78) .

[2] http://www.gehealthcare.com/usen/ultrasound/genimg/products/voluson730/index.html

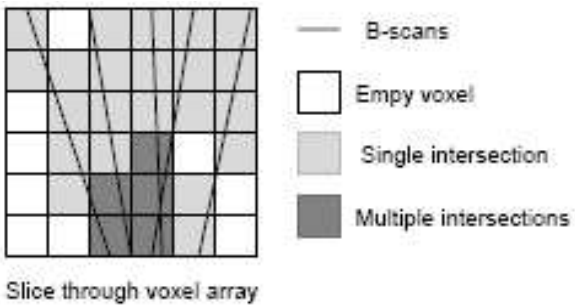

Figure 3-1: Constructing a voxel array from 3D Ultrasound data. Not all voxels will be intersected by an Ultrasound image and some voxels may be intersected by more than one (79).

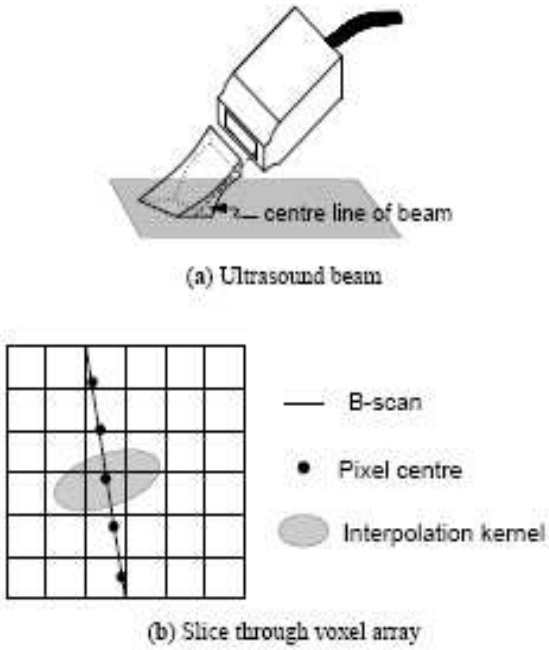

Figure 3-2: Interpolation for freehand 3D Ultrasound. The Ultrasound beam (a) has a finite thickness so each pixel in the B-scan samples a region of space which extends some distance normal to the B-scan. The interpolation kernel (b) should resemble this sampling function. Each B-scan pixel influences the contents of voxels lying within its interpolation kernel (79).

After constructing the 3D dataset a method to visualise the data is required. Common methods include: 2D any plane slicing, volume rendering and surface fitting. 'Any plane slicing' allows the operator to view a 2D slice through the 3D data at any point and in any orientation, this can provide views of anatomy which would otherwise be unobtainable using conventional US. Surface fitting and volume

rendering are both methods of producing 3D images from the dataset. A surface can be fitted to an object of interest such as a bone surface once it has been highlighted, through a segmentation process, to produce a 3D model. Surface rendering can also be used to highlight an object of interest by making use of differences in voxel intensities between objects in the US images. For example, surface rendering can be used to highlight the foetal skeleton by exploiting the difference in intensity of voxels showing the skeleton and those showing the soft tissues (3) .

The *StradX* software (Medical Imaging Group, Engineering Department, University of Cambridge) was developed as part of a *sequential freehand 3D Ultrasound* system devised to provide an accurate method of freehand 3D US (78, 79). The requirements for their system and software were established by carrying out a systematic review of all the aspects of freehand 3D US scanning (80). This review took into account the problems that arose during 2D US imaging and considered how those issues would affect a 3D US system. The effects of imaging artefacts such as speckle, refraction, shadowing and contrast resolution had to be taken into account when considering the image capture process and how best to display those images within a 3D dataset. *StradX* has a number of advantages over the software used by other freehand systems. The most prominent is the way in which it reconstructs the position and image data into a 3D dataset without the use of a voxel array. Removing the voxel array step reduces the time it takes to build the dataset and removes a stage of image processing that could otherwise introduce significant anomalies to the image data. Voxel arrays are ideal for CT or MR data where all the recorded images are parallel to one another but with freehand 3D US the B-scan images are seldom orientated in this way and placing non-parallel US images into a voxel array can lead to significant image artefacts (79). Instead, a method was devised whereby the properties of the B-scan images were used to generate the 3D dataset, this process discussed in detail in section 3.3.2. An advantage of this new technique was that only artefacts arising from the 2D scans would be present in the images and these should be easily identified by a trained Sonographer.

Calibration is a key process in setting up a freehand 3D US system for use. It determines the required transforms between the coordinate systems of the US probe, the tracking device and the real world in order to arrange the US images in a 3D dataset. Calibration also ascertains the clock drift between the images recorded from the US machine and the position data registered by the tracking device. Methods of calibration involve the use of phantom objects that are scanned in a specific way in order to obtain information from the images which is then used in a calibration algorithm. Common phantoms are the cross-wire phantom where the location of the crossed wires is used in the calibration algorithm, and single walled phantoms which provide a uniformly flat surface. The latter forms the best method of calibrating a freehand 3D US system (81). A series of images obtained from scanning the flat surface are used to establish coordinate relationships in order to construct a 3D dataset.

Confhusius (CalibratiON for FreeHand UltraSound Imaging USage) (82) is a robust and fully automatic calibration procedure for freehand 3D US that is claimed to be more accurate than other available techniques including that employed by the *StradX* software package. It is a single walled phantom calibration technique similar to that utilized by *StradX*. It uses US images of a flat plane, obtained from scanning a Plexiglas plate phantom in a water bath, to provide the visual information required to run the calibration algorithm. Both intensity and gradient information are used to extract points of interest from the US images which correspond to the US echo from the flat plane of the phantom. Rosseau at al. found that neither the use of intensity or gradient information alone was sufficient to carry out accurate extraction of point of interest from the B-scan images to obtain the required data points for calibration. The validity of this new method for extracting points of interest was tested using both 2D and 3D data. Tests carried out to compare the accuracy of the *StradX* calibration process with that of the *Confhusius* process found that the latter method was more accurate and reliable. Residual mean square (RMS) errors returned from the final iterative process used to optimise the calibration results were 0.545 mm with a standard deviation of ±0.095 mm for *Confhusius* compared to 1.487mm with a standard deviation of ±0.729 mm for *StradX*. Although *Confhusius* provided a

calibration algorithm which required no operator input, unlike *StradX*, thus removing operator error, it was significantly more time consuming taking twice as long to carry out.

3D US offers a method of obtaining more accurate volume measurements than 2D US (4, 83). When using conventional 2D US, organ volumes are calculated by approximating it to a known mathematical shape before applying correction factors. This process can lead to errors of more than 20% (84). One of the earliest studies into the use of 3D US for volume measurements of organs used an acoustic spark gap tracking system to track the position of the US probe during scanning (83). A spark gap tracking system consists of an array of three spark gaps mounted on the US probe and a series of three microphones positioned over the region of interest. Spark gap systems require the operator to push a foot pedal when the position of a point of interest is to be recorded. This causes the spark gaps to be fired in turn, with the time between the spark gap firing and the microphones detecting the noise being used to determine the location and orientation of the probe through a process of triangulation. *In vitro* experiments showed the system to work well, the volumes of simple phantoms could be measured to within ±2% of their actual volume. For more complex phantom objects the volume measurements varied from the actual measurements by ±6%.

During the development of the *StradX* software two algorithms were investigated for displaying and calculating the volume of 3D models for a scanned object, these were *Cubic Planimetry* and *Maximal-Disc Guided Shape-Based Interpolation*. Both techniques were subject to a series of *in vitro* and *in vivo* test scans to evaluate accuracy (84). The test scans also provided a means of determining the minimum number of B-scan images required to produce a detailed 3D model and return accurate volume measurements. *Cubic Planimetry* was found to give the most accurate measurements and as few as ten segmented B-scans could be used to calculate the volume of the scanned object to within ±1% of its actual volume. The *Maximal-Disc Guided Shape-Based Interpolation* algorithm was found to be better at surface reconstruction of the volumes, particularly for complex shapes. It was

suggested both algorithms could be utilised in turn, firstly to calculate the volume of the object and then to construct a precise surface model.

An adapted *Shape-based Interpolation* algorithm improved on the abilities of the *Maximal-Disc Guided Shape-Based Interpolation* in a further development of *StradX* (85). To test *Shape-Based Interpolation* it was applied to a variety of different types of image data including CT; MR and 3D US data along with the *Maximal-Disc Guided Shape-Based Interpolation* algorithm. This provided a visual comparison between surface reconstruction methods. The original process was limited by the distance between segmented contours as if adjacent contours were more than a set distance apart the contours could not be used to form a surface. For the adapted *Shape-Based Interpolation* method detailed surfaces could be constructed from less contours than the previous method allowing quicker surface fitting. This algorithm was incorporated in to *StradX*.

There are a variety of external tracking systems that can be used for freehand 3D US. Electromagnetic (EM) tracking systems are commonly used for tracking the position and orientation of the probe. One of the considerations when using this type of system is the distorting effect that metal objects or sources of other EM fields in or near the scanning region may have on the tracking field. Assessment of two direct current (DC) systems, the Ascension Birds and Ascension Mini Bird, in comparison to an acoustic spark gap system has been carried out in a mock clinical environment (86). Ellipsoid phantoms of known volume were used to compare the volume measurement accuracy of a freehand 3D US system for each of the tracking systems. Three experiments were carried out where the amount of ferromagnetic metal within the scanning environment and the proximity of the US machine (a potential source of additional EM fields) to the tracking system was varied. The different scanning scenarios were:

1. There was no ferromagnetic metal within the scanning environment and the US machine was not within 30 cm of the tracking system.

2. The phantom object and the tracking system were placed on a metal frame patient examination table. The US machine remained in the same place.
3. The phantom and the tracking system remained on the patient examination table and the US machine was brought within the field of the tracking system.

Both of the EM tracking systems improved on the method and restrictions of the acoustic spark gap system. However, it was found that both the presence of other EM fields and ferrous metal in the near field scanning environment caused underestimation of the measured volumes. In the second experiment, both the Bird and Mini Bird tracking systems were found to underestimate phantom volume equally while during the third experiment the Bird system performed worse than the Mini Bird system. It was noted that there were no obvious visual signs of distortion to 3D models constructed from the datasets of any of the experiments. The conclusion was that if there was no conductive metal or other sources of EM radiation, such as the US machine itself, within the field of the tracking system then either of the DC EM field tracking systems would be suitable for clinical use.

A different model of the Ascension Bird DC EM tracking system was evaluated by Detmer et al. using a non planar cross-wire phantom (87). This was used to assess the spatial precision of the system and determine what effect the presence of the US machine and positioning of the receiver unit of the tracking system had on calibration accuracy. This was achieved by repeatedly scanning the phantom and locating the point where the wires crossed whilst the US machine was operated in different modes. The RMS uncertainty of the tracking system when the US machine was turned off was 1.2 mm and this remained the same when the US machine was switched on and operating in different modes. It was concluded that the US machine, the metal within the probe head and also the EM fields generated within the probe had no detrimental affect on the tracking system. The phantom was moved to different points in the tracking field to ascertain whether RMS uncertainty varied with location. As the distance between the receiver and transmitter of the tracking

system increased there was a marginal increase in the RMS uncertainty returned by the calibration process. This also increased as the distance between the receiver and the object being imaged increased. It was concluded that the receiver should be mounted as close to the head of the probe as possible to minimise this error as for every 1cm away from the probe head that the receiver was mounted added 0.1 mm to the RMS uncertainty.

Despite 3D US being around for more than 15 years, there have been no randomised control trials published that have compared the abilities and validity of 3D US systems against those of 2D US (75). In many of the 3D US trials that have been conducted the problem that was examined would often be first identified using 2D US before further 3D US investigations took place. In order for 3D US to be considered as a clinically useful and viable tool it would need to improve on the imaging abilities and the positive predictor value of 2D US. Although 3D US is seen to be a progression over 2D US it must be remembered that 3D US is highly dependent on the 2D US machine and also the skill of the operator. Manipulation of the 2D images by the 3D US software and image interpretation must also be taken into account. Furthermore, there are artefacts that are unique to 3D US, which include patient motion as well as segmentation and rendering errors. Artefacts carried through from the B-scan images are also a source of 3D US artefacts. The potential of 3D US to be a highly accurate diagnostic tool is acknowledged particularly for making estimates of foetal weight (75), however, further investigation is required before 3D US becomes a widely accepted clinical tool.

3.2.1. Applications of 3D Ultrasound

Applications of 3D US are varied and wide ranging covering a number of medical fields including obstetrics, gynaecology, orthopaedics, cardiology and urology (5-7, 26, 88). The earliest reported use of 3D US imaging was in the field of Cardiology in 1974 (88, 89). The most familiar application is for foetal imaging where it can provide surface rendered 3D images that allow the whole foetus to be examined more easily, especially the extremities, meaning potential birth defects may be more readily

identified (5). However, studies comparing 2D and 3D imaging of the foetal skeleton have found 3D US to be only as good as and no better than 2D US; 3D US simply provides easier to comprehend images (90-92). Studies measuring foetal lung and heart volumes have been carried out (93-96) and 3D US has also been investigated as a method of identifying occurrences of cleft palate in unborn children (97).

In urology there is particular interest in using 3D US to determine the size of, and monitor changes in, the prostate gland (7). Gynaecological applications of 3D US include measuring the length of the cervix and determining the shape and volume of the uterus as well as examining the ovaries to diagnose polycystic ovary syndrome (6). 3D US has undergone clinical testing for the imaging of large organs (76, 98) and also as an alternative method to mammograms for imaging lesions and tumours of the breast (99-102).

The musculoskeletal system is one of the more difficult structures of the body to image with US as it is made up of a number of tissue components: skin, subcutaneous fat, ligaments, tendons, muscles and bone. All of these components have different acoustic properties which will affect how they are displayed in an US image, see discussion in section 2.3.1. The advantage of a 3D US scan is that a greater amount of anatomy can be visualised making it easier to identify structures (88). Studies looking at the detection and identification of muscle hernias and lesions have found 3D US to be as good as 2D US at evaluating these types of musculoskeletal injuries (26, 103). For small lesions the scans provided by 3D US made identification easier and provided better visualisation of lesion boundaries. In Chapter 7 3D US is investigated as a means of measuring muscle volume *in vivo*.

The *StradX* freehand 3D US system has been trialled for carrying out examinations of the brachial plexus (104) and also the neonatal foot (105). MR imaging can provide detailed views of the brachial plexus, however, careful positioning of a 2D US probe can also provide images of nerve and arterial structures allowing it to be used for image guided administration of anaesthesia for nerve blocking. 3D US

provided a map of the region around the brachial plexus. The nerve and arterial structures could be identified and modelled along with the location of the first rib. 3D US allowed scanning across the required region of the neck without any restriction and provided detailed models of the flattened shape of the brachial plexus which may be useful for diagnosing injuries and for radiotherapy planning.

Abnormalities in development of the neonatal foot are normally diagnosed by physical assessment as conventional radiology is of limited use due to the un-ossified nature of infant bones (105). Using *StradX* a 3D model of the deformed foot could be constructed which may provide a surgeon with a better understanding of the composition of the bones prior to surgical intervention. Alternatively, when using conservative methods to treat a deformity, 3D US could provide a safe and easy way of monitoring the progress of treatment.

Imaging of the intra-articular structure of the knee joint is possible with 3D US potentially offering a new imaging methodology in the field of rheumatology (106). The use of 3D US for imaging bone has been trialled in a few areas. A system which incorporated a volume probe was used to image occurrences of hip dysplasia in infants (107). Diagnosis was compared to conventional 2D US and it was found that 3D US could provide views of the hip which were otherwise unobtainable using only 2D US. However, drawbacks were identified, the most notable being the time taken to acquire the scan as the patient must remain still for approximately five seconds to avoid degradation of the image data. Also, construction of the data into a viewable 3D dataset took up to four minutes, negating the real time benefits of US imaging. It was concluded that 3D US had demonstrated potential for use in imaging dysplasia in the infant hip, though further development of the 3D US system was required.

The feasibility of using 3D US to image bone lesions has previously been investigated (108). In a study involving 40 patients 3D US scans were carried out on sites of confirmed bone or soft tissue lesions. In 51% of cases the 3D US data enhanced the diagnostic value compared to conventional 2D US. Additional findings from 3D US scans led to a change in planned treatment for ten patients. Normally

radiography is used to determine the presence of a suspected bone lesion, but, 3D US was proposed as an alternative method.

3.3. StradX

StradX is a software package specifically designed for *sequential freehand 3D US* which runs on the Linux operating system (79). The 3D US system comprised of an Ultrasound machine, an additional PC to run *StradX* and an external tracking device. The process of acquiring and displaying 3D US data using *StradX* is broken down into three separate stages. First, the position and image data is acquired, then the data is then constructed into a 3D dataset, and finally the dataset is converted into an easily interpreted visual form. It is in the second stage that *StradX* differs from other 3D US software packages as it constructs the dataset without the use of a voxel array. Avoiding the use of a voxel array eliminates the problem of putting irregularly sampled data into a regular array as was discussed in section 3.2.

StradX is a real time system as the process of calculating the position and orientation of the images and construction of the dataset is done as the data is received making it possible to display the dataset as it is constructed. During scanning two acquisition processes are occurring simultaneously within *StradX*: image acquisition from the US machine and position data acquisition from the tracking device. Acquired images and position data are both stored in circular buffers within the computers main memory. Each B-scan image obtained is labelled with a time stamp and stored in sequence in one circular buffer. Position readings are requested from the tracking device at a set rate and each time one is requested a time stamp is generated. The time delay between position requests being issued and the reading being recorded is approximately constant and is calculated during the calibration process (79). Adding this time offset to the position reading request time stamp gives the approximate time at which the reading was recorded.

The most recently acquired position reading is not simply assigned to the most recently acquired US image. To ensure there is minimal error introduced into the dataset a more accurate approach is adopted. The process of matching the correct position to a recorded B-scan image is achieved using the circular buffers in the computer memory. One circular buffer contains the five most recently acquired B-scan images while the other buffer contains the five most recently acquired position readings, see figure 3-3. An age offset is built into the image sampling process meaning that the most recently obtained image is ignored; instead the most recently obtained image within the set age range of the sampling window is selected. By ignoring the last recorded image and choosing a slightly older one, it is highly likely that there will be position readings available at time points either side of the sampled image. Linear interpolation is used to determine the position of the sampled image from the position information available just before and just after the image was recorded. To ensure an image is always available within the sampling window, the age range of the window is set to be approximately one and a half times that of the image sampling period. The age offset of the sampling window is dependent on the type of tracking system used; different tracking systems have differing latencies. Latency is determined during the spatial calibration process which is discussed in section 3.3.1.

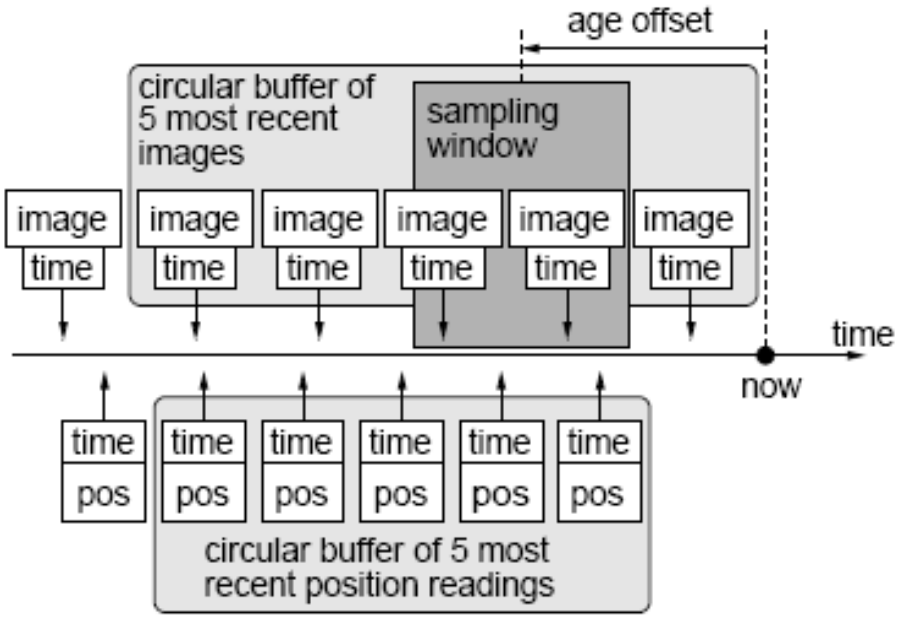

Figure 3-3: Visual representation of the image sampling process used to match up image and position data correctly (79).

3.3.1. Calibration

Two separate calibration processes must be carried out each time the 3D US system is switched on, *Temporal Calibration* and *Spatial Calibration*. *Temporal Calibration* involves calculating the approximate latencies in the position sensor device and taking them into account during *Spatial* calibration if required. *Spatial Calibration* involves determining the transformation relationships between the co-ordinate systems of the US images, the tracking system and the real world. The co-ordinates of each pixel in the B-scan image are transformed into the co-ordinate frame of the tracking sensor using the calibration parameters. These are then transformed into real world space using the tracking sensor readings. The final part of the *Spatial Calibration* process involves an iterative algorithm to optimise the calibration parameters which determine the co-ordinate transform relationships. The RMS error from this iterative process is returned at the end of the calibration and its size provides a guide as to the quality of the calibration. An RMS error of less than 0.06 cm is indicative of an accurate calibration (109). Both calibration processes require the use of a single walled phantom in a water bath to obtain the series of US

images necessary to run the calibration algorithms. Full details of the calibration process are given in appendix A. It is the coordinate transform relationships determined during the calibration process which are used to position the recorded B-scan image sequentially in the 3D dataset.

3.3.2. Visualisation

Two visualisation tools are immediately available in *StradX* once a scan is complete; *Reslice* and *Panoramic* imaging. The immediate availability of these visualisation tools is down to the way in which *StradX* takes into account the full properties of the US images when constructing the 3D dataset. Although a B-scan appears as a 2D image on the US machine (and within the display window in *StradX*) the US beam actually has a finite thickness of a few millimetres. The most relevant data comes from the centre of the finite thickness of the image and this is what is shown on the screen. By taking into account this extra dimension of the beam, *StradX* provides almost instant 3D visualisation of scan data. Images are acquired at a sufficiently high frame rate during scanning so that when they are recorded, placed in the 3D dataset and the finite width of each B-scan is taken into account the series of images overlap. The data from the centre of the B-scan is used first in the production of a continuous 3D dataset with any remaining gap between the adjacent images filled using equal amounts of image data from the finite thickness of both images.

Reslice allows the operator to take a 2D slice through the 3D US dataset in any plane and orientation thus permitting views of the scanned object which may not normally be visible using ordinary 2D US. When a *Reslice* is requested the point at which the *Reslice* plane intersects each B-scan in the 3D dataset forms a polygon surface through the width of that image. The US greyscale intensity information from the polygon slice of the B-scan is transferred onto the slice plane. Repeating this process for each B-scan that the *Reslice* plane intersects allows it to be tiled with polygons of greyscale intensity data, thus, producing the *Reslice* image. Figure 3-4 shows an example *Reslice* image taken from a scan down the length of a calf muscle. This

Reslice is taken in a plane parallel to the direction of scanning and provides an extended view of the calf muscle, a single image from an US probe would not be able to cover such a large field of view.

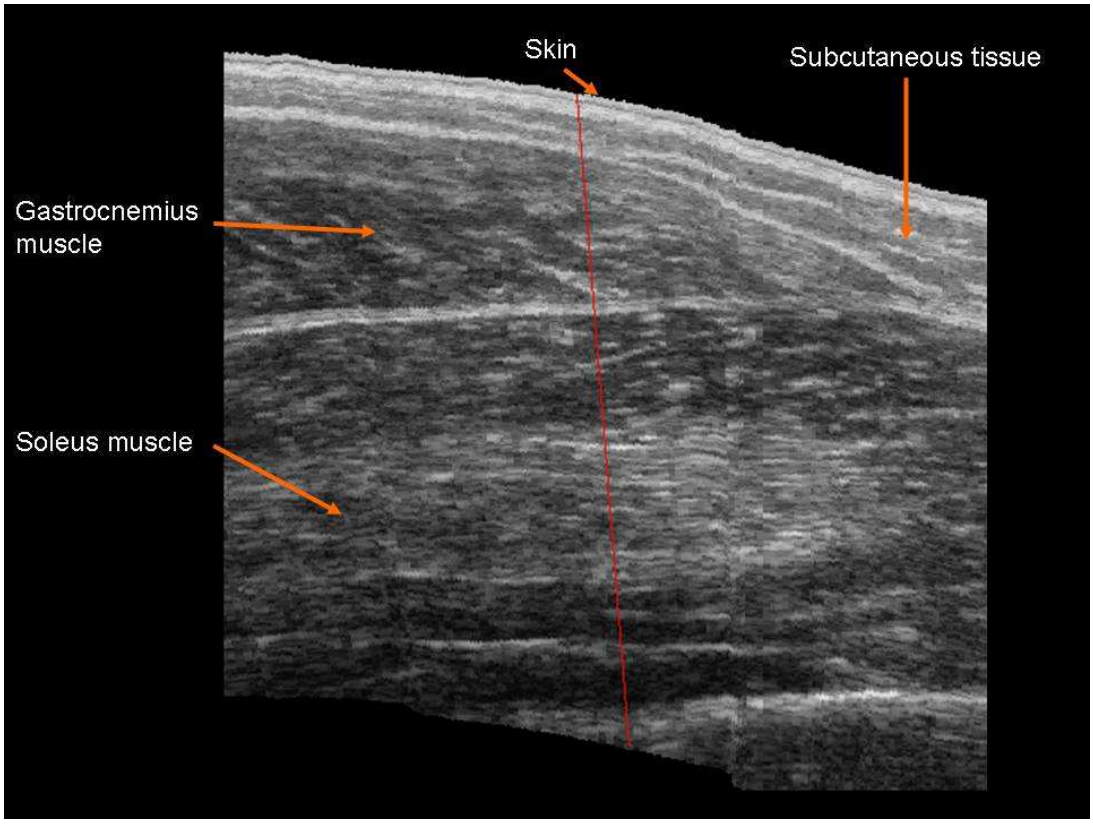

Figure 3-4: *Reslice* image of the calf.

Panoramic imaging can be used to provide a wide angled view of long structures by stitching together information from a series of B-scan images into one seamless panorama. In order to do this the US images must have been recorded within the same plane, i.e. the probe is moved in a sideways motion capturing a band of images only one B-scan thick. The information used to generate the *Panoramic* image comes from the centre of the finite width of the US images. *Image Registration* is first carried out on the B-scan images to correct for small errors in position sensor readings and probe pressure fluctuations (110). A rigid body transformation is then calculated using the position sensor readings obtained from the n^{th} and neighbouring

n+1 US images. This transform is used to map pixels present in the *n*+1 US image onto the co-ordinate system of the n^{th} image so that both can be visualised seamlessly stitched together as one. This process is repeated for the series of images making up the panoramic scan. An example *Panoramic* image of the front of the neck is shown in figure 3-5.

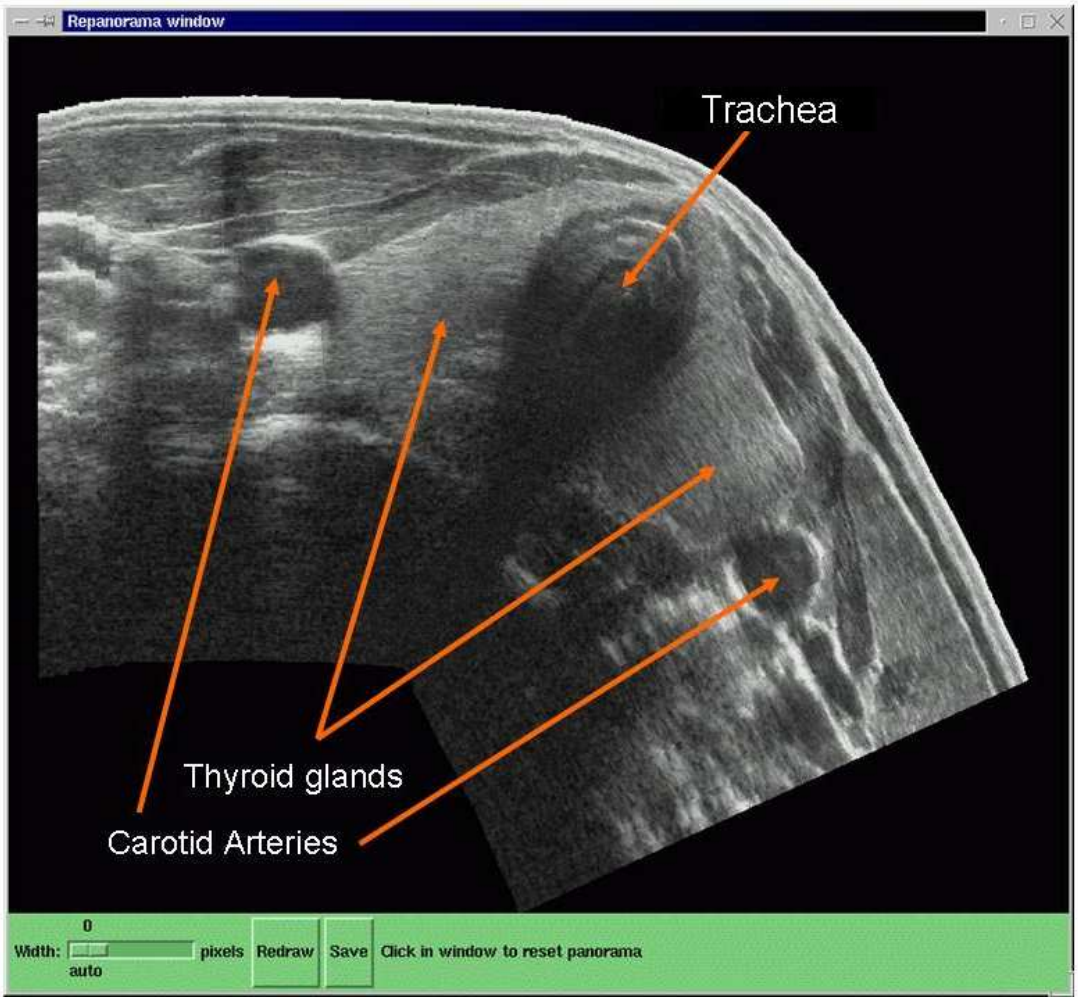

Figure 3-5: *Panoramic* image obtained from a scan of the front of the neck. Both lobes of the thyroid gland can be seen.

3.3.3. Surface Fitting, Manual Segmentation and Volume Measurements

When using a standard 2D US machine, volume estimations are calculated by finding the best view of the object's width and height and recording measurements before rotating the probe by 90° and measuring the object's length. Taking into consideration the approximate shape of the object these measurements can be used to estimate volume. However, calculated volumes can be out by as much as 20% (98). When measuring the volume of an organ, for example, several correction factors are taken into account; these include the age and sex of the patient and the type of organ. By obtaining a 3D US scan of an organ it is possible to make an accurate volume measurements as its full shape can be observed. If the organ or object of interest cannot be fully captured within one sweep of the US probe *StradX* has a *Multiple Sweep* function which allows multiple parallel scans to be stitched together into one 3D dataset (111).

Construction of a 3D model in *StradX* begins with *Image Registration* before objects of interest are segmented at regular intervals throughout the dataset. Two methods of segmentation are available in *StradX*, manual segmentation carried out by hand and semi-automatic segmentation that requires both user input and as well as an automated algorithm. Manual segmentation involves highlighting the object of interest on multiple B-scan images. Normally, the first and last images which show the object are segmented along with a selection of images in between. Semi-automatic segmentation requires operator input to initially highlight the object using a pair of threshold controls. Regions of the US images which have greyscale intensities within a set range, specified using two slider controls, are highlighted on screen as magenta in colour. The interval at which the images are segmented is set by the operator before initiating the algorithm to carry out the automatic segmentation process. The basis for the algorithm is that the structures of interest that have been highlighted magenta will have boundary contours plotted round them. Semi-automatic segmentation is most effective when there is good contrast between the intensity of the object and its surroundings, such as the foetus in the womb.

Once segmentation (manual or semi-automatic) is complete it is possible to obtain a volume measurement for the segmented region. There are two ways in which *StradX* calculates volume, one method uses the C*ubic Planimetry* algorithm and can be carried out without first fitting a surface to the segmented data while the other method uses S*hape-Based Interpolation* and fits a surface to the segmented data before returning a volume.

3.4. Setup of the Freehand Electromagnetic 3D US System

This section describes the components and setup of the freehand EM 3D US system consisting of a Diasus US machine (Dynamic Imaging, Livingston) with two US probes suitable for musculoskeletal imaging (5-10 MHz and 8-16 MHz), a PC running the Linux operating system and *StradX* software (Medical Imaging Group, Engineering Department, Cambridge University), and a Flock of Birds (FOB) electromagnetic tracking system (Ascension Technology, USA). Versions 7.2, 7.3 and 7.4 of the *StradX* software were used during these investigations.

The FOB is a pulsed Direct Current (DC) EM tracking system that is made up of three main components: a transmitter, a receiver and a control unit. These are shown in figures 3-6 and 3-7. A schematic diagram of the complete EM 3D US system is shown in figure 3-8.

Figure 3-6: Flock of Birds electromagnetic field transmitter (left), Flock of Birds control box (right).

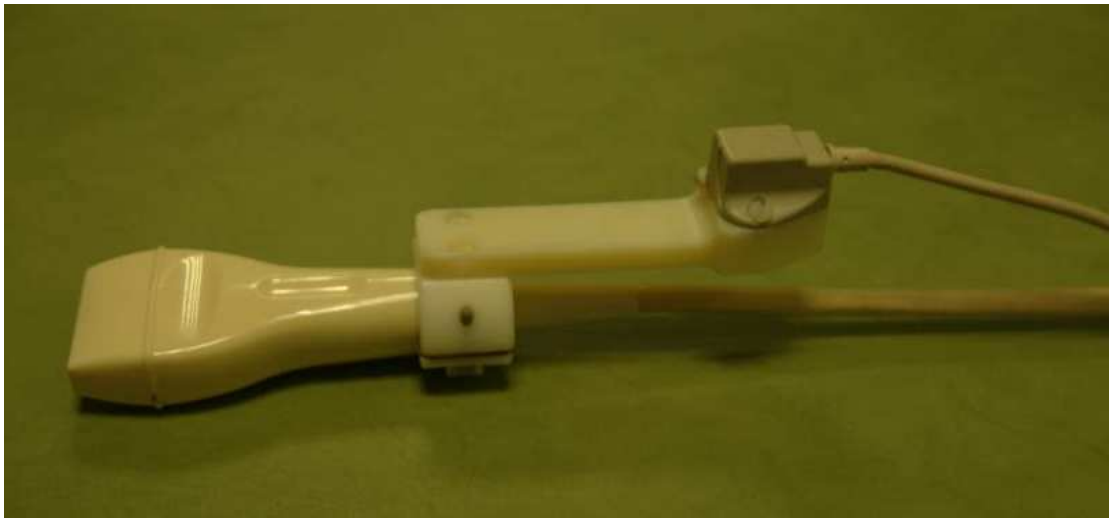

Figure 3-7: Flock of Birds receiver mounted on a 5-10 MHz Ultrasound probe.

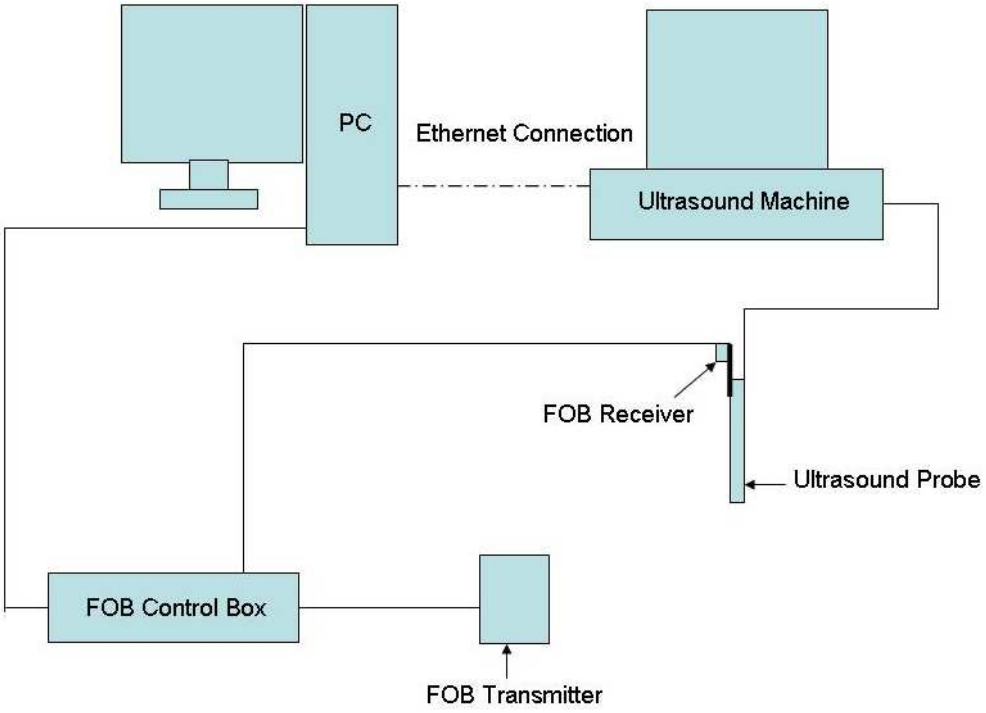

Figure 3-8: Schematic diagram of the electromagnetic freehand 3D Ultrasound system.

The transmitter unit generates a pulsed DC EM field extending out from the front half of the transmitter to a radius of 1.2 m. The field has been evaluated by Ascension Technology as having a positional accuracy of 1.8 mm RMS for tracking between distances of 20.3-76.2 cm from the unit[3]. No other details are given by the manufacturer as to the specification of the field. The FOB receiver unit is attached to the US probe using a specialist mount purpose built to ensure the receiver unit is offset from the probe head, see figure 3-7, in order to minimise any interference from the electronics within the probe (112). The receiver is capable of making up to one hundred and forty-four measurements of position and orientation per second when it is within the tracking field and this information is handled by the FOB control unit and passed to the PC using an RS232 interface.

One advantage of the EM 3D US system is that tracking of the probe is not restricted to line-of-sight, i.e. the receiver unit does not have to remain within in direct view of

[3] http://www.ascension-tech.com/realtime/RTflockofBIRDS.php

the transmitter unit during tracking. However, there are recommendations for the positioning of the FOB transmitter which are restrictive. In particular it is recommended that the transmitter unit is mounted on a wooden stand or platform at least 1 m from the floor and not near walls or the ceiling as they may contain unknown metal objects and electrical cabling that could interfere with the tracking system. Plus, the presence of metallic objects or sources of other EM fields within or near to the tracking system could degrade the accuracy of the positional information.

The Diasus US machine is designed for musculoskeletal use and has a standard PC base with an Ethernet network interface. Image capture from the US machine is real time with the images being transferred from the Diasus US machine to the *StradX* software using the Ethernet connection. The two US probes supplied were of frequencies 5-10 MHz and 8-16 MHz, specifications and recommended applications for the two probes are given in table 3-1.

Probe Frequency (MHz)	Available Imaging Depths (mm)	Array Width (mm)	Suitable Applications (not depth specific)
5-10	30 41 61 81 102	40	Shoulder Hip Knee Breast
8-16	20 30 41 61	26	Elbow/Knee Wrist/Ankle Hand/Foot Breast

Table 3-1: Diasus Ultrasound probe specifications.

3.4.1. System Arrangement

An experimental approach was adopted to find the optimum location and arrangement for the FOB transmitter unit in order to avoid distortion of the EM tracking field. Two outcome measures were defined as highlighting distortion and these were the RMS error for calibration and visual inspection of a test scan conducted after calibration. *StradX* provides an *Outline* window to view a recorded 3D US scan which shows the position of every US image within the 3D dataset as a white frame. Figure 3-9 shows an example. If there was distortion to the tracking field this would alter the positioning of the 2D US images warping the 3D dataset.

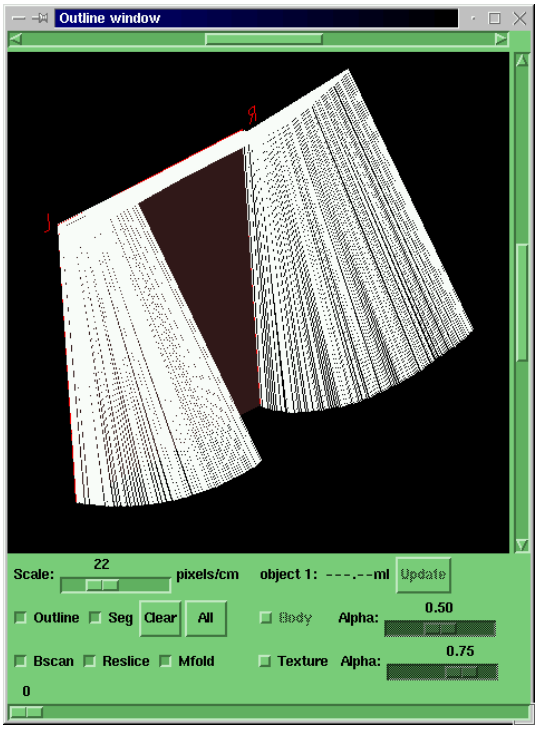

Figure 3-9: An example of the Outline View window in *StradX*. The position of each B-scan image in the dataset is represented by an individual white frame (113).

An RMS error of 0.06 cm was indicative of a good quality calibration. A larger error could be a sign of poor calibration technique or a problem within the system such as distortion of the tracking field (109). If a high RMS error was returned the calibration process was repeated. If a similar result was then obtained a test scan

would be carried out of the flat bottom of the water bath (i.e. a single walled phantom) and the *Outline* view checked for signs of significant distortion that would indicate problems with the tracking field. The *Outline* was also checked for low calibration errors to ensure there were no unexpected irregularities in the positioning of frames which may indicate a problem with the system setup or calibration technique.

During the experimental investigations additional factors were identified that contributed towards achieving successful calibration and acceptable scanning:

- A low sided water bath should be used to allow good angulations of the probe during calibration as it was this motion that was of particular importance when determining the coordinate transforms.
- A 9% Glycerol solution in the water bath would give a more accurate calibration as the speed of sound in this solution was the same as the US pulse aiding impedance matching between the probe and the solution.
- An acoustic mat in the bottom of the water bath provided a flat and highly reflecting surface to carry out calibration. Roughening the surface of the acoustic mat provided better line definition within the calibration images.
- A test scan should still be conducted and checked for irregularities even if a good RMS error was achieved at calibration

It was recommended that the transmitter unit was mounted on a non-metallic stand to elevate it from the floor. A wooden stand was ideal, however, the limited flexibility it would offer would have restricted the region where scanning could take place. Instead, a microphone stand was used because the flexible top section allowed the transmitter box to be easily manoeuvred into the best position. To avoid distortion of the tracking field caused by metal in the microphone stand, the transmitter box was mounted on a wooden plate which was offset forward from the main body of the stand, this can be seen in figure 3-11.

An arrangement of the EM 3D US system was established which returned an RMS calibration error of 0.06 cm and showed no sign of visible distortion of the 3D dataset for the test scan, see figure 3-10. The microphone stand was not used and the region for scanning was limited to the area immediately surrounding the water bath. This set up was ideal for scanning small objects in the water bath but was not suitable for general scanning use.

Figure 3-10: Initial setup of EM 3D US system which enabled accurate EM tracking.

The microphone stand was introduced to the setup in place of the chair and the Perspex box, used previously to elevate the transmitter, to assess the affect of the metal stand on the calibration. The calibration error increased to 0.09 cm, however, there was no visible signs of distortion to a test scan.

A proposed clinical setup to provide the means to conduct a wide variety of patient scans included a metal frame patient examination table. This setup, shown in figure 3-11, returned a RMS error for calibration of 0.97 cm.

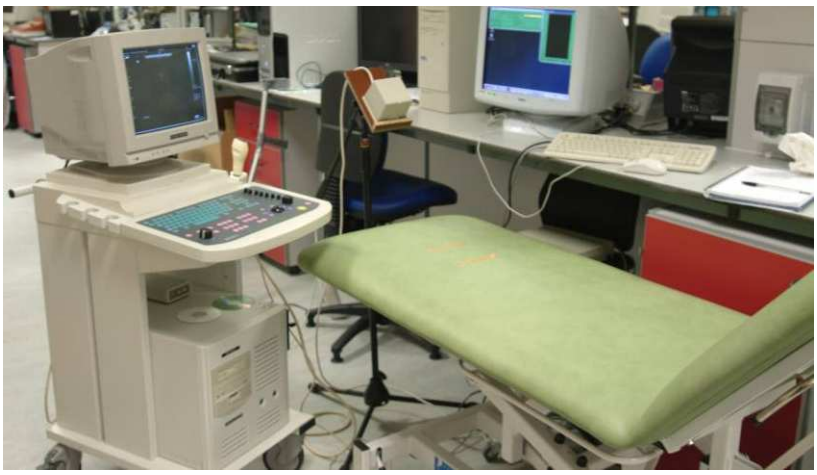

Figure 3-11: Proposed setup of the EM 3D US system for clinical scanning.

3.5. System Evaluation

A series of phantom experiments were devised to evaluate the EM freehand system and determine its suitability for imaging the musculoskeletal system in a clinical environment.

3.5.1. Probe Resolution

3.5.1.1. Methods

The resolution of the two probes (5-10 MHz and 8-16 MHz) was assessed to check that they could image objects with a diameter of the order of 1 mm. This diameter was chosen so as to determine whether small changes in fracture gap size and callus growth would be detectable for the proposed clinical application of monitoring fracture repair. To carry out these assessments a phantom object was created from a Perspex rod. A series of ten grooves of known width were cut into it, the first was 10 mm wide with each successive grove decreasing in diameter by 1 mm so that the last groove was 1 mm in diameter. The Perspex rod was set into a small box and surrounded by tissue mimicking material (TMM). TMM has the same speed of US propagation as the average speed of US in human tissue, 1540 m/s (32) and provided

impedance matching with the US probe. Both the 5-10 MHz and the 8-16 MHz US probes were used to scan the rod. A series of scans were conducted perpendicular to the length of the rod to obtain images showing the changing widths of the sets of grooves.

3.5.1.2. Results

Figure 3-12 shows the 2D US image of the smallest three grooves taken using the 5-10 MHz probe. Figure 3-13 shows the 2D US image of the smallest two grooves taken using the 8-16 MHz probe.

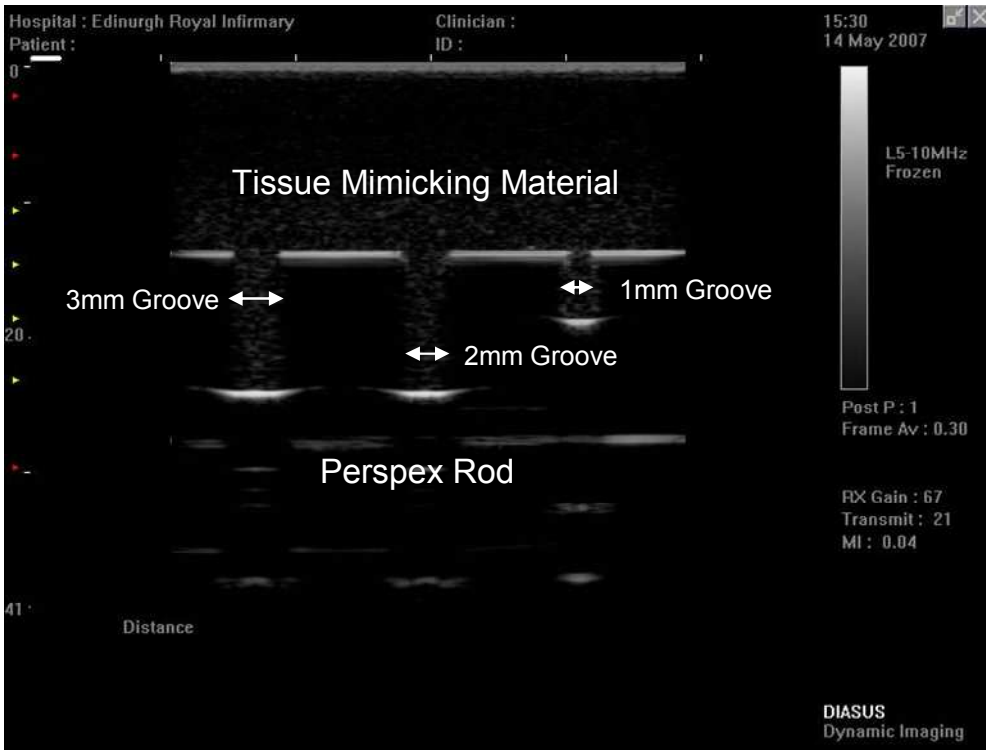

Figure 3-12: Ultrasound image recorded using the 5-10 MHz probe across the width of the three smallest grooves cut into the Perspex rod. The lengths indicated show the width of the grooves and were measured using vernier callipers. Depth scale of the image is 4 cm

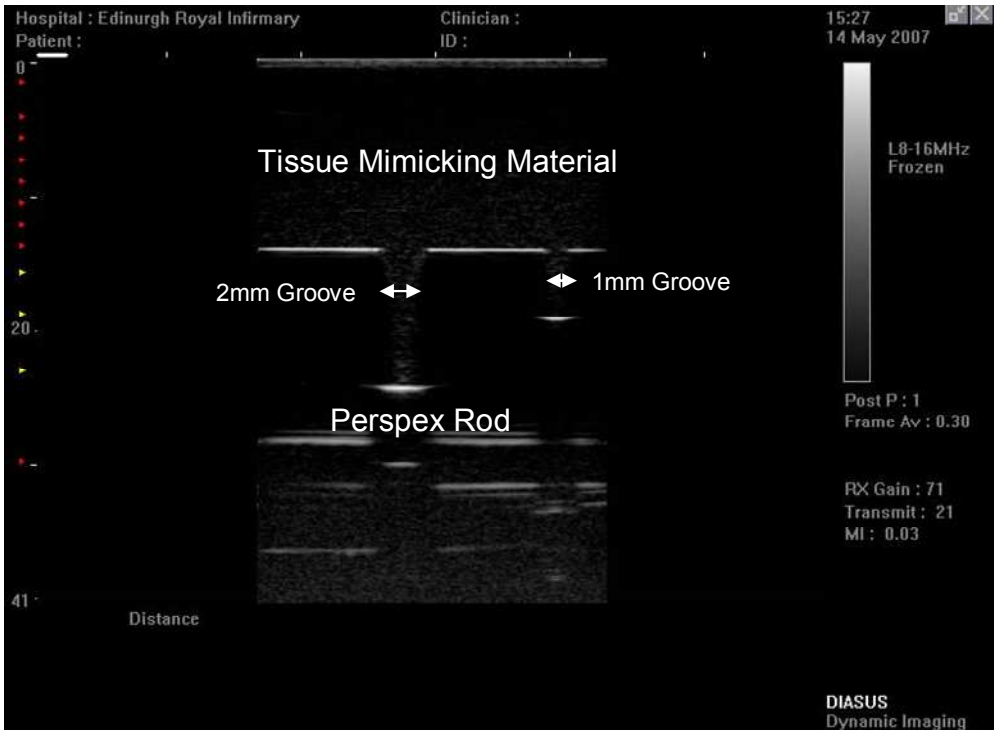

Figure 3-13: Ultrasound image recorded using the 8-16 MHz probe across the width of the two smallest grooves cut into the Perspex rod. The lengths indicated show the width of the grooves and were measured using vernier callipers. Depth scale of the image is 4 cm

As can be seen from the two figures both US probes could image the 1 mm groove. Although, for both probe frequencies it was noted that refraction around the edges of the 1 mm groove made it appear narrower at the top; this was not the case for the 2 mm groove. Refraction may be a result of the difference in acoustic impedance between the Perspex rod and the TMM.

3.5.2. FOB EM Tracking Field Assessment

3.5.2.1. Methods

To gain a better understanding of the FOB tracking system (i.e the shape, size, and strength of the pulsed DC field) an investigation was carried out to map the transmitted field by measuring its strength at different points. The FOB technical guide state that the pulsed DC EM field extended out to 1.2 m in all directions

around the transmitter box and that the field had been verified as accurate for tracking between the region 20.3-76.2 cm from the front half of transmitter (114). No indication as to how the field was mapped or the strength of the field were given, it was only stated that when the receiver was further than 9 inches from the transmitter unit the pulsed DC field would be at maximum strength.

During this investigation the setup shown in figure 3-10 was used as it had been previously established that it did not suffer interference from other EM field sources or metal objects. Minor modifications were made to the setup the water bath was removed and the US probe was placed within the tracking field. The distance between the transmitter and receiver was 53.4 cm, this was beyond the 9 inch separation to ensure the transmitter was operating at full power, if the transmitter and receiver are within 9 inches the strength of the transmitted field is reduced proportional to the separation of the receiver and transmitter.

A Hall probe was used to measure field strength. Before the FOB system was switched on the Hall probe was calibrated in the area where measurements were to be taken. This allowed the size of the background EM field in the laboratory to be established and this was found to be 0.35 Gauss (G). The field was sampled at regular intervals over a volume of 75000 cm^3. The centre of the transmitter unit was taken to be the origin of a coordinate system used for plotting the field. Figure 3-14 shows a side view diagram of the setup and region sampled, while figure 3-15 shows the plan view.

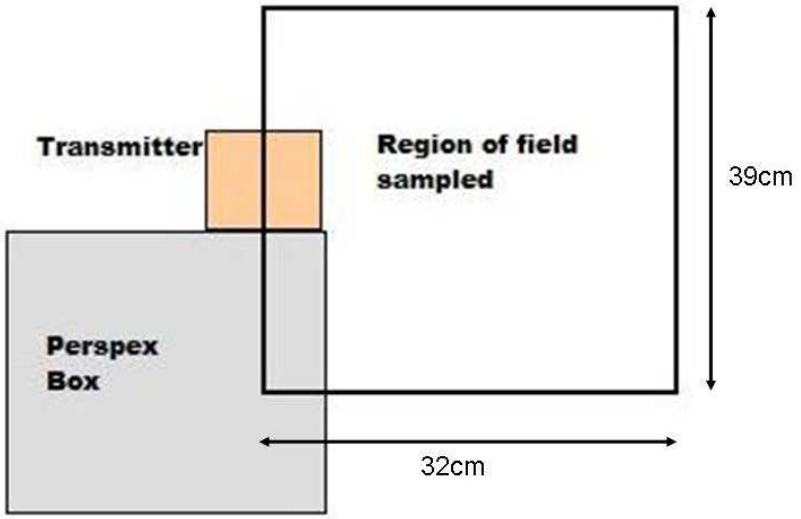

Figure 3-14: Side view diagram of the sample region for investigating the pulsed DC field.

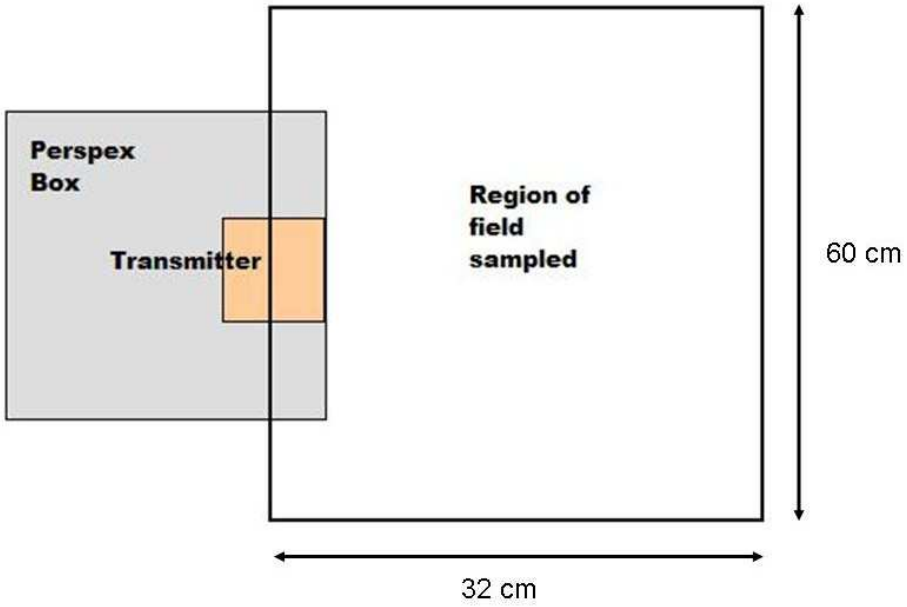

Figure 3-15: Plan view diagram of the sample region for investigating the pulsed DC field.

3.5.2.2. Results

Figure 3-16 shows the shape and strength of the field measured where red represents the strongest part and dark blue the weakest. The results show that the strongest field was found at the surface of the transmitter box and that the field strength decayed rapidly across a short distance. Field measurements made on the right hand side of the box were found to be slightly higher than those made on the left. Further investigation around the right side of the setup, conducted when the transmitter was switched off, identified an additional EM field of approximately 1.2 G emanating from the floor which would be adding to the measured field from the box. Measurements of field strength at 50 cm from the transmitter were comparable in size to that of the measured background field. No significant field could be detected beyond 50 cm from the transmitter. At 30 cm from the transmitter only tiny fluctuations in the strength above the measured background could be detected.

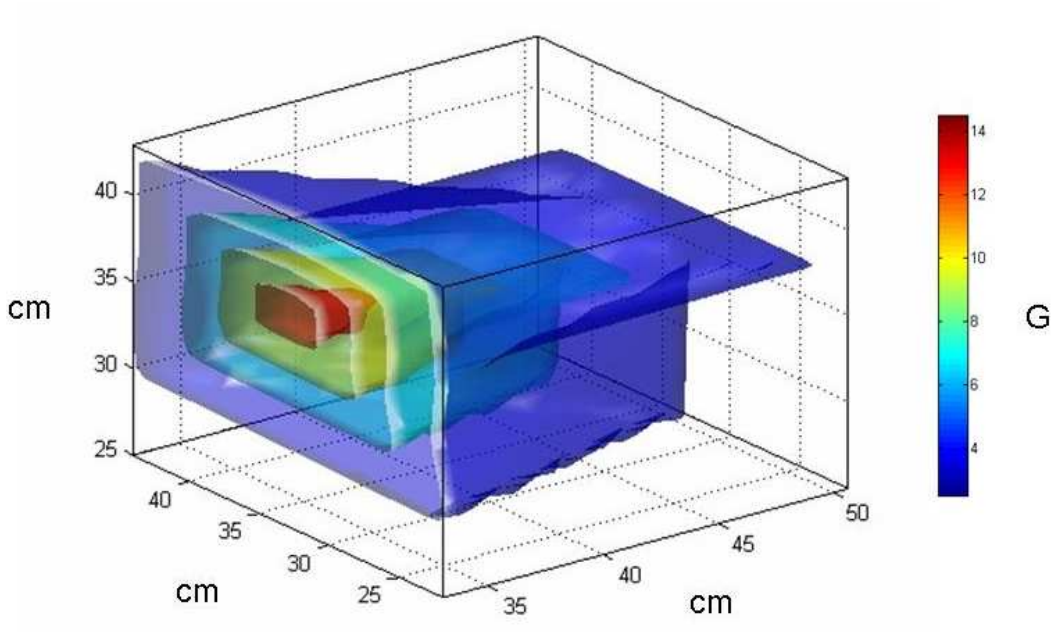

Figure 3-16: The measured EM field transmitted by the FOB system. The centre of the transmitter box is located at (35, 35, 35).

3.5.3. Accuracy

3.5.3.1. Methods

Within the clinical environment there can be limited control over the close proximity of other equipment in examination rooms or being used in adjoining rooms. In small rooms it may not be possible to avoid being close to walls where there may be enclosed metal structures and electrical cabling. The EM 3D US system was assessed to determine how accurately the 3D datasets were being constructed in *StradX* and what effect the introduction of the microphone stand and patient examination table, as required for the clinical setup, would have on dataset construction. There are three ways to test the accuracy of a 3D US system:

1. Make repeat measurements of a point in space and check for variation in the coordinates.
2. Use a pin phantom or an object of known dimensions and compare it with a measurement derived from a 3D US scan.
3. Scan an object of known volume and compare its measured volume with the volume returned by the 3D US software.

Any distortion to the positions of the US frames in the 3D dataset will be carried though to 3D models constructed and will also effect volume measurements. Thus, the third method of assessing accuracy was chosen.

The phantom was a small rectangular object made of rubber. It could be scanned completely within one sweep of the 5-10 MHz US probe, was easy to construct into a 3D model and its dimensions could be measured accurately using digital vernier callipers (RS, Corby, UK). The volume of the phantom was calculated to be 14.24 ± 0.04 ml for measurements obtained from a vernier callipers. Four different scanning scenarios were used in the assessment:

1. The same setup as shown previously in figure 3-10 was used as this arrangement appeared to be unaffected by additional metal objects or EM

fields. This would give a direct comparison between the volume measurements returned by *StradX* and the actual volume of the phantom. The RMS calibration error for this setup was 0.06 cm.

2. The FOB transmitter was mounted on the microphone stand in place of the chair and Perspex box used previously, the rest of the setup remained unchanged. This would indicate the extent of distortion to the tracking field caused by the stand. This scenario had an RMS calibration error of 0.09 cm.
3. The microphone stand was removed and a patient examination table added to the setup to determine what effect the metal frame of the table would have. The transmitter box was returned to its original position on the Perspex box on the chair. Scenario 3 had an RMS calibration error of 0.107 cm.
4. A proposed clinical setup using both the microphone stand and patient examination. The calibration RMS error returned for was 0.137 cm.

For each scenario the phantom was scanned five times in a water bath containing 9% Glycerol solution using the 5-10 MHz probe.

One of the intended uses for the EM 3D US system was to scan patients with lower limb fractures who may have been treated using a metal fixation such as an IM nail or an Ilizarov frame. In order to gauge the effect of the presence of metalware an Ilizarov external fixation frame was added to each scenario and the phantom was scanned a further five times. In each case the Ilizarov frame was placed in the water bath surrounding the phantom, see figure 3-17, to mimic the clinical situation of the Ilizarov frame being fitted around a limb.

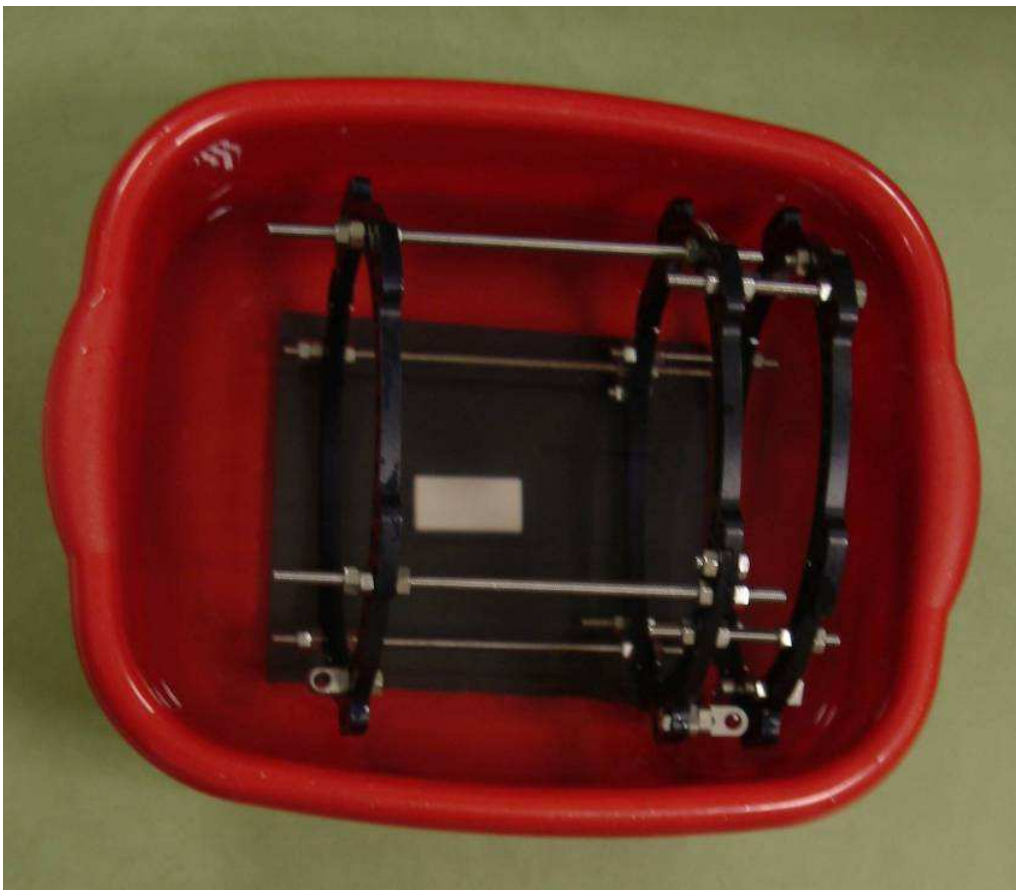

Figure 3-17: Ilizarov frame and phantom in the water bath.

3.5.3.2. Results

Figure 3-18 shows the mean difference of the 3D US and vernier callipers derived volumes of the phantom without the Ilizarov frame present. Figure 3-19 shows the mean difference in volume measurements derived when the Ilizarov frame was present compared to the vernier calliper measured volume.

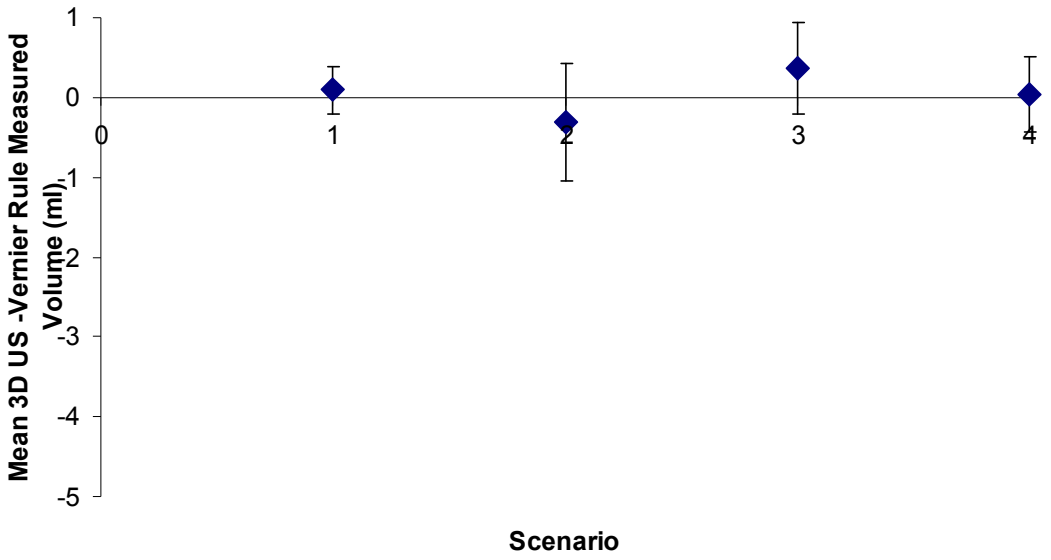

Figure 3-18: Mean 3D US derived volume minus the vernier calliper measured volume for the phantom scans without the Ilizarov frame present. Error bars indicate 95% confidence intervals.

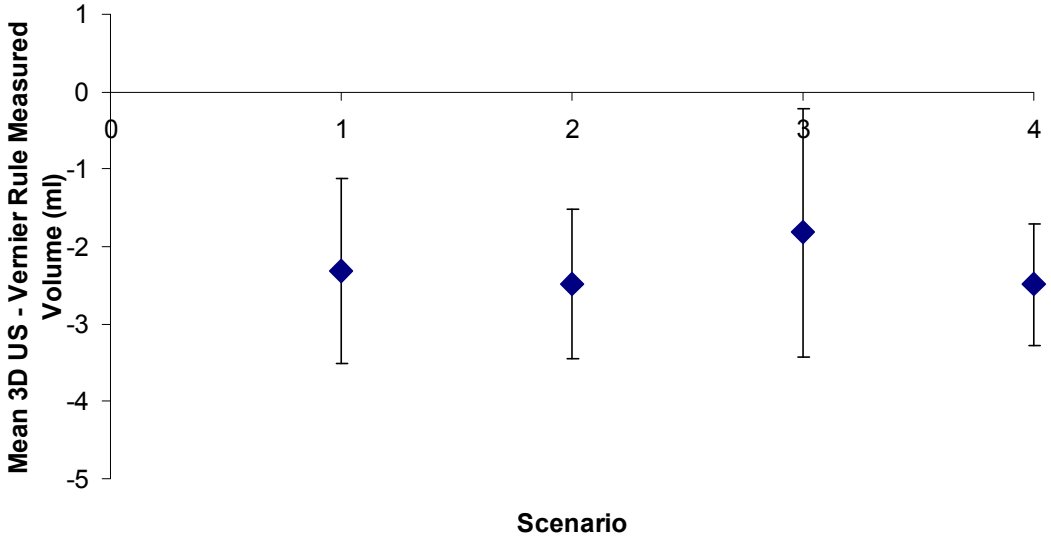

Figure 3-19: Mean 3D US derived volumes minus the vernier calliper measured volumes for the phantom scans with the Ilizarov frame present. Error bars indicate 95% confidence intervals.

When taking into account the properties of the phantom it was expected that the 3D US scans would show a slight underestimation of volume. The speed of sound in rubber is around 1600 m/s, compared to 1540 m/s in the Glycerol solution. Rubber has a slightly lower acoustic impendence than the Glycerol solution resulting in only a small percentage (0.05%) of the US pulse being reflected at the solution - rubber boundary. Despite the majority of the incident US pulse being transmitted into the phantom the high attenuation property of rubber caused most of the US pulse to be absorbed, resulting in the black appearance of the inside of the phantom. Only the sides and top surface of the phantom were visible which is where the US pulse was reflected. There was no visible bottom edge of the phantom; the reflection from the acoustic mat visible on either side was used as a guide to the position of its base for the segmentation process.

The mean value for the volume of the phantom measured from the 3D models obtained in scenario 1 was 14.33 ± 0.61 ml. This was within confidence intervals of the volume of the phantom measured using the vernier callipers and no obvious distortion of the model was visible. Variation in size of the five models constructed was due to operator dependency in the segmentation of the data and slight angulations of the probe during scanning which lead to the ends of the phantom appearing in more than one US image.

For scenario 2, the average volume of the phantom determined form 3D US was 13.93 ± 0.74 ml which was an underestimation of the vernier calliper measured volume of 2.2%. The 3D US measurements of the phantom varied between -6.25-0.42% of the actual phantom volume. These result showed agreement with the findings of King, that the introduction of additional metal into the near field scanning environment causes a decrease in the volume accuracy of models constructed from that data (86). When inspecting the *Outline* view for this scan it was noted that the US frames appeared ‘squashed’ together along the long horizontal axis of the phantom.

It was expected that the volume underestimation would be greater in scenario 3 due to the presence of the metal frame of the patient examination table directly within the tracking field. Instead, the volume of the phantom was overestimated at 14.60 ± 0.57 ml. On inspection of the *Outline* and the constructed models it was found that 'squashing' together of US frames along one axis was still occurring. However, frames were now also being displaced slightly upwards and outwards causing warping of the model. The degree of warping can be seen when comparing figures 3-20 and 3-21 which show the 3D models constructed from the scan data using *StradX,* both figures are shown oriented along the same axis. The 'squashing' together of the US frames resulted in volume underestimation, but the upwards displacement of the frames compensated by increasing the distance between adjacent frames.

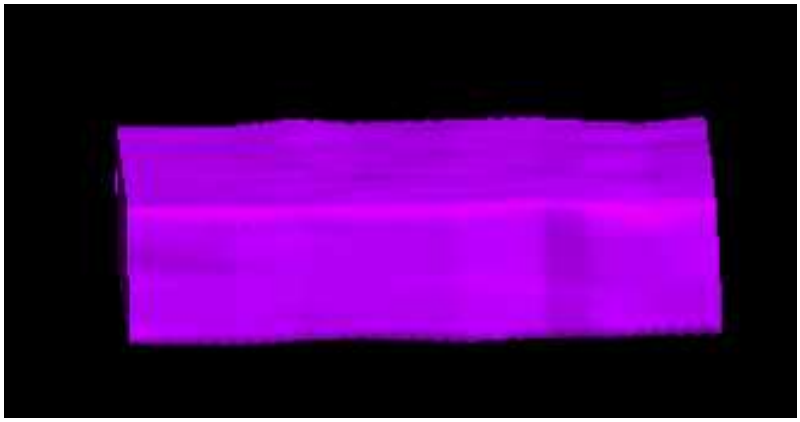

Figure 3-20: 3D model constructed from a scan of scenario 1 without the Ilizarov frame present.

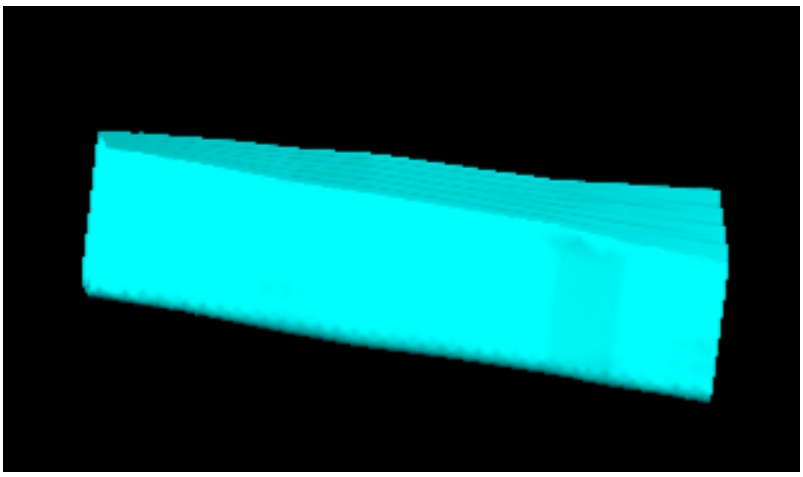

Figure 3-21: 3D model constructed from a scans of scenario 3 without the Ilizarov frame present. This figure is orientated along the same horizontal axis as figure 3-20.

A similar volume overestimation was observed in the models constructed from the scans from scenario 4. Given the size of the calibration errors for scenarios 3 and 4 it would seem likely that the volume underestimation was still occurring. However, the warping of the dataset was, in a negative way, compensating for this by causing a volume over estimation.

Figure 3-19 shows the results of the phantom scans when the Ilizarov frame was present in the water bath. Introducing the Ilizarov frame into scenarios 1 and 2 affected the EM tracking field to such a degree that it caused underestimation of the phantom volume of between 12-23% in both cases. In scenario 3 the volume underestimation was between 5-19% and for scenario 4 the presence of the frame caused an underestimation of between 13-20%. Both the 'squashing' together and displacement upwards of the US frames were visible in the *Outline* view windows for all the scans.

The results of the study by King showed a decrease in volume measurements as increasing amounts of metal were introduced to the near field environment of the tracking system (86). This was not found to be the case in this investigation. The calibration errors quoted for each setup gradually increased as was expected, however, the volume measurements of the phantom were overestimate for scenarios

3 and 4 (both with and without the Ilizarov frame present) rather than underestimated as found by King.

3.5.4. Healthy Volunteer Study

3.5.4.1. Methods

In order to assess the clinical potential of 3D US for musculoskeletal imaging a healthy volunteer study was carried out. The aim of this study was to image a section of the lower leg and construct 3D models of the surface of the tibia and surrounding soft tissues. Fifteen healthy volunteers (9 males, 6 females, age range 18-62 years) were recruited through informed consent; ethical approval for the study was given by Lothian Local Research Ethics Committee and Lothian Research and Development Management. Each participant underwent two scans around the midpoint of the left shin with the 5-10 MHz probe. This probe was chosen as it allowed the largest volume to be scanned with one sweep. A silicon stand-off pad aided scanning by improving probe contact at the apex of the shin. The clinical setup incorporating the patient examination table and microphone stand was used for scanning the volunteers.

3.5.4.2. Results

For each participant, the *Outline* view and series of recorded 2D US images were reviewed to identify problems that may effect model construction. Eight of the thirty datasets were not suitable for model construction: six due to image artefacts and two due to poor image quality throughout the scan. The artefacts that occurred were the result of loss of contact either through tilting of the probe or insufficient gel for coupling. Due to the angle of the probe as it was moved across the apex of the tibia there were small discontinuities at this point in some of the models.

Figure 3-22 shows one of the 2D images recorded during a scan; each structure of interest that was segmented to build the 3D model has been labelled. The black band at the top of the image was caused by the silicon stand off. A 3D model showing the surface of the tibia is shown in figure 3-23 while a full 3D model of both bone and soft tissue is shown in figure 3-24.

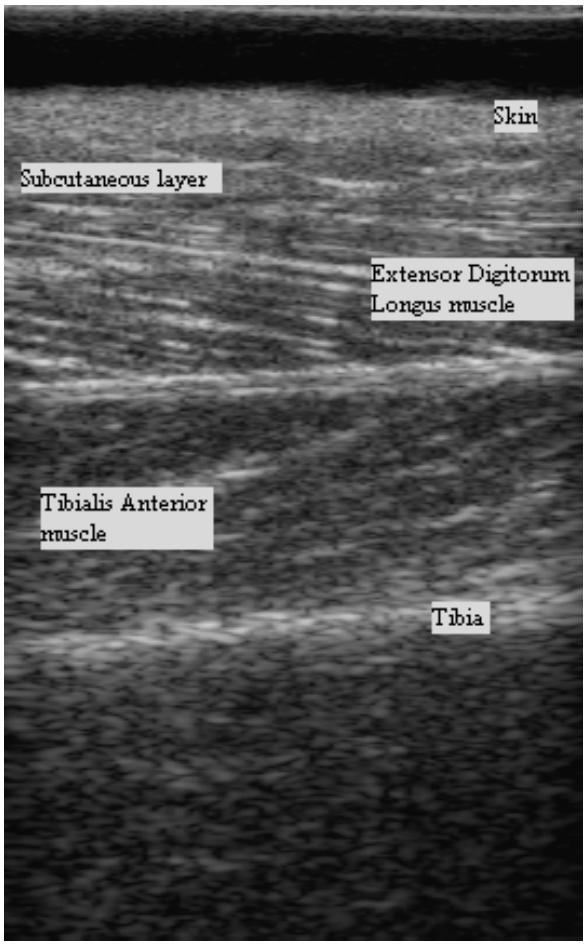

Figure 3-22: A 2D Ultrasound frame from a healthy volunteer scan, each anatomical feature of interest has been labelled. The depth scale of the image is 3 cm.

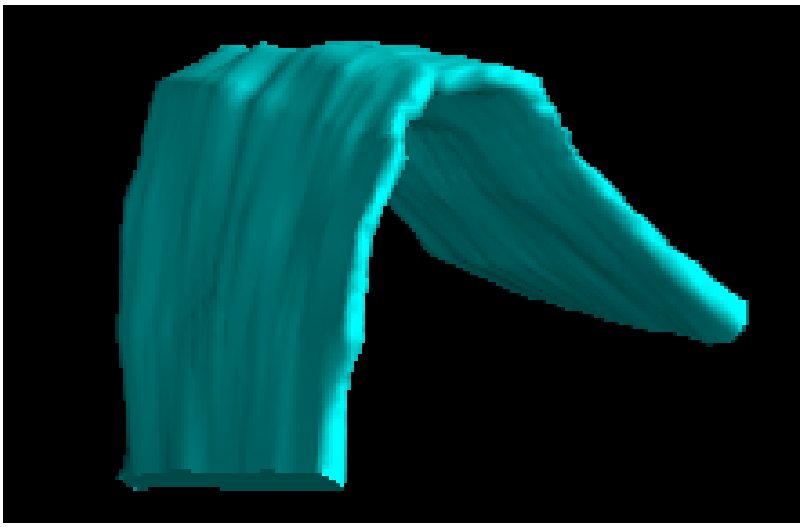

Figure 3-23: 3D model of the surface of the tibia.

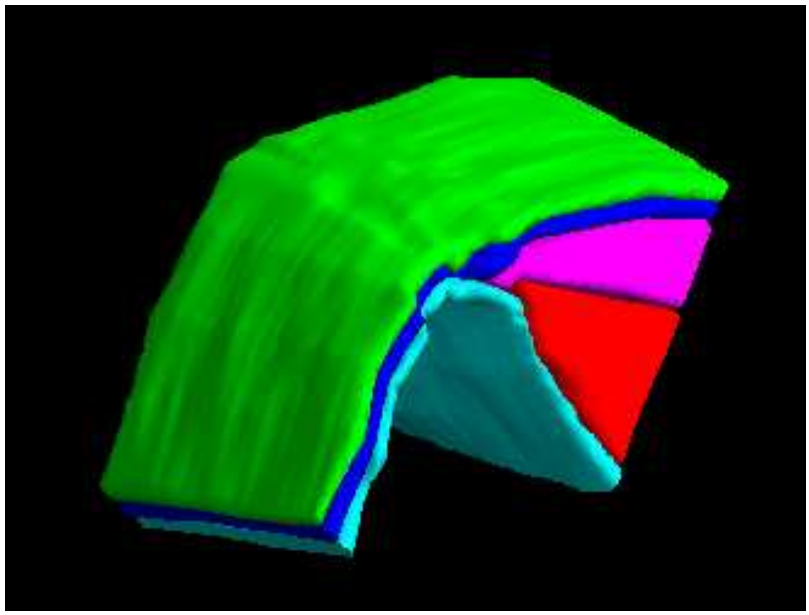

Figure 3-24: 3D model of the surface of the tibia and surrounding soft tissue. Surface of the tibia - cyan, tibialis anterior muscle - red, digitorum longus muscle - purple, subcutaneous layer –dark blue and the skin – green.

3D models were fully rotatable in any orientation within *StradX*. Any segmented section of the model could be removed or added depending on visualisation requirements. The *Reslice* facility provided additional views of the anatomy which

may not otherwise have been possible with 2D US. Figure 3-25 shows a reslice through a healthy volunteer scan; the triangular shape of the mid shaft tibia is visible.

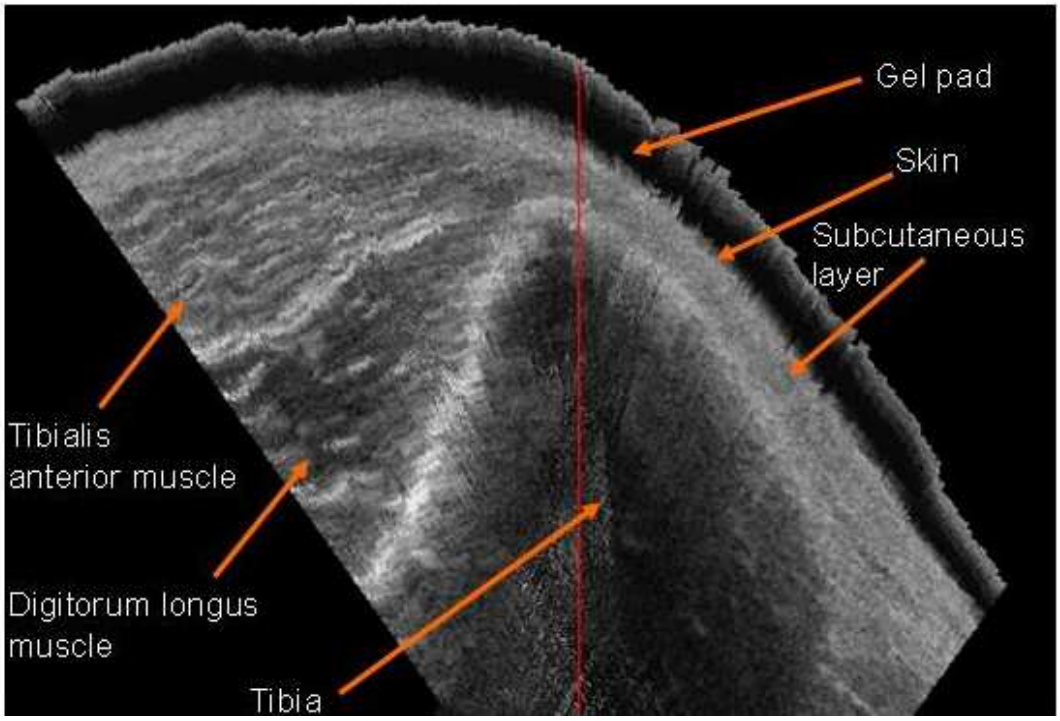

Figure 3-25: A Reslice through a scan dataset showing the triangular shape of the tibia and the surrounding soft tissues.

3.6. Discussion

The development of 3D US has overcome a number of the operator dependent limitations of 2D US (3). The datasets constructed from 3D US scans provide an easier means of interpreting the scanned anatomy, views of the anatomy which would otherwise by unobtainable with US, and accurate length and volume measurements. *StradX* offered the most accurate method of constructing 3D datasets and was chosen for use along with the FOB EM tracking system to form the EM freehand 3D US system.

EM tracking offered the best flexibility for freehand scanning as there were no restrictions on the range of motion that could be tracked. This was ideal for musculoskeletal scanning as it would allow the operator to move the probe around the circumference of a limb unhindered. For the intended clinical applications of monitoring fracture repair and measuring muscle volumes this was advantageous. However, the recommendations for the positioning of the FOB transmitter, to avoid distortion of the tracking field, were restrictive.

Distortion to the tracking field was highlighted by the size of the calibration errors returned when trialling different equipment setups. Through the use of a phantom object, the extent of distortion caused by the microphone stand and metal framed patient examination table, which were incorporated into the proposed clinical setup, revealed significant warping of tracking field. This had a resultant effect on dataset construction and thus the accuracy of volume measurements. Introducing the Ilizarov frame to the setup, to simulate a likely patient situation, worsened the distortion. An investigation into the magnitude and shape of the tracking field was inconclusive. The field plot obtained was very different from that described by the manufacturer and no field above that of the background could be detected beyond 50 cm from the transmitter unit.

Previous investigations of similar EM tracking systems by King (86) identified the effects of volume underestimation due to tracking field distortion but made no mention of the second warping effect noted here which resulted in volume overestimation. In another study, it was found that the effects of EM fields and metal within the probe head itself caused no distortion to the tracking field and that the presence of the US machine had a negligible effect on calibration accuracy (87) In early clinical scanning work carried out using the *StradX* system Treece et al. mounted the FOB transmitter on a stand with an arm that allowed it to be positioned centrally above the region, and facing, the area to be scanned (98). The design ensured the tracking field was away from walls and ceilings and equipment which may be sources of other EM fields. It is not stated what material the stand was made

of, a non metallic frame would be ideal, however, the weight of the transmitter unit would put considerable stress on the frame.

Electromagnetic field tracking systems have been used successfully in 3D US research studies, although, details are not always given about the issues considered here (77, 95, 115). Wooden examination tables have been suggested as a means of minimising distortion of the tracking field, but they do not offer the same flexibility for positioning patients (77, 87, 116). Even if a non-metallic stand and wooden examination table were incorporated the problem of distortion caused by ferromagnetic material present in metalware used to stabilise fractures remains.

Despite the problems of EM tracking the 3D US scans obtained from the healthy volunteer study provided views of the anatomy that would be unavailable with conventional 2D US or X-ray. Scan data was available near real time for examination unlike with MR. Overall, this study was successful in demonstrating the potential of 3D US for musculoskeletal imaging. However, the results of the system evaluation ruled out the use of EM tracking for further clinical scanning as it did not provide a suitably accurate and reliable method of obtaining probe positions. To overcome the limitations encountered the use of an alternative optical tracking system is considered in Chapter 4.

4. Optically Tracked Freehand Three Dimensional Ultrasound

4.1. Introduction

Optical tracking systems do not suffer the same limitations of EM tracking systems, i.e. interference from the presence of metal objects or other EM fields within the scanning region. In order to use an optical tracking system components of the previously used EM 3D US system had to be upgraded. Alterations were made to the US machine to improve image capture and the 3D US software package was upgraded from *StradX* to *StradWin*. This new system is referred to as the Optical 3D US system. This Chapter introduces the *StradWin* software and covers the evaluation of the Optical 3D US system using a series of phantom based experiments.

4.2. The Optical Freehand 3D Ultrasound System

StradWin (MIG, Engineering Department, Cambridge University) is the freehand 3D US software designed to supersede *StradX*. Both *StradX* and *StradWin* only support two specific optical tracking systems and these are the Ascension LaserBird and the Northern Digital Inc. (NDI) Polaris. Technical specifications for the LaserBird quote a tracking accuracy of 0.70 mm RMS[4] while specifications for the Polaris state a tracking accuracy of 0.35 mm RMS[5], i.e. half that of the LaserBird. In comparison, the FOB EM tracking device had an accuracy of only 1.8 mm RMS[6]. Based on these

[4] http://www.ascension-tech.com/products/laserbird2.pdf
[5] http://www.ndigital.com/medical/polarisoriginal-techspecs.php
[6] http://www.ascension-tech.com/realtime/RTflockofBIRDS.php

specifications and the need to obtain accurate length and volume measurements over a small scale the NDI Polaris system was selected for this study.

The Polaris system consisted of the position sensor unit, figure 4-1, and the tool docking station, figure 4-2, and required a further tracking tool that is attached to the US probe. The position sensor unit has two sensors each consisting of a central lens containing Infrared (IR) detectors that is surrounded by a ring of IR emitters. The position sensor unit can act as both a transmitter and a receiver for optical tracking dependent on the type of tracking tool used. Tracking tools that have a series of IR light emitting diodes (LED's) built into them emit IR light that is detected by the lenses of the position sensor unit. Triangulation of the detected IR light is used to establish the position and orientation of the tool and thus the US probe which it is mounted on. This process is known as *active* tracking. Alternatively, the ring of IR emitters on the position sensor unit can be used to flood a set volume of space with pulses of IR light. In this case the tracking tool used will have a series of IR reflective marker spheres mounted on it. The IR light reflected by the marker spheres that is detected by the lenses is used to triangulate the position of the tool and US probe. This process is known as *passive* tracking. The optical tracking unit has a set volume within which the position of the tracking tool can be accurately detected and this is referred to as the measurement volume. To gain flexibility in the positioning of the measurement volume the tracking unit was mounted on a monopod stand which was easy to move and occupied minimal space.

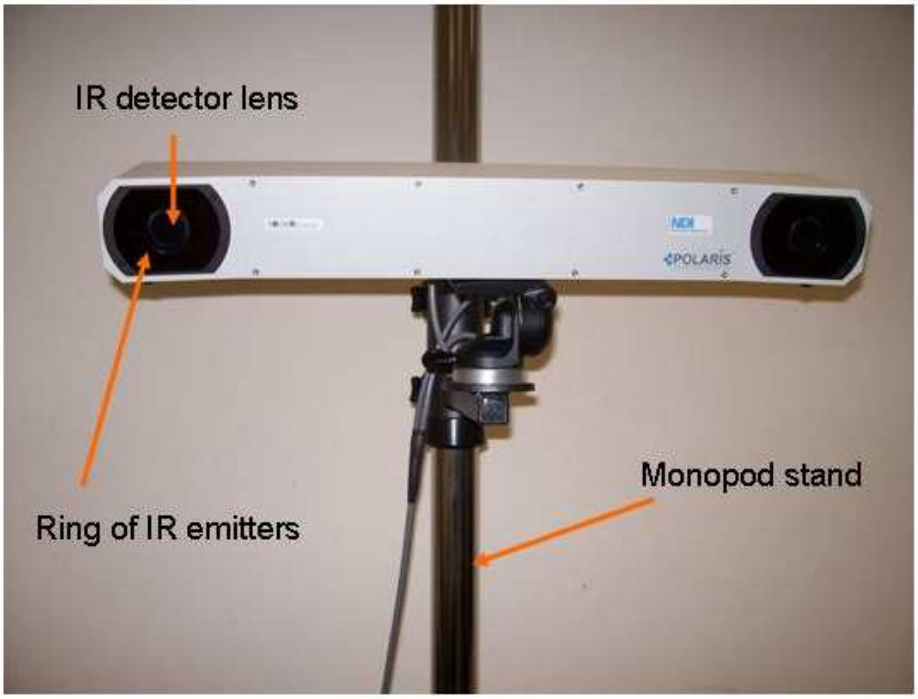

Figure 4-1: The position sensing unit of the NDI Polaris optical tracking unit mounted on a monopod stand.

Figure 4-2: Tool docking system for the NDI Polaris optical tracking system.

StradWin requires *active* tracking. The multi-faced *active* tracking tool recommended for freehand scanning by the MIG was the Adaptrax tool (Traxtal, Toronoto, Canada) and this is shown in figure 4-3 mounted on the 5-10 MHz US probe. The Adaptrax tool has fifteen IR LED's built into it in a configuration that allows the tool to be tracked with six degrees of freedom. Mounting the Adaptrax tool directly onto the US probe allows the probe position to be tracked. Specialised mounts were made for each of the US probes and the mount for the 5-10 MHz probe is visible in figure 4-3. Both mounts consists of a split plastic collar where the two parts of the collar are fitted round the narrow top part of the probe before being secured in place by two fastening screws.

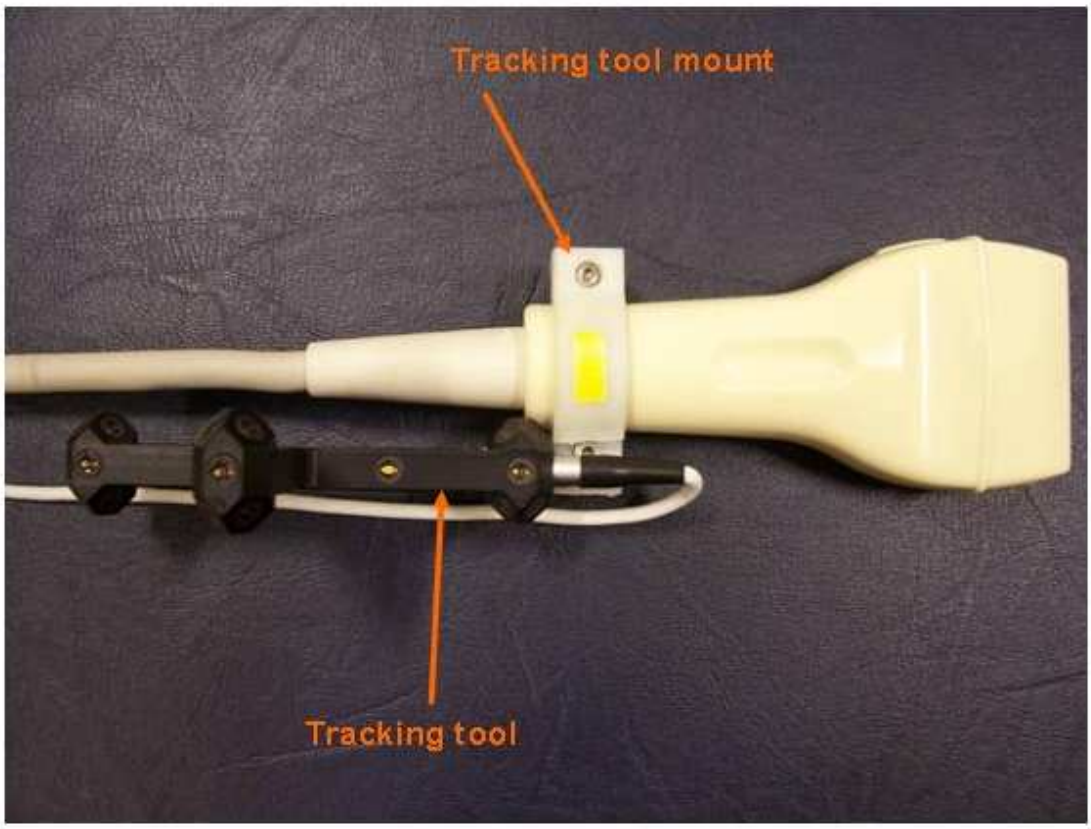

Figure 4-3: Traxtal Adaptrax IR active tracking tool mounted on the 5-10 MHz Ultrasound probe.

To operate *StradWin* a PC with an NVIDIA G-FORCE graphics cards, increased memory capacity and a faster processor were used (Pentium 4, 3.60 GHz PC running Microsoft Windows XP). *StradWin* does not accept an Ethernet connection as was used previously to obtain the images from the US machine. Image acquisition can only be carried out using either video capture cards or by directly intercepting the raw Radio Frequency (RF) signal from within the Diasus machine.

To conduct novel image analysis of recorded US data (see Chapter 6) it is necessary to obtain the images before they undergo unknown post-scan processing by the Diasus scanner. This occurs before the images are displayed on the US machine. Video capture does not allow acquisition before post-scan processing as it captures the US images after they have undergone digital to analogue (DA) conversion required for screen on display. RF capture, on the other hand, provides a method of acquiring the images before they undergo the series of post-scan processing steps. Full details of the RF capture process are covered in section 4.3.1. Figure 4-4 shows a schematic diagram of the Optical 3D US system while figure 4-5 shows the system setup for clinical scanning.

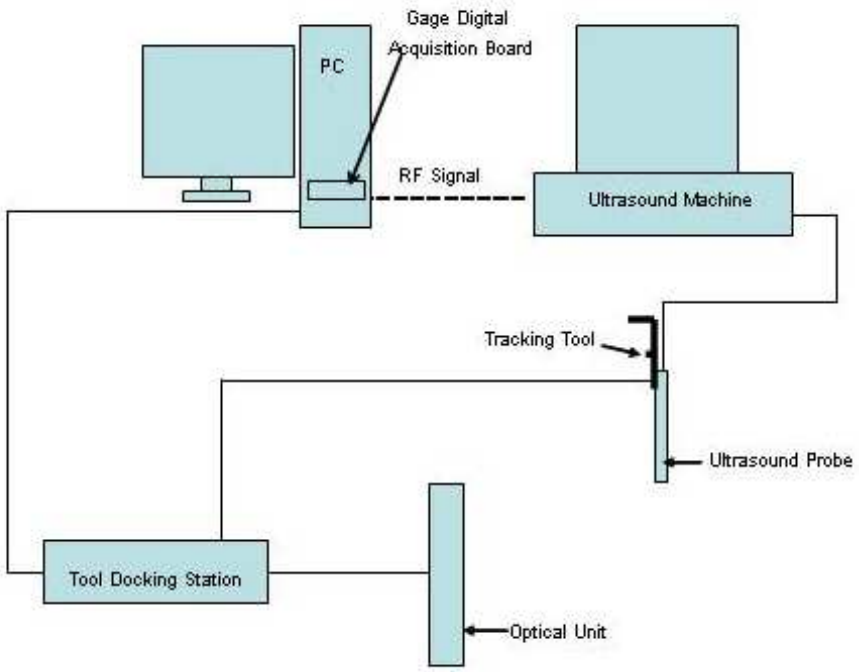

Figure 4-4: Schematic diagram of the Optical 3D Ultrasound system.

Figure 4-5: The Optical 3D Ultrasound system set up for clinical use.

4.3. StradWin

StradWin is heavily based on *StradX* but has the added advantage that it is compatible with both the Linux and Windows computer operating systems. Versions 3.1, 3.2, 3.3, 3.4, and 3.5 were used during these investigations. *StradWin* uses the same image and position data acquisition processes as described for *StradX* in section 3.3. Image and position data acquisition happens simultaneously, with position data being stored in one circular buffer within the computers memory and the image data being stored in another. When using RF capture, there are preceding processes required to obtain the RF signal relating to one complete US image and then import that data into the computer's circular memory buffer for use in dataset construction.

4.3.1. RF Capture

The required modifications to the Diasus were carried out by Dynamic Imaging to give access to the necessary RF signals after receive focusing and TGC have been applied but before log compression and envelope detection, see section 2.3. A two channel digital acquisition board (CompuScope 14200-128M, Gage, USA), referred to as the Gage card, is used to sample the RF signals.

Modification of the Diasus gave access to the four signals required by *StradWin* to conduct RF capture. These were: a once per frame sync signal (SC_SYNC), a signal which is high when the RF data is valid (Tx_FIRE), the focused RF signal after TGC had been applied (RF_TGC) and finally the 66.67 MHz external clock signal from the Diasus. RF capture is possible using only the first three signals if a 50 MHz or 100 MHz signal sampling rate is being used. However, the addition of the 66.67 MHz external clock rate allows the RF signal to be sampled in sync with the Diasus internal clock. Sampling at this frequency has been found to reduce phase mismatch between sampled sections of the signal when it is reconstructed into an image (117) and so was adopted for this study.

Figure 4-6 illustrates how the acquired RF signal is converted into an RF vector which makes up one section of the final B-scan image. The vector shown overlain on the section of the US image it makes up, this is indicated by the arrow in figure 4-6, is made up from three separate segments of the RF signal in this case. These segments arise as there were three points of focus used when conducting the US scan. With a single point of focus the RF vector is made up from a single segment of the RF signal. If multiple points of focus are used, the vector is made up from multiple segments of the RF signal where each segment is assumed by *StradWin* to be of increasing focal depth. Best practice is to use a single point of focus as this removes the additional processing involved in stitching together multiple signal segments.

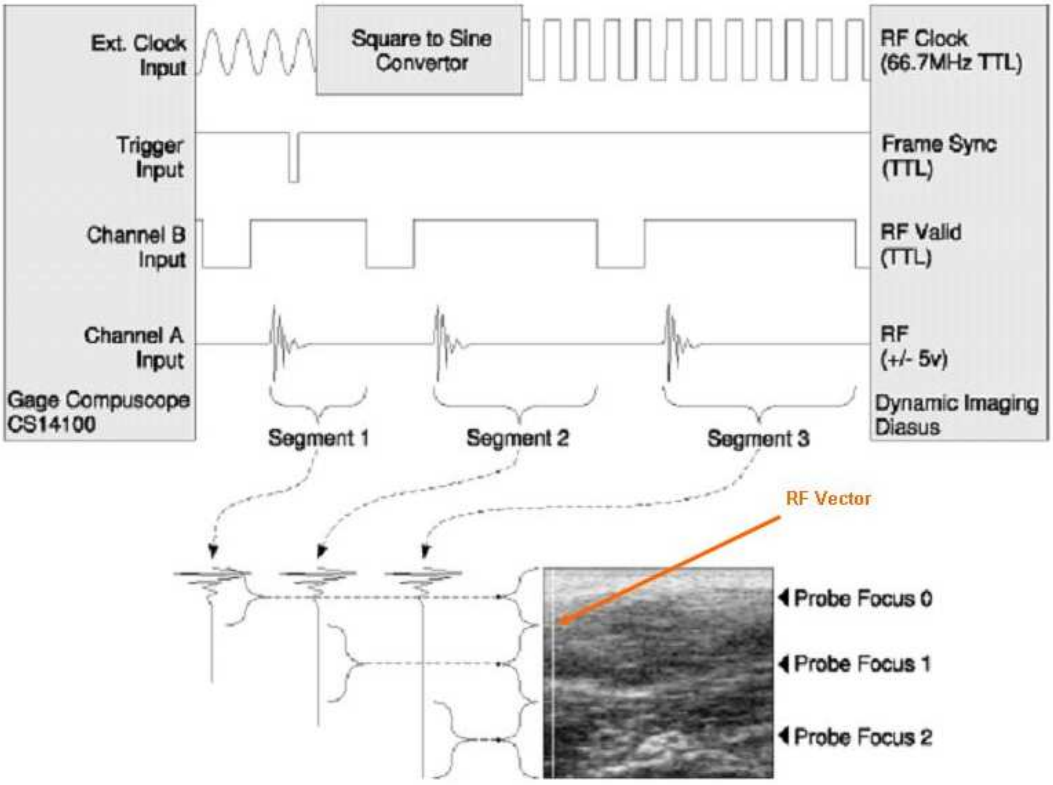

Figure 4-6: The process of reconstructing the required RF signals to build one complete RF vector. The arrow indicates one of the 127 RF vectors that make up one B-scan image (118).

B-scan images from both the 5-10 MHz and the 8-16 MHz probes are constructed from a series of 127 RF vectors. During RF capture all the vectors are stored in sequential order on the Gage card to generate one complete US image and when the group of vectors is complete it is transferred across to the PC's memory. Each group of vectors making up one image has a time stamp associated with it which is used in the circular buffer for dataset construction. The same process as described for *StradX* in section 3.3 is used to determine the correct position and orientation of the images by taking into account latencies in the position reading process. This data is then used to sequentially orientate the US images in a volume of free space governed by the real world co-ordinate system to produce a 3D dataset.

To convert the RF data into a series of B-scan images for display in *StradWin* requires the use of *Probe Configuration Files*. These files contain details about the size, frequency and points of focus for the probe used during scanning as well as the number and sizes of the vectors which make up an US image. Further to this, they contain details of the sampling rate used to collect the RF data and the filters which should be applied to it in order to convert it into B-scan image format. Each US probe requires a separate *Probe Configuration File*. The files used for the 5-10 MHz and 8-16 MHz probes were supplied by Dr Graham Treece of the MIG.

4.3.2. Calibration

The calibration process for *StradWin* is very similar to that of *StradX*. The same *Spatial Calibration* process, with a predefined set of probe movements to record a series of US images of a flat surface within a water bath, is used to determine the transform relationships between the co-ordinate systems of the optical tracking unit, the US images and the real world. As part of the calibration process the appropriate probe frequency and corresponding *Probe Configuration File* must be selected in the *Image Source Configuration* menu in *StradWin* in order to convert the RF vectors into US images. In addition to the RMS error returned from the calibration process as

an indicator of the quality of the calibration carried out, it is also possible to verify a calibration using a tracked pointer. Full details of the calibration process and the tracked pointer verification process are provided in appendix B.

With *StradWin* it is possible to carry out a calibration for a particular probe frequency, depth setting and point of focus, and to save the result and settings as a calibration template file. This template can then be reloaded at a later date for scanning resetting the parameters of the 3D US system to those resulting from the original calibration. The advantage of templates is that they remove the need to calibrate the system each time it is switched on, a template file can be loaded instead reducing the time to setup the system for scanning. When using calibration templates there is the restriction that the optical tracking tool must remain, or be re-mounted, in the same position and orientation on the US probe as when the calibration was originally carried out. Also, the settings of depth and point of focus must be the same as when the calibration was originally conducted. Failure to do this will result in errors in position tracking and in the reconstruction of the RF vectors into B-scan images.

Thirty calibration templates were created, fifteen for each of the two US probes in order to give a variety of depths and point of focus settings and allow quick change over between probe types and settings. Each template was named according to the probe frequency, depth and point of focus setting. The 5-10 MHz probe was designated T and the 8-16 MHz probe was designated U. For example, the calibration template for the 5-10 MHz probe with a depth setting of 81 mm and point of focus of 74 mm has been named T8174. For the 8-16 MHz probe a template with a depth setting of 41 mm and point of focus of 17 mm was named U4117. Appendix C contains details of the thirty calibration templates created. Calibration templates can be kept long term, however, they must be periodically checked using the tracked pointer verification to ensure they are still consistent and accurate.

4.3.2.1. Visualisation

The 3D dataset can be viewed in a number of ways. The *Reslice, Outline* and *Panorama* displays described for *StradX* have been incorporated into *StradWin*. Additional display options include: *Ortho*, *Isocentre* and *RF Oscilloscope*. The *Ortho* display provides two orthogonal *Reslice* views through the 3D dataset and is centred on the 2D US slice which is being viewed when the option is selected. *Isocentre* displays a *Reslice* image aligned with a predefined external co-ordinate system. The *RF Oscilloscope* feature enables the operator to examine the RF signals for the series of RF vectors making up each B-scan image. Further details about these display methods can be found in the *StradWin* user guide[7].

3D models and volume measurements are obtained by manually segmenting objects of interest at small intervals throughout the dataset. *StradWin* fits a surface to the set of contours and returns a volume measurement. As well as being able to see the region segmented on the selected 2D US images, the surface fitting process generates dashed line contours showing the interpolated surface on all intervening images. Displaying these additional contours allows the operator to judge if further segmentations are required to enhance the surface fit or 3D model. Additional measurement can be made in *StradWin* using *Landmarks* which can be placed on B-scan, *Panoramic* or *Reslice* images to measures lengths and angles.

Within *StradX*, the *Image Registration* tool could be used to correct for small variations in the position sensor readings and contact pressure between the skin and the US transducer. *StradWin* offers a similar tool called *Pressure*, however, it is only applicable to data which has been recorded in B-scan format and not RF. The format in which data is recorded is one of the specifications which must be set before recording a scan and will have been specified when creating a calibration template. The RF format has the advantage that the way in which the image information is displayed post-scan can be altered. It can be displayed in envelope format which is the conventional B-scan display of log-weighted RF signal envelope, phase format which displays the phase of the RF signal from 0º to 360º mapped onto a black and

[7] http://mi.eng.cam.ac.uk/~rwp/stradwin/

white image, or strain format where two adjacent images are compared in order to highlight areas in the image which are harder or softer than the surrounding tissues.

4.4. System Evaluation

The system was evaluated using a series of phantom based experiments. The first experiment was designed to assess accuracy and to establish an error margin for distance measurements made from the 3D US data. Further experiments investigated the effect of remounting the tracking tool on calibration accuracy, the process of constructing the 3D datasets and also the ability of *StradWin* to model small fracture gaps.

4.4.1. Accuracy Assessment

4.4.1.1. Methods

In section 3.5.3, three methods of assessing the accuracy of a 3D US system were described. To evaluate the accuracy of the optical tracking system and the calibration templates created, the method of comparing a known distance measured directly from a phantom against the same measurement obtained from a scan of that phantom was used. This indicated how accurately the 3D datasets were being constructed as well as established the error value in distance measurements.

Each of the calibration templates created for this project had an RMS error of less than 0.06 cm indicating that the system as a whole had been accurately calibrated for each templates. The quality of each template was further verified using the tracked pointer method described in appendix B. No problems were identified with any of the calibration templates.

A pin phantom was constructed to provide a separation measurement and allow the precision and accuracy to be determined. This phantom consisted of a rectangular

rubber base with two flat topped pins secured collinearly within the base, see figure 4-7. The separation between the centres of the two pin heads was measured five times using a vernier callipers and the mean separation was found to be 19.72 ± 0.04 mm. The pin phantom was placed in a water bath containing 9% glycerol solution for 3D US scans. Five scans of the phantom were recorded for each of the calibration templates created for the two US probes. Separation between the central points of the pins was measured in *StradWin* and the mean values calculated for each of templates.

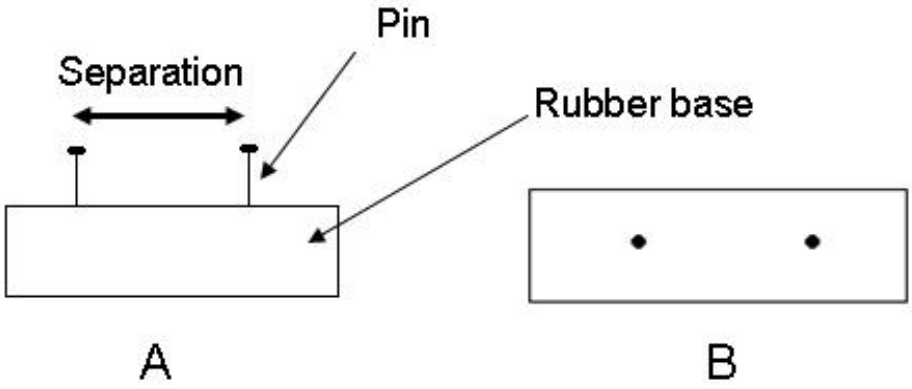

Figure 4-7: (A) Side view and (B) plan view of the pin phantom.

4.4.1.2. Results

The flat tops of the pins took on a mushroom type appearance in the 2D US image. Figure 4-8 shows a *Reslice* image obtained taken through the midline of the phantom, parallel to the direction of scanning. Moving the US probe over the phantom at a slow scanning speed meant that more than one US image was recorded over the site of each pin. The width of each US image used to construct one of the datasets can be seen in the *Reslice* shown in figure 4-8, with the finite width of the three US frames obtained over the two pin sites causing the pins to appear smeared. The US images which corresponded to the centre of the pin heads were the ones where the reflection from the pin was brightest. When reviewing the series of 2D US

images from a scan in *StradWin* only the information from the centre of the US beam width is displayed. Having identified these frames the separation between the two pin heads was measured on the 2D US images, rather than on the *Reslice* image, using the *Landmarks* tool in *StradWin*. Making the measurements on the 2D US images allowed the *Landmarks* to be positioned more accurately.

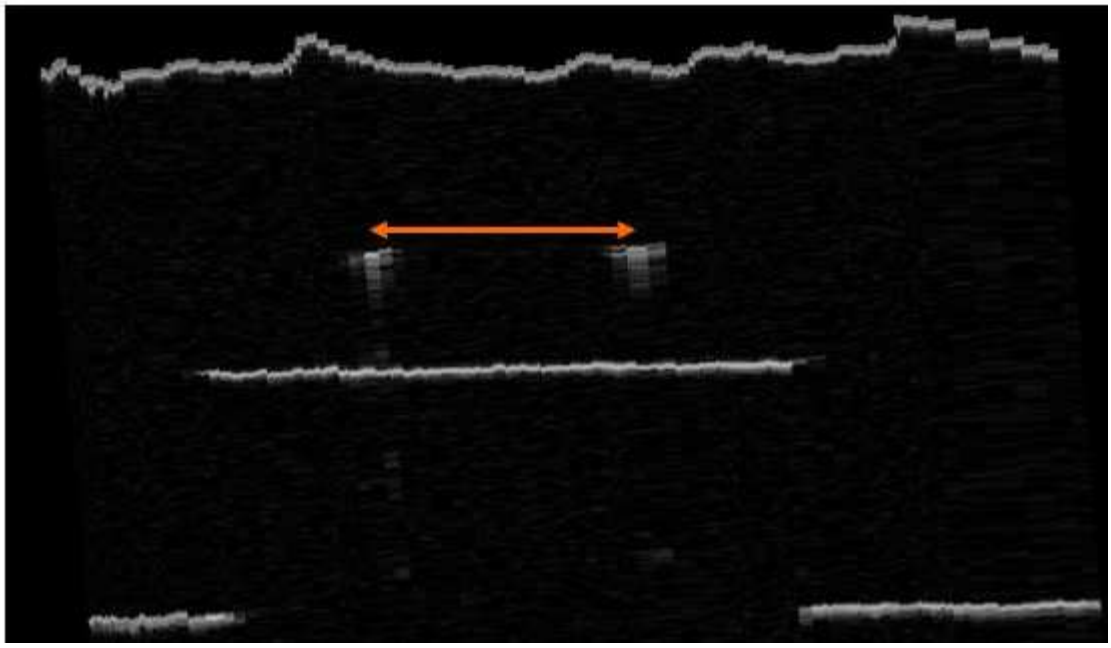

Figure 4-8: Reslice image taken through the pin phantom parallel to the direction of the scan. The arrow indicates the separation measured.

Figure 4-9 shows the results from the phantom scans with the calibration templates for the 5-10 MHz probe. For each of the templates the mean measurement from 3D US minus the calliper measurement of pin separation are plotted along with error bars indicating the 95% confidence intervals.

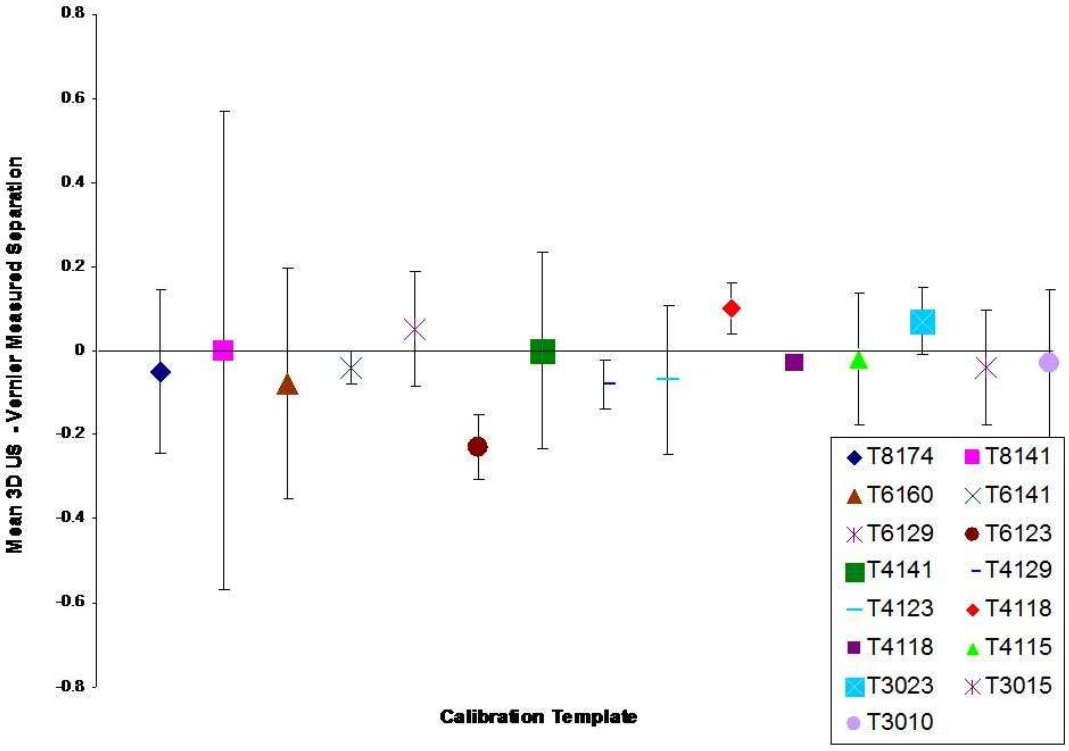

Figure 4-9: Results for pin phantom scans using the 5-10 MHz calibration templates. The mean 3D US minus the vernier calliper measured separations are plotted. The error bars indicate the 95% confidence intervals.

Each template for the 5-10 MHz probe had an RMS calibration error of less than 0.04 cm. Comparisons were drawn between the magnitude of the RMS errors for each calibration template and the magnitude of the corresponding pin phantom scan result. No obvious link was found, indicating that all the calibration templates created for the 5-10 MHz US probe were accurate and reliable for use.

All 3D US measurements were within ±0.25 mm of the measured separation of the pins obtained using the vernier callipers. Variation between the 3D US derived separations compared with the vernier calliper measurement was the result of three main factors. The speed at which the probe was scanned across the phantom, the rate at which *StradWin* acquired the US frames and the identification of measurement points by the operator. The speed of scanning and frame acquisition rate affected how many images of the phantom were captured during a scan. Ideally, when

measuring the separation between the two pins an image should be captured over the central point of each pin. However, the finite width of the US beam means that the image of the pin appeared smeared throughout the width of an US image. To decide upon the centre points of the two pins, both the series of 2D images and *Reslice* images were examined. In the 2D images the centre of the pin head was taken as the brightest reflection, however, depending on the number of images recorded this only indicated the image closest to the centre of the pin. By reviewing both the 2D US images and the *Reslice* image, the operator dependency for image selection should have been minimised. These results showed that for the 5-10 MHz calibration templates the Optical 3D US system could return distance measurements to within ±0.25 mm.

Results of the series of scans of the pin phantom using the 8-16 MHz probe and calibration templates are plotted on the figure 4-10. Comparing between figures 4-9 and 4-10 it was observed that the pin separation measurement results for the 8-16 MHz calibration templates were of higher accuracy than for those for the 5-10 MHz templates. All the calibration templates gave separation measurements that were within an error bound of ±0.1 mm.

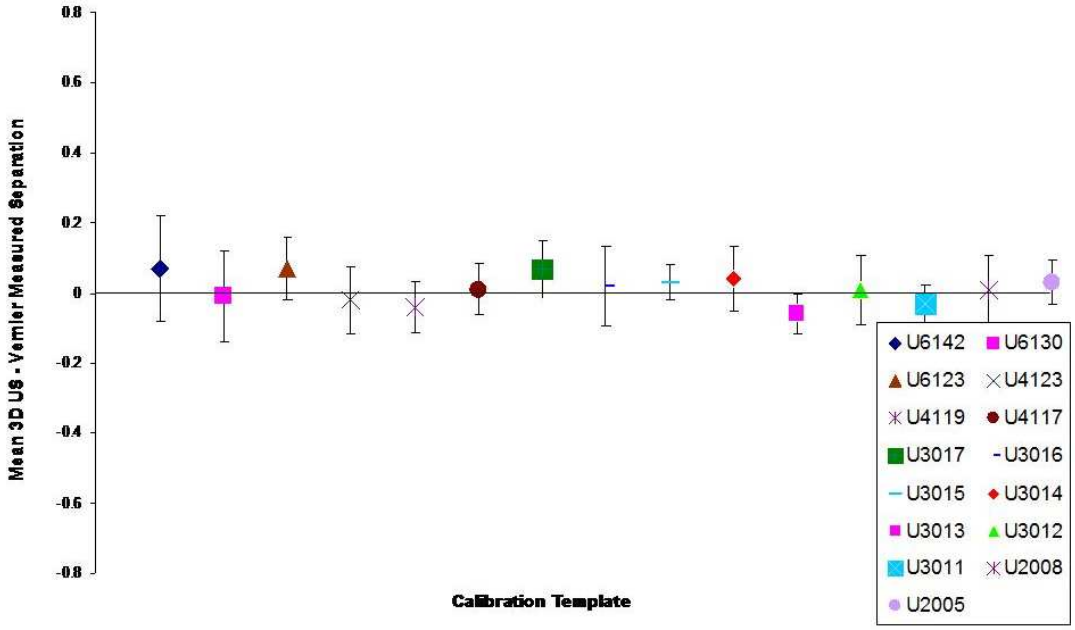

Figure 4-10: Results for the pin phantom scans using the 8-16 MHz calibration templates. The mean 3D US minus the vernier calliper measured separations are plotted. The error bars indicate the 95% confidence intervals.

The smaller error bounds may result from more detailed datasets being obtained. This could be due to the operator scanning at a slower rate despite trying to maintain a consistent scanning speed through out (frame acquisition rate was kept the consistent). It is also likely that the finite beam width of the 8-16 MHz probe is smaller than that of the 5-10 MHz probe which would have contributed towards more detailed 3D datasets. As the separation measurements were obtained from the 2D US images, the beam width of each US image used to make up the 3D dataset becomes a source of error. The more overlap between adjacent US images in the dataset, the less of the beam width of each image is required to build the dataset and the smaller this error will be. Comparing between the size of the RMS calibration errors and the results for the separation measurements showed no linked trend for the 8-16 MHz probe. It was concluded that the 8-16 MHz calibration templates were accurate and reliable for use.

If the system was calibrated improperly or there were unknown sources of error present it would be expected that the pin separation measurements from the scans results would have had much larger errors. It was concluded that both probes could return separation measurements to within an error bound of ±0.25 mm, with the main factors affecting the accuracy being the scanning speed and the frame acquisition rate.

4.4.2. Remounting the Tracking Tool

4.4.2.1. Methods

The MIG assessed whether removing and remounting the tracking tool, as would be done when changing from one US probe to another, would affect calibration accuracy (119). To test this they used a phantom object containing a series of beads set in predetermined locations. The phantom was scanned before and after the probe was removed and remounted. An iterative process was applied to the images to determine the locations of the spheres in comparison to there actual measured locations, this returned an RMS error similar to that for the calibration process. Before removing the tracking tool the RMS error returned for locating the beads was 0.26 mm, after removing and remounting the tracking tool it was 0.35 mm. It was concluded that remounting the tracking tool did cause a slight degradation to the accuracy of the 3D US system but given the high overall degree of accuracy this was not a significant affect.

To confirm this result for the Optical 3D US system a further series of scans of the previously used pin phantom were conducted. A random selection of calibration templates were sampled to check the effect of remounting the tracking tool at different depth settings and points of focus. For the 5-10 MHz probe templates T8174, T6141 and T4118 were used and for the 8-16 MHz probe calibration templates U6123, U3015 and U2008 were used (see Appendix C). The tracking tool was removed and remounted in the same position on the US probe before each scan of the phantom was carried out. Five scans of the phantom were conducted for each

template and the pin separations were measured in *StradWin* and compared to the vernier calliper measurement.

4.4.2.2. Results

The mean pin separation measurements determined from the 3D US scans minus the vernier callpier measured separation are plotted in figure 4-11, the error bars indicate the 95% confidence intervals. Remounting the tracking tool on the probe appeared to have no significant affect on the overall accuracy of the calibration templates. The Optical 3D US system was still capable of making separation measurements to within an error bound of ±0.25 mm.

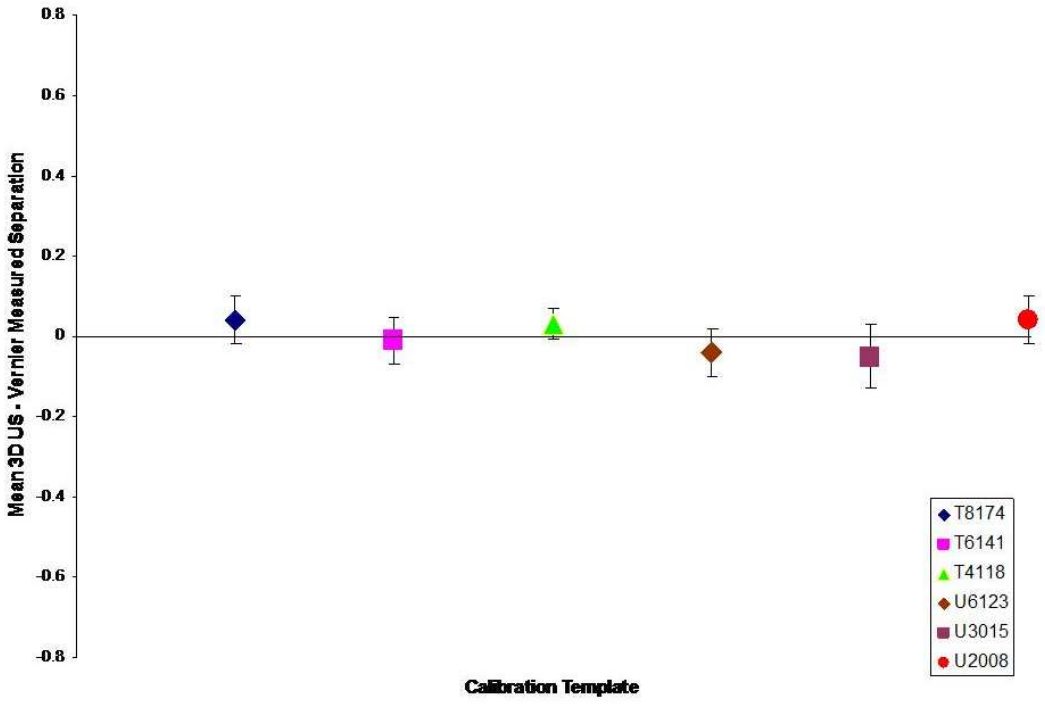

Figure 4-11: Results from pin phantom scans to assess the affect of remounting the tracking tool. Mean 3DUS minus the vernier calliper measured separations are plotted. The error bars indicate the 95% confidence intervals.

4.4.3. Image Acquisition Rate

4.4.3.1. Methods

Assessment of the optical tracking system using the pin phantom identified that scanning speed and frame acquisition rate effected how many US images were captured during a scan. This influences the level of detail contained within the 3D dataset and effects the accuracy of separation measurements. To obtain a continuous and detailed 3D dataset the US images should be recorded using a frame acquisition rate and scanning speed that will cause the finite width of each US image to overlap when placed in the dataset. When this occurs the information from the centre of the of the US image width is used first to fill in the dataset with the gaps between frames being filled in equally using the remaining US image beam width from adjacent images. The more adjacent images over lap the less of the beam width has to be taken into account giving more image detail and reducing the error on the length measurements caused by beam width.

Within *StradWin* there are a six pre-determined frame rates at which the US images can be captured: 5 fps, 10 fps, 15 fps, 20 fps, 25 fps and full speed (fps = frames per second), where full speed gives the maximum available frame rate which, depending on the demands on the PC's processor, may be above the fastest set rate of 25 fps. However, running the live image display in *StradWin* (this allows the US images captured to be viewed during scanning) whilst recording a 3D US scan causes extra demands on the processor reducing the rate at which frames are recorded. For example, a frame rate of 25 fps may be selected but a frame rate varying between 11-20 fps is actually achieved.

Speed of scanning is an operator dependent variable. To determine the best combinations of scanning speed and frame rate that will provide detailed 3D US datasets, a series of test scans of a phantom object were carried out. The phantom was a metal plate with a circular hole in its centre, a diagram of which shown in figure 4-12. The metal plate was chosen as its surface was easily identifiable on US images and its design offered both a simple separation measurement in the form of

the diameter of the plate, and a more complex measure of the diameter of the hole. The diameter of the plate was termed measurement (1) and the diameter of the hole was measurement (2). Using the vernier callipers measurement (1) was determined to be 90 ± 0.04 mm and measurement (2) was 50 ± 0.04 mm. The metal plate was placed in a water bath containing 9% Glycerol solution for scanning.

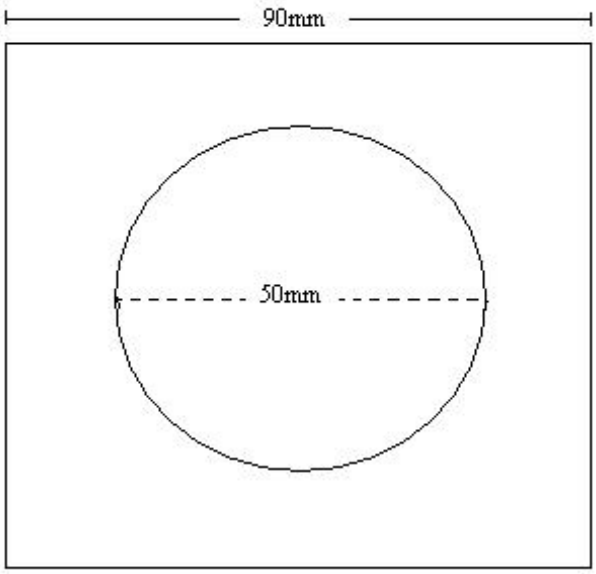

Figure 4-12: Diagram of the metal phantom used to determine the optimum scanning speed and frame rate to obtain detailed 3D US datasets.

Three different scanning speeds were established by the operator: 'fast'; 'normal' and 'slow'. The phantom was scanned at each speed five times to obtain average scanning speeds, a 'fast' scan was 1.20 ± 0.04 s, a 'normal' scan was 6.30 ± 0.31 s and a 'slow' scan took 12.91 ± 0.55 s. For each of the six frame rates, five phantom scans were conducted at each of the three scanning speeds and the mean separation measurements calculated. The same calibration template was used throughout the series of scans, template U3015.

Measurements (1) and (2) were made from the 3D US scans using the *Landmarks* tool in *StradWin*. The points between which to make measurements (1) and (2) were

identified by reviewing both the 2D US images and the *Reslice* image from each scan. Measurement (1) was made between the centres of the first and last US images containing a complete echo from the surface of the metal plate. Measurement (2) was made between the centre of the first US image indicating the hole to the centre of the last image indicating the hole. The hole appeared gradually on the scans starting off as a small dip in the centre of the reflection from the surface of the plate which quickly increased in width and depth until it filled the full view of the probe. As the other side of the hole was reached this appearance was reversed.

4.4.3.2. Results

The results of measurement (1) determined from the mean 3D US scans measurements minus the calliper measured separation are shown in figure 4-13. Comparative results for measurement (2) are presented in figure 4-14. Table 4-1 provides the mean separation measurement results and details of which combination of scanning speed and frame rate relates to the scan numbers for both graphs.

Scan	Frame Rate (fps)	Scan Speed	3D US Measurement 1 (mm)	Standard Deviation (mm)	3D US Measurement 2 (mm)	Standard Deviation (mm)
1	5	Fast	-	-	-	-
2	10	Fast	-	-	-	-
3	15	Fast	85.87	2.13	46.65	0.85
4	20	Fast	84.23	1.01	46.09	1.37
5	25	Fast	85.2	2.51	-	-
6	Full Speed	Fast	84.65	1.49	48.02	1.76
7	5	Normal	85.46	2.9	47.71	1.55
8	10	Normal	88.49	1.41	47.97	0.98
9	15	Normal	89.28	0.38	49.94	0.44
10	20	Normal	88.26	0.97	50.06	0.59
11	25	Normal	88.84	0.87	50.11	0.45
12	Full Speed	Normal	88.09	0.68	50.12	0.66
13	5	Slow	87.64	1.52	49.64	0.62
14	10	Slow	88.03	0.63	49.64	0.68
15	15	Slow	89.66	0.43	50.16	0.32
16	20	Slow	89.31	0.73	50.25	0.38
17	25	Slow	89.27	0.44	50.15	0.24
18	Full Speed	Slow	88.71	0.27	50.37	0.43

Table 4-1: Details of frame rate and scanning speed combinations and the results and errors for measurements (1) and (2).

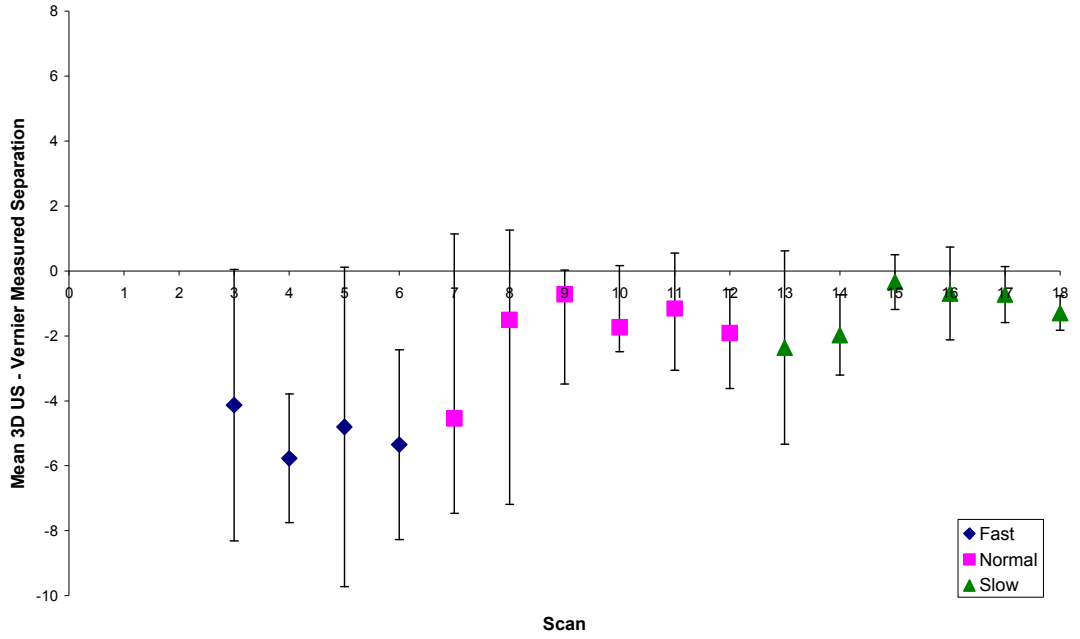

Figure 4-13: The results for measurement (1). Mean 3D US minus the vernier calliper measured separation for various frame rate and scanning speed combinations, the error bars indicate the 95% confidence intervals.

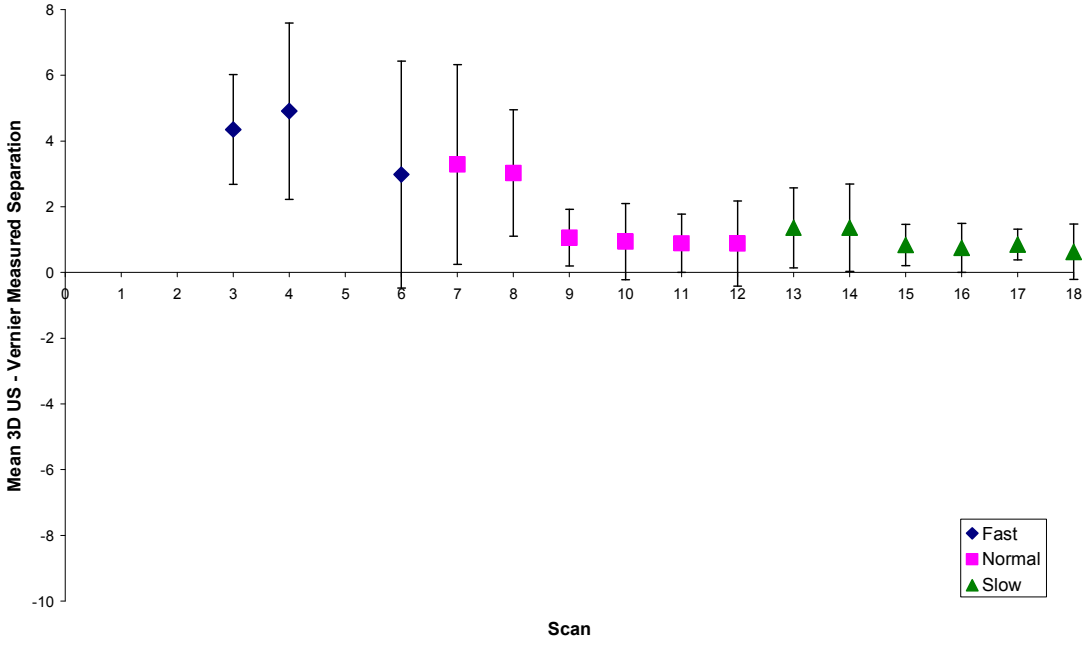

Figure 4-14: The results for measurement (2). Mean 3D US – veriner rule measured separation for various frame rate and scanning speed combinations, the error bars indicate the 95% confidence intervals.

At the slower frame rates of 5 fps and 10 fps it was not possible to obtain sufficient images of the phantom when using the 'fast' scanning speed to make either measurements. Even at faster frame rates of 15 fps and above it was difficult to obtain scans where the datasets contained enough detail to make measurements. Figure 4-15 shows the *Reslice* images acquired using the 15 fps frame rate and the 'fast' scanning speed. Each *Reslice* was obtained through the centre of the dataset parallel to the direction of scanning. The construction of the dataset using the beam width of each US images can be clearly seen. When there were no adjacent or overlapping frames the full width of the US image was displayed. In scan 1, the dataset was complete and each US image overlaps the previous image. For the other four *Reslice* images there were gaps in the datasets and in many places the full beam width of the US frames had been used when constructing the dataset. Despite this, the speed of scanning did not allow enough US images to be recorded to produce a continuous dataset. From this series of 3D US scans measurement (1) could be determined from all the dataset, however, only datasets one contained points between which to make measurement (2). For comparison, figure 4-16 shows the *Reslice* images for the scans of the phantom using a frame rate of 25 fps at the 'normal' scanning speed. For that combination all of the 3D datasets were complete and the degree of overlap between adjacent images meant that considerably less information was required from the beam width of each US image to construct the datasets.

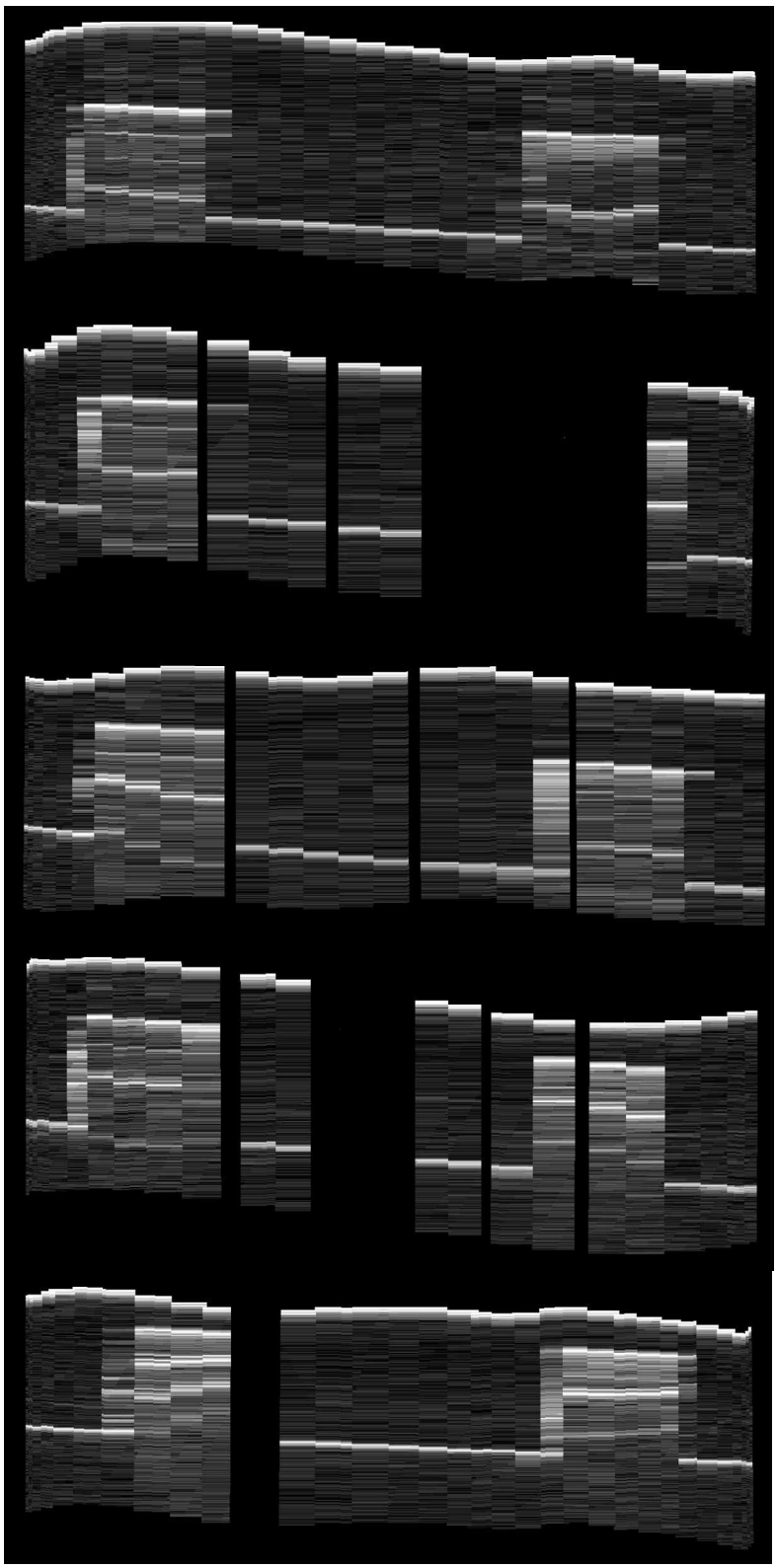

Figure 4-15: *Reslice* images from the five scans of the phantom at 15 fps for the 'fast' scanning speed. Reslices were taken through the middle of the datasets parallel to the direction of scanning.

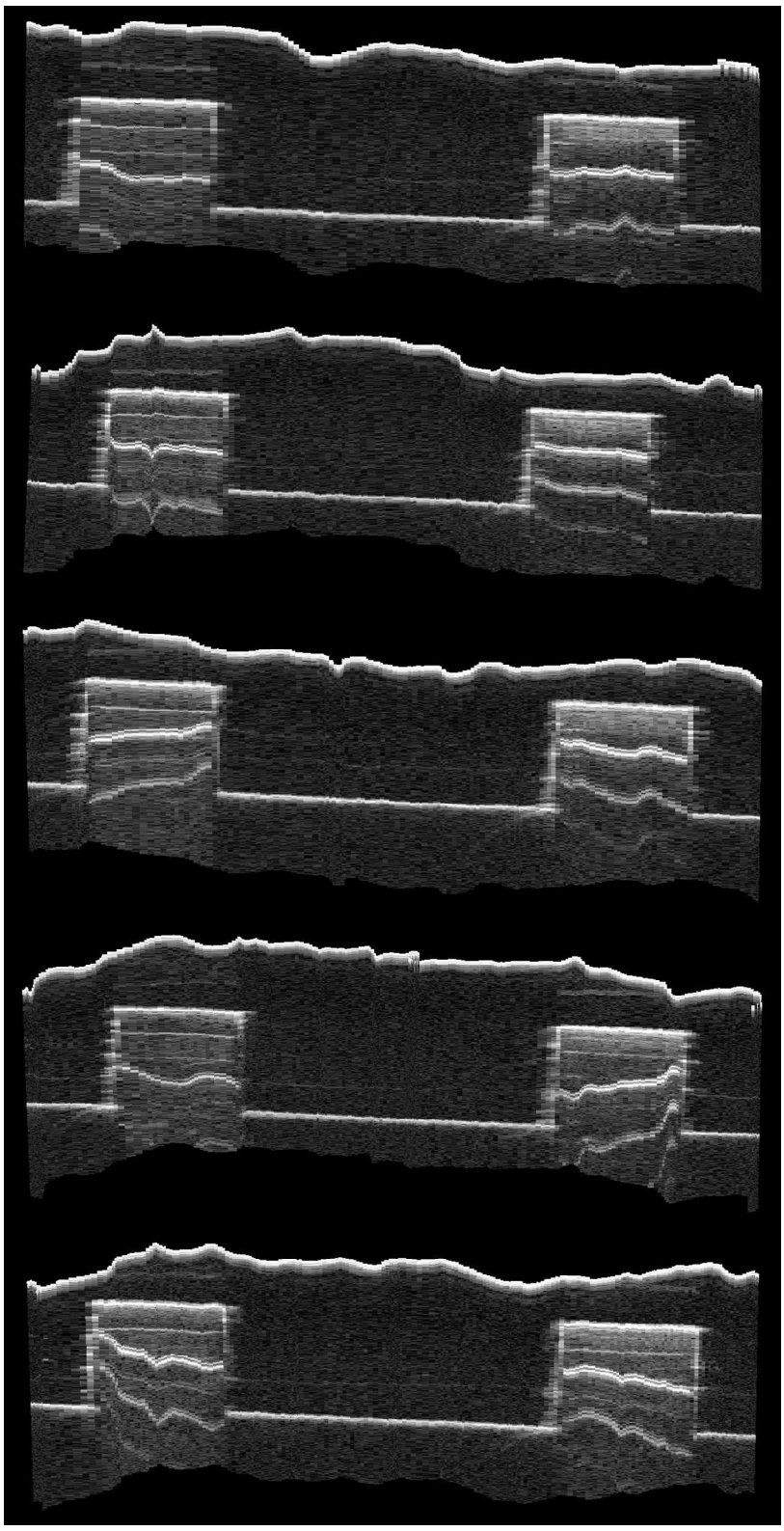

Figure 4-16: *Reslice* images from the five scans of the phantom at 25 fps for the 'normal' scanning speed. Reslices were taken through the middle of the datasets parallel to the direction of scanning.

From both the results shown on figure 4-15 and 4-16 and visual examination of the *Reslice* images in figure 4-15 it was clear that the 'fast' scan speed, especially at lower frame rates, was not suitable for detailed scanning. Also, the spread of results for frame rates 5 fps and 10 fps indicated that neither rate, regardless of scanning speed, was suitable for use.

The frame rate and scan speed combination of 15 fps 'slow' gave the best results for measurement (1) and the frame rate and scan speed combinations of 20 fps 'slow' gave the best results for measurement (2). The frame acquisition rate did not stay steady during scanning but varied dependent on the available processor power of the PC available during the scan. For the frame rate of 15 fps, found to give the best results for measurement (1), it was recommended that scanning be conducted at a higher frame rate to limit the occurrence of the frame rate dropping below 15 fps.

4.4.4. Probe Resolution Assessment

4.4.4.1. Methods

Previous assessment of the resolution of the US probes, using the Perspex rod phantom, had shown both to be able to resolve objects down to 1 mm in width, see section 3.5.1. A second set of probe resolution assessments were carried out to build on these results using a phantom that offered a closer model to real life. This phantom allowed a sub-millimetre wide fracture gaps to be created and could also simulate a crack in the bone. The phantom was constructed from a SawBones Tibia (SawBones Worldwide) which had been cut in two at the mid-shaft to simulate a fracture. The two sections were reunited using a unilateral external fixator (Orthofix) as shown figure 4-17. As well as examining the 2D US images of the simulated fractures recorded in *StradWin*, 3D models would be constructed using *StradWin* to establish if the small simulated fracture gaps could be adequately modelled using the segmentation process or would poor resolution render them invisible in the 3D models.

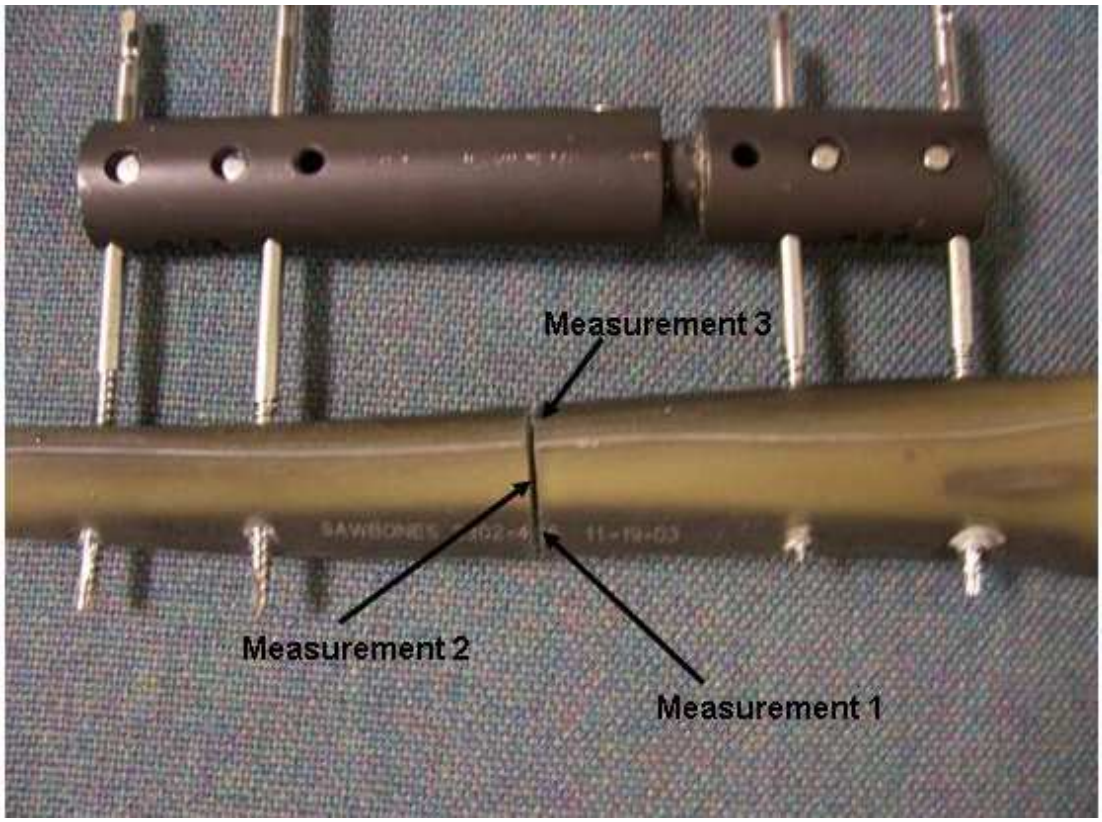

Figure 4-17: Fracture gap phantom constructed from a SawBones tibia and an Orthofix external fixator. The three points at which the width of the simulated fracture gap was measured are indicated.

The fixator was attached to the bone sections in a way that ensured one of the flat faces of the tibia was presented uppermost for scanning when the phantom was placed in the water bath. By making small adjustments to the external fixator it was possible to change the separation between bone ends to simulate fracture gaps of varying size. The process of sawing the bone in half to create the fracture resulted in a small section of the bone being lost meaning that when the bone ends were brought back together they were no longer a perfect fit and there was a visible step in the surface of the bone. This also meant that any gap simulated was not completely uniform in width. To overcome this problem the width of any simulated fracture gap was measured at three points as indicated in figure 4-17. Four different scenarios were simulated using the phantom.

1. Bone ends pushed together to simulate a crack in the bone
2. A fracture gap of less than 1 mm
3. A fracture gap of approximately 2 mm
4. A fracture gap of approximately 3 mm

When setting the size of the fracture gap the bone ends were moved into place and the external fixator tightened before a the vernier calliper was used to measure the width of the simulated gap at the three points across the face of the tibia. Table 4-2 gives the details of the fracture gap measurements determined using the callipers. The phantom was placed in a water bath containing 9% Glycerol solution and was scanned using both US probes for each scenario. The probe was held a short distance above the bone surface, centred over and perpendicular to, the simulated fracture and then swept over the bone.

Scenario	Measurement Site	Gap Measurement (mm)
1	1	0±0.02
	2	0±0.02
	3	0±0.02
2	1	0.79±0.02
	2	0.8±0.02
	3	0.85±0.02
3	1	1.96±0.02
	2	1.82±0.02
	3	1.74±0.02
4	1	3.13±0.02
	2	3.06±0.02
	3	2.93±0.02

Table 4-2: Details of each fracture gap scenario set using the SawBones phantom. Measurements of the gap were made using the vernier callipers.

4.4.4.2. Results

A 3D model of the phantom was constructed in *StradWin* for each scan and an US image extracted from each dataset to show the appearance of the fracture gap. Figure 4-18 shows the models and images obtained for scenario 1.

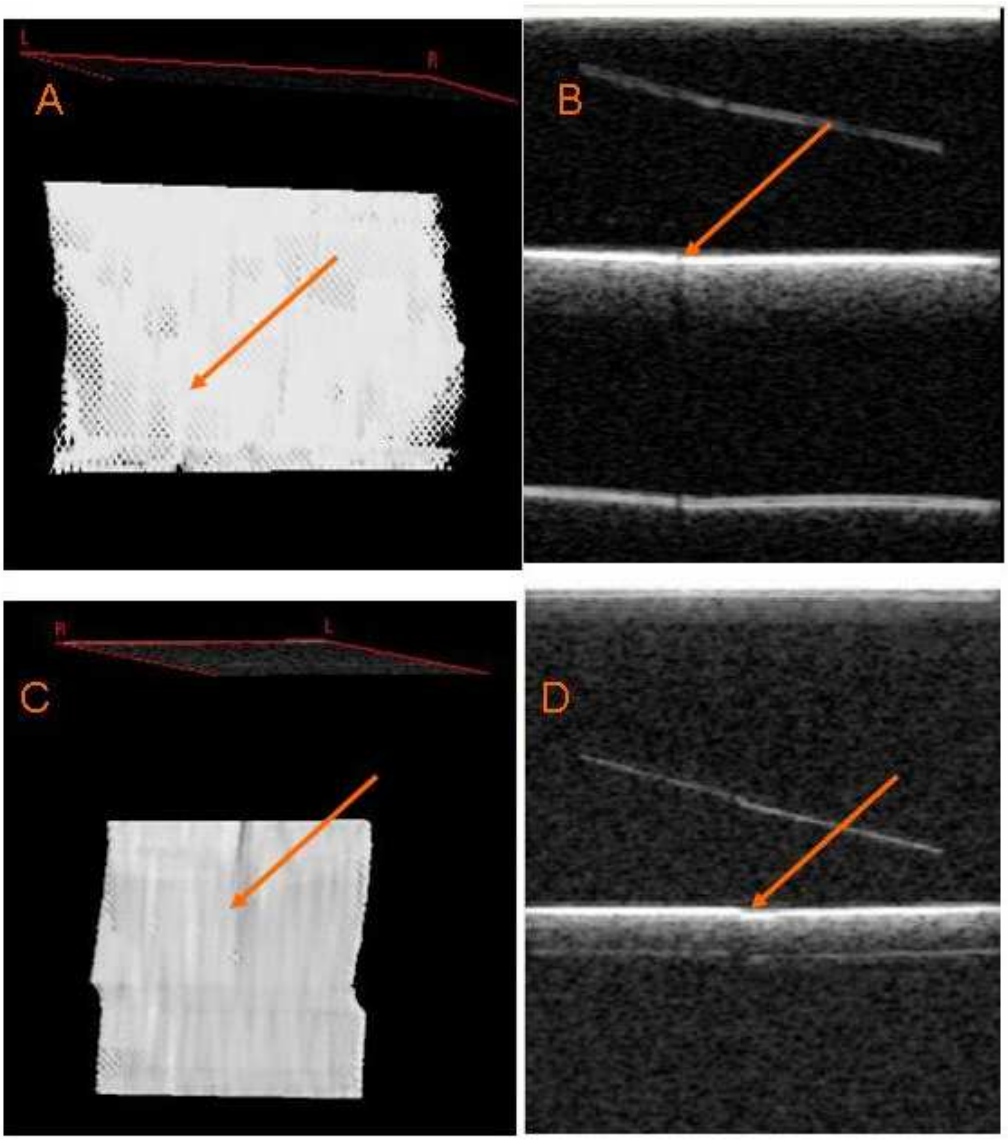

Figure 4-18: Scenario 1, no gap. (A) 3D model and (B) 2D US image from the 5-10 MHz scan. (C) 3D model and (D) 2D US image from the 8-16 MHz scan. The arrows indicate the location of the gap.

In the 5-10 MHz scan of scenario 1 a small discontinuity was visible in the 2D US image figure 4-18(A) but was not evident in the 3D US model, figure 4-18(B). Similarly a small discontinuity could be seen in the smooth surface of the phantom obtained with the 8-16 MHz probe, figure 4-18(D) indicating the presence of the crack, however, was not visible in the 3D model, figure 4-18(C).

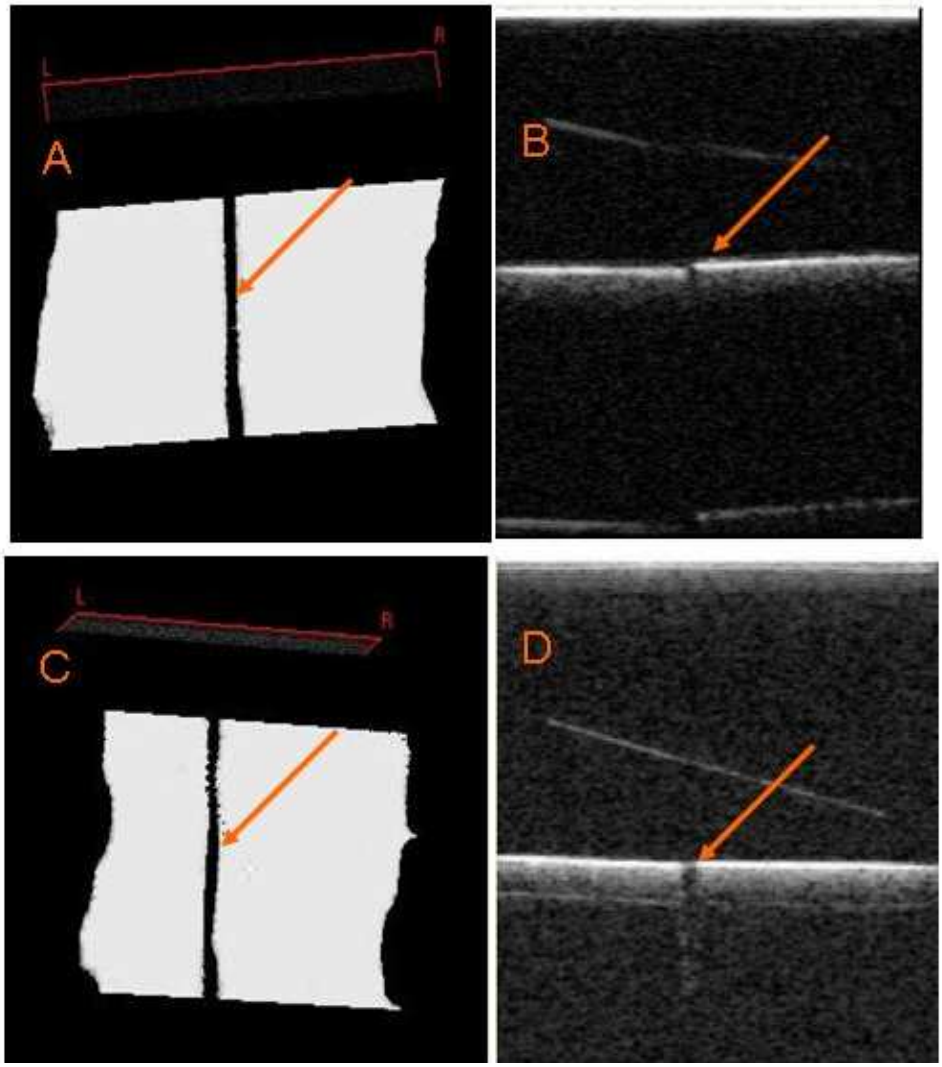

Figure 4-19: Scenario 2, a gap of less than 1 mm. (A) 3D model and (B) 2D US image from the 5-10 MHz scan. (C) 3D model and (D) 2D US image from the 8-16 MHz scan. The arrows indicate the location of the gap.

In scenario 2 a fracture gap of approximately 0.8 mm was simulated. This gap was visible on both the 2D US images and 3D models, see figure 4-19. The 8-16 MHz 2D US image of the gap gave a clearer view of the width of the gap than the 5-10 MHz scan. The cause in the difference in appearance of the gap is likely to be down to angualtion of the US probe during scanning. One of the bone ends appears to be elevated relative to the other, see figure 4-19(B) causing refraction of the US beam around the elevated edge.

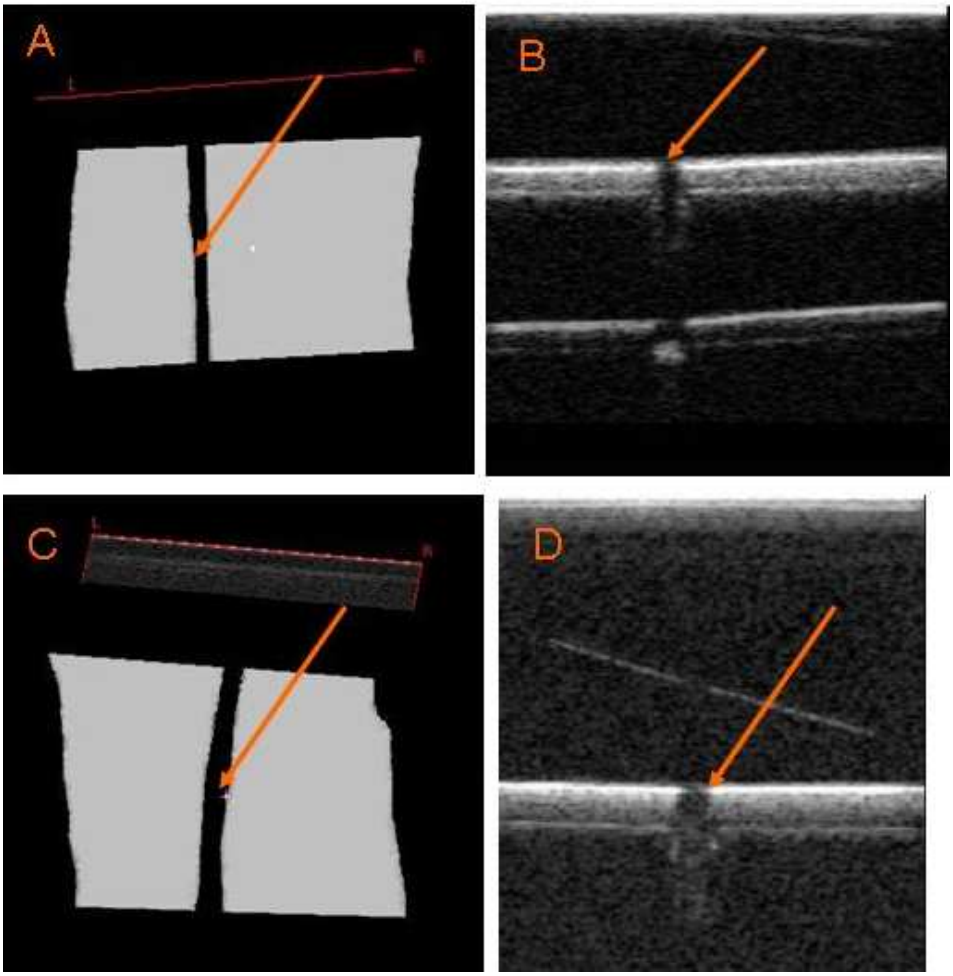

Figure 4-20: Scenario 3, a gap of 2 mm. (A) 3D model and (B) 2D US image from the 5-10 MHz scan. (C) 3D model and (D) 2D US image from the 8-16 MHz scan. The arrows indicate the location of the gap.

A fracture gap of approximately 2 mm in width was simulated for scenario 3. In the 5-10 MHz 2D US image, figure 4-20(B), the fracture gap was clearly visible. In the 2D US image from the 8-16 MHz scan, figure 4-20(D) the surface reflection from the SawBone protruded into the gap making it appear smaller than it actually was, this may have been due to refraction of the US beam at the edges of the gap.

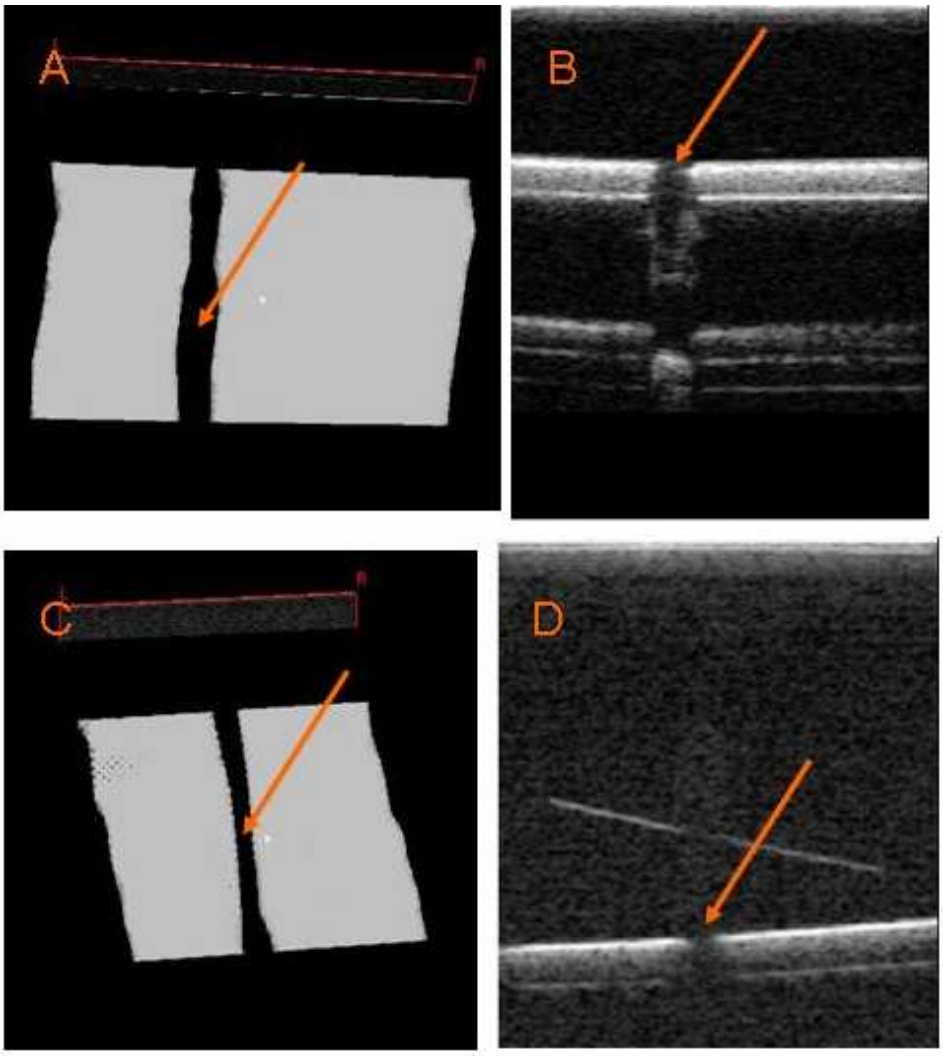

Figure 4-21: Scenario 4, a gap of 3 mm. (A) 3D model and (B) 2D US image from the 5-10 MHz scan. (C) 3D model and (D) 2D US image from the 8-16 MHz scan. The arrows indicate the location of the gap.

The final scenario simulated a fracture gap of approximately 3 mm in width. The protrusion of the surface reflection into the gap was again seen in the 8-16 MHz scan, figure 4-21, and the corresponding 3D model appeared narrower than that of the 5-10 MHz scan. Refraction and angulation of the US probe during scanning remain likely causes for the difference in size of the gap seen. The difference in acoustic properties of the phantom compared to the Glycerol solution will have been a factor.

4.5. Discussion

The Polaris optical tracking unit offered a higher degree of positional accuracy for tracking objects than the previously used FOB EM system. Furthermore, the optical tracking system did not suffer from interference when used in close proximity to EM field sources and metal objects. Capturing the image data in raw RF format meant that the 2D US images underwent less processing before being displayed in *StradWin* and would also be suitable for later use in novel image processing and analysis techniques.

One of the major advantages of the *StradWin* software was the ability to create calibration templates for a specific probe, depth setting and point of focus. These could be loaded to reset the system to the results of a previous calibration, thus, removing the need to calibrate the system each time it was switched on or when any of the system settings were changed.

The pin phantom assessment of the system and calibration templates verified that the 3D datasets were being constructed accurately and reliably and that each calibration template created was suitable for use. The results of this assessment showed that there were no signs of interference affecting the tracking system and also allowed the associated error for separation measurements to be determined, this was found to be ±0.25 mm. Further use of the pin phantom to test the effect of removing and

remounting the tracking tool showed that this had no significant effect on the accuracy of the calibration templates.

The biggest factors identified as influencing dataset construction and, thus, separation measurement accuracy, were the US frame acquisition rate and scanning speed. The more adjacent US images overlapped in the 3D dataset the less information from the finite width of the US beam was required for construction and the greater the detail obtained. Using a second phantom the different combinations of frame rate and scanning speed were tested to find which would produce detailed dataset. From these results it was concluded that a 'slow' or 'normal' scanning speed in combination with a frame rate of 20 fps or above would provide detailed 3D datasets from which accurate measurements could be made.

A phantom simulating a fractured bone was used to determine whether the US probes could resolve small gaps as may be required when imaging fracture repair. This series of phantom scans showed both US probes were able to resolve fracture gaps of less than 1 mm. When the bone ends were pushed together to simulate a crack in the bone this was detectable on the 2D images, though when modelled into 3D the small discontinuity in the surface of the bone was no longer visible. In a clinical situation an un-displaced fracture resulting in a crack in the bone would also cause a haematoma to forms which would draw attention to the presence of the crack on a 3D US scan.

The evaluation of the Optical 3D US system has shown it can provide an accurate and reliable means of conducting 3D US scans that is suitable for clinical use. This system has been adopted for the clinical application of monitoring fracture repair, see Chapter 5, and is trialled as a means of measuring muscle volumes *in vivo*, see Chapter 7.

5. Monitoring Fracture Repair using Freehand 3D Ultrasound

5.1. Introduction

Riccardi et al. found that Ultrasound could image the earliest stages of the fracture repair process often detecting signs of healing weeks before they were evident on X-ray (48). However, the operator dependency of image interpretation and problems of making accurate repeat measurements led to the conclusion that 2D US was not a viable alternative to X-ray for monitoring fracture repair. The development of 3D US has greatly reduced operator dependency. The 3D datasets that it creates can be used to construct models of objects of interest as well as provide additional views of the anatomy which are not available using X-ray or 2D US. 3D US could be used to monitor the healing process, as frequently as required, without hazard to the patient. The ability to image the initial stages of healing would allow for earlier detection of complications. It was hypothesised that 3D US could provide a more effective alternative imaging tool than X-ray for monitoring fracture repair and limb lengthening.

To establish whether 3D US could provide a suitable alternative to X-ray for monitoring fracture repair a clinical study was carried out. Patients who had sustained a long bone fracture of the lower limb or who were undergoing a limb lengthening procedure were followed up using both modalities. Comparisons were drawn between what could be detected and at each follow-up appointment.

5.2. Methods

Inclusion criteria for participants were that they were healthy, skeletally mature males and non-pregnant females who had sustained a closed fracture to one of the long bones of the lower limb or who were undergoing limb lengthening. Patients being treated conservatively using a plaster cast were excluded as a window would have had to have been cut in the cast to allow scanning. Approval for the study was granted by Lothian Research Ethics Committee and NHS Lothian Research and Development Management.

Suitable patients were approached whilst on the ward, shortly after fracture had occurred, and were recruited through informed consent. Patients were followed up from their first attendance at the out patients fracture clinic at the Edinburgh Royal Infirmary until their consultant deemed full weight bearing could be resumed or until the occurrence of complications had been identified. Seven participants were recruited to the study, however, two had to be withdrawn due to complications arising during the healing process. Thus, 5 patients (age range 17-38 years, median age 30 years) participated. Three patients had sustained tibial fractures which were stabilised using an IM nail. One patient had a fractured femur that was stabilised using a unilateral external fixation device and the remaining participant was undergoing tibial lengthening using an Ilizarov frame.

Of the two withdrawn participants, one was withdrawn after an initial set of scans identified complications the other was withdrawn before any scans could be recorded. The participant who was withdrawn after scanning was undergoing limb lengthening through the use of an ISKD nail. This patient was recruited after lengthening had been started in order to determine what differences would be seen during healing compared to the Ilizarov patient. It was thought that the presence of the nail would result in a reduction in the amount of callus produced compared to the Ilizarov patient. However, the first scan of this patient revealed complications in the form of a cyst within the lengthening gap. The patient was withdrawn from the study and no further scans were carried out. Results from that scan have been included in

this study as they demonstrated how well the complication was picked up on the 3D US scans. The other participant who was withdrawn had sustained a tibial fracture which was stabilised using an IM nail. This patient developed fracture blisters early on which were dressed to such an extent that scanning was not possible. More than two months post fracture the blisters were still being treated and scanning was still not possible. By this point signs of callus were visible on X-ray and as the patient was not due to return to clinic for a number of weeks they were withdrawn from the study.

On attendance at the outpatients fracture clinic, for routine assessment, each patient underwent a series of 3D US scans. Standard procedure was to obtain four 3D US scans at each clinic appointment. Two scans were recorded using the 5-10 MHz probe, the first was taken with the probe positioned over the fracture site, held parallel to the length of the leg and swept around the circumference of the limb over the fracture site. This was referred to as a "width" scan. The second scan was recorded with the probe held perpendicular to the length of the limb and was swept along the length of the leg to incorporate sections of healthy bone either side of the fracture gap. This was referred to as a "length" scan. These scans were then repeated using the 8-16MHz probe. For each scan the series of 2D US images recorded and the series of *Reslice* images perpendicular to the original scan direction were reviewed in order to interpret the fracture site anatomy. If a significant change was noted in the fracture site anatomy a 3D model was constructed from that dataset.

The tibial fracture patients were followed up at 2 weeks, 6 weeks and 3 months as per the standard clinical protocol. The follow-up appointments for the femoral fracture patient and tibial lengthening patient were more frequent and were dictated by the attending consultant. All patients were followed up until full weight bearing was resumed. On the first attendance at clinic the depth, point of focus and received gain settings for both probes were set to give an optimised image of the fracture site for each patient. These settings were noted for each probe and used for each subsequent scan of that particular patient. The set up of the Optical 3D US system shown previously in figure 4-5 was used to scan the lengthening patient and tibial

fracture patients. In order to scan the femoral fracture patient the position of the examination table had to be reversed. The corresponding X-rays, taken as part of routine care for each participant, were obtained from Radiology after the clinic appointment. It should be noted that these were not used as a guide for interpreting the 3D US data.

5.3. Results

Results are presented for each case in turn before being summarised in table 5-1 to highlight the difference in time scale between the signs of healing detected using 3D US compared to X-ray. The original X-ray images and the annotated X-ray images used in this chapter have been included on a DVD at the end of the thesis for reference if required.

5.3.1. Case 1

Spiral fracture of the left distal tibia stabilised using an IM tibial nail.

On the first attendance to clinic, 2 weeks post fracture, the patient was scanned using both frequencies of US probe, however, the site of fracture could not be located. On reviewing the X-rays the fracture was found to be more distal than had been indicated in the patient's notes thus the wrong portion of the leg was scanned at the first follow up. There were no signs of callus on the X-rays obtained at 2 weeks as can be seen in figure 5-1. The spiral nature of the fracture was visible in the anterior-posterior (AP) view, however, was not as apparent in the lateral view.

At the 6 week follow-up, the location of the fracture was identified using 3D US, however, the close proximity of the fracture to the ankle joint made it difficult to maintain skin contact with the probe allowing only a short section of the bone to be scanned. Despite this limited scan region, the 3D model constructed from the data, see figure 5-2(A), was able to show the spiral pattern of the break. Areas where the first signs of healing were detected, in the form of echogenic deposits, have been

highlighted in yellow on the model. Material could be seen on the 3D US scans filling in the fracture gap as well as extending from the periosteal surface of the bone. There were still no signs of callus on the corresponding X-rays.

The third follow-up was at 19 weeks post fracture at which point the patient was encouraged to resume normal weight bearing. On the 3D US scans an increase in the volume of callus was seen when comparing the 3D models built at 6 weeks and 19 weeks, see figure 5-2. Bridging of the fracture had occurred at some points. The appearance of the callus material was brighter in greyscale intensity on the US images indicating that the callus was maturing. On X-ray, bridging callus could be seen extending across the fracture gap on both sides of the tibia as viewed on the AP X-ray, see figure 5-3(A & C) and parts of the original fracture line had become obscured. The most substantial area of callus on the lateral X-ray (figure 5-3(B & D)) was on the posterior aspect of the tibia. In neither view did the callus appear to have fully united the fracture. The patient was due to attend a 6 month follow-up appointment to ensure the fracture had reach consolidation satisfactorily but did not attend.

Figure 5-1: (A) AP and (B) lateral X-rays of the spiral tibial fracture taken at 2 weeks follow-up. The location of the fracture is indicated by the arrows. (C) and (D) show close ups of the fracture site on the AP and lateral X-rays respectively.

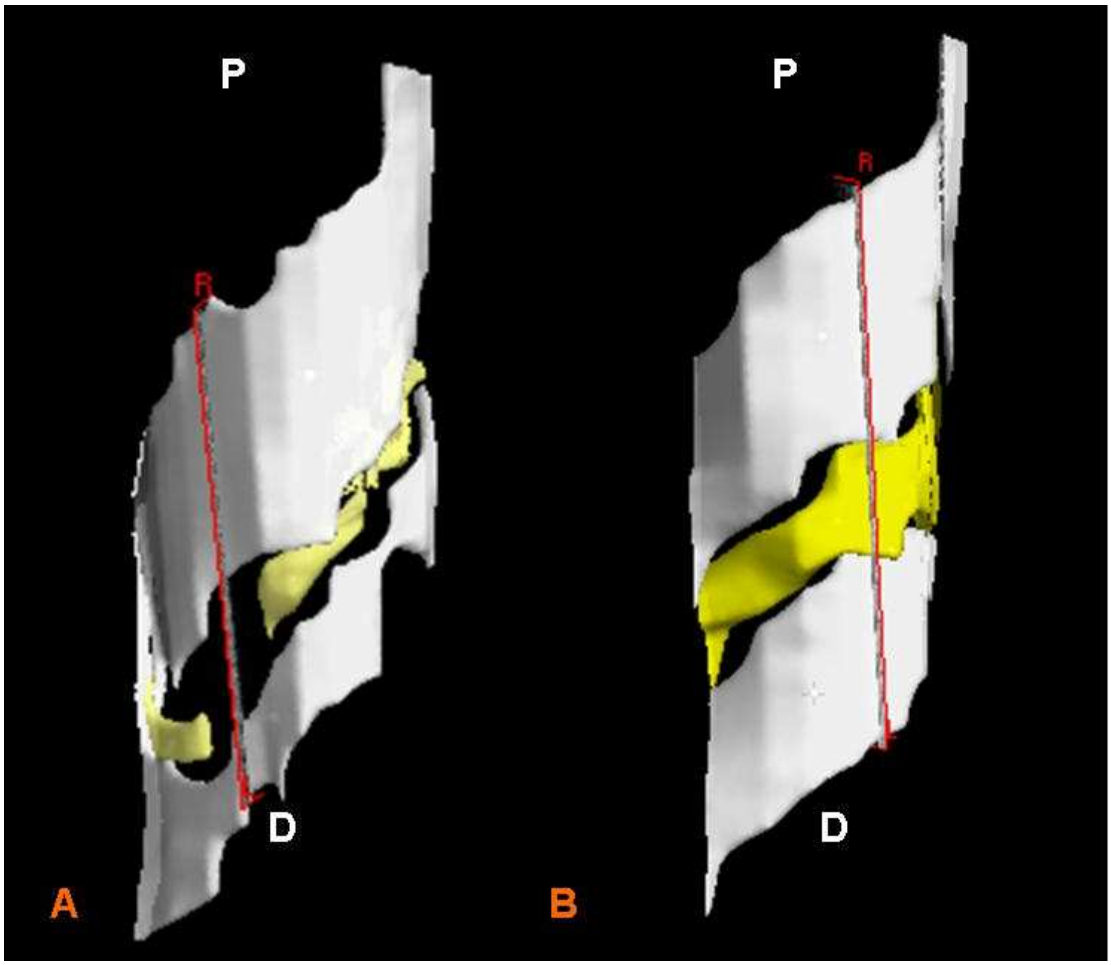

Figure 5-2: 3D models of the tibial fracture at (A) 6 weeks and (B) 19 weeks post fracture. Both models orientated to show the anterior surface uppermost. The spiral nature of the break can be seen and the increase in the region of forming callus, shown in yellow, is also notable. (P) proximal, (D) distal.

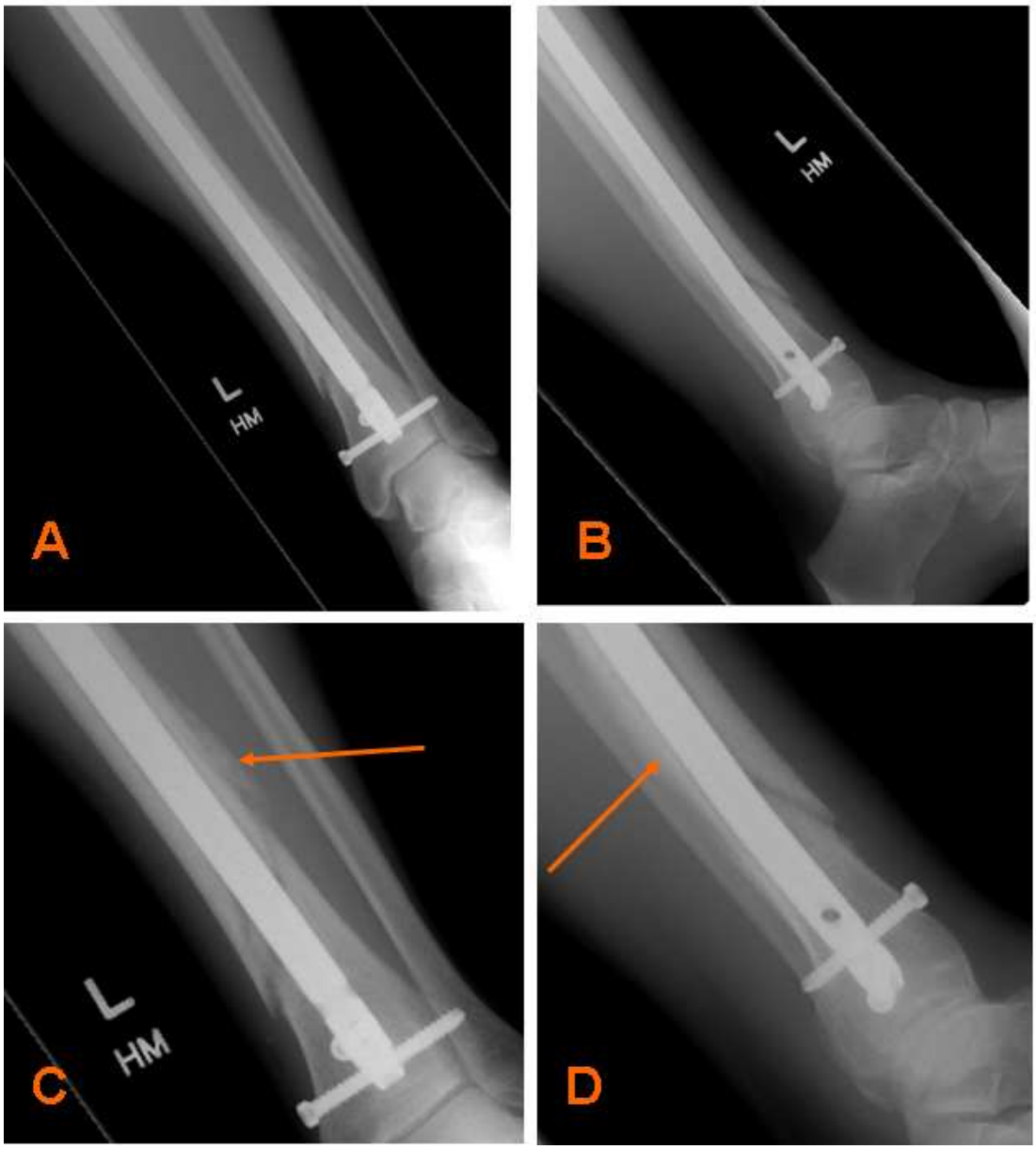

Figure 5-3: (A) AP and (B) lateral X-rays taken at 19 weeks post fracture. Callus can be clearly seen on the AP X-ray this is indicated on the close up views of the (C) AP and (D) lateral X-rays. Although callus is present it does not appear to bridge the fracture.

5.3.2. Case 2

Midshaft fracture of the right tibia stabilised using an IM tibial nail.

The first 3D US scans were taken 2 weeks post fracture. The edges of the fracture gap appeared well defined and echogenic deposits could be seen between the bone ends indicating healing was underway. These deposits are thought to show the

fibrous material and mineral deposits laid down in the early stages of callus formation (58). The regions of early callus formation have been highlighted on the *Reslice* image, see figure 5-4. Swelling of the tissue above the fracture was observed along with a faint outline showing the initial extent of the haematoma. On the 5-10 MHz scans it was noted that there was a repeated bone surface artefact under the sections of normal bone on the *Reslice* image, however, this was not visible below the fracture site. It was hypothesised that this repeated surface artefact may relate to the higher density of the normal bone which was why it was not present below the fracture site. There were no X-rays obtained at the first follow-up visit for comparison to the 3D US findings.

In the 3D US scans obtained at 7 weeks post fracture, substantial regions of callus were visible within the fracture gap and forming on the periosteal surface of the bone ends, but, bridging had not yet occurred. Figures 5-5(A) and 5-5(B) show *Reslice* images from the 5-10 MHz scan along the length of the bone and around the width of the bone, the regions of callus have been indicated. On the AP X-ray, see figure 5-6(B & D), there was a large volume of callus visible across the fracture site, however, it was not clear whether this was periosteal bridging callus or callus material within the gap. The edges of the break still appeared well defined in the lateral X-ray, see figure 5-6(A & C), though, a region of periosteal callus was visible on the front face of the tibia that was seen to extend a good distance above and below the fracture line.

After 16 weeks bridging callus was visible at all points across the fracture gap on the 3D US scans. In places the callus had a greyscale intensity comparable to the adjacent normal bone indicating that it was maturing and returning to a pre-fracture state. Figure 5-7 shows a series of 3D models constructed from the scans of the anterior-medial face of the tibia as healing progressed, the regions of callus formation are shown in yellow. Initially, only a small area of echogenic material was detected, however, at 7 weeks regions of periosteal callus as well as callus material deposited within the fracture gap were observed. At 16 weeks the callus had fully bridged the gap and there was a notable difference in shape and volume of the callus.

The callus at the edges of the break had matured taking on a similar appearance to the patient's healthy bone. It should be noted that when constructing the 3D model it is not possible to seamlessly move from one object of interest to another i.e. from bone to callus making the callus appear separate from the bone ends rather than extending from it.

The original line of fracture was only faintly visible on the AP X-ray, see figure 5-8 (A & C), as it was obscured by an increasingly calcified region of bridging callus identified in the previous AP X-ray. In this view the fracture appeared to have united and was close to reaching full consolidation. On the lateral X-ray, the fracture line was no longer visible indicating successful consolidation of the fracture (20). However, it must be kept in mind that the appearance of the fracture line will be subject to inter-observer variability and may also be dependent on the angle at which the X-ray was obtained (10, 31).

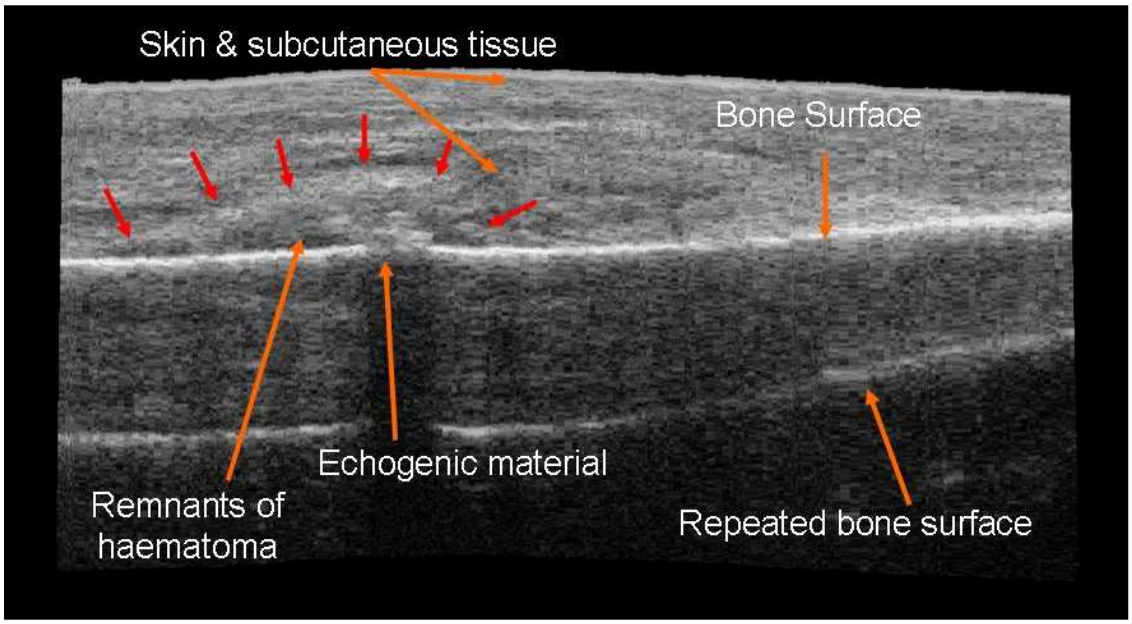

Figure 5-4: ***Reslice*** **from the 5-10 MHz length scan of the bone at 2 weeks post fracture captured through the anterior race of the tibia. The red arrows indicate the initial extent of the haematoma.**

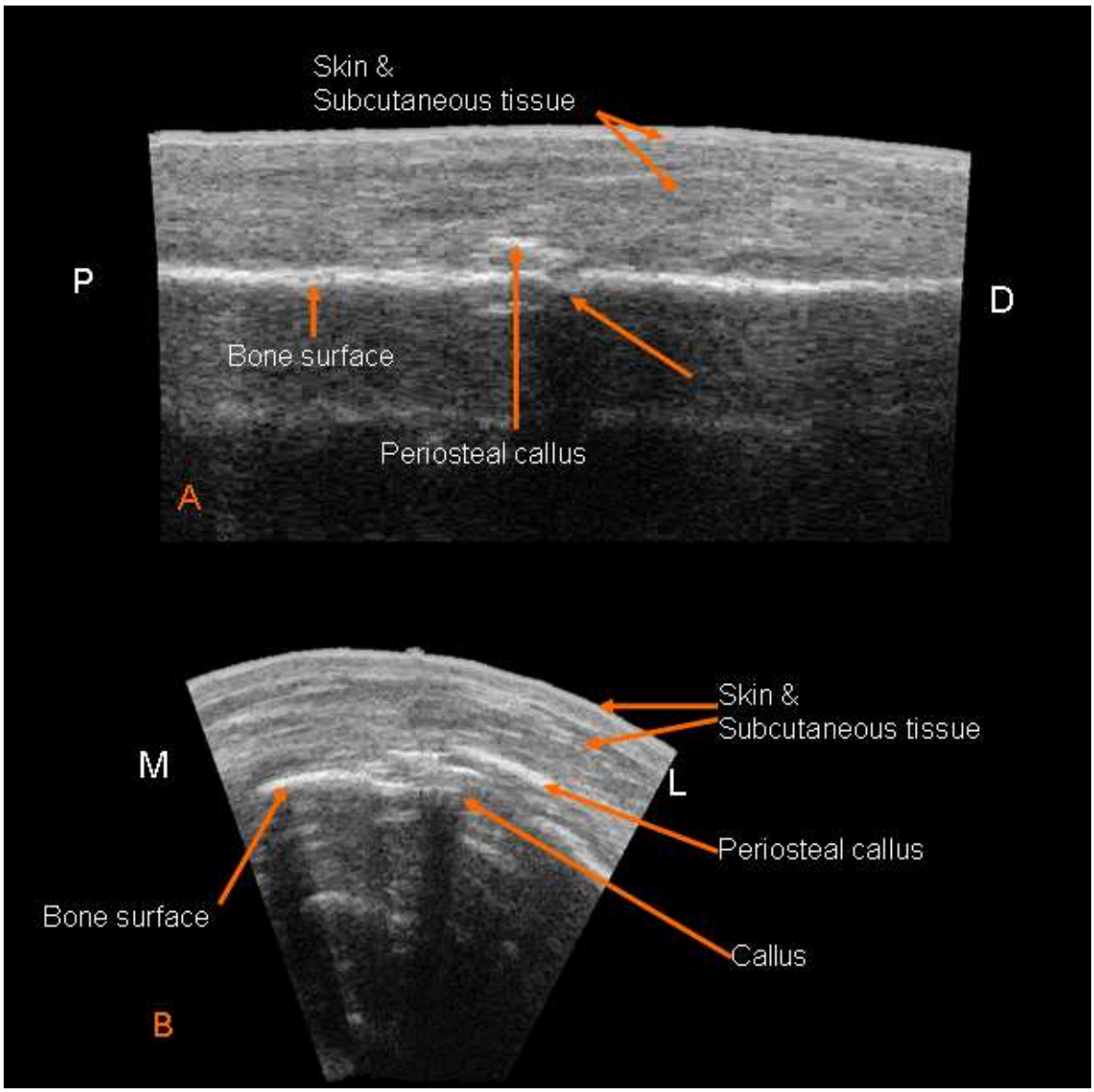

Figure 5-5: ***Reslice*** **images from the 5-10 MHz (A) length scan (through the anterior-medial bone surface) and (B) width scan (captured perpendicular to the anterior surface) at 7 weeks. The regions of callus growth have been indicated. (P) proximal, (D) distal, (M) medial, (L) lateral**

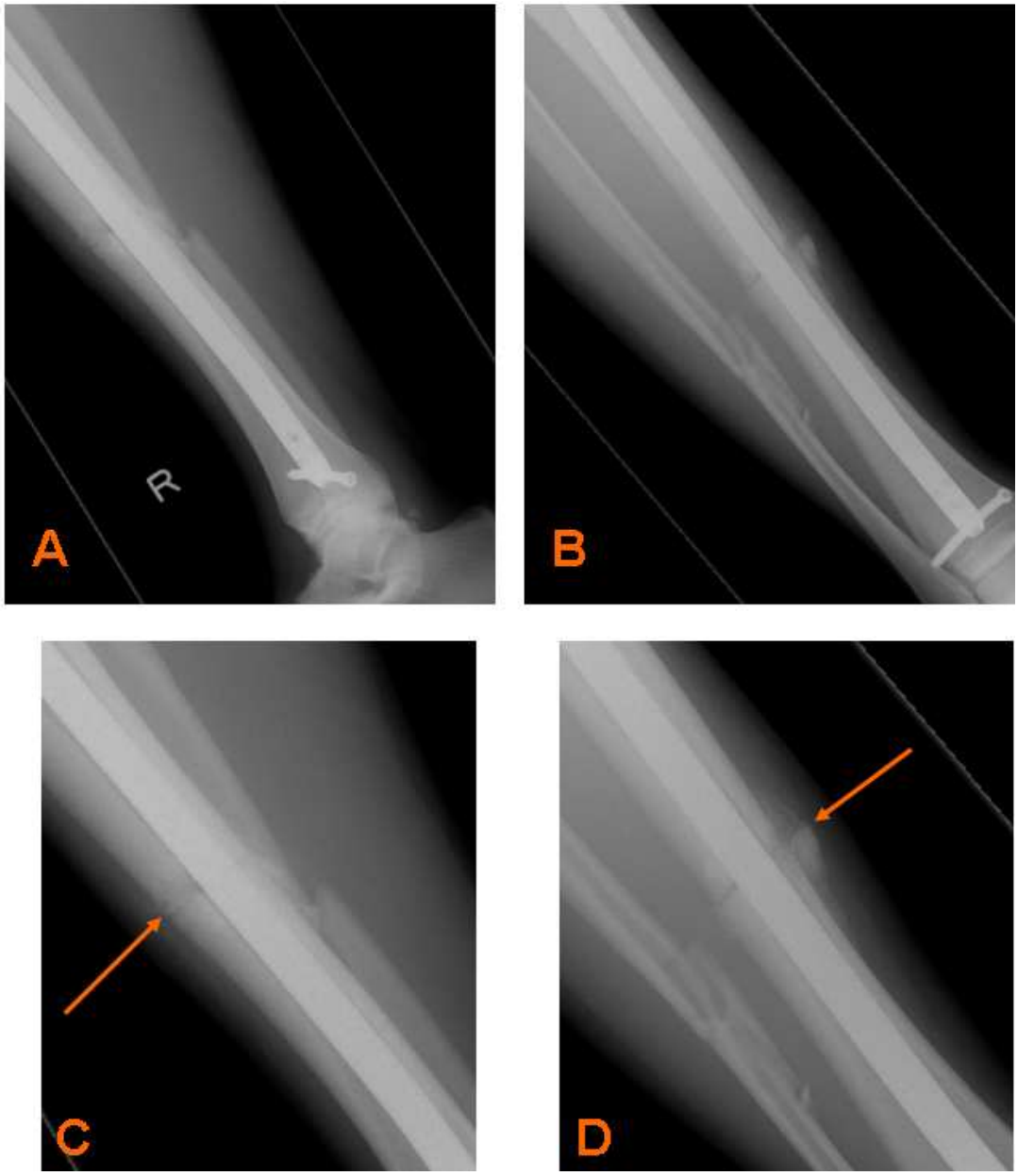

Figure 5-6: (A) Lateral (B) AP X-rays obtained at 7 weeks post fracture the regions of callus growth are indicated by the arrows on the close up (C) lateral and (D) AP views.

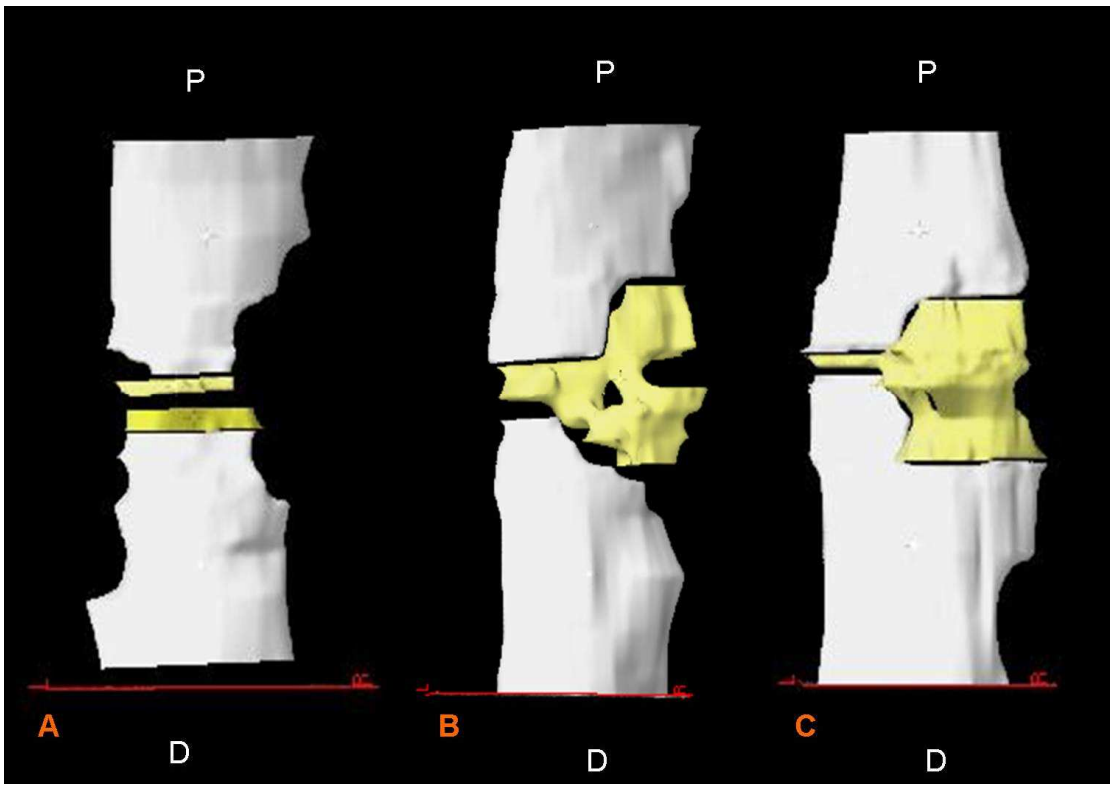

Figure 5-7: Series of 3D models constructed from the (A) 2 week, (B) 7 week and (C) 16 week scans showing the anterior medial face of the tibia. (P) proximal, (D) distal.

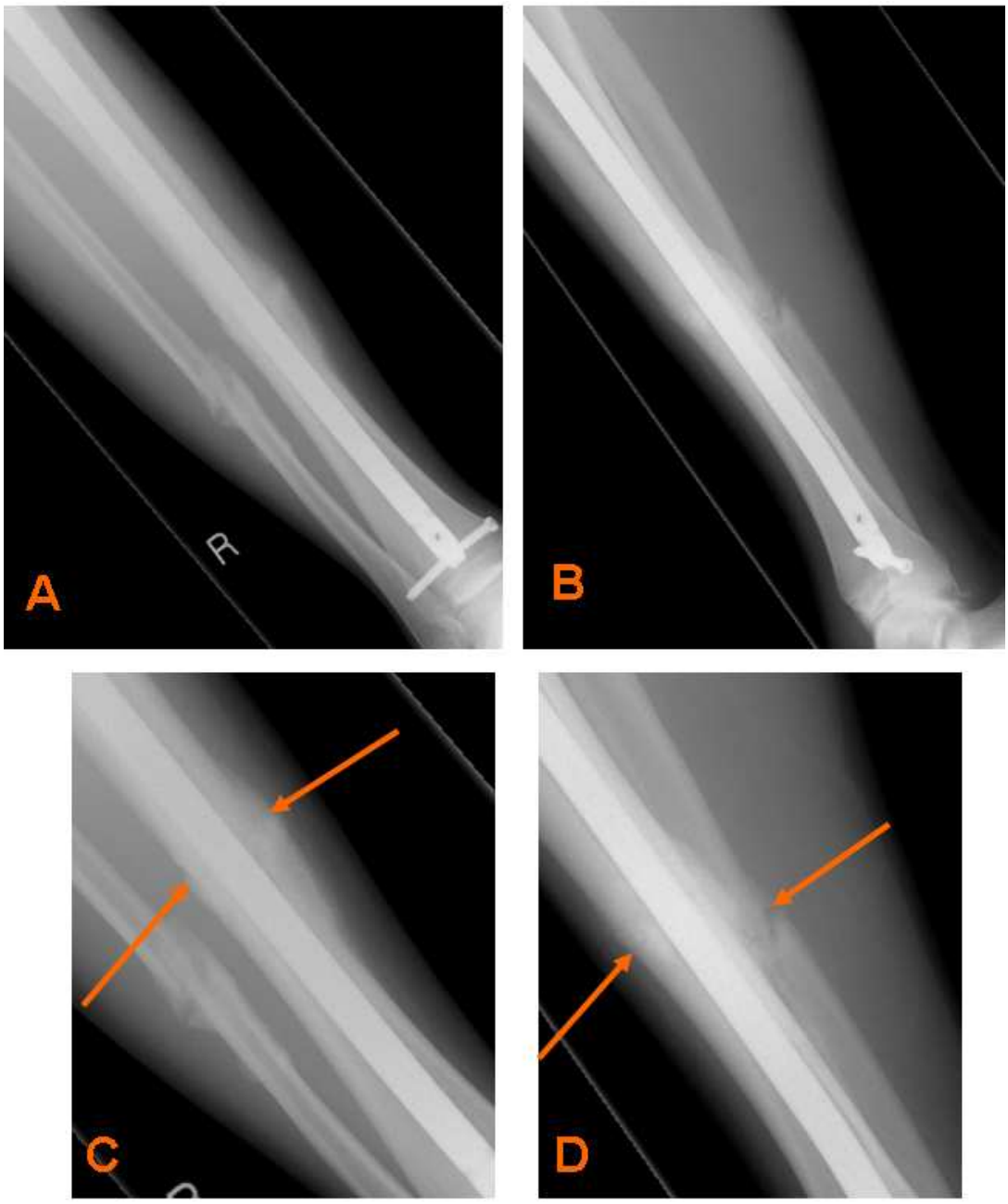

Figure 5-8: (A) AP and (B) lateral X-rays obtained at 16 weeks post fracture. The arrows in the close up (C) AP and (D) lateral views indicate the location of the original fracture.

5.3.3. Case 3

Spiral fracture of the midshaft of the right tibia stabilised using an IM nail.

The first follow-up was at 3 weeks post fracture and already on the 3D US scans a significant amount of callus material was observed. On the distal side of the break

callus was forming on the periosteal surface of the bone and extending into the fracture gap. This can be seen in the *Reslice* image figure 5-9. No periosteal callus was evident on the proximal side of the fracture, however, large deposits of fibrous callus material were visible within the fracture gap and these have been indicated on the *Reslice* image. These deposits were more substantial on the lateral side of the break.

The spiral nature of the fracture resulted in a butterfly fragment of bone extending from the distal side of the break that was displaced slightly outwards from the main body of the tibia at its tip. The spiral pattern of the fracture and the presence of the bone fragment were clear on the AP X-ray, see figure 5-10(A & C). The fracture gap was less well defined on the lateral X-ray, see figure 5-10(B & D), as this view was not in the direction of the fracture plane. No signs of callus were visible on either X-ray.

The second follow-up was at 8 weeks post fracture and on the 3D US scans callus could be seen bridging the fracture gap at all points except for a small region on the medial side of the break. The collars of periosteal callus were less substantial in appearance on the lateral side of the break, however, there were areas of echogenic material filling in the gap. In comparison, there was very little callus visible on X-ray, see figure 5-11. On the AP X-ray small patches of callus had formed on the edges of the butterfly bone fragment at the lateral side of the fracture. No signs of callus were visible on the lateral X-ray.

After 17 weeks periosteal callus had completely bridged the fracture site as viewed on the 3D US scans. A small section of callus on the lateral side of the break remained less substantial than the main body of callus, but, had matured significantly compared to the previous scan. The change in the shape and greyscale intensity of the callus region was apparent when comparing *Reslice* images taken at 8 weeks and 17 weeks, see figures 5-12. The greyscale intensity of the callus had become brighter and more uniform in appearance. There was no longer a dip where the callus was less mature and the length of bone over which the callus had formed was

almost double at 17 weeks compared to 8 weeks. The change in size and shape of the callus could also be seen when comparing the series of 3D models constructed from the scans at 3 weeks, 8 weeks and 17 weeks., see figure 5-13.

On the corresponding X-rays, the fracture gap was still well defined, see figure 5-14. The AP X-ray showed periosteal callus had formed on the medial side of the gap obscuring the fracture line. More extensive callus was visible on the lateral side of the break and had formed between the butterfly fragment of bone and the main shaft of the tibia, though, this did not completely bridge the gap. The edges of the break had been smoothed over and in some places obscured by the presence of callus as seen on the lateral X-ray. It remained difficult to quantify the amount of callus present at the anterior side of the break, as viewed on the lateral X-ray, due to the location of the bone fragment.

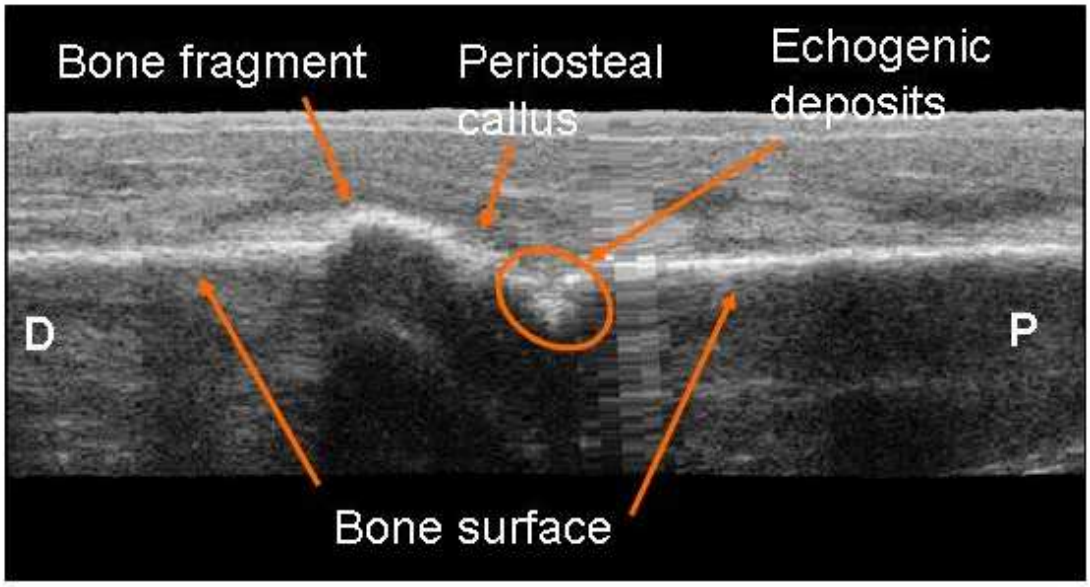

Figure 5-9: ***Reslice*** **image obtained at 3 weeks post fracture through the anterior face of the tibia, the two regions of callus growth are indicated. (P) proximal, (D) distal.**

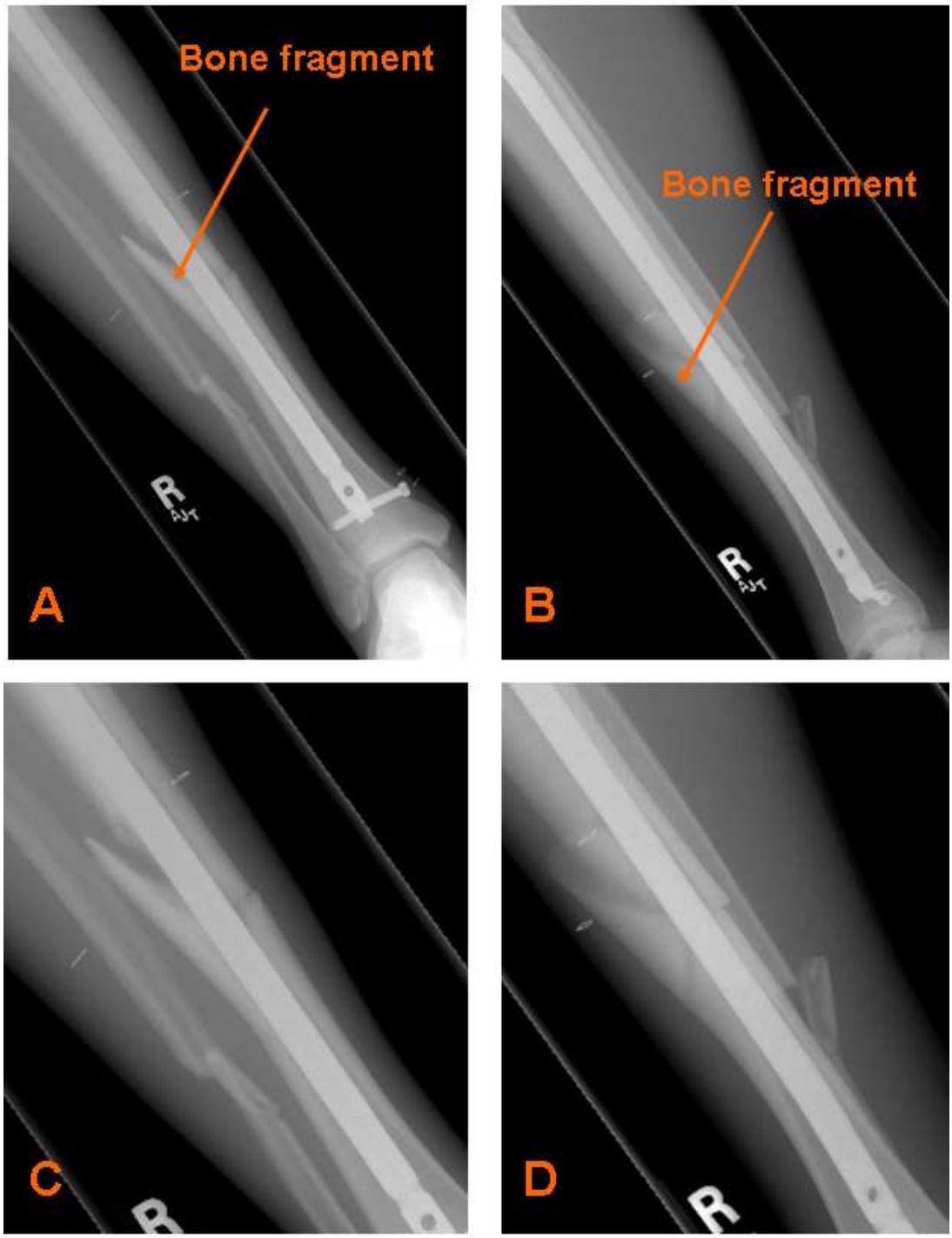

Figure 5-10: (A) AP and (B) lateral X-rays taken at 3 weeks post fracture. The location of the bone fragment is indicated by the arrows. (C) AP and (D) lateral X-rays shown close up.

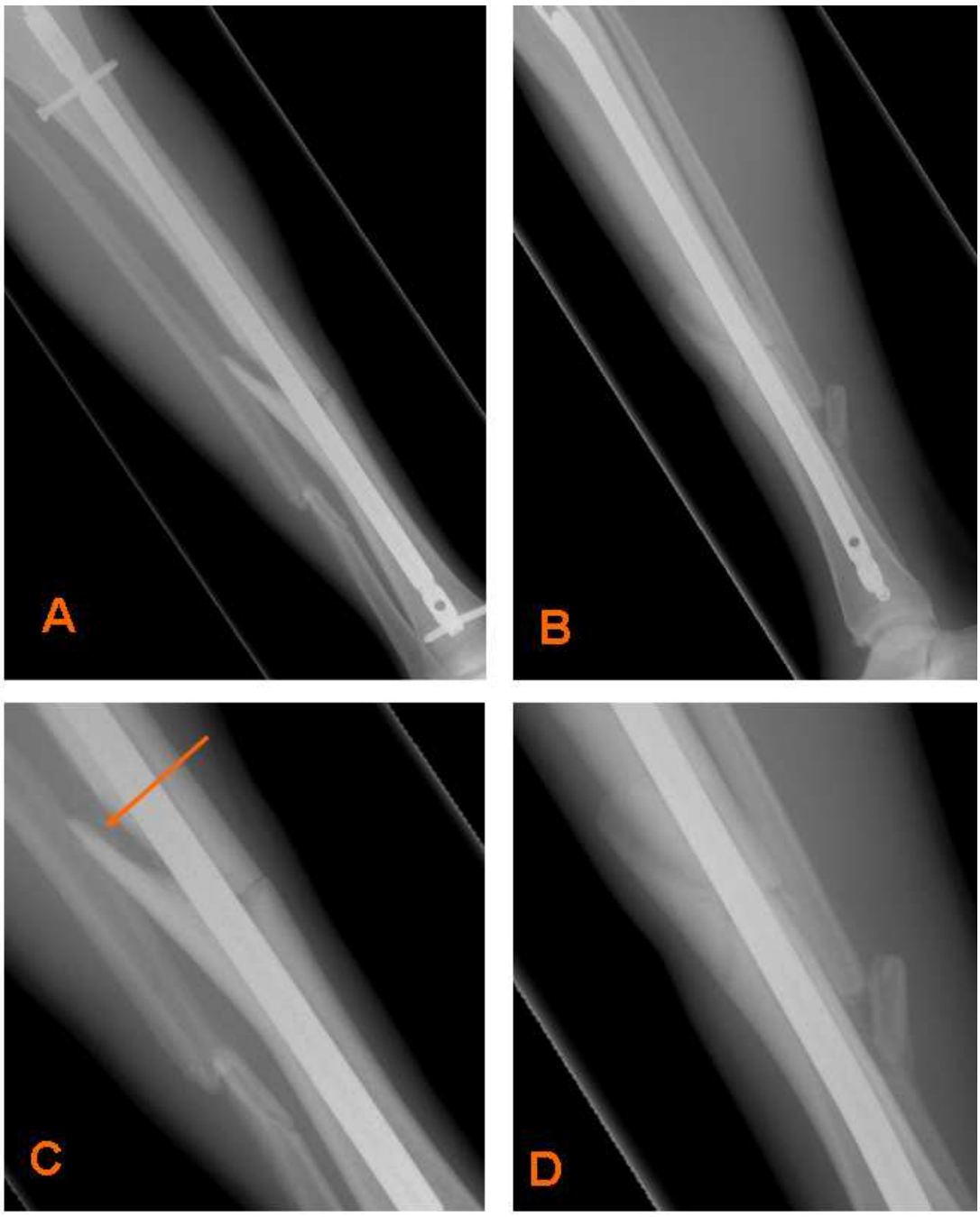

Figure 5-11: (A) AP and (B) lateral X-rays taken at 8 weeks post fracture. The fracture shown in close up from the (C) AP and (D) lateral X-rays. The region of callus growth is indicated by the arrow.

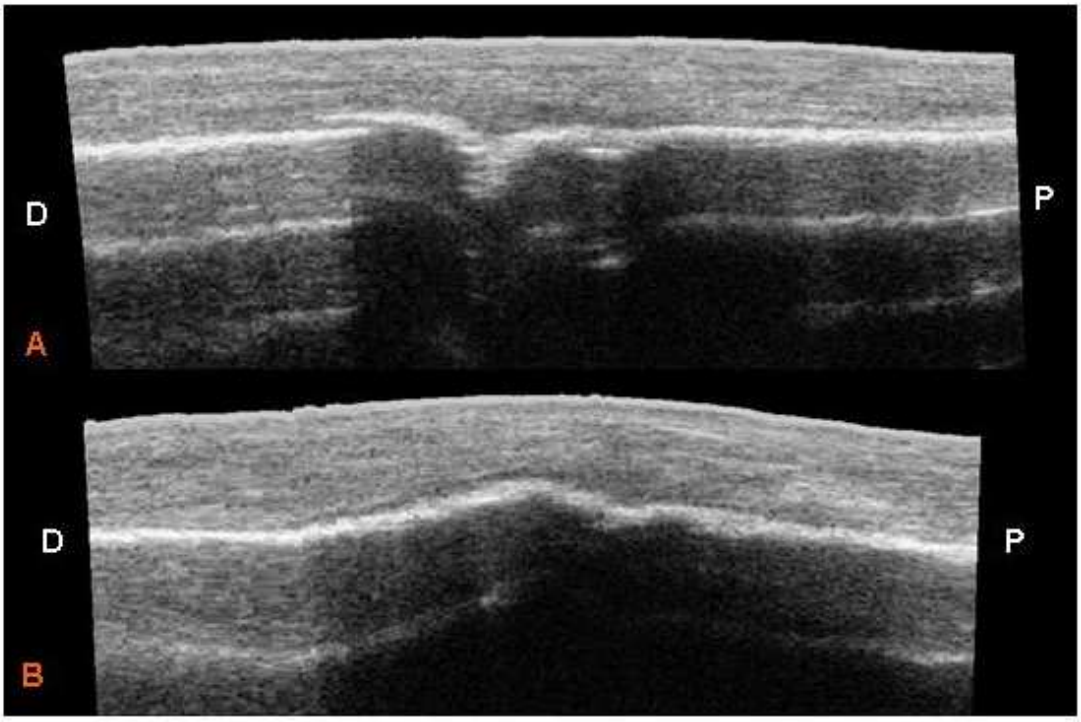

Figure 5-12: ***Reslice*** **images showing the change in the callus appearance at (A) 8 weeks compared to (B) 17 weeks post fracture. Both images are through the anterior face of the tibia at approximately the same point. (P) proximal, (D) distal.**

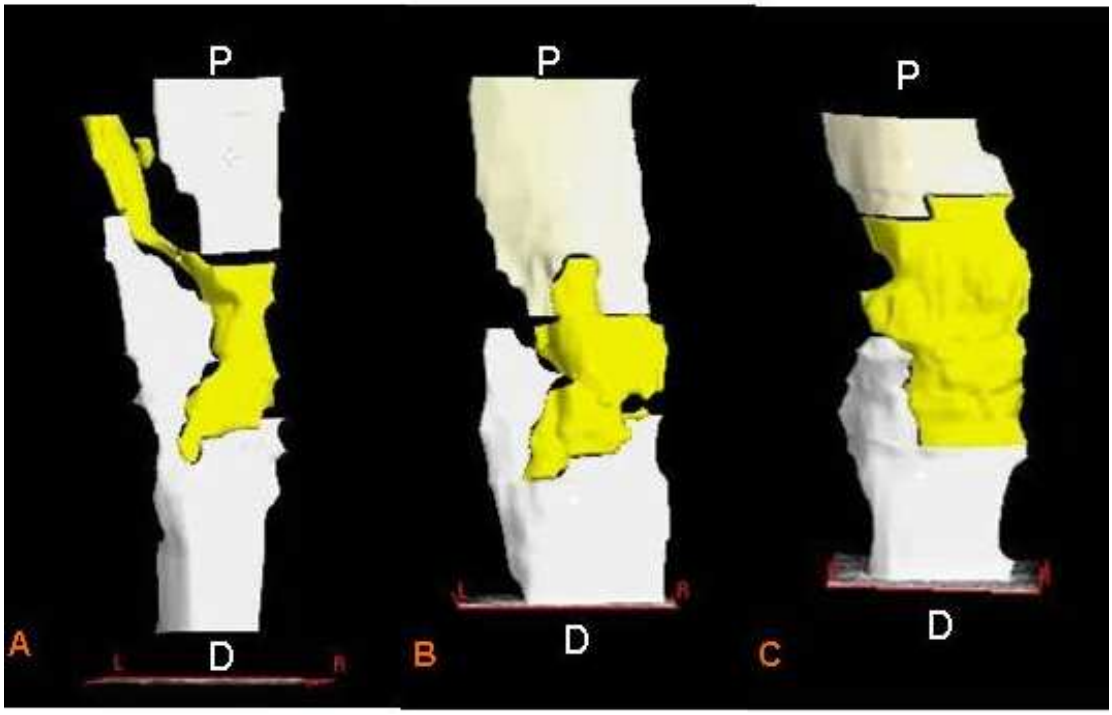

Figure 5-13: Series of 3D models showing the anterior face of the tibia constructed from scans taken at (A) 3 weeks, (B) 8 weeks and (C) 17 weeks post fracture. (P) proximal, (D) distal.

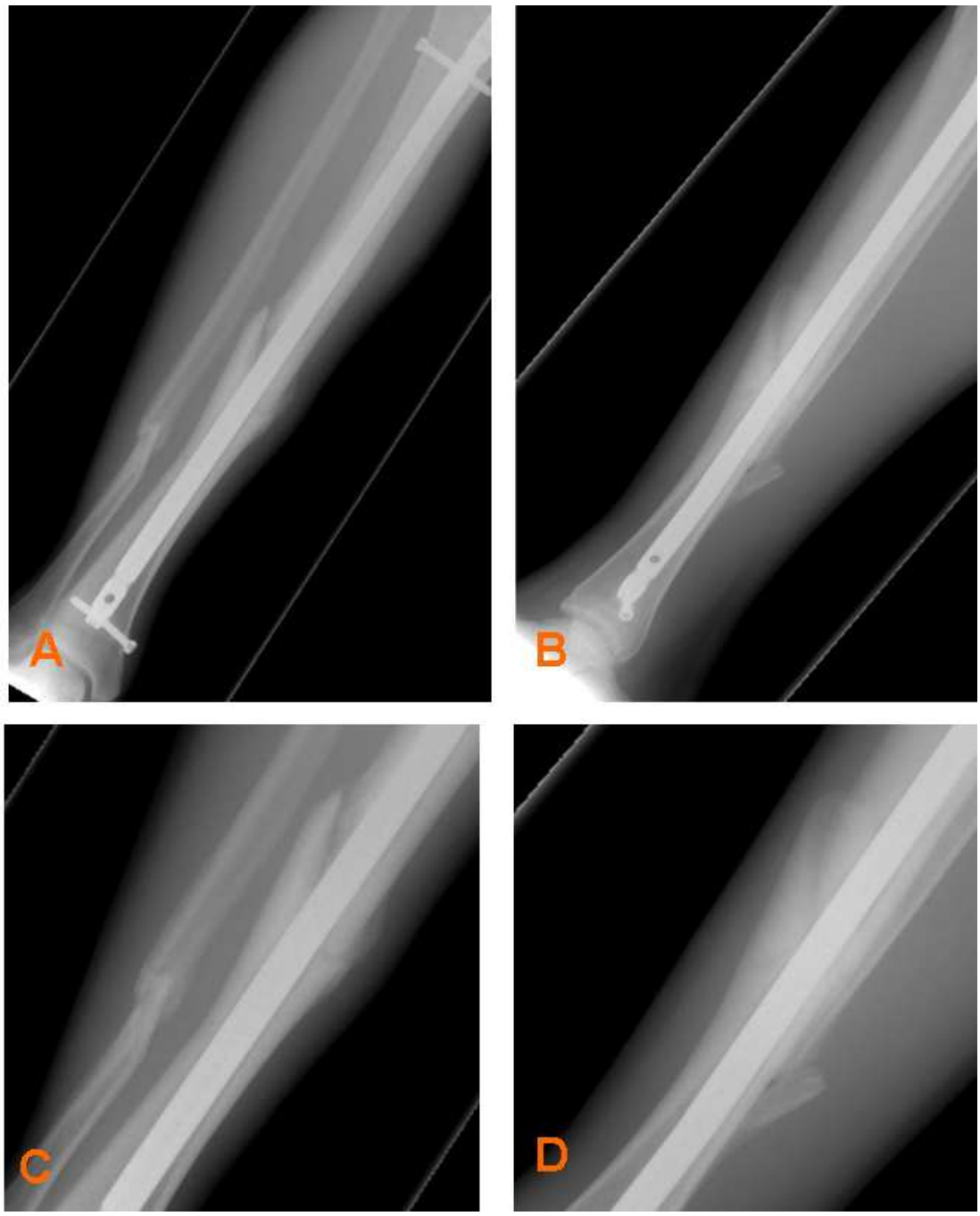

Figure 5-14: (A) AP and (B) lateral X-rays obtained at 17 weeks post fracture. The fracture line remained well defined and only small regions of callus were visible as can be seen in the close up (C) AP and (D) lateral X-ray images.

5.3.4. Case 4

Fracture of the left distal femur stabilised using an external fixation device.

Approximately 6 weeks after the femoral fracture was sustained complications arose in the healing process due to bone infection. The infected regions of bone were surgically removed and an external fixation device was used to stabilise the fracture. This patient was recruited after the surgery to remove the infected bone, however, all follow-up dates are taken from the initial injury date when the fracture repair process would have been initiated.

Due to the depth of the femur within the thigh it was only possible to obtain clear images of the fracture site using the 5-10 MHz probe. The first set of 3D US scans were obtained 8 weeks post fracture and a large region of callus was already visible extending across the fracture site, this has been highlighted in the *Reslice* image shown in figure 5-15. On the corresponding X-rays, small cloudy regions of callus were visible blurring the line of the fracture and these have been indicated in figure 5-16.

At 11 weeks post injury it was noted on the 3D US scans that the section of bone just above the fracture site had changed from having a smooth surface to becoming bulbous in nature. This can be seen in the 3D model shown in figure 5-17 and was a result of diffuse callus forming above the fracture site. Signs of this change to the bone were not detected on X-ray until 28 weeks post fracture, see figure 5-20. The section of callus previously seen on the 3D US images to be extending across the break had now bridged the fracture gap on the medial side, see figure 5-17. More echogenic deposits were also visible within the fracture site. No X-rays were obtained during the third clinic visit.

The callus material within the gap had increased in echogenicy on the 3D US scans at 15 weeks post fracture, however, there were still areas across the fracture site where no callus formation was evident. On the corresponding X-rays shown in figure 5-18 the increasing bulk of the callus could be seen in both views. On the lateral X-ray there was a small area on the anterior face of the femur where there was less callus and the edges of the break remained well defined. At all other points on the lateral X-ray and the AP X-ray, the fracture line had become blurred and in some

places obscured by the presences of callus. This indicated that union was close to being achieved.

After 19 weeks the 3D US scans showed that the amount of callus within the fracture gap was still increasing and the section of bridging callus had also expanded. The greyscale intensity of the bridging callus had increased with the callus on the proximal side of the break now comparable in greyscale intensity to the patient's normal bone. On both the AP and lateral X-rays the main body of the callus now obscured the fracture line completely indicating that the fracture had reached consolidation. Further to this, above and below the fracture site callus could be seen stretching out along the surface of the bone.

The external fixation device had been removed and conservative use of the leg had resumed when the patient attended clinic at 28 weeks post fracture. The callus bridging the fracture gap had greyscale intensity comparable to the patient's normal bone, as seen on the 3D US scans, indicating that it had become mature. The callus was bulbous in appearance on the medial side where bridging had occurred. On the lateral side of the break there was a dip in the callus which can be seen on the 3D model, see figure 5-19. At this point callus forming inside the fracture gap was beginning to bridge the break rather than periosteal callus.

On the lateral side of the femur as viewed on the AP X-ray, see figure 5-20(A & C), the dip in the shape of the callus was pronounced. The overall shape of the callus across the rest of the fracture site had become smoother and less bulbous in shape indicating that remodelling was under way. The previously noted callus forming and stretching out above and below the fracture site along the bone surface, had also increased in size, see (figure 5-20(B & D)). The change in shape of the section of bone above the fracture site, noted on the 3D US scans at 11 weeks post fracture, was now visible on X-ray.

In the final series of 3D US scans at 44 weeks post fracture, the dip in the callus on the lateral side of the fracture was still visible, but, was reduced in size. This can be

seen when comparing the 3D models constructed at 28 weeks and 44 weeks, see figure 5-21. When comparing the *Reslice* images at 28 weeks and 44 weeks, see figures 5-22, the callus which was extending to bridge the gap (point 1) had increased in greyscale intensity indicating increased density. At point 2 on the *Reslice* image, where bridging was yet to occur at 28 weeks, callus had now bridged the fracture, however, this section of callus still lagged behind in terms of greyscale intensity.

Remodelling of the medullary canal could be seen on the lateral X-ray as shown in figure 5-23(B & D), but, was not evident on the AP X-ray, see figure 5-23(A & C). The dip in the callus remained visible on the lateral side of the femur as viewed on the AP X-ray. No signs of the original fracture line were visible in either X-ray indicating that consolidation of the fracture had been reached, although, the bone still looked thin in places particularly in the lateral view.

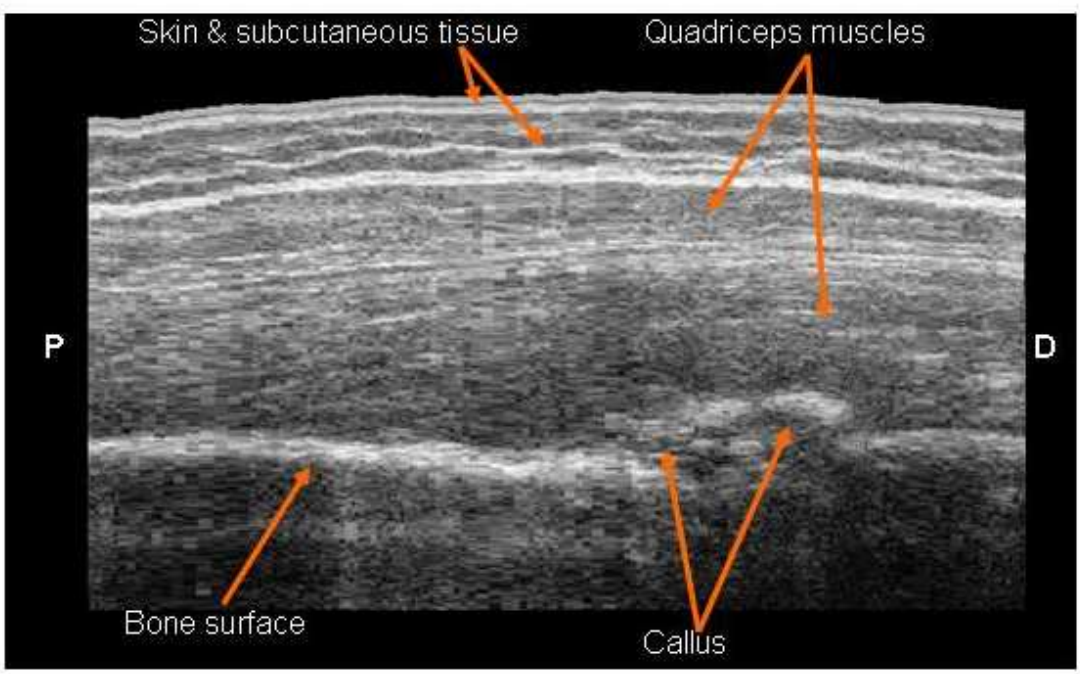

Figure 5-15: A *Reslice* image obtained at 8 weeks post fracture through the anterior face of the femur. A large region of callus could be seen forming. (P) proximal, (D) distal.

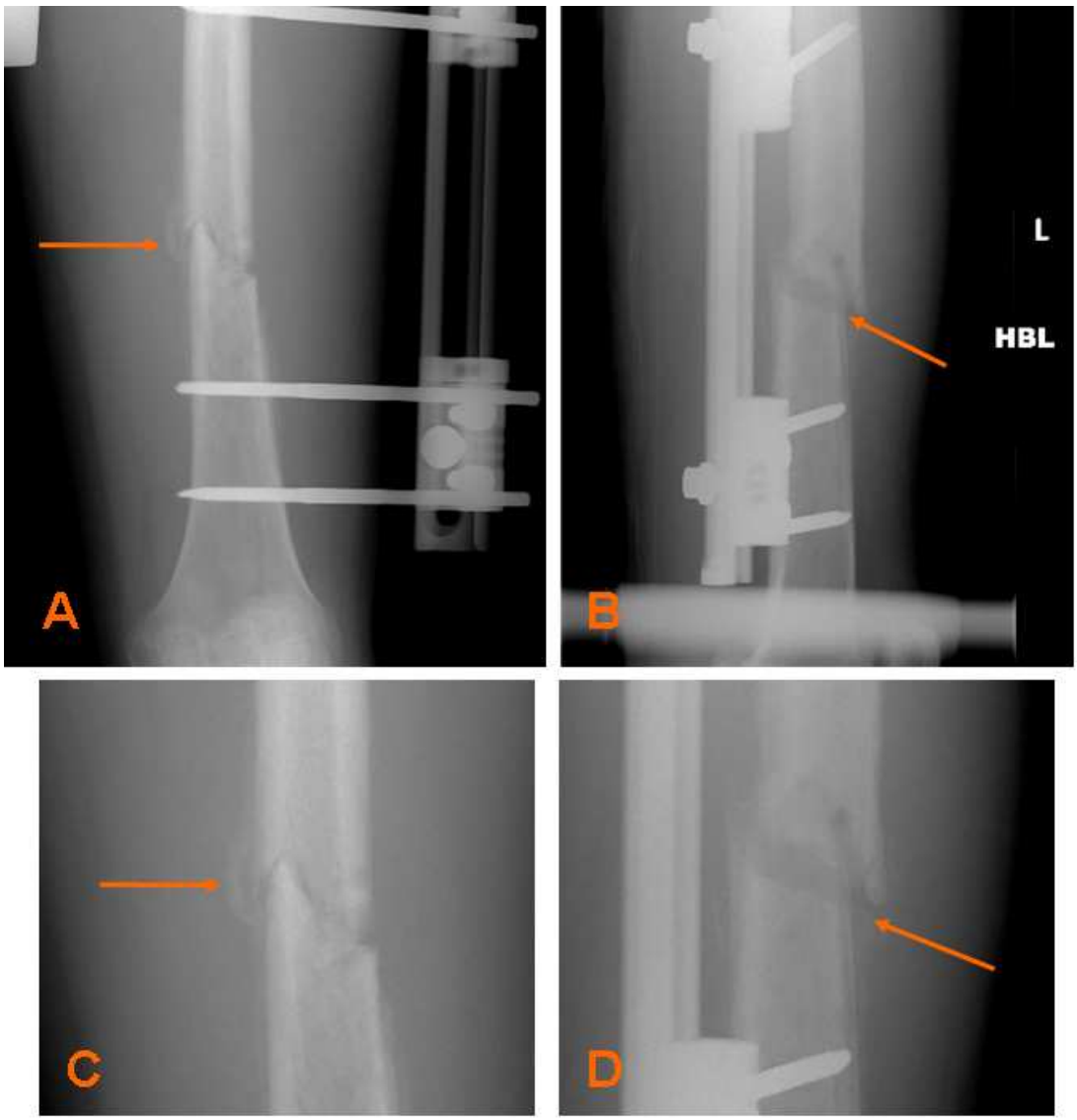

Figure 5-16: (A) AP and (B) lateral X-rays obtained at 8 weeks post fracture. Small regions of callus were already visible, these are indicated by the arrows. (C) AP and (D) lateral X-rays shown in close up.

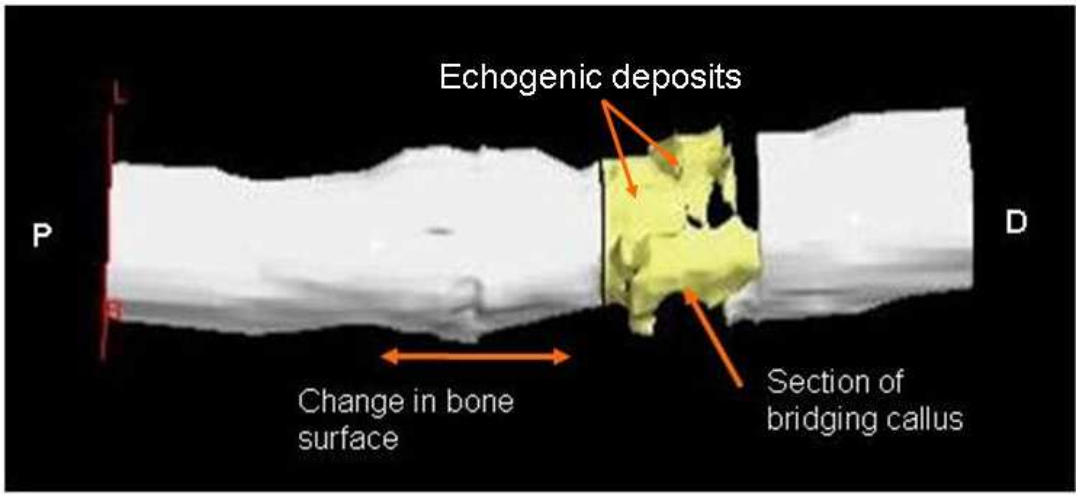

Figure 5-17: 3D model constructed from the scan data at 11 weeks post fracture showing the anterior face of the femur. The section of bridging callus and area of bulbous bone are indicated. (P) proximal, (D) distal.

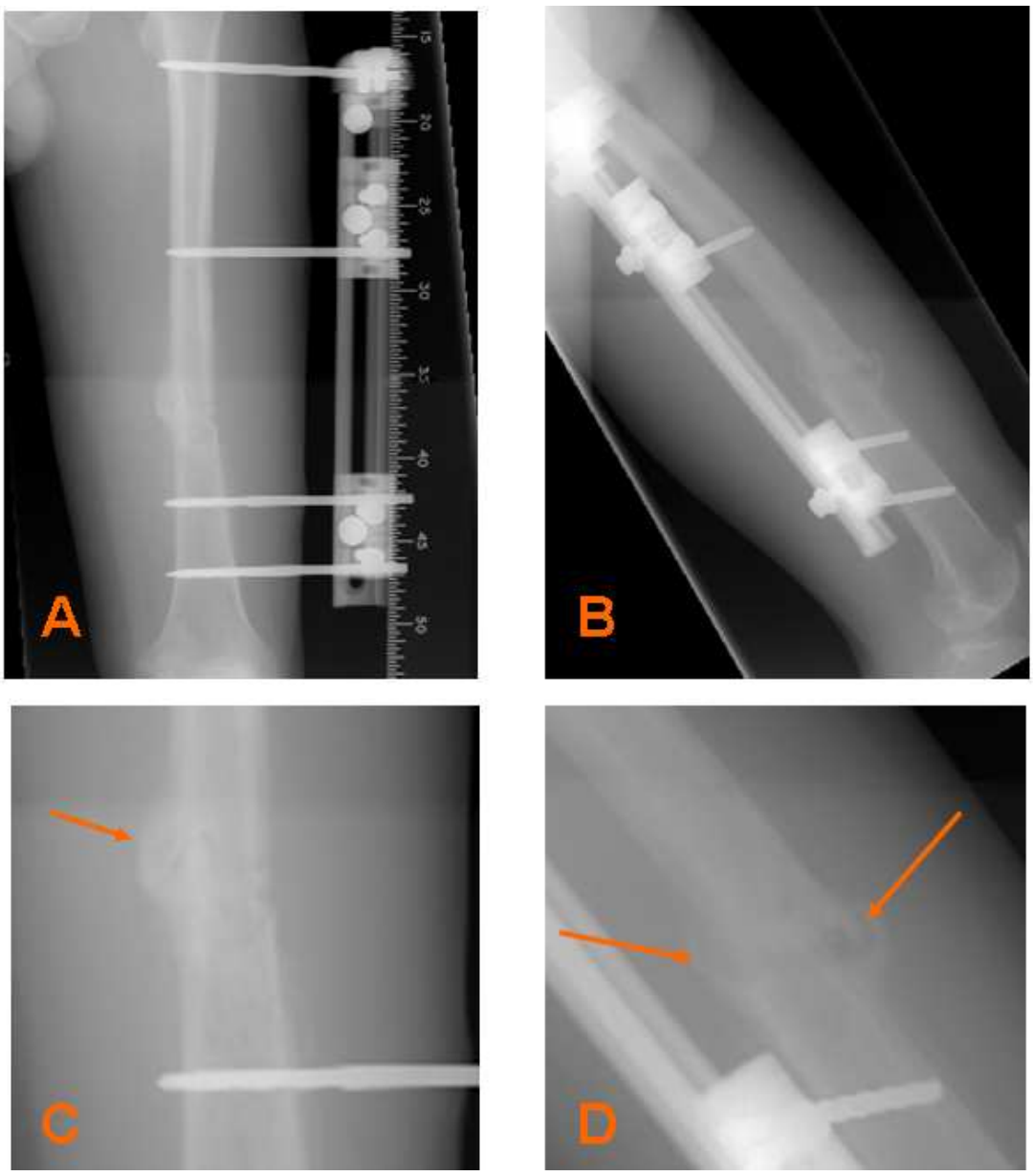

Figure 5-18: (A) AP and (B) lateral X-rays obtained at 15 weeks post fracture. The original fracture lines were no longer clearly visible and substantial regions of callus were visible in both views indicated by the arrows in the close up (C) AP and (D) lateral X-ray views.

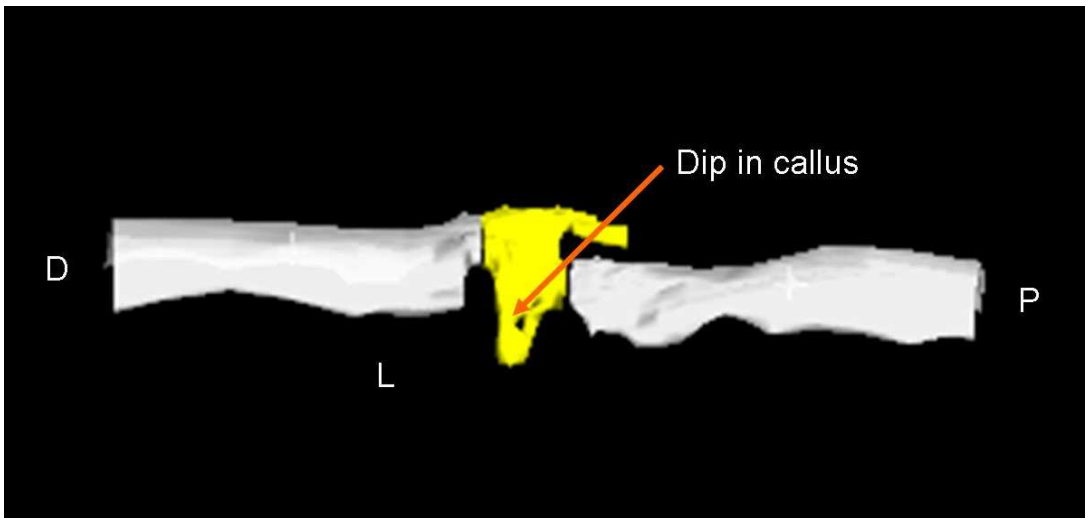

Figure 5-19: Lateral view of a 3D model of the femur constructed from a 3D US scan taken at 28 weeks. A dip in the callus was present on the lateral side. (M) medial, (L) lateral, (P) proximal and (D) distal.

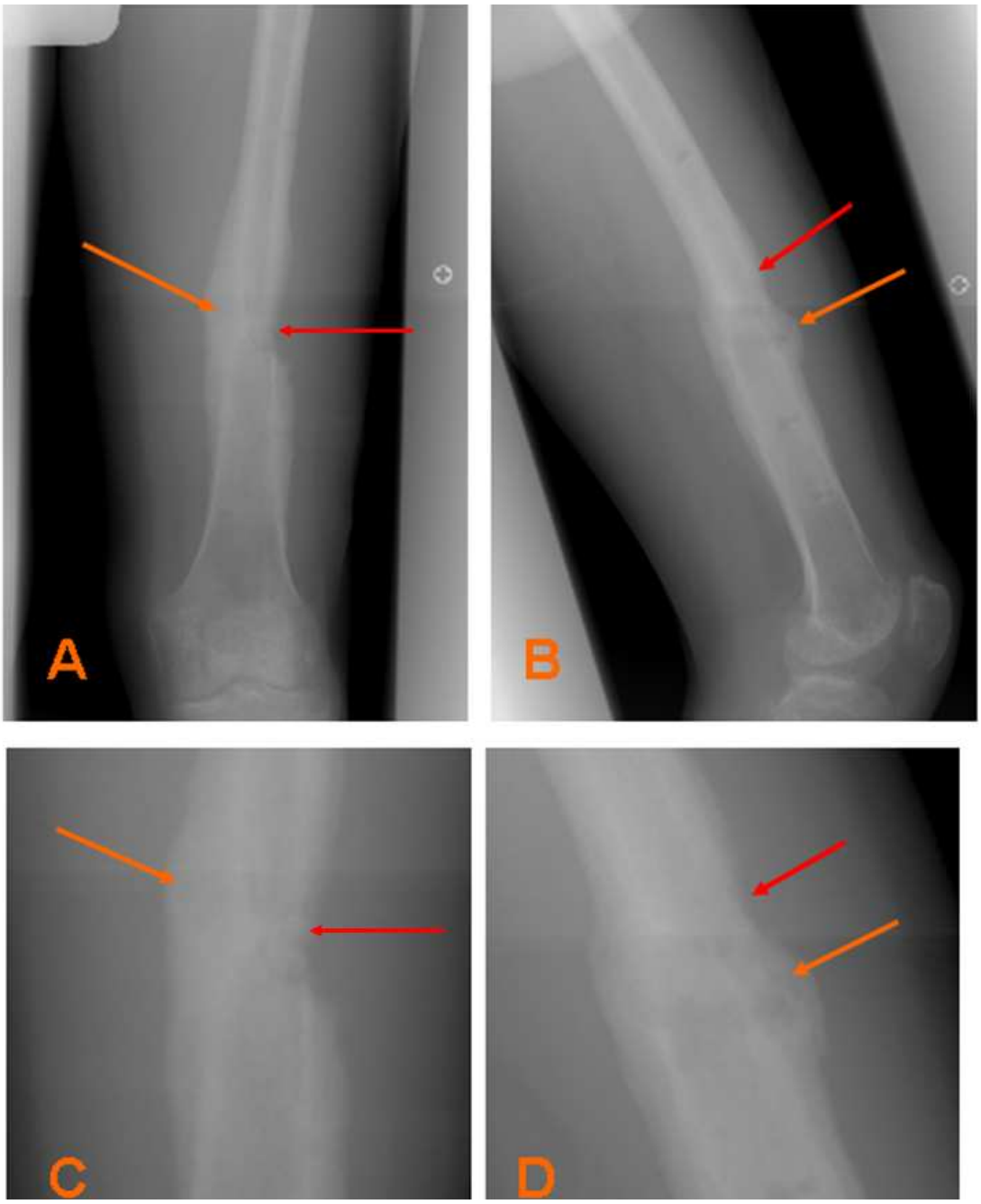

Figure 5-20: (A) AP and (B) lateral X-rays obtained at 28 weeks post fracture and close up (C) AP and (D) lateral views of the fracture site. Substantial regions of callus are visible on both the lateral and AP views as indicated by the orange arrows . The dip in the callus is indicated by the red arrows.

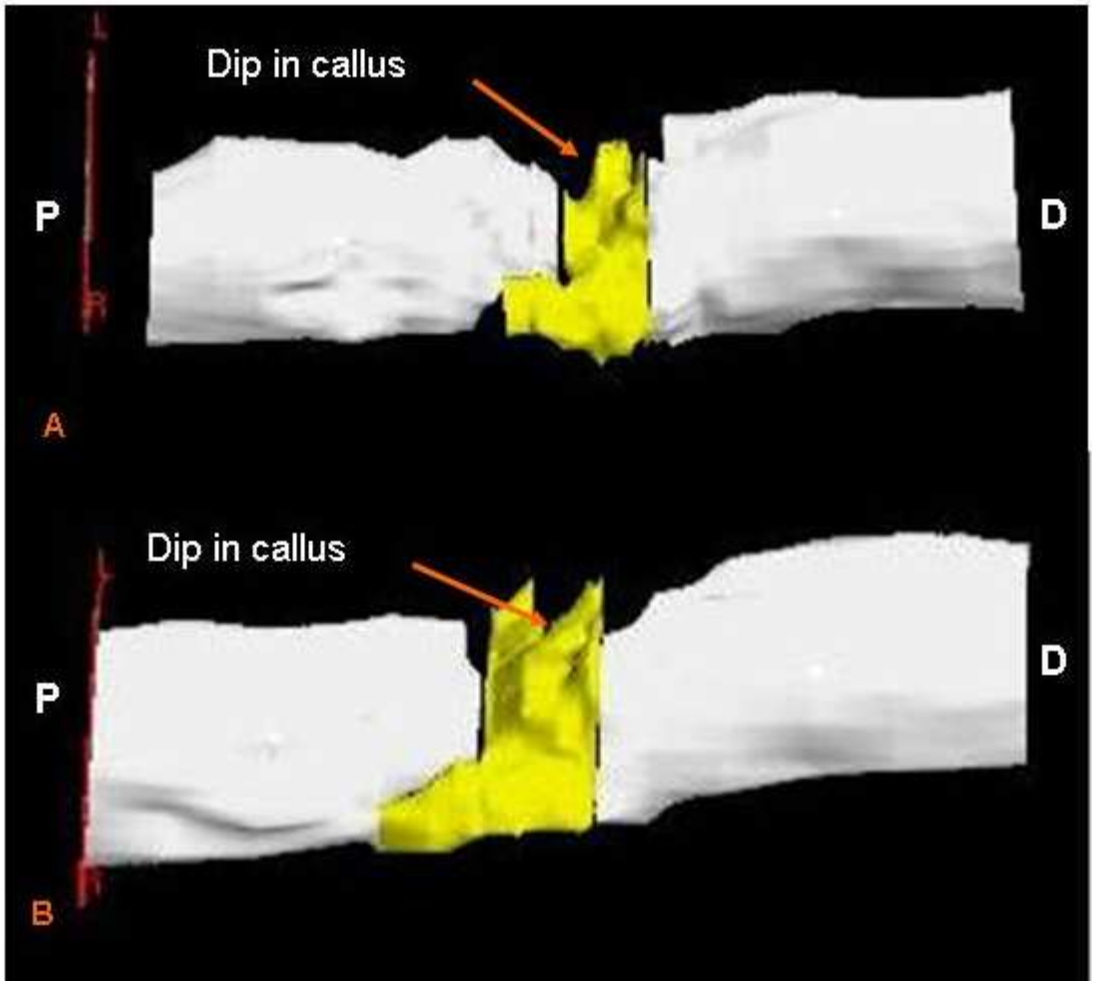

Figure 5-21: 3D models constructed from the 3D US scans at (A) 28 weeks and (B) 44 weeks post fracture showing the anterior face of the femur. The region of callus has increased in size and the bone on the proximal side of the break has been remodelled, however, a dip remained in the lateral side of the callus. (P) proximal and (D) distal.

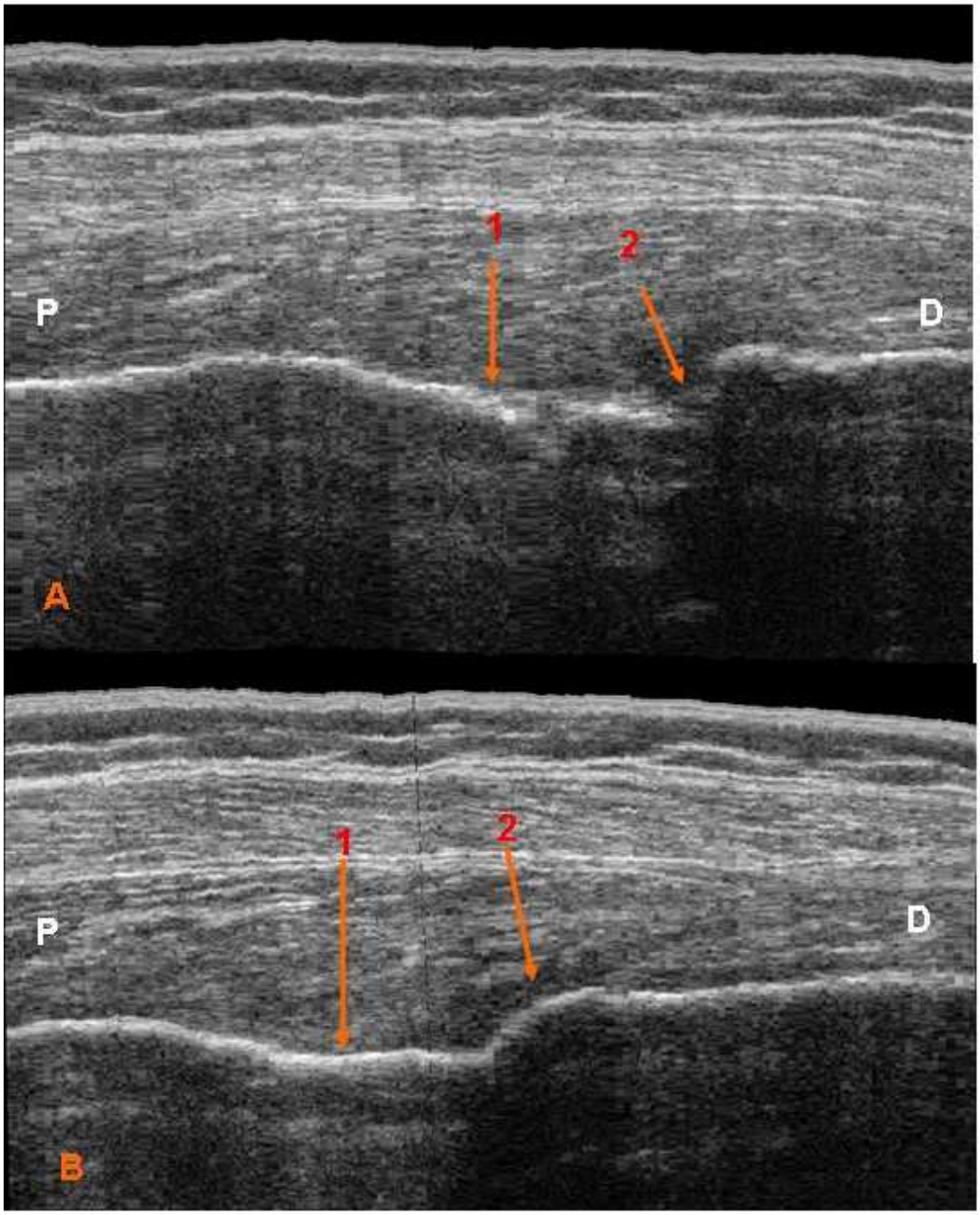

Figure 5-22: *Reslice* images obtained at the(A) 28 weeks and (B) 44 weeks post fracture showing a slice through the middle of the anterior face of the femur. There has been a significant increase in the greyscale intensity of the callus particularly at regions 1 and 2 indicated on both images.

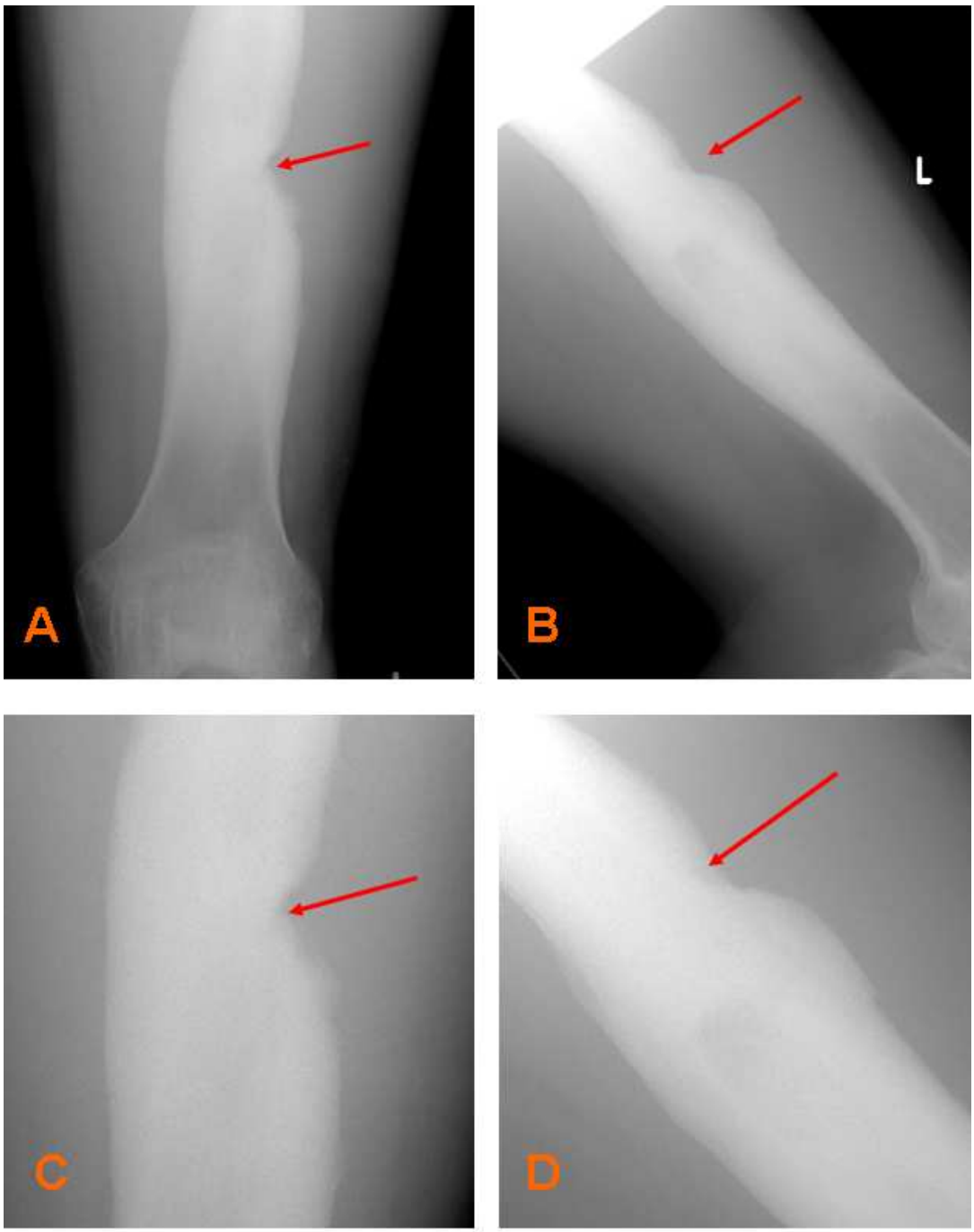

Figure 5-23: (A) AP and (B) lateral X-rays obtained at 44 weeks post fracture. The arrows indicate the remaining dip in the callus. (C) and (D) show a close up view of the AP and lateral X-rays respectively.

5.3.5. Case 5

Lengthening of the left tibia using an Ilizarov frame.

The osteotomy site was just below the proximal diaphysis of the tibia. The positioning and construction of the Ilizarov frame gave a small scanning window over the anterior part of the leg which has been highlighted in figure 5-24(A). The proximity of the two ring sections of the frame, positioned either side of the osteotomy site, did not restrict 3D US scanning.

The first 3D US scans were recorded at 1 week post op and revealed that the osteotomy had fragmented edges causing the two sections of bone to appear to overlap in places on the 5-10 MHz images, see figure 5-25(A). The gap appeared clearer in images obtained using the 8-16MHz probe, see figure 5-25(B), this probe had better resolution at this depth. Overlapping of bone ends visible in the 5-10 MHz scan may have been due to a refraction artefact which was identified previously in the phantom work investigating the resolution of the US probes, see 3.5.1 and 4.4.4. The fragmented nature of the osteotomy site was confirmed on inspection of the corresponding X-rays shown previously in figure 5-24(C & D). There were no sign of callus on the 3D US scans or the X-rays at this stage. The repeated bone surface artefact noted in previous *Reslice* images cases was again visible in the *Reslice* images obtained for this case.

At 4 weeks post op, lengthening was underway with a distraction of approximately 7 mm already achieved. This increase in distance between the bone ends was observed on the *Reslice* image, see figure 5-26. Also of interest on the *Reslice* image was the substantial amount of echogenic material within the gap. From the 3D model constructed from the 5-10 MHz length scan, as shown in figure 5-27, the extent and depth of the echogenic material within the gap could be seen. In some regions the material was only visible deep within the gap while in others it appeared to be filling in the gap almost to the level of the bone surface.

On X-ray much smaller “fluffy” regions of early callus could be seen. These were present on the medial and lateral sides of the gap as viewed on the AP X-ray, see figure 5-28(A & C), and on the posterior part of the tibia as viewed on the lateral X-ray, see figure 5-28(B & D). There did not appear to be any callus forming on the

anterior face of the tibia at this stage. The presence of small but much higher density regions within the gap visible in figure 5-28(C) are thought to be bony fragments from the osteotomy rather than callus.

At 6 weeks post op, the depth of penetration of the US beam into the lengthening gap was almost half that seen on the previous scans. This could be seen when comparing the *Reslice* images shown in figures 5-26 and 5-29. Echogenic material had filled in the gap to the level of the normal bone surface at all points visible in the 3D US scans. In some places small sections of periosteal callus, indicated on figure 5-29, had formed and started to extend across the gap making it difficult to depict the original edges of the lengthening gap.

The edges of the osteotomy site were also less well defined on X-ray, see figure 5-30. On the AP X-ray it was observed that the lateral and central regions of the gap contained immature callus material, however, it was not possible to tell at what depth within the gap this material was located. On the lateral side of the tibia callus material could be seen extending across the gap, but, on the medial side there was an absence of callus. On the lateral X-ray, at the posterior of the tibia, a substantial region of callus was forming and beginning to obscure the edges of the gap and at the midpoint of the break small columns of callus could be seen reaching across the gap. On the anterior surface of the bone the regions of periosteal callus visible on the 3D US scans were not visible on the lateral X-ray.

As lengthening continued more echogenic material became visible deep within the centre of the gap on the 3D US images. The regions of periosteal callus continued to extend further across the gap and the sections of periosteal callus adjacent to the patient's normal bone increased in greyscale intensity. The lengthening process was complete by 9 weeks post op.

On a *Reslice* image obtained at 9 weeks from the 3D US scans, see figure 5-31, it could be seen that the regions of periosteal callus closest to the bone ends had a greyscale intensity comparable to the patient's normal bone. The volume of callus

material continued to increase on X-ray as seen in figure 5-32 and the edges of the break had been smoothed over in appearance by the presence of callus. On the anterior face of the tibia, callus could be seen stretching out from both sections of bone, but, it had not yet bridged the gap. From X-ray it was difficult to determine whether the material clouding the gap was callus forming internally or the projection of callus forming on the opposite face of the bone. Callus formation on the medial side of the gap, as viewed on the AP X-ray, lagged in development.

The frame was still in place after 16 weeks, but, now that lengthening had been completed the healing process had advanced. The frame remained in place to allow the callus to mature and become strong enough to support full weight bearing without risk of re-fracture. The portion of the lengthening gap visible on the 3D US scans was completely bridged and the callus had become smoother in appearance as can be seen from the 3D model in figure 5-33. This indicated that remodelling was underway. When comparing the *Reslice* image with previous ones it was observed that the repeated surface artefact, first noted in case 2, was visible underneath this patient's normal bone but not below the lengthening site. As the callus matured and became denser the artefact began to appear faintly underneath the callus on the 5-10 MHz *Reslice* image as indicated in figure 5-34.

The edges of the bone sections were completely obscured by callus on the AP X-ray, see figure 5-35(A & C), with large regions of callus visibly extending across the gap and bridging at many points. Callus formation on the anterior face of the tibia was still markedly behind that on the posterior face as can be seen on the lateral X-ray in figure 5-35(B & D).

The final 3D US scans were acquired at 30 weeks post op when the frame had been removed and the patient was being encouraged to resume normal weight bearing. The repeated artefact noted on the previous *Reslice* image was now visible at all points underneath the bone surface, see figure 5-36, and the location of the lengthening site was no longer distinguishable on the *Reslice* image or the 3D model, see figure 5-37. On X-ray the bulbous shape of the callus and the area of increased

calcification on the AP view, see figure 5-38(A & C), indicated the lengthening site. On the lateral X-ray in figure 5-38(B & D) substantial callus was now present at both the anterior and posterior faces of the tibia.

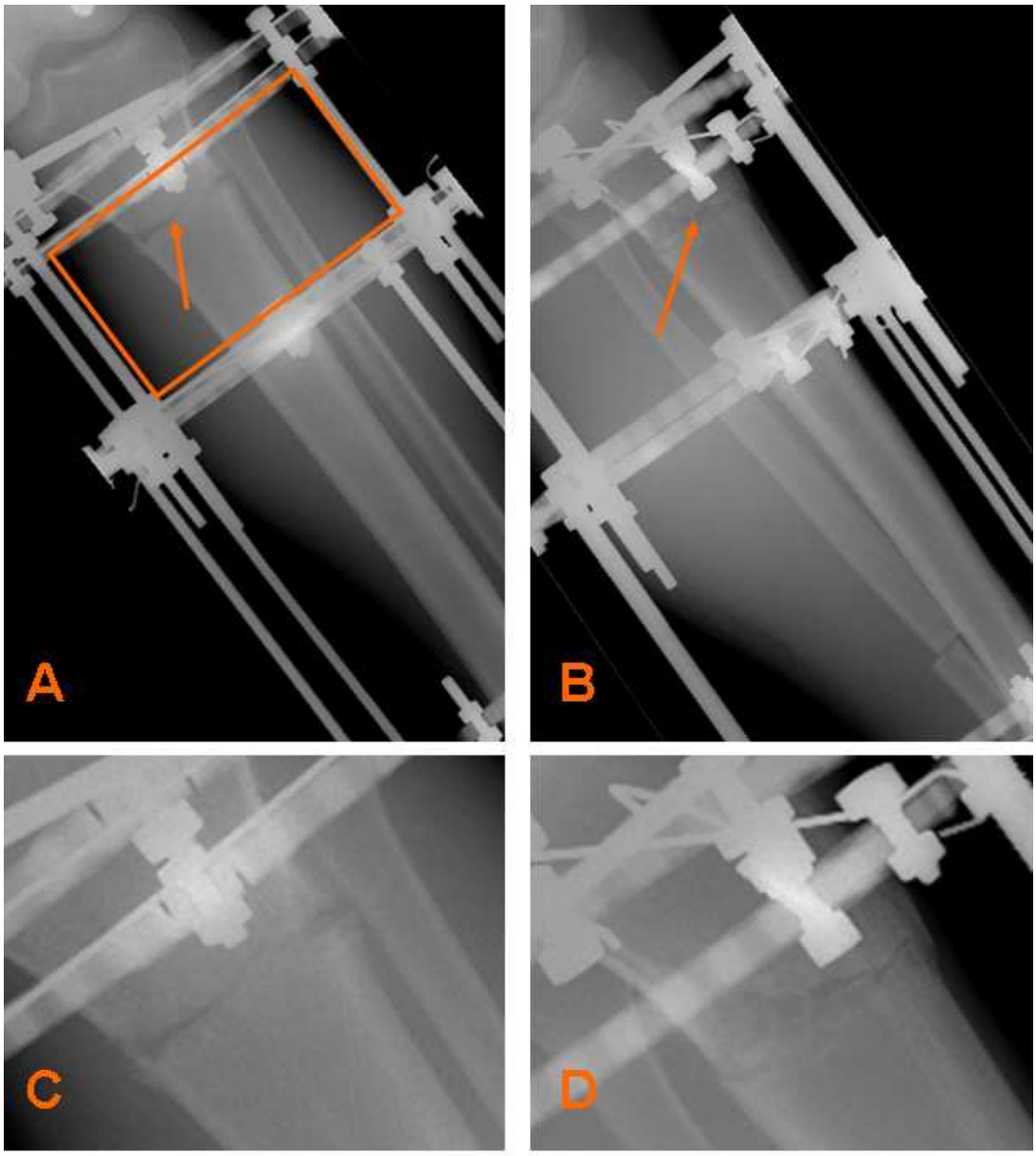

Figure 5-24: (A) AP and (B) lateral X-rays taken at 1 week post op. The site of the osteotomy is indicated by the arrows, the edges of the break were fragmented in appearance. The region where 3D US scanning was carried out is highlighted on the AP view. (C) and (D) show close up views of the AP and lateral X-rays respectively.

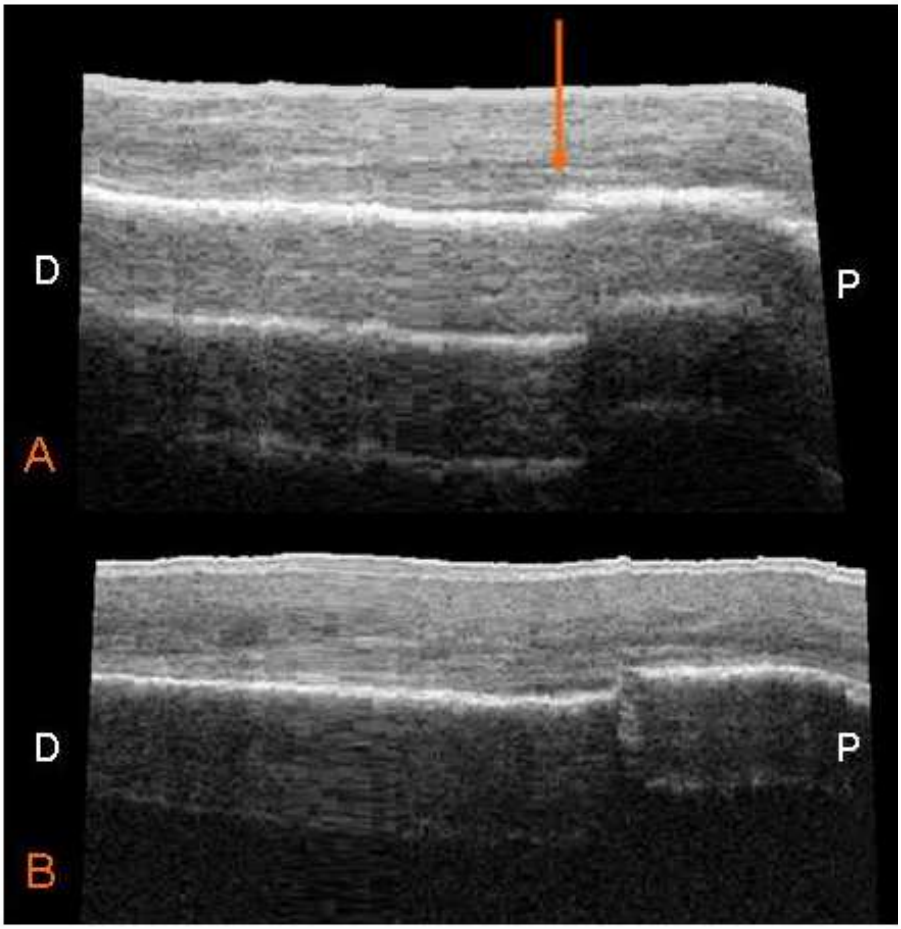

Figure 5-25: ***Reslice*** **images obtained through the anterior face of the tibia from the (A) 5-10 MHz and (B) 8-16 MHz 3D US scans at 1 week post op. The fragmented nature of the bone ends caused them to appear to overlap in the 5-10 MHz** ***Reslice,*** **this is indicated by the arrow. (P) proximal, (D) distal.**

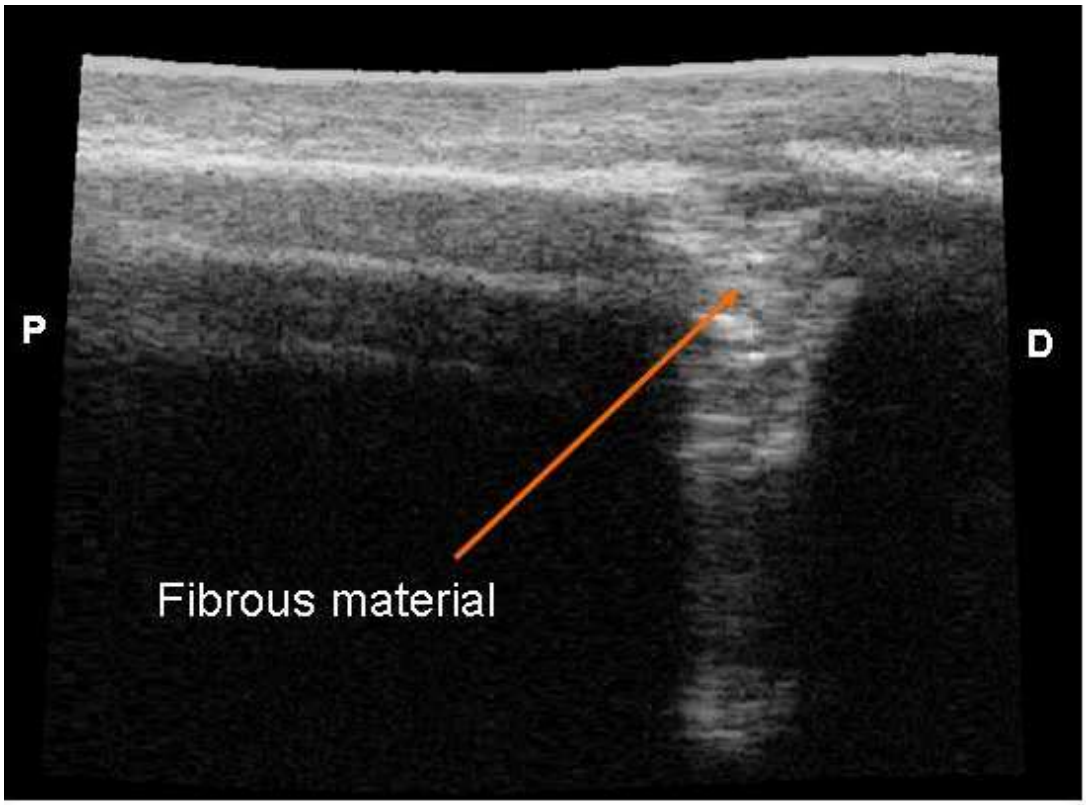

Figure 5-26: *Reslice* image from the 5-10 MHz length scan at 4 weeks post op taken through the anterior face of the tibia. The changing size of the break due to lengthening can be seen. A substantial amount of fibrous material has been deposited within the gap. (P) proximal, (D) distal.

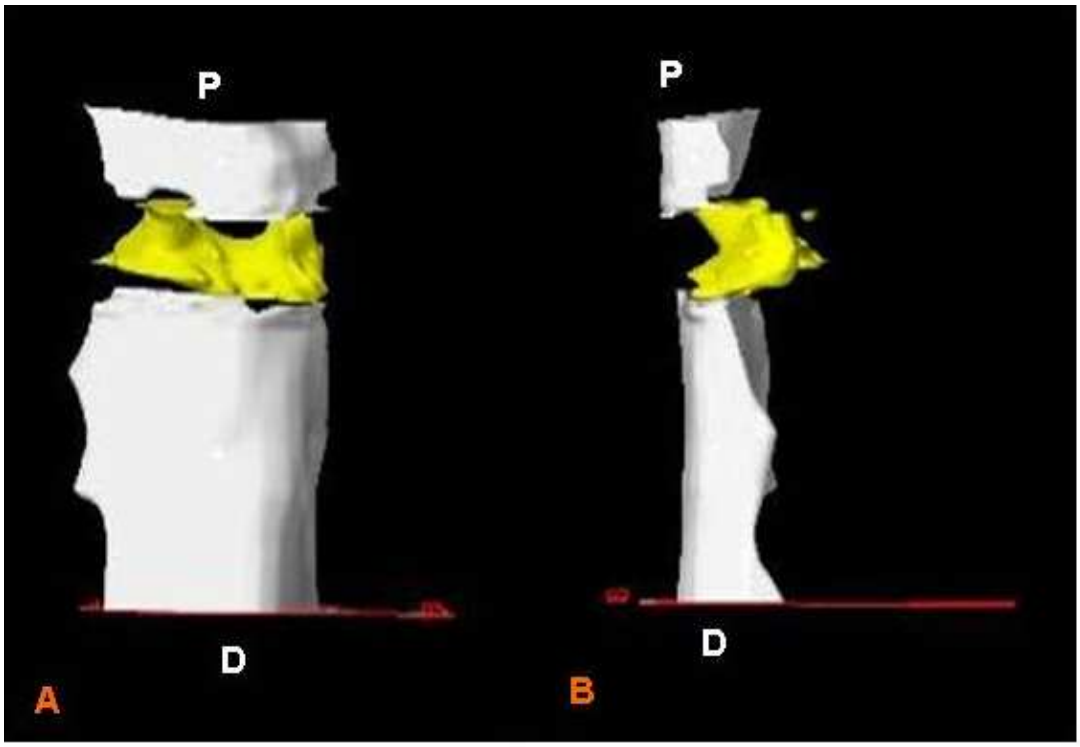

Figure 5-27: 3D Model constructed from the 5-10 MHz scan at 4 weeks post op. (A) view of the anterior face of the tibia. (B) 3D model rotated to show the lateral side of the tibia where the depth of the fibrous material deposited within the gap can be seen. (P) proximal, (D) distal.

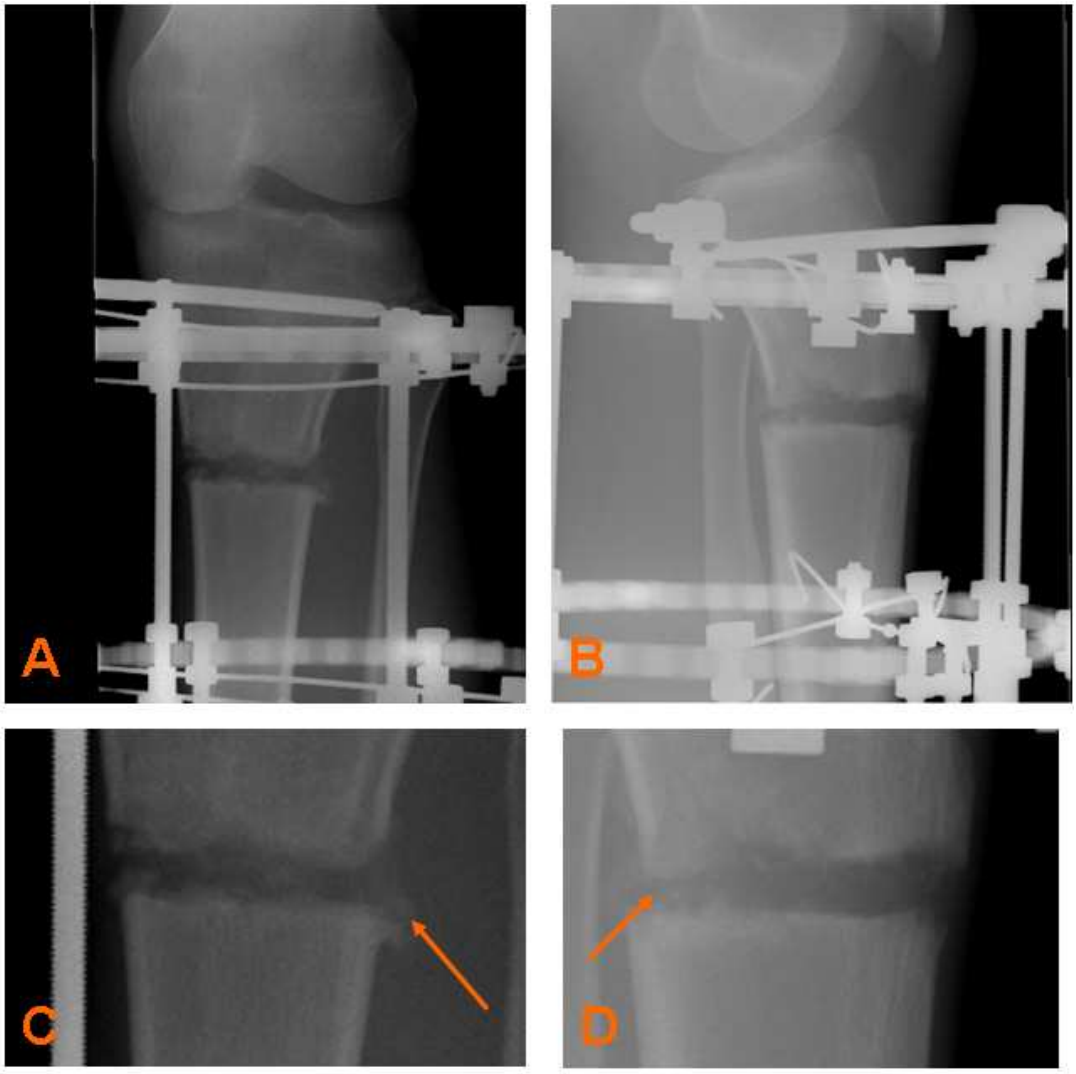

Figure 5-28: (A) AP and (B) lateral X-rays taken at 4 weeks post op. Regions of callus growth are indicated by arrows in the close up (C) AP and (B) lateral views.

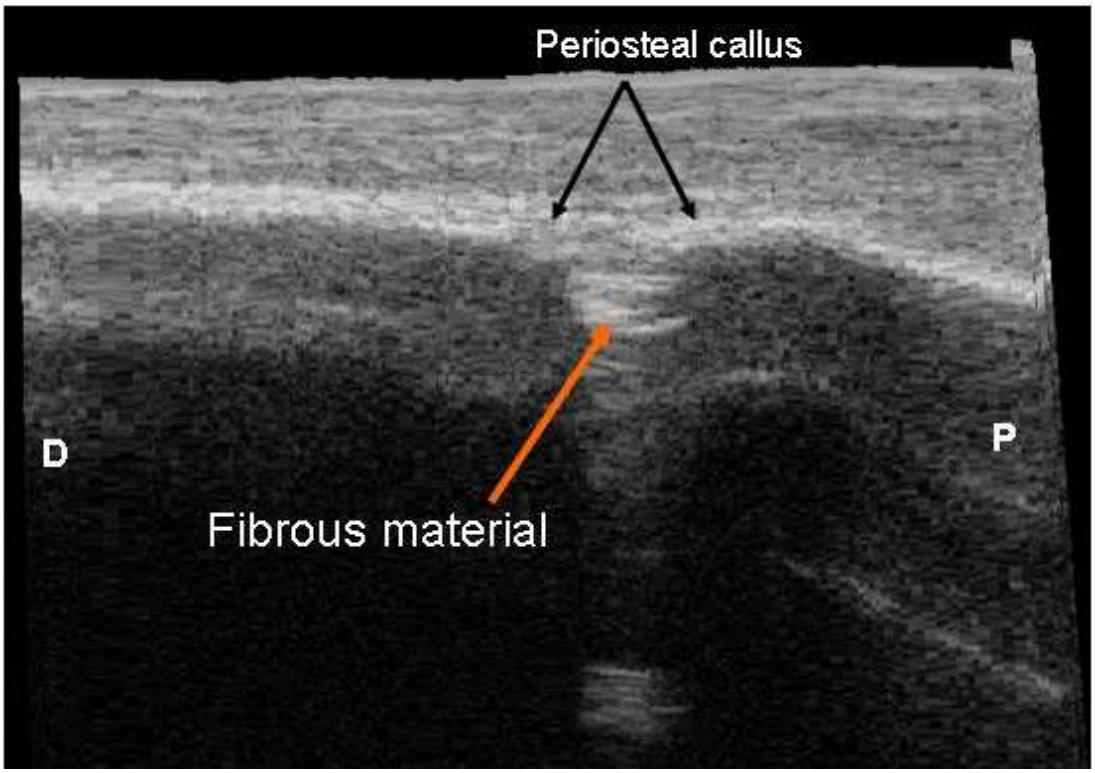

Figure 5-29: ***Reslice*** **image through the anterior face of the tibia from the 5-10 MHz length scan at 6 weeks post op. Fibrous material has filled in the lengthening gap and periosteal callus has started to extend across the gap. (P) proximal, (D) distal.**

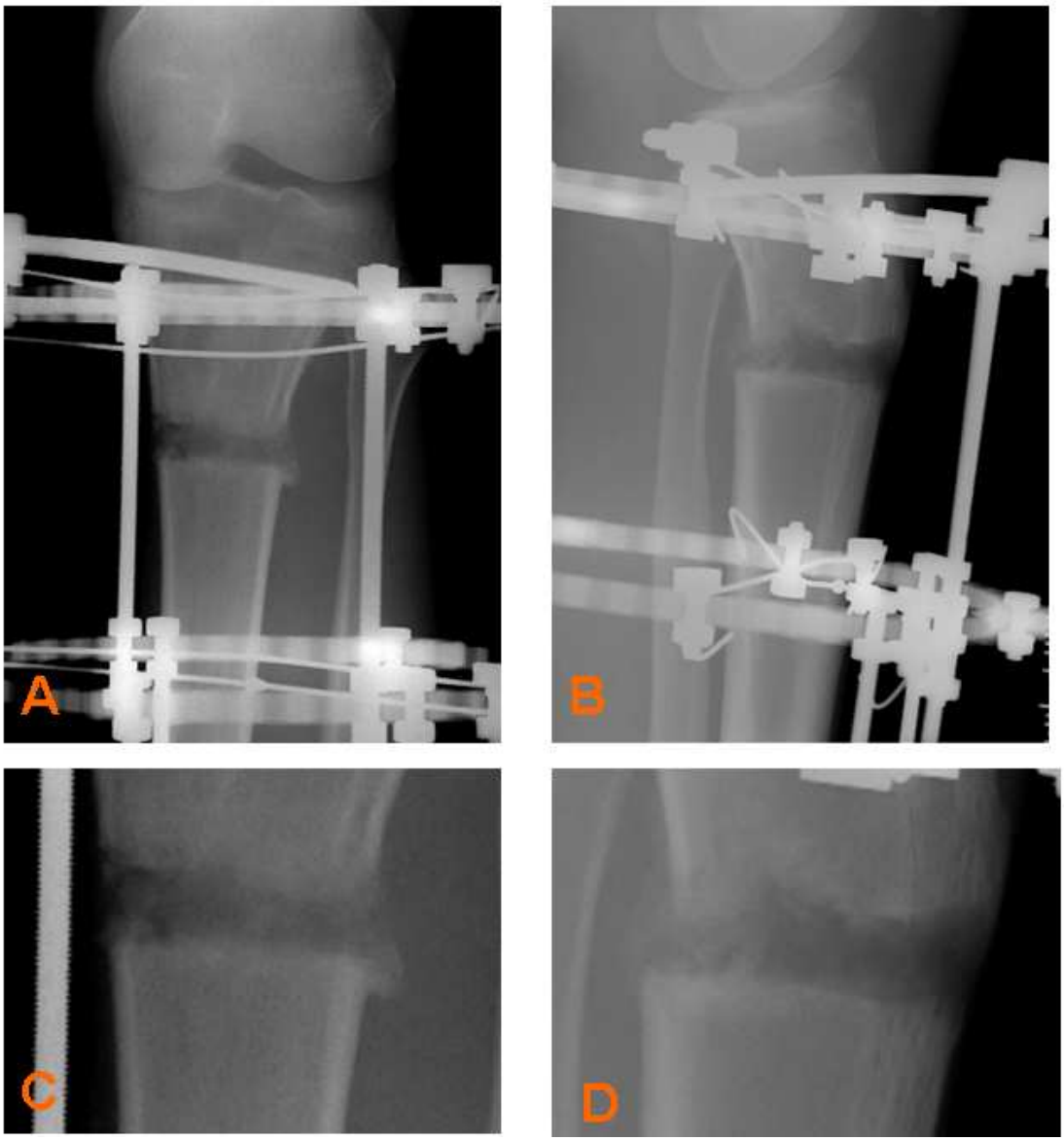

Figure 5-30: (A) AP and (B) lateral X-rays taken at 6 weeks post op. (C) and (D) show close up views of the lengthening site on the AP and lateral X-rays respectively.

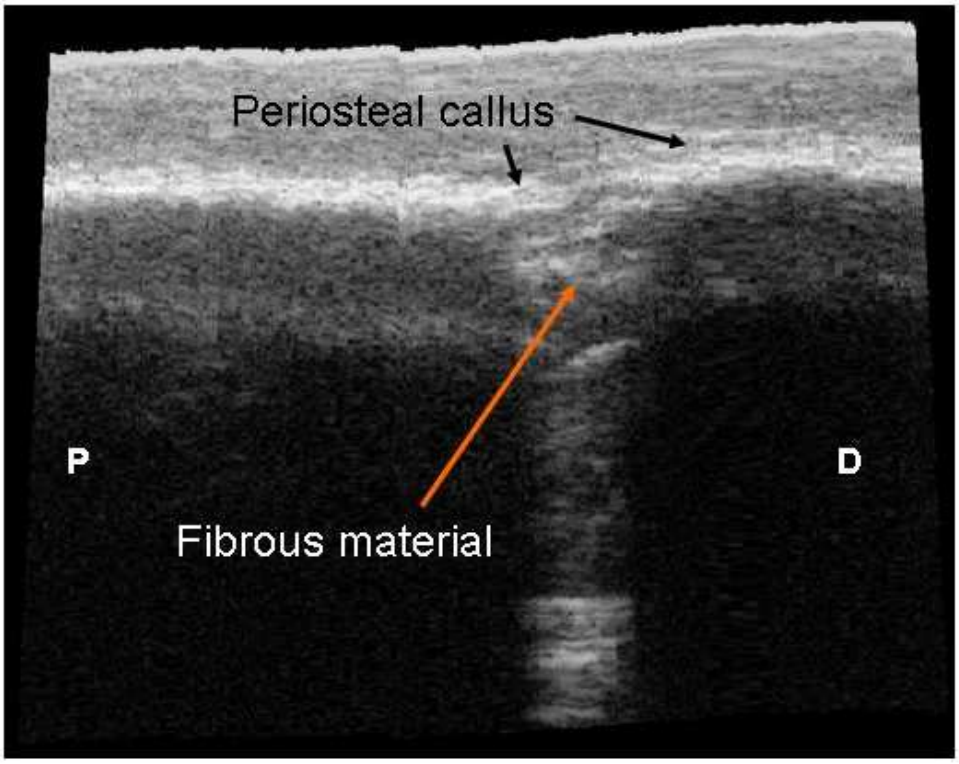

Figure 5-31: ***Reslice*** **from 5-10 MHz scan at 9 weeks post op through the anterior face of the tibia. The periosteal callus extending across the gap has increased in greyscale intensity. (P) proximal, (D) distal.**

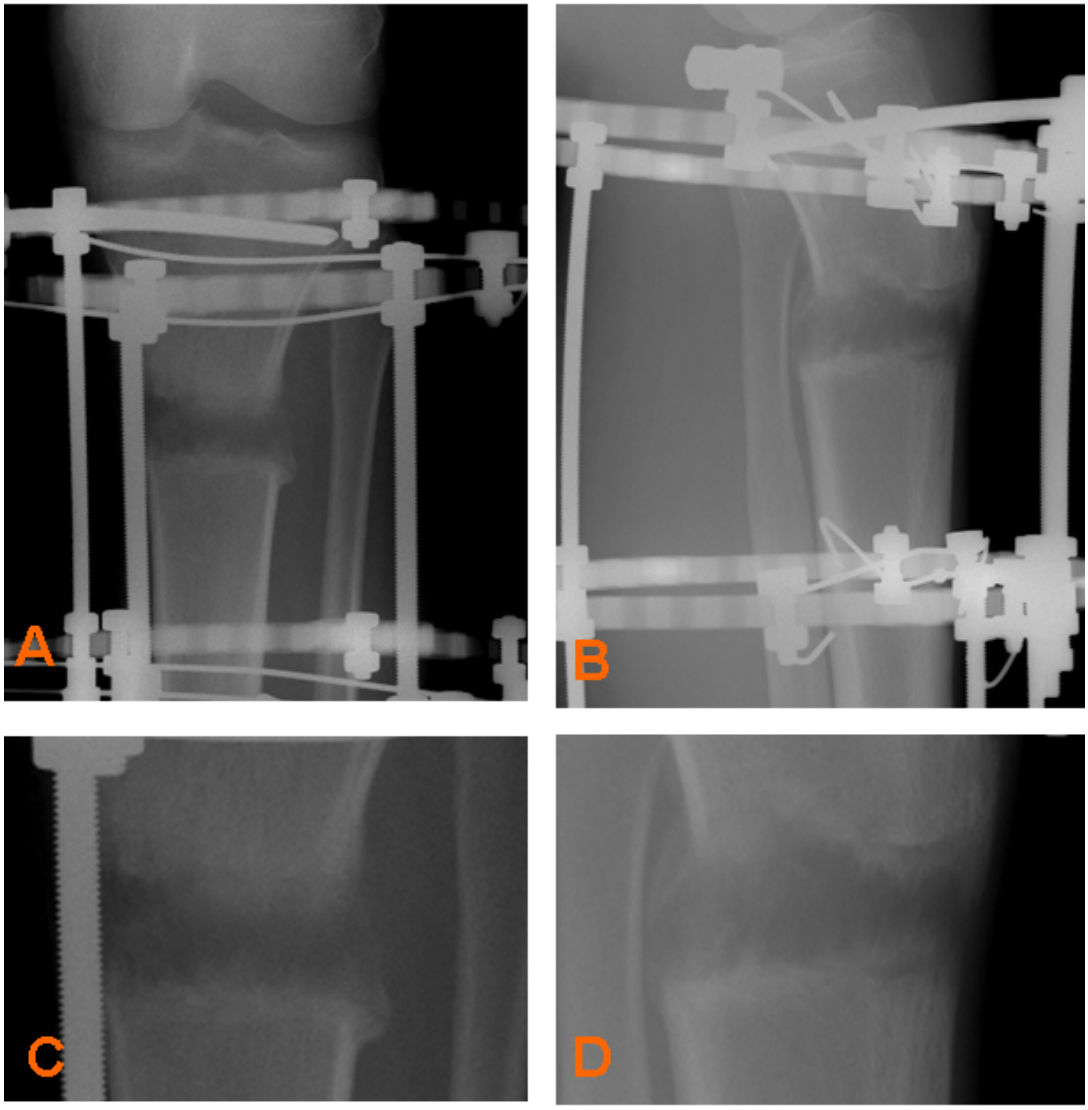

Figure 5-32: (A) AP and (B) lateral X-rays taken at 9 weeks post op. The amount of visible callus had increased as can be seen in the close up (C) AP and (D) lateral views and could now also be seen forming on the anterior face of the tibia.

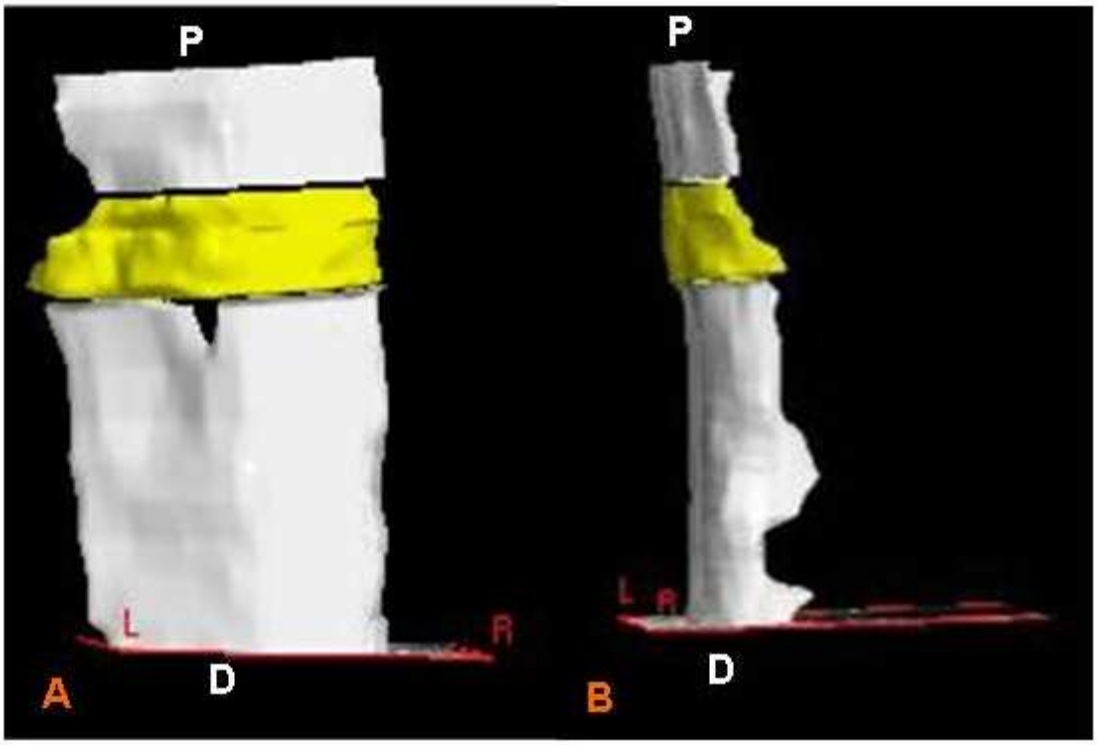

Figure 5-33: (A) anterior view and (B) medial view of the 3D model constructed from the scans taken at 16 weeks post op. The gap was now fully bridged by periosteal callus. In addition, the callus was smoother in appearance indicating remodelling was underway. (P) proximal, (D) distal.

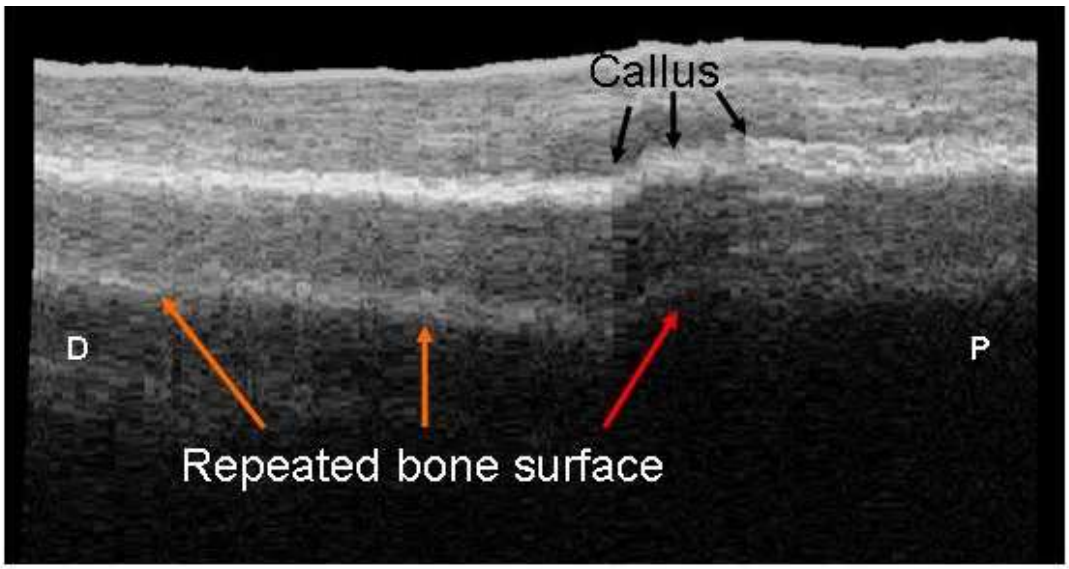

Figure 5-34: ***Reslice*** **image obtained at 16 weeks post op through the anterior face of the tibia. A faint repeated bone surface artefact, highlighted by the red arrow, can be seen below the callus region which indicated that it was maturing and gaining the same properties as normal bone. The black arrows indicate the fracture callus and the orange arrows indicate the repeated bone surface artefact under the normal bone. (P) proximal, (D) distal.**

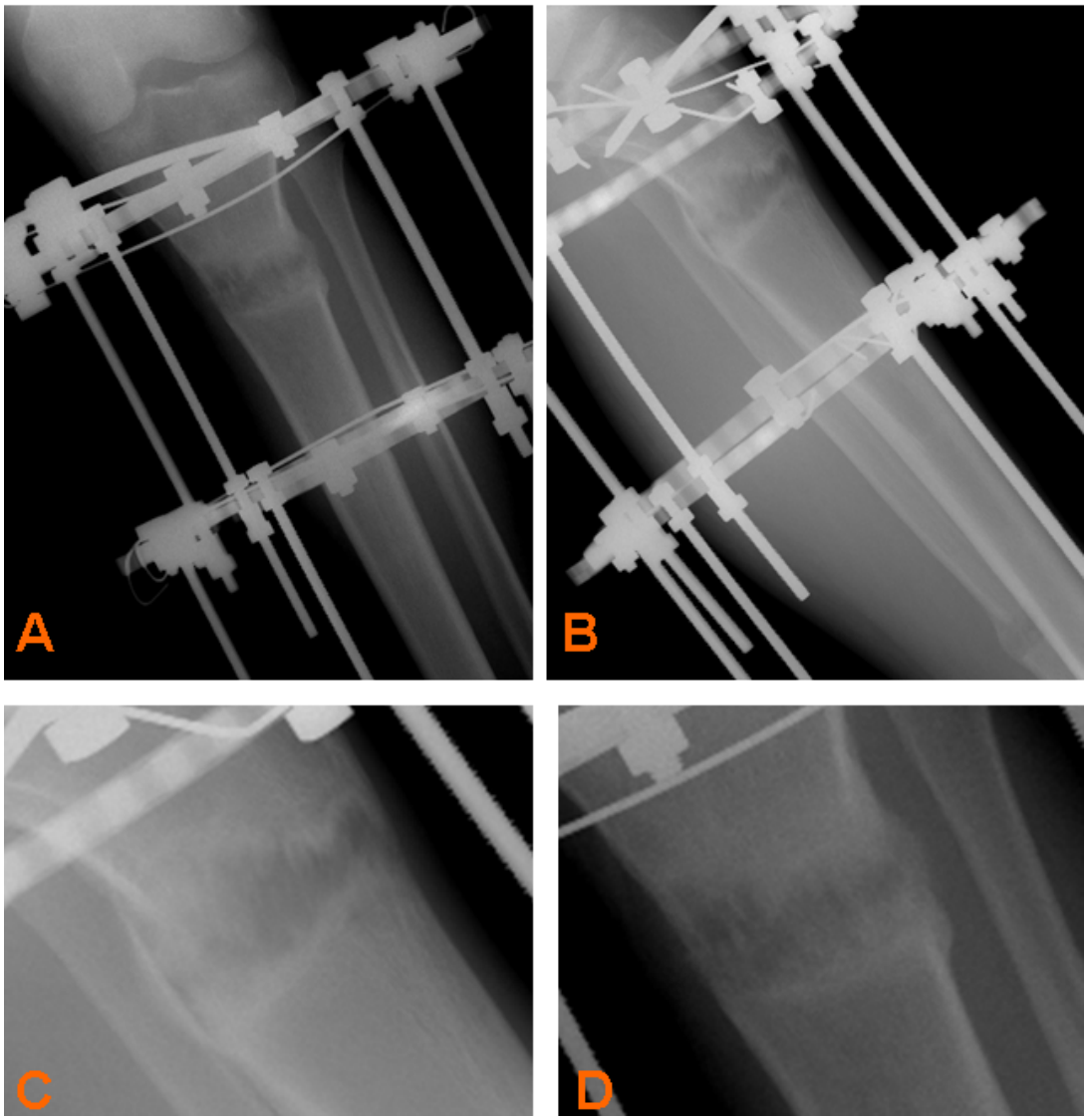

Figure 5-35: (A) AP and (B) lateral X-rays taken at 16 weeks post op. The original edges of the break are completely obscured as can be seen in the close up (C) AP and (D) lateral views and large regions of callus can be seen extending across and bridging the gap.

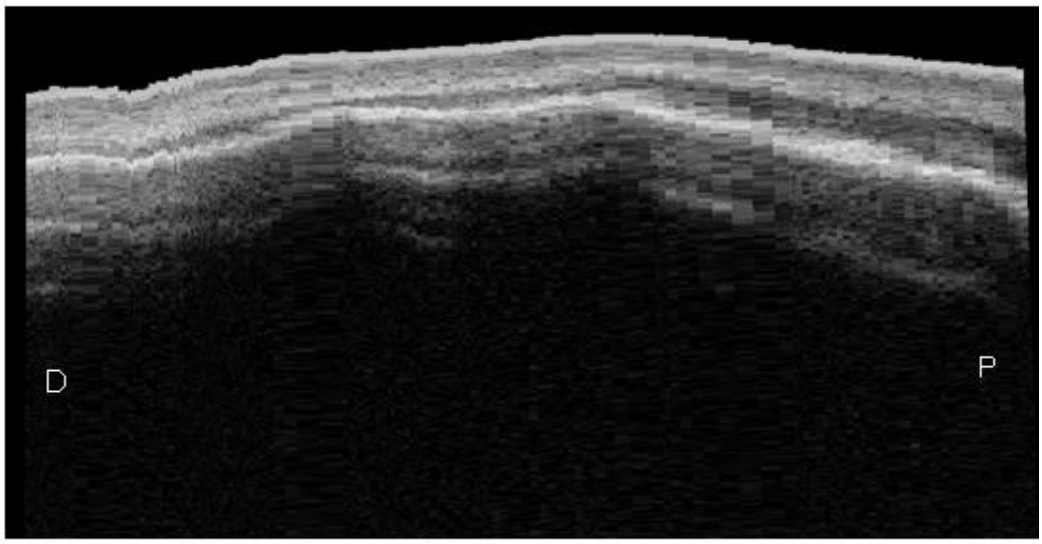

Figure 5-36: *Reslice* image obtained at 30 weeks post op through the anterior face of the tibia. The region where lengthening was undertaken was no longer distinguishable. The repeated surface artefact could be seen under the whole bone suface. (P) proximal, (D) distal.

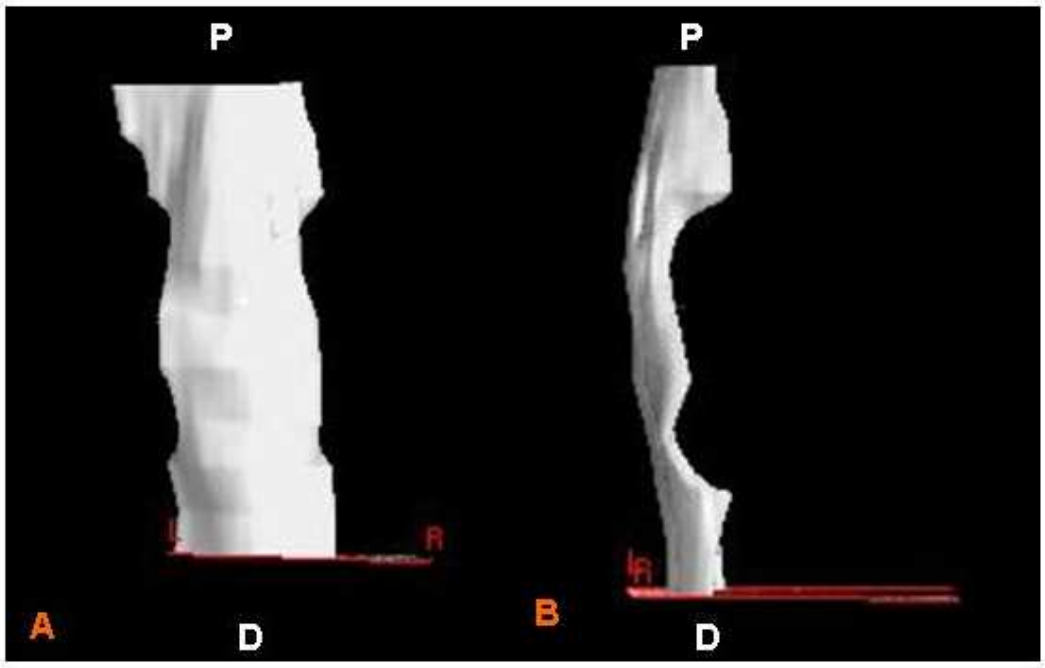

Figure 5-37: (A) anterior and (B) medial views of the 3D model constructed from the scans at 30 weeks post op. The site of lengthening was no longer identifiable. (P) proximal, (D) distal.

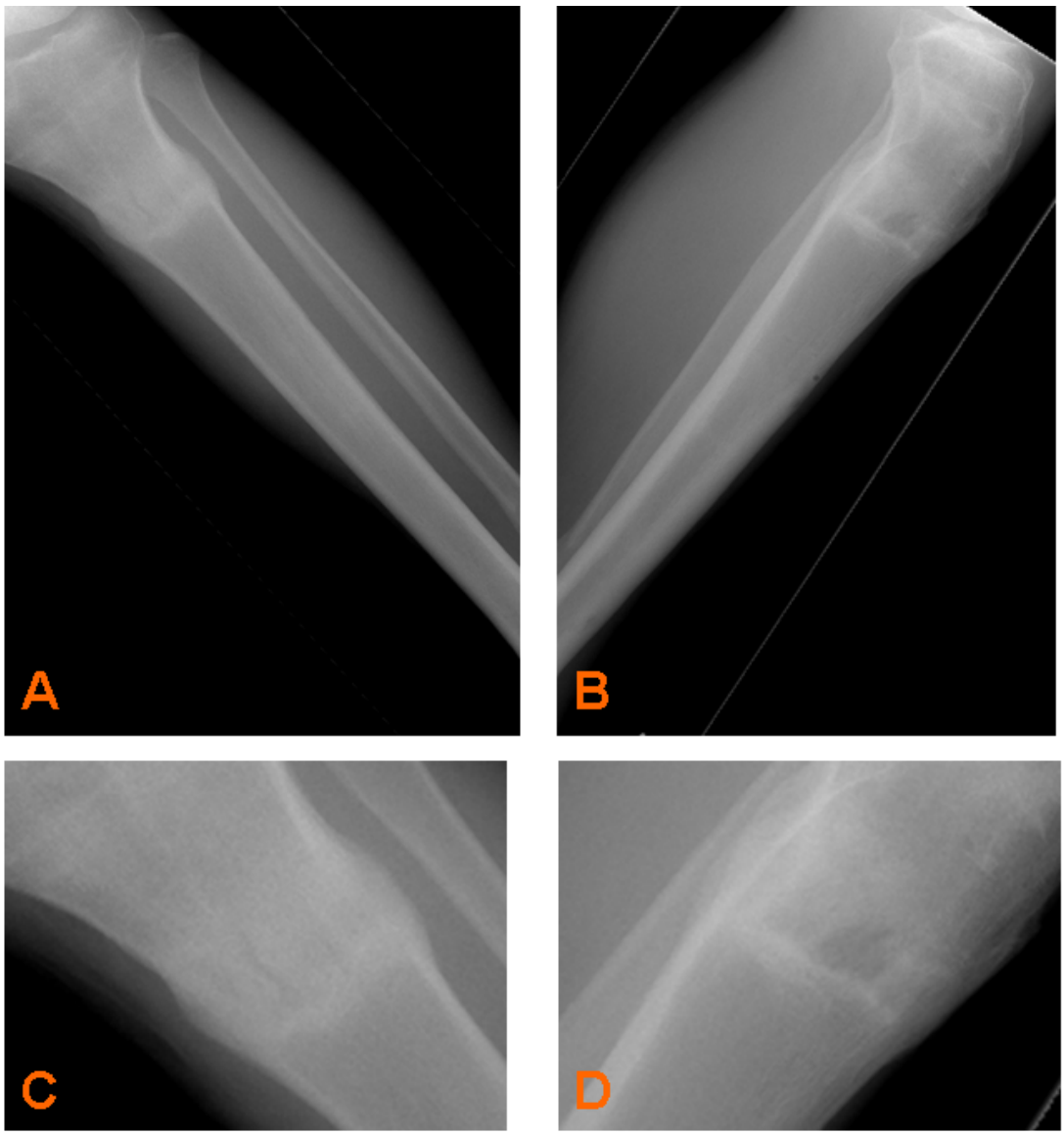

Figure 5-38: (A) AP and (B) lateral X-rays taken at 30 weeks post op. In (C) the close up view of AP X-ray the callus appears uniform in density, however in the (D) close up lateral view this is not the case.

As the bone was lengthened, the width of the gap between the bone ends, as visible on X-ray, increased. On 3D US, as the bone was lengthened periosteal callus began to form on each side of the gap making it difficult to detect the location of the original bone ends. Subtracting the width of the lengthening gap measured using 3D US from the width of the gap measured using X-ray gave the amount of new periosteal callus growth. Plotting the amount of periosteal callus growth against time, see figure 5-39, allowed the rate of new callus formation to be monitored.

Although only six post op scans are discussed his patient attended clinic more frequently during the lengthening phase of treatment. At each appointment scans were obtained and the size of the lengthening gap measured on the 3D US scans and corresponding X-rays, thus, there additional time points and measurements on the graph. For this patient the rate of periosteal callus formation paralleled the rate of lengthening seen on X-ray indicating the correct rate of lengthening was applied for the patient (52). After lengthening was complete there was a marked decrease in the size of the gap on both the X-rays and 3D US as the amount of mature callus increased.

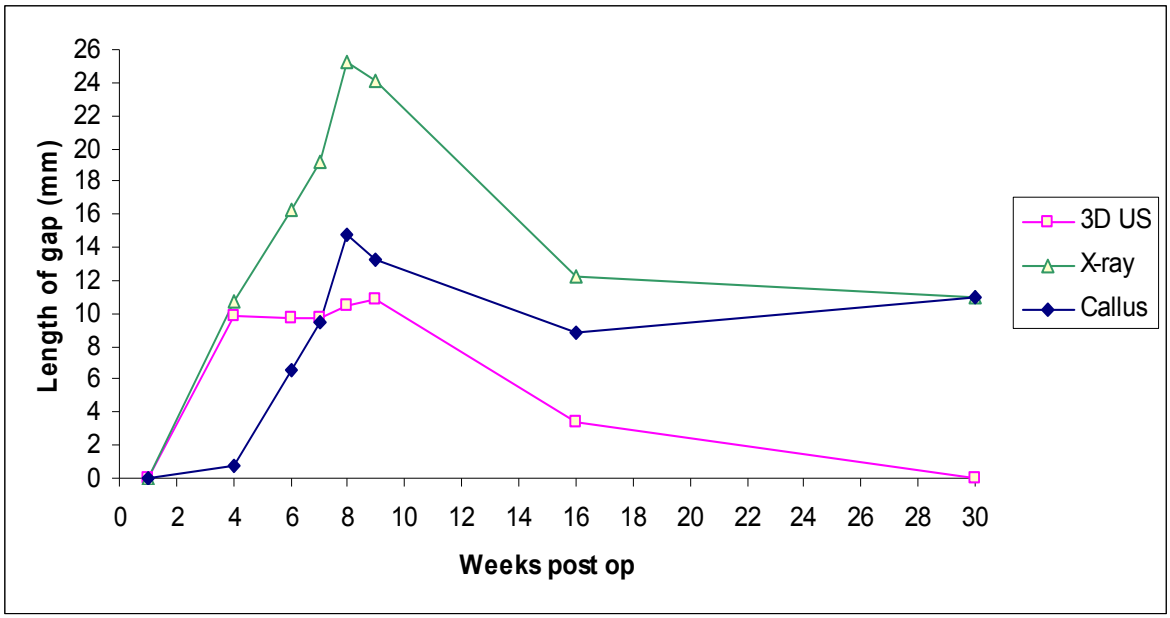

Figure 5-39: Graph showing the rate of lengthening compared to the rate of callus formation.

5.3.6. Case 6

Lengthening of the left tibia using an ISKD nail.

The first set of 3D US scans of this patient were obtained after 8 weeks of lengthening and revealed a cyst within the lengthening gap and defective callus formation. On the *Reslice* image, see figure 5-40, the cyst can be seen within the lengthening gap residing on the surface of the ISKD nail. The full extent of the cyst

(shown in red) can be seen from the two views of the 3D model shown in figure 5-41. Using *StradWin* the length of the cyst was measured to be approximately 2.5 cm in length. On close inspection of the scans small areas of callus growth were detected at the edges of the lengthening gap and these have been shown in yellow in the model, while the patient's normal bone has been shown in white. It was possible to see the surface of the ISKD nail beneath the cyst and this has also been included in the model shown in blue. On X-ray there were no obvious signs of problems, however, new bone growth was occurring slower than expected. The identification of the cyst by 3D US lead to an intervention in treatment by the consultant, the patient was referred for to Radiology for an US scan to confirm the presence of the cyst and to have it aspirated. In normal practice a 2D US scan would not have been requested for further weeks.

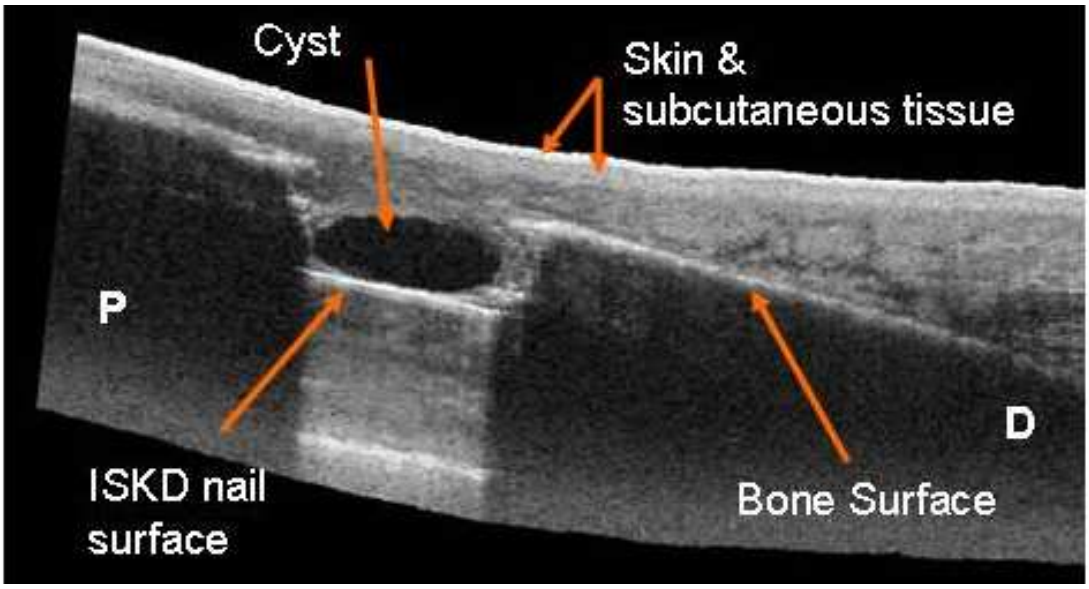

Figure 5-40: *Reslice* image obtained after 8 weeks of lengthening showing the location of the cyst within the lengthening gap. *Reslice* taken through the anterior face of the tibia.

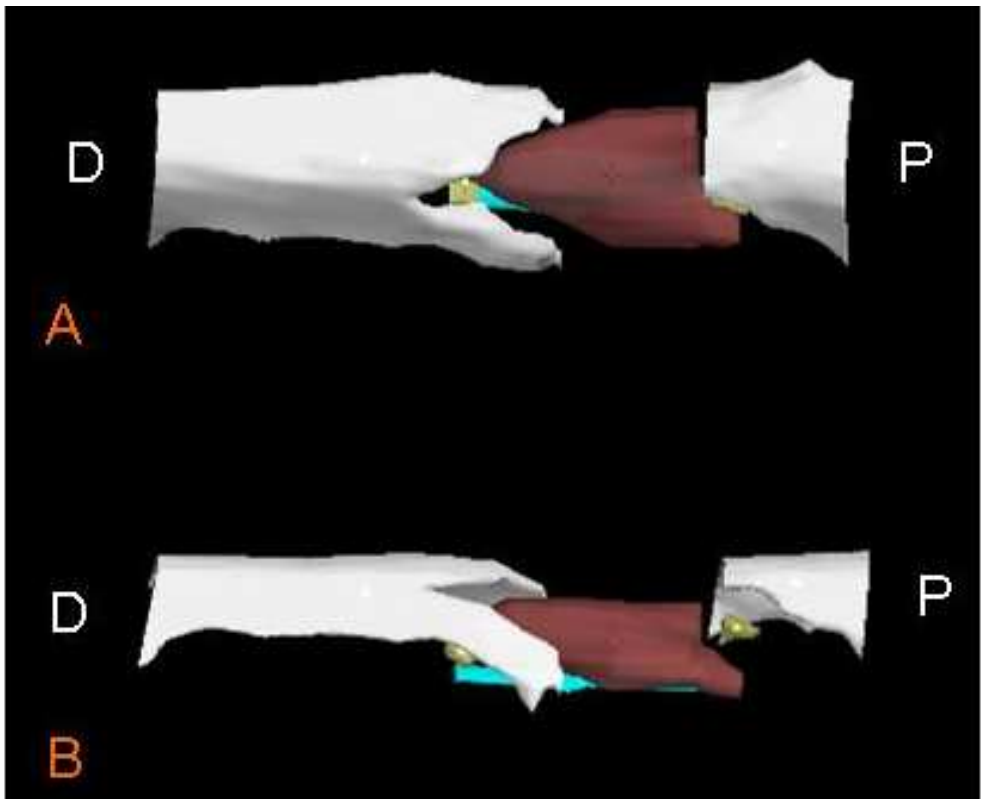

Figure 5-41: 3D models obtained after 8 weeks of lengthening showing (A) the anterior view and (B) the lateral view of the tibia. The extent of the cyst (red) can be seen. Small areas of callus can be seen (yellow) as well as the surface of the ISKD nail (blue). (P) proximal, (D) distal.

5.3.7. 3D Ultrasound compared to X-ray

Table 5-1 summarises the signs of healing detected using 3D US compared to X-ray at each follow-up appointment for each case.

Case	Week	3D US	X-ray
1	2	-	No callus
Spiral fracture left distal tibia	6	Fibrous material filling gap	No callus
	19	Periosteal callus and partial bridging	Periosteal callus and partial bridging
2	2	Fibrous material	No X-ray available
Midshaft fracture right tibia	7	Fibrous material and periosteal callus	Periosteal callus visible on two bone cortices
	16	Bridging	Partial bridging
3	3	Fibrous material and periosteal callus	No callus
Spiral fracture midshaft right tibia	8	Fibrous material and partial bridging of periosteal callus	Small regions of periosteal callus on lateral side as seen on AP X-ray. No callus on the lateral X-ray
	17	Fracture fully bridged	Increased periosteal callus with bridging on one bone cortex.
4	8	Fibrous material and early periosteal callus	Small regions of callus

Left distal femoral fracture	15	Periosteal callus beginning to bridge gap. Increase in callus material	Increase in callus material
	19	Increase in amount of callus material and in the size of the bridged region. Dip in callus beginning to be bridged by endosteal callus	Bridging has occurred and the fracture line was obscured. Dip present in the fracture callus
	28	Bulbous callus with greyscale intensity comparable to the healthy bone. Dip in callus being filled in.	Bulbous callus. Dip in callus still present
	44	Dip in callus reduced in size and remodelling evident	Fracture line completely obscured. Dip in callus still present with no visible reduction in size
5	1	No callus	No callus
Right tibial lengthening	4	Large regions of fibrous material	Small regions of callus on two bone cortices
	6	Fibrous material has filled in lengthening gap. Periosteal callus extending across gap.	Periosteal callus visible extending across the gap on the two cortices. No signs of callus on the medial or anterior bone cortices
	9	Increase in periosteal callus, bridging almost achieved. Greyscale intensity of regions of the callus comparable to normal bone.	Increase in amount of callus. Callus now visible on anterior face but no bridging. Delayed callus formation on lateral bone cortex

	16	Gap completely bridge. Callus smoother in appearance. Remodelling is underway.	Bridging on 3 cortices. Callus formation on the anterior cortex still markedly behind in development.
	30	Lengthening site no longer visible. Greyscale intensity of the callus reached that of healthy bone.	Gap fully bridged. Substantial callus visible on all bone cortices.

Table 5-1: Summary of signs of healing detected using 3D US compared to X-ray for each case.

5.4. Discussion

3D US scanning was tolerated well by all participants. One patient had initial reservations that the contact pressure of the probe would cause discomfort, however, this was not the case. The probe was held in such a way as to ensure skin contact but minimise any pressure.

Closed fracture patients were chosen for this study as the dressings covering the wounds of an open fracture would have restricted 3D US scanning, the presence of air in the bandages would have made it impossible to scan through them. One of the participants withdrawn from the study had developed fracture blisters post op and these were bandaged in such a way that scanning was not possible. All three of the tibial fracture patients had small dressings covering the incision sites created during the surgery to insert the IM nail. These dressing did not inhibit scanning and had been removed by the second follow-up appointment. One of the tibial fracture patients also had surgical staples used to close a wound above the site of fracture. These staples are visible in the X-rays shown in figure 5-10 but did not restrict 3D US scanning.

The location of the fracture in case 1 restricted the area that could be scanned. The flared shape of the distal end of the tibial and the close proximity of the fracture to

the ankle meant maintaining skin contact with the probe was difficult. The use of a gel pad to offset the probe from the skin surface and provide a more even surface for scanning would have overcome the restrictions encountered.

In a previous study using 2D US to investigate the rate of new bone production during lengthening it was noted that during the initial stages of lengthening the rings on the Ilizarov frame may be too close together to accommodate an US probe (11). In case 5, the positioning of the Ilizarov frame allowed the anterior face of the tibia to be scanned unhindered from the first follow-up appointment, the proximity of the two rings was not restrictive. In previous studies using 2D US for monitoring lengthening, the US probe was placed over the lengthening site and orientated perpendicular to the break in order to measure the width of the gap and amount of periosteal callus growth (52, 54). An advantage of the 3D US system is that if the rings were too close together to allow the probe to be positioned perpendicular to the line of the break, the probe could instead be held at an angle to fit between the rings and moved over the break. Despite the images being obtained at an angle, the *Reslice* facility could be used to view an image slice across the lengthening site, and accurate length and volume measurements could still be made.

The projection nature of X-ray images means that details of the bone surface and depth are lost and it can be difficult to determine at what depth within the fracture gap that callus is forming. To image a fracture sufficiently two X-ray views are required AP and lateral (medial-lateral projection). It was shown in Chapter 2 that a simple fracture in an AP view could actually be a displaced fracture when viewed in the lateral plane, see figure 2-4. Even with two orthogonal X-rays the shape and appearance of the fracture is subject to inter-observer variability (10, 25, 31). The spiral shape of the fracture in case 1 and the presence of the bone fragment in case 3 meant that the fracture gap was not clearly visible. This made it difficult to determine the location of the forming callus within the fracture gap.

The series of 3D US scans obtained allowed the fracture pattern to be properly identified. Despite the limited area that could be scanned for case 1, the spiral

pattern of the fracture was still clearly evident with 3D US. A further advantage of 3D US was the ability to determine where the callus was forming. Fibrous callus material forming within the gap to stabilise the fracture could be identified along with the developing periosteal callus.

In previous studies using 2D US to monitor fracture repair, US was able to detect signs of healing weeks before they were apparent on X-ray (11, 48, 49, 55). The first signs of healing visible with 2D US were the appearance of echogenic areas within the fracture gap which appeared disorganised in nature before becoming aligned as the healing process progressed. From the results of a pre-clinical study (58), this echogenic material was shown to be fibrous immature callus material. As the healing process progressed collars of periosteal callus began to form and bridge the gap and the amount of echogenic material within the gap decreased.

In this study it was hypothesised that signs of healing would be detected earlier using 3D US scans compared to X-ray, and this was found to be true for cases 1, 2, and 3. In case 1 signs of healing were visible on the 3D US scans at 6 weeks post fracture but were not visible on X-ray until the follow-up appointment at 19 weeks post fracture. In case 2 echogenic deposits could be seen between the bone ends at 2 weeks post op unfortunately there were no radiographs recorded at that point to determine if signs of healing were visible. Close inspection of the *Reslice* image shown in figure 5-4 revealed the faint outline of where the haematoma was before it was invaded by cellular material and reabsorbed. Neither of these signs of healing were visible on the corresponding X-rays. In case 3, fibrous material was detected within the gap and also forming as periosteal collars of material at 3 weeks post fracture on the 3D US scans. On the corresponding X-rays the first signs of callus formation were seen at 8 weeks post fracture. In cases 4 and 5 signs of callus formation were detected with 3D US and X-ray at the same time. Despite this, there was still a notable lag between the amount of callus material seen on X-ray compared to 3D US as the healing process progressed in both cases. This lag was even more prominent for the tibial fractures patients when comparing the amount of bridging callus visible on 3D US compared to X-ray at the three month follow-up point.

The ability to manipulate the models constructed from the 3D US scans provided a means of seeing where the callus was forming and how the location of the callus changed as healing progressed. The *Reslice* facility could also be used to provide views of the fracture site in order to determine where callus was forming and to check for complications as well as allowed comparisons to be drawn between the greyscale intensity of the callus and healthy bone. As the callus matured the difference between the acoustic impedance of the callus and the surrounding soft tissue increased causing the reflection at the soft tissue – callus boundary to intensify on the US image. This change in intensity relates to the density and calcification of the callus (48). The repeated surface artefact that was noted underneath the patient's normal bone on the *Reslice* images also appeared faintly underneath the section of callus in the later stages of healing. The appearance of this artefact underneath the callus has been found to mark an acceleration in the calcification process (48). Strain gauges used to determine the mechanical properties of the callus at this stage found that its properties were approaching a similar state to normal bone. Further work investigating a means of determining the mechanical properties of the callus directly from the US images obtained during 3D scanning are discussed in Chapter 6.

The occurrence of complications such as mal-union, angulation of the bone and re-fracture are stated as being better detected using X-ray rather than 2D US (53, 54). The limited field of view of 2D US made it difficult to detect such complications. 3D US can overcome this problem, the incorporation of a multiple sweep function in *StradWin* allows US probe to be swept over the fracture site multiple times and the multiple image datasets to be stitched together. This means it is possible to incorporating larger sections of bone above and below the break. An extensive 3D model could be constructed to look for visible signs of angulation or the *Landmarks* tool within *StradWin* could be used to check the angle between the sections of bone above and below the break. Further work on the line-of-sight restriction for scanning when using optical tracking may allow larger angle scans around the effected limb to be carried out. Inspection of the 3D model could then reveal if there was angulation or mal-union of the fracture.

The ability of 3D US to detect the early signs of healing during limb lengthening and in particular to monitor the rate of periosteal callus growth and detect complications were advantages over X-ray. Even when callus was of sufficient density to be visible on X-ray, the lag between what can be detected on X-ray compared to 3D US means complications may occur and remain undetected on X-ray for several weeks (11). When using 3D US, R*eslice* images can be used to check the width of the lengthening gap to ensure premature bridging has not occurred. However, one limitation of 3D US is that as the newly formed periosteal callus begins to mature its greyscale intensity increases making it difficult to determine the position of the original bone ends, thus, making it difficult to determine the amount of lengthening achieved. X-ray would still be required for this purpose but could be carried out less frequently. Alternatively, a solution would be to insert a pair of metal marker beads in the patients bone each side of the break during the surgery to fit the lengthening device. These beads would be easily identifiable on the US images and would provide a clear measure of the amount of lengthening achieved.

This pilot study has consistently shown the potential of 3D US as a tool for monitoring fracture repair. Initial signs that the healing process is under way can be detected earlier, complications have been detected that were not visible on X-ray and also it can be used to monitor lengthening to ensure premature bridging of the lengthening gap dose not occur. There is no gold standard against which the success of 3D US can be compared which raises the question does it offer false hope when signs of healing are detected? Although in this study only a small region of the fracture site could be scanned it was possible to look into the fracture gap and detect fibrous material deposits which indicate the fracture repair process is underway. If there is a delay or halt to this process this would be visible on follow up scans, however, compared to X-ray this stage of the healing process cannot be detected. Callus formation is unlikely to occur uniformly across the fracture site, however, being able to detect the second stage of healing is underway is a positive indicator that fracture repair is underway. If complications occur at this stage intervention can be taken earlier than if only X-ray images were being used.

From the results of this pilot study it is recommended that a further study involving a larger patient group is carried out examining both fracture and limb lengthening patients. In both cases patients should be monitored more regularly, every 2 weeks for the fracture patients for the first 8 weeks, and every 2 weeks for limb lengthening patients during the distraction process. Ideally larger volumes of the fracture site should be scanned to give a better understanding of the whole fracture site and to determine if 3D US is offering false hope when only a small section of the fracture site is scanned or whether the detection of fibrous pre-callus material in the gap is indicative of a successful healing outcome.

6. Development of a Fracture Callus Density Measure

6.1. Introduction

As a bone heals its mechanical properties will return to a similar state as pre-fracture. Methods of determining the mechanical state of the fracture callus during healing include physical assessment of the fracture site and indirect imaging derived measurements. For lower limb fractures, obtaining a quantitative measure of the mechanical properties of the callus would provide an accurate means of establishing when a patient can safely resume full weight bearing. This Chapter covers the development and evaluation of a callus density measure derived from 3D US data.

6.2. Background

Fracture union is the stage in the healing process (described in Chapter 2) where the callus has formed uniting the bone fragments and stabilising the fracture. The callus is sufficiently calcified at this stage to be visible on X-ray, however, it is still maturing into lamellar bone and does not have the mechanical strength to cope with the demands of full weight bearing (12, 21). It is during the following consolidation stage of healing that the mechanical properties of callus should return to a similar state as pre-fracture; allowing normal use of the affected limb to resume (29).

Successful bony union and consolidation are determined by physical assessment of the fracture site and should be supported by radiological findings (120). If consolidation has occurred there should be no mobility of the fracture site when physically tested and the patient should experience no pain or discomfort when moderate stress and pressure are applied (20, 21). If union has occurred but

consolidation is only just underway the fracture site will still be tender, in particular, when a bending force is applied across the fracture.

Review articles which have looked at outcome measures of fracture repair studies have found there is no agreed standardised method for determining the point at which union and then consolidation have occurred and thus when full weight bearing can safely resume (10, 25, 31). In a study by Morshed et al. different methods of assessment used by consultants to identify when weight bearing could be resumed ranged from full physical assessment supported by visible consolidation of the callus on X-ray to simply asking if the patient could weight bear and checking that there were signs of callus visible on X-ray (25). In the majority of cases both clinical criteria and radiological evidence were used to determine if a fracture had healed. The lack of consensus about the time lines for delayed and non union was examined in a study by Bhandari et al (10). Opinions on the definition of delayed union varied from 1 - 8 months and for non-union from 2 - 12 months between the 444 Orthopaedic surgeons surveyed

Neither the use of physical assessment criteria or radiology findings, whether used separately or combined, provide a definitive means of determining healing. It was noted in the results from Chapter 5 and also in other studies that there is a lag between what can be observed at the fracture site using X-ray and what is actually occurring (11, 48, 49, 55). This is due to the amount of calcification required for the callus material to become visible on X-ray. Even with two orthogonal views of the fracture site, the projection nature of X-ray images can make it difficult to establish whether callus has formed equally well at all points around a fracture. Callus can take on different patterns of bridging dependent on whether the fracture is healing by endosteal, periosteal or intercortical bridging (121). If an internal fixation device such as an Intramedullary (IM) nail or metal plate has been used to stabilise the fracture there is often less callus produced as it is not required to initially stabilise the fracture (120). In theses cases there is a reduced amount of callus to monitor on X-ray and physical assessment of the fracture will be limited by the presence of the device. Although internal fixation may provide enough support to allow weight

bearing (as may be the case with an IM nail) it is still important to monitor these fractures to ensure they progress to a fully healed state without complications. If the internal device loosens or fails and the callus is not sufficiently strong to withstand weight bearing, the bone may re-fracture. Furthermore, too much movement at the fracture site can lead to delayed healing and possible non-union (21).

The need for a method of obtaining information about the mechanical strength of callus is a long held concern. A pre-clinical study by Siegel et al. found that X-ray examination often correlated poorly with the actual amount of callus formed and that physical assessment tests did not perform much better (47). Early methods of obtaining mechanical information about the healing callus were based on principles that had been long established in the field of material testing. Measuring the velocity of sound through a material of known density provides a measure of the elastic modulus that relates directly to the strength of the material. The relationship between velocity, *V*, density, *D,* and Young's modulus of elasticity, *E,* is,

$$V = (E/D)^{1/2}. \qquad (6.1)$$

By calculating the average velocity of a sound pulse transmitted across the site of a fracture, the elasticity and thus the strength of the forming callus can be deduced. A pre-clinical study allowed measurements to be compared directly with histology and the known stages of fracture repair (47). Using a separate transmitter and receiver placed either side of the fracture site, a series of short sound pulses were transmitted across the break. By measuring the time it took to receive the pulse over a known distance the velocity could be calculated. Good agreement was found between the velocity measurement and the actual histology as well as the accepted histology of healing. When the haematoma had formed sound could travel relatively unhindered across the fracture site giving a measure of velocity only slightly reduced compared to normal bone. As cellular proliferation started the haematoma began to become organised and the average velocity across the fracture site decreased significantly. It is only when the collagen fibres were impregnated with calcium deposits and became

more rigid that the average velocity across the fracture gap gradually returned to its pre-fracture value. A further pre-clinical study by Abendschein et a. using this technique identified different mean velocities that related to different progressions of healing including non union, mal-union and normal bony union (122). One concern about the accuracy of this method was the value used for density in equation (6.1) Siegel et al. made no mention of the consideration of the effect of density, instead, results were based more on the measure of velocity as an indication of strength through the relationship with Young's modulus. Abendschein et al. made calculations of Young's modulus of elasticity, however, the value of *D* was derived from measurements of mass and volume obtained after the bone had been excised.

In another pre-clinical study looking at tibial fractures, the results of velocity measurements across the fracture gap during healing were compared to the results of 3-point bending test on the excised bones (123). The correlations between velocity measurement and stiffness, load at failure and elastic modulus during bending were not strong enough to support the use of velocity measurements as an accurate and useful indicator of fracture callus strength. A bending stiffness of 15 Nm/º has been proposed as a reliable indicator that fracture union has occurred and that an external fixation device can be safely removed. In a study assessing conservatively treated tibial fractures it was found that all fractures that reach a bending stiffness of 7 Nm/º progressed on to full healing (121). When applying the proposed 15 Nm/º limit to bones other than the tibia it was found that the values of bending stiffness and the correlating value of bone strength varied significantly due to the differences in bone geometry. The age of the patient and shape of the bone also needed to be taken into consideration when applying the 15 Nm/degree limit (124). A study of clinical judgement requiring Orthopaedic consultants to rate the bending stiffness of mock tibial fractures, simulated using phantoms, found that 83% overestimated bending stiffness and would have recommended the removal of an external fixation device (125). A reliable and accurate means of determining the mechanical properties of the fracture callus would provided a definitive point at which weight bearing could resume, reduce rates of re-fracture and also decrease rehabilitation times for patients where healing has occurred rapidly.

A measure called the Callus Index has been devised to determine the amount of new periosteal bone that has formed at the fracture site. The Callus Index is defined as the ratio of the maximum width of callus to the diameter of the original shaft of the bone at the same level as measured from X-ray (126). Measurements of Callus Index have been compared to the bending stiffness values obtained in the previously discussed study by Marsh to try and define the occurrence of union, delayed union and non-union (121). No correlation was found between the Callus Index and bending stiffness measurements.

6.2.1. Development of a Callus Density Measure Derived from Ultrasound

The aim of this investigation was to determine whether additional information about the mechanical properties of the healing callus could be deduced from 3D US data. As explained in section 2.2 it is the difference in acoustic impedance of the two tissue types such as bone and muscle that give rise to the reflection of the US pulse at tissue boundaries. The percentage of the US pulse reflected is dependent on the acoustic impedance of the materials and thus the densities of those materials, as described previously by equation (2.2). Immediately after fracture when the haematoma forms in the fracture gap the amount of US which is reflected at the soft tissue - haematoma boundary is less than 0.01%. At the start of the healing process the US pulse is transmitted almost completely by the haematoma and the inside of the fracture gap can be imaged clearly. As the bridging callus forms the US pulse cannot penetrate as far into the gap. During the calcification process the depth of US penetration is reduced as the percentage of US reflected increases and attenuation within the callus also increases. When the callus has fully matured into lamellar bone the amount of reflected US at the soft tissue – bone boundary is approximately 43%. The rate of attenuation within the healed bone means that it is no longer possible to image below the bone surface. It was hypothesised that as the callus matures and the

percentage of reflected US increases, the density of the callus material must also be increasing as the soft tissue density will remain unchanged.

Bone density will vary from person to person and is dependent on factors such as age, health, gender, diet and levels of exercise undertaken. In order to gain the most detailed information about change in callus density a patient specific measure was developed. This involved comparing an individual patient's callus against their healthy normal bone to obtain a percentage measure that could indicate how the density of the callus changed during healing. It was hypothesised that as the callus calcifies and formed woven and then lamellar bone, the ratio of callus density to healthy bone density should approach a value of 1. On a B-scan image, the percentage of reflected US is indicated by the greyscale intensity representing the echo at the tissue - bone boundary. It was proposed that comparing the greyscale intensity of a section of callus with a section of healthy bone will give an indication as to the density of the callus.

Software was developed using Matlab (Mathworks, USA) to compare the greyscale intensity of a section of callus against the greyscale intensity of a section of the patient's healthy bone and return a percentage measure. Before greyscale intensity information could be obtained from the 3D US data the effects of image processing applied to the US images before they were captured in RF format had to be taken into account. The B-scan image data was acquired from the Diasus in its RF format after received gain (Rx) and Time Gain Compensation (TGC) had been applied to the RF signal. A set method of removing the effects of Rx gain from the image data was not required as the density measure was to be patient specific. Instead, it was acceptable to establish the best setting for the Rx control to provide an optimum image of the patient's fracture site during the first scan and then kept the same settings for each consecutive scan of that patient thus negating the effects of Rx. The same approach was adopted for the power (Tx) setting. The TGC settings were kept the same for each scan of every patient. TGC was set to give a gradually increasing gain with depth to counter the effects of attenuation. The position of each TGC

slider control was marked on the US machine to ensure they remained constant and these settings were checked before each scan.

The rate of attenuation, α, of the US beam, a function of both depth and frequency, and the effect of the point of focus of the US beam also had to be taken into account. In order to quantify the effects of attenuation, TGC and point of focus, a phantom object, for which the rate of US attenuation with depth was known, was required. By scanning the phantom using the same settings as the patient's scan it would possible to analyse the images and remove these effects from corresponding patient's images. The phantom used (CIRS 055 Phantom, Imaging Equipment, UK) had a known attenuation of $\alpha = -0.5$ dB/cm/MHz.

Only one US image of the phantom object was required to quantify these effects for each scan. Before the required image analysis could be carried out the surface artefact present in the US image of the phantom had to be removed; this was achieved by a simple cropping process.

Using the depth setting and frequency of the probe, the effects of attenuation were calculated. For the 5-10 MHz probe a central frequency of 7.5 MHz was assumed while a central frequency of 12 MHz was assumed for the 8-16 MHz probe. This gave attenuation of -3.75 dB/cm for the 5-10 MHz probe and -6.0 dB/cm for the 8-16 MHz probe. Using equation (6.2) the effects of attenuation on the intensity of the greyscale levels throughout the image were determined.

$$G = G_s x 10^{\left(\alpha/10\right)}. \qquad (6.2)$$

G is the value of greyscale intensity to be removed due to the effects of attenuation and G_s is a reference greyscale level taken at the surface of the US image so that it was minimally affected by attenuation. By calculating the attenuation with depth on the pixel scale of the US image rather than in centimetres the effect of attenuation

could be removed from the greyscale intensities of the US image on pixel by pixel basis.

Summing the greyscale intensities across each row of pixels for the phantom image and plotting the mean value for each row against depth provided a graph, shown in figure 6-1, from which TGC and point of focus effects could be obtained through a curve fitting process. The point of focus effect created the peak in the graph which was best described by a Gaussian distribution. TGC gave the gradually increasing curve making up the remainder of the plot, which was best described by a quadratic polynomial. Both terms are included in equation (6.3) which was used for curve fitting where the coefficients *a,b* and *c* in the Gaussian term described the height, position and the full width at half maximum height of the peak, respectively. The parameters a, b, c, p_1, p_2, p_3 and the best fit line were found by least squares fitting.

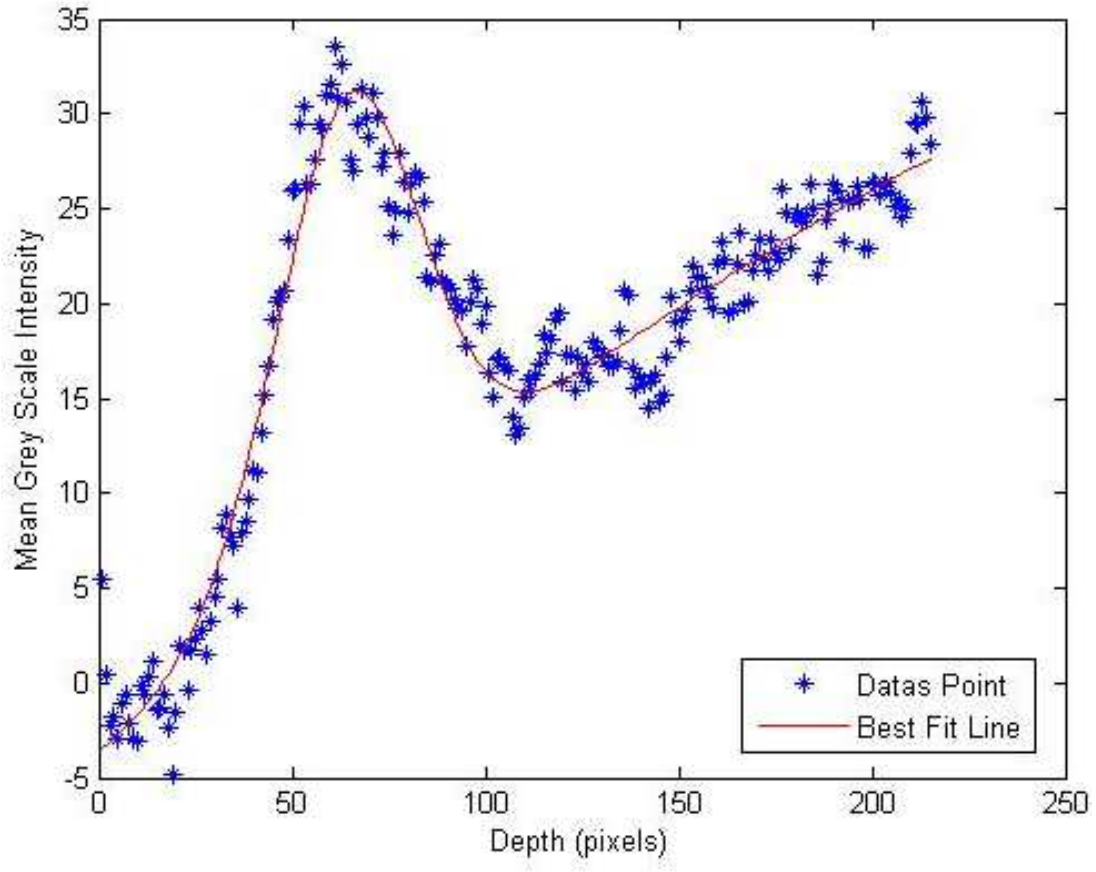

Figure 6-1: A graph showing the plot of mean greyscale level against depth for the analysis of a phantom image. Curve fitting was applied (red line) using equation (6.3) to quantify the effects of TGC and point of focus.

$$y = \underbrace{a\exp\left(-\left(\frac{x-b}{c}\right)^2\right)}_{Guassian} + \underbrace{p_1x^2 + p_2x + p_3}_{Polynomial} \qquad (6.3)$$

With the effects of TGC, point of focus and attenuation of the US beam calculated they could be removed from patient images to allow the greyscale intensity of a region of callus to be compared against a region of normal bone. Two regions for comparison were selected by the operator and the resulting greyscale intensity ratio of callus to healthy bone was given as a percentage termed the *Healing Index*. This value should indicate how close a patients callus was to returning to normal healthy

bone. An error value for the *Healing Index* was also provided. As the callus matures and forms lamellar bone the *Healing Index* value should approach 100%. To validate the *Healing Index* a pre-clinical study was carried out on sections of sheep femur which were decalcified to different degrees to act as a simple model of the fracture repair process in reverse. Decalcifying the bone samples to different degrees simulated fracture callus at different densities and thus different stages of healing.

6.3. Methods

Five pairs of fresh sheep femurs were obtained and two 2 cm long sections of bone were cut from the mid shaft of each. The ten sections taken from the right femurs were used as the test bones to be decalcified and the ten sections taken from the left femurs were used as controls. The controls were matched to the corresponding section of bone from the right femur. Each bone sample was weighed and its volume measured using water displacement. All bones samples were then fixed in 10% buffered Formalin solution for 24 hours to preserve them. During this time the bones were kept in a cold room at 5ºC.

Before decalcification all the test and control bones underwent 3D US scanning to check for anomalies, none were found. Each bone was scanned down its length and across its width using both the 5-10 MHz probe and the 8-16 MHz probe. For the 5-10 MHz scans a depth setting of 30 mm and point of focus of 10 mm was used. For the 8-16 MHz scans a depth setting of 20 mm with a point of focus of 8 mm was used. The Rx and TGC controls were set before the first scans were recorded and these same settings were used for all scans throughout this investigation.

The protocol for the decalcification process was adapted from a study looking at the effects of decalcifying feline femurs (127). Test bones were decalcified to different degrees using 14% ethylene diaminetetra acetic acid (EDTA) with a pH of 7.4. They

were put in individual sample bottles containing 140 ml of EDTA solution (volume of EDTA approximately 20 times the volume of each bone sample) and placed in a shaker rack within an incubator set at 37ºC; the rack was set to shake at 150 rev/min to assist the decalcification process. Control bones were placed in identical sample bottles containing 140 ml of distilled water. Due to limited room in the incubator the control bones were kept in the cold room. Both the EDTA solution (and the distilled water) were changed every 24 hours to ensure the EDTA did not saturate.

Test samples were removed from the EDTA at periodic intervals to achieve different degrees of decalcification. Table 6-1 gives the period of decalcification for each test bone. When a test bone reached the end of its allotted decalcification time it was removed from the EDTA solution and the corresponding control bone was removed from its distilled water. Then, both the test and control bone underwent series of 3D US scans down the length (length scan) and across the width (width scan) of the bone sample using the same scan settings as previously. The phantom object was also scanned. After scanning, the bones were placed into sealed bags and refrigerated to maintain tissue preservation. The images from each test bone scan were analysed 5 times using the software to calculate the mean values of *Healing Index*.

Test Bone	Days of Decalcification
1	1
2	2
3	3
4	6
5	7
6	10
7	14
8	16
9	20
10	22

Table 6-1: Duration of decalcification for test bones.

6.4. Results

US images used to calculate the *Healing Index* were captured over the mid point of the bone sample for the length and width scans. Figure 6-2 shows the series of US images obtained with the 5-10 MHz probe that were used to calculate the *Healing Index* from the length and width scans of test bone 6. Decalcification was evident from the presence of the second bright surface echo from within the bone, indicated in figure 6-2(B) and (D). The first surface echo marked the boundary of the water – decalcified region of the bone, while the second reflection marked the decalcified – calcified bone boundary. In order to calculate the *Healing Index* a region of interest was selected on the test bone image incorporating the first surface echo and was compared to the region of interest on the control bone image that incorporated the single surface echo. These regions of interest are indicated by the boxes in figure 6-2. The regions of interest were rectangular in shape which meant that the regions selected were considerably smaller for the length images than for the width images to ensure only the surface echoes of interest were analysed.

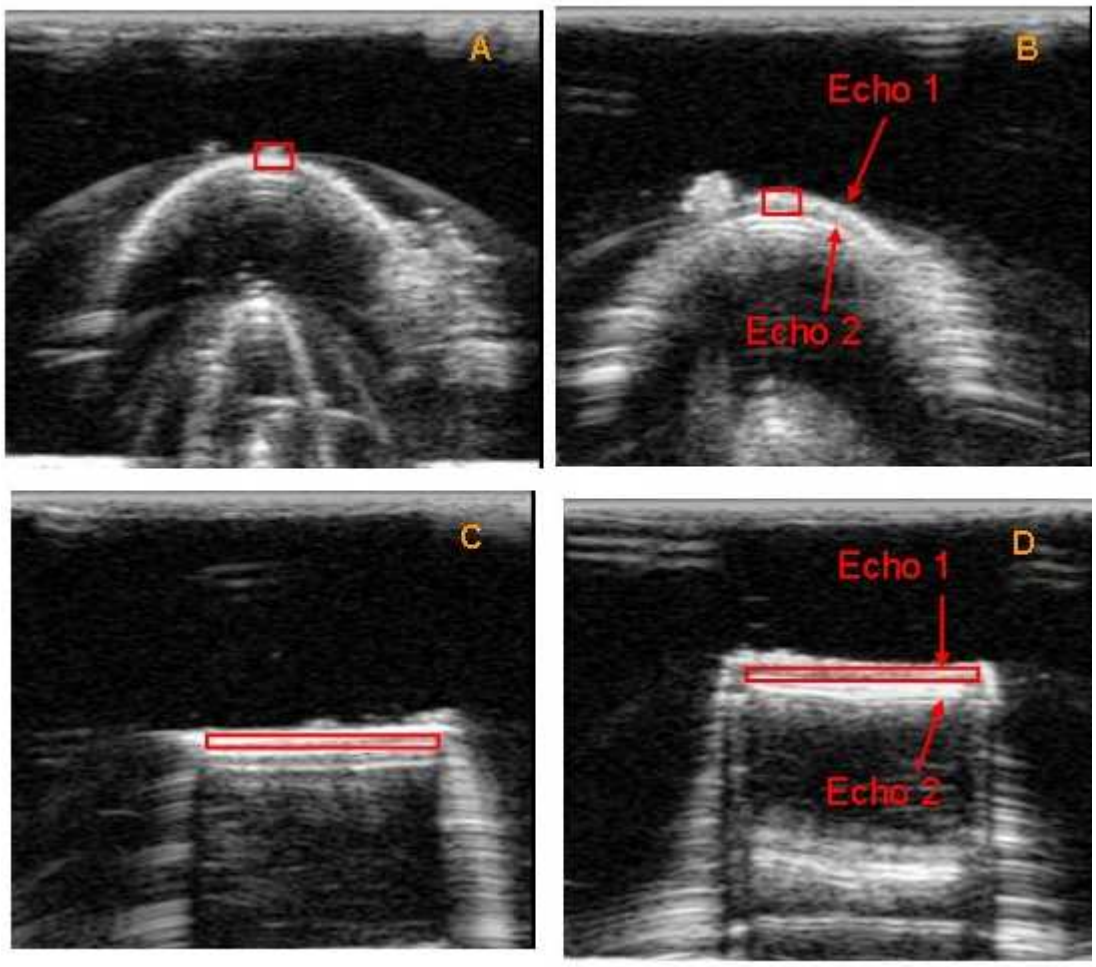

Figure 6-2: Ultrasound images taken from the 5-10 MHz scans of test bone 6 after 10 days of decalcification and the corresponding control bone images. The regions of interest used to calculate the *Healing Index* are indicated by the boxes. (A) Length scan image of control bone 6. (B) Length scan image of test bone 6. (C) Width scan image of control bone 6. (D) Width scan image of test bone 6.

The results for the mean *Healing Index* are given in tables 6-2 for the 5-10 MHz probe and table 6-3 for the 8-16 MHz probe. Data for the 8-16 MHz US scan of test bone 10 was corrupted and had to be omitted from the analysis.

		5-10 MHz Length Scan			5-10 MHz Width Scan		
Test Bone	Days of Decalcification	Healing Index (%)	SD	δ Healing Index	Healing Index (%)	SD	δ Healing Index
1	1	104.31	0.60	16.06	105.56	1.46	23.50
2	2	92.88	1.44	18.46	104.23	1.37	19.37
3	3	93.40	1.19	24.40	88.37	1.01	19.19
4	6	85.43	1.68	33.29	75.02	1.30	25.98
5	7	75.77	1.60	36.08	77.71	1.56	36.48
6	10	69.05	1.33	20.38	57.53	0.30	22.30
7	14	52.87	1.37	22.06	51.41	1.53	34.22
8	16	44.64	0.89	27.62	58.80	1.28	26.71
9	20	62.21	0.89	26.91	71.99	0.32	26.19
10	22	53.64	1.55	23.77	83.07	0.76	34.27

Table 6-2: *Healing Index* results for the length and width scans of the 10 test bones using the 5-10 MHz probe.

		8-16 MHz Length Scan			8-16 MHz Width Scan		
Test Bone	Days of Decalcification	Healing Index (%)	SD	δ Healing Index	Healing Index (%)	SD	δ Healing Index
1	1	89.02	0.39	17.59	94.12	0.34	14.68
2	2	94.41	1.86	21.50	79.33	0.34	19.60
3	3	80.12	1.00	21.83	92.54	1.13	20.29
4	6	67.06	1.15	16.67	80.13	0.97	19.52
5	7	54.06	1.10	19.66	57.61	1.26	17.85
6	10	65.68	0.69	15.29	59.31	0.41	20.55
7	14	48.26	0.40	22.05	34.24	0.64	13.31
8	16	56.14	0.51	12.44	59.62	0.93	14.64
9	20	73.79	0.74	14.95	71.74	1.41	20.00

Table 6-3: *Healing Index* results for the length and width scans of the 10 test bones using the 8-16 MHz probe.

Results for the length and width scans using the 5-10 MHz probe are plotted in figure 6-3 and results for the analysis of the 8-16 MHz scans are shown in figure 6-4. For both graphs *Healing Index* is plotted against days of decalcification to illustrate the rate of decalcification. It was expected that as the duration of decalcification increased the value of the *Healing Index* would decrease.

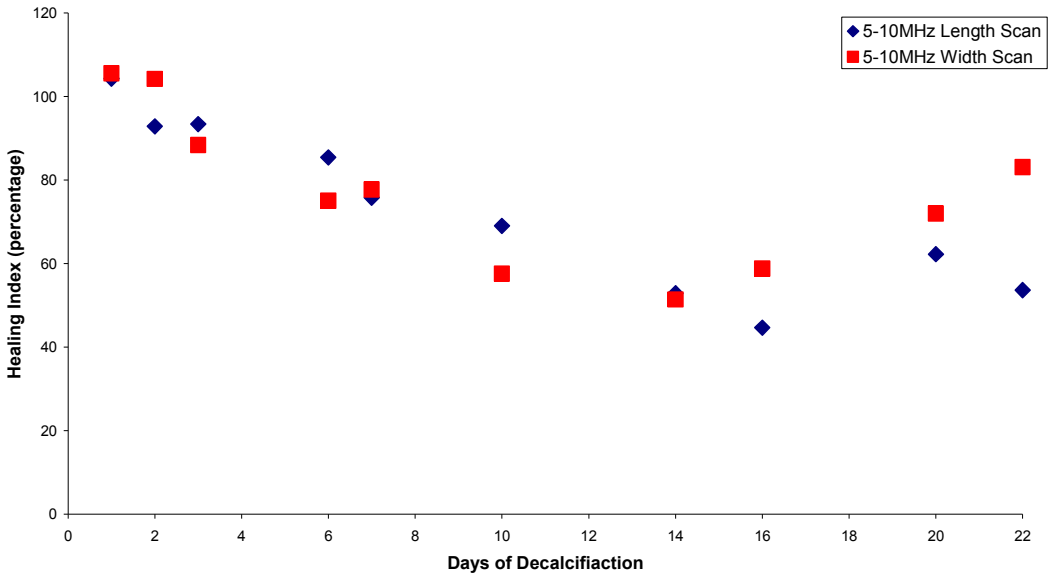

Figure 6-3: *Healing Index* results for Ultrasound scans of the test bone samples using the 5-10 MHz probe.

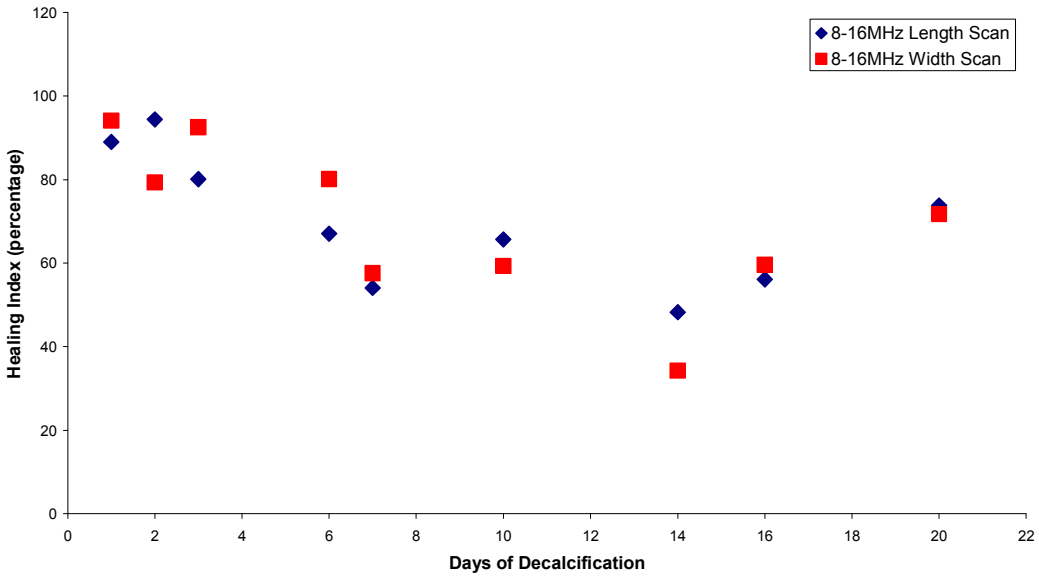

Figure 6-4: *Healing Index* results for Ultrasound scans of the test bone samples for the 8-16 MHz probe.

It was thought that the *Healing Index* would start at approximately 100% for test bone 1 and gradually decrease as the duration of decalcification increased. The rate of decalcification was expected to be approximately linear initially, before decreasing in rate as the calcium content of the bone became less. For the 5-10 MHz scans the expected trend in *Healing Index* was seen up to day 16 (test bone 8). The results for test bones 9 (20 days) and test bone 10 (22 days) were larger than predicted. A similar trend was seen in the *Healing Index* results for the 8-16 MHz US images. However, the decreasing trend in the *Healing Index* was only evident in test bones 1 through 7 (decalcification durations of 1-14 days). The *Healing Index* values for test bones 8 and 9 were larger than expected despite the increased duration of decalcification. Overall, both sets of results indicated that between 50 - 60% decalcification of the bone samples had been achieved.

An additional investigation was briefly carried out into the frequency dependent appearance of fracture callus using patient data from the clinical study (see Chapter 5). The aim was to determine if different frequencies of US could depict different densities of the fracture callus. As the B-scan images were captured in RF format it was possible to change the format in which they were displayed in *StradWin* by using a series of predefined image processing filters. *StradWin* contains a series of discrete frequency band filters which can be applied to the RF data in order to filter out data obtained at specific frequencies and thus show only the US image made up from chosen specific band of frequencies. For example, with the 5-10 MHz probe it was possible to apply filters to view the parts of the image from the frequencies bands of 5-6 MHz, 6-7 MHz, 7-8 MHz, 8-9 MHz and 9-10 MHz. To determine if there was a detectable frequency dependency in the appearance of the forming callus an US image of the callus was chosen in *StradWin* and the 9-10 MHz filter was applied, the resulting image was exported to Matlab. Similarly, the 5-6 MHz filter was also applied to the same image and the resulting image exported to Matlab. Subtracting the greyscale intensities of the 5-6 MHz image from the 9-10 MHz image on a pixel by pixel basis yielded no difference in the appearance of the callus material. This process was repeated using the data from the 8-16 MHz probe for the

frequency bands 15-16 MHz minus 8-9 MHz with similar results. It was concluded that there was not a sufficiently large difference in the frequency spectrum available within each individual probe to detect a difference in the appearance of the callus. Due to the difference in dimensions between the 5-10 MHz and 8-16 MHz images further work would be required to be able to compare filtered images over a wider range of frequencies.

6.5. Discussion

The experimental protocol was based on a decalcification experiment using the same concentration of EDTA solution to remove the calcium content from whole feline femur samples (127). For the feline femur samples to reach total decalcification took approximately 13 days. Although the sheep femur samples were smaller in volume they had a thicker bone cortex so in order to reach full decalcification the duration over which the bones were left in the EDTA solution was increased to 22 days. Despite this increase in duration the *Healing Index* results indicated that only around 50 - 60% decalcification was achieved.

The expected trend in results for the *Healing Index* was not observed for all the bone samples. Potential sources of error in the calculation of the *Healing Index* may have arisen due to the region of interest selected and background speckle in the US image. Being restricted to selecting rectangular regions of interest meant only a small area could be sampled on the length scan images due to the curvature of the bone. For the width scans, if the image of the bone was captured at an angle the area that could be sampled had to be reduced to avoid selecting parts of the image not related to the bone surface. This was the case for figure 6-2(D). To increase the accuracy of the regions of interest sampled it would be better to sample non-uniform regions that follow the contours of the bone surface echoes.

The effect of background speckle was a source of systematic error in this method and was evident from the large errors in the *Healing Index* values (δ *Healing Index*). These errors were not plotted on the graphs of results as they were not believed to be indicative of a problem with the calculated values. Instead, it was thought that they reflected the variation of the greyscale intensity of the pixels within the regions selected for comparison. Speckle is a result of random constructive and destructive interference of scattered US reflections giving rise to a wide range of greyscale intensities within the regions of interest selected (35). It was the mean greyscale within each region of interest that was compared and the error in the *Healing Index* was calculated using the percentage errors of the standard deviation against the mean greyscale for each region. Variation in the greyscale level between the background speckle and the bright echoes from the bone surface resulted in consistently high errors on the *Healing Index*. In comparison, the standard deviations on the mean values were small, almost all less than 2% indicating that the selection of the regions of interest for the *Healing Index* had good repeatability.

Only decalcification at the bone surface would have been detectable on US any decalcification on the inner bone surface would have been undetected as the region of non-decalcified bone between the two regions of decalcification would have stopped the US beam penetrating to the second region of decalcification. In this situation the measure of *Healing Index* would have been ineffective. In the case of fracture repair, regions of callus fill in the fracture gap and also extend as collars of bridging material from the bone ends. If it was possible to select non uniform regions of interest more detailed comparisons could be drawn between a volume of bridging callus and a volume of healthy bone. Comparing volumes of interest would remove one of the current limitations of the callus density measure, that only a single 2D US image of the callus is used give a value for the *Healing Index*. It would be unsuitable to take the analysis of one point in the callus as indicative of the strength of the whole callus. Also, it would be difficult to ensure that that same point was measured for future comparison. The selection of a volume of callus to compare with a volume of the patient's healthy bone would be the ideal as this would give a more accurate overview of the density of the whole callus.

7. Freehand Three-Dimensional Ultrasound for Determining Muscle Volume

7.1. Introduction

3D US offers a flexible and non invasive method of imaging the musculoskeletal system which has the added advantages of being portable and having few exclusion criteria for use. 3D US is less resource intensive than MR and can provide real time data. To establish whether 3D US can provide a comparable method to MR for determining muscle volume *in vivo* a healthy volunteer study was undertaken, whereby, volume measurements of a section of the rectus femoris muscle were derived from 3D US and compared to measurements obtained from MR.

7.2. Methods

The rectus femoris which is part of the quadriceps muscle group was chosen as the object of interest as its small size and superficial position at the anterior part of the thigh make it ideal for both MR and 3D US scanning. Eleven healthy volunteers (median age 79 years, range 24–85 years) were recruited to the study through informed consent. Approval for the study was granted by Lothian Research Ethics Committee and NHS Lothian Research and Development Management. The section of the rectus femoris measured was centred on the mid thigh as this point could be determined using anthropomorphic measurements by measuring the distance between the greater trochanter of the hip and the lateral joint line of the knee. The position was marked on the skin surface with a pen on each volunteer before MR and 3D US scanning. Both scans were carried out within a maximum of 14 days of each other.

During 3D US scanning participants sat on a patient examination table with the knee of the thigh to be scanned flexed at an angle of approximately 30°, as shown in figure 7-1. The exact angle of flexion of the knee was not recorded and may have varied by ±10° between subjects. Having the knee flexed in this way maximised the circumference of the thigh which could be scanned with 3D US without blocking the required line-of-sight between the tracking tool and the optical system. The 5-10 MHz probe was used to conduct all scans as it gave greater depth penetration providing a maximal view of the thigh tissue down to the surface of the femur. Being able to image the full depth of the thigh allowed comparable images to those of MR to be produced from the 3D US data.

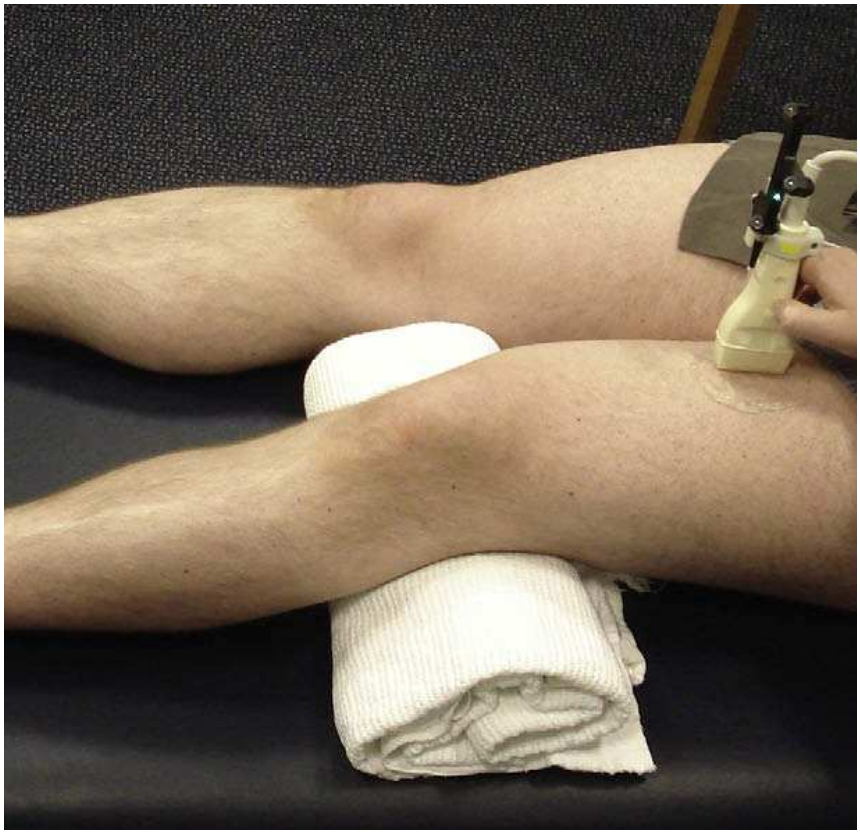

Figure 7-1: A healthy volunteer undergoing a 3D Ultrasound scan.

The point of focus and depth setting for the probe varied between participants dependent on the size of their thigh. For all subjects the depth setting was chosen so that the surface of the femur was visible and the point of focus was set at the level of the rectus femoris to give the best definition of the muscle boundaries. The anterior mid thigh region of the left leg was scanned. Starting at the medial posterior region the US probe was held parallel to the length of the thigh and scanned round the mid thigh in a single smooth sweep ending at the posterior lateral region. Figure 7-2 shows the outline of a scan superimposed on a *Reslice* image to demonstrate the scanning motion. It took approximately 3 minutes to position a subject and carry out a scan. All scans were carried out by the same operator.

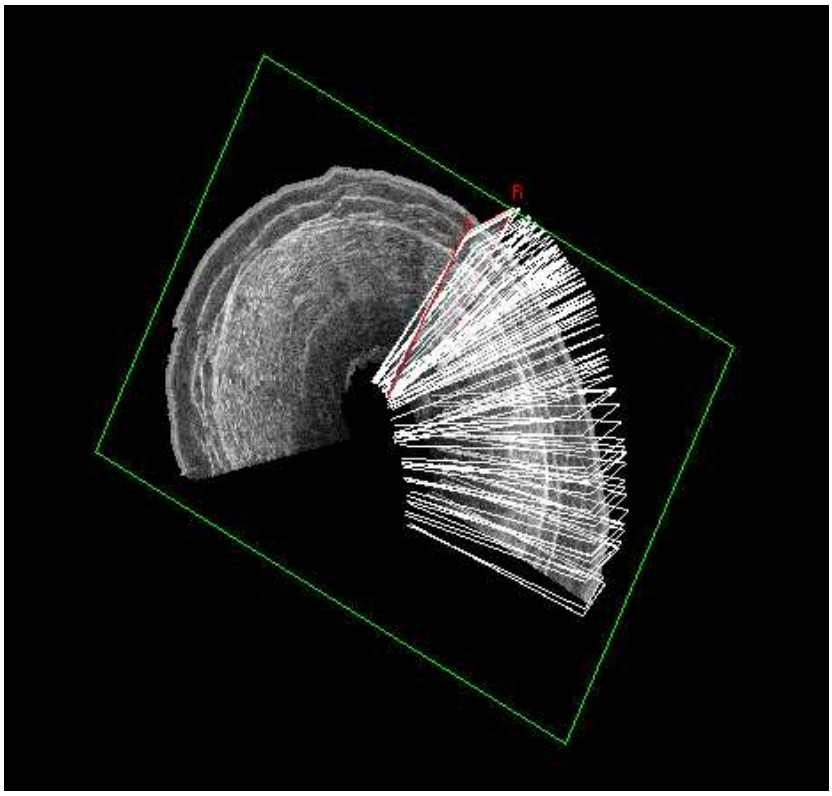

Figure 7-2: A *Reslice* image taken perpendicular to the length of the thigh with a partial scan outline overlaid to demonstrate the motion of the probe sweep around the anterior portion of the mid thigh.

The MR scans were recorded using a 1.5T scanner (Phillips Medical Systems, Edinburgh) using a T1 spin echo sequence with a 462 ms repetition time, 15 ms echo-time, one excitation, and with a resolution of 0.98 mm x 0.98 mm x 10 mm (128). Subjects lay supine on the examination table with their knees fully extended and relaxed. The MR scans were centred on the mid thigh point and imaged the whole length of the thigh. To assist in the identification of the mid thigh point a marker (cod liver oil capsule) which was visible on the MR images was placed at the measured mid thigh point. It took approximately 9 minutes to conduct the scan, this included the time taken to position the patient and carry out a 'scout' scan to centre data acquisition at the mid thigh level.

7.3. Analysis

The *Reslice* view in *StradWin* provided cross-sectional views through the 3D US dataset which were comparable to the MR images. The width of the US probe allowed a 37 mm wide section of the thigh to be imaged. However, the freehand nature of scanning meant that the operator was likely to deviate slightly from a completely straight sweep around the mid thigh. When taking into account these deviations the actual width of data centred on the mid thigh was closer to 30 mm.

In order to make volume measurements of the 30 mm section of the rectus femoris the 3D US data had to be exported as a voxel array orientated in the same direction as the MR image slices. The 3D US data was exported as a voxel grid where each voxel had dimensions of 0.1 mm x 0.1 mm x 1 mm. This provided a method of viewing the 3D US data as a series of 1mm thick image slices which were similar to those produced by MR. In comparison to the 3D US data, each MR slice had a thickness of 10 mm. Both the exported 3D US and MR data were analysed using the ANALYZE software package (Mayo Clinic, Rochester, USA).

Anatomical knowledge was used to locate the muscles of the quadriceps group and identify the boundaries of the rectus femoris muscle on the MR and 3D US images. The MR slice showing the mid point of the thigh was identified by the appearance of the marker in the image and the boundary of the rectus femoris muscle was segmented by hand in the three images centred on this slice. This allowed a volume measurement to be obtained for a 30 mm section of the muscle. For the 3D US data the boundary of the rectus femoris muscle was segmented by hand on thirty images centred around the mid thigh point. Once the segmentation was complete the volume of the region highlighted on each slice was summed to give the total volume for the section of muscle.

Analysis of the MR and 3D US data was carried out by two separate raters to allow intra and inter-operator repeatability to be assessed. Segmentation of the data was done without conference between the raters and the MR data was not used as a guide for muscle boundary identification on the 3D US images. A paired t-test was used to check for inter and intra-rater differences in the segmentation and thus volume measurements obtained from the scan data of both modalities (129). The mean difference between volume measurements derived using MR and 3D US were also calculated.

7.4. Results

Identification of the boundaries of the rectus femoris muscle was easier on the MR images than on 3D US. Figures 7-3 and 7-4 show the segmentation of the rectus femoris muscle on the MR and 3D US data respectively. Segmentation of the MR data took approximately 10 minutes, whilst segmentation of the 3D US data took approximately 20 minutes due to the greater number of slices to be analysed and the difficulty in identifying some of the muscle boundaries. The muscle volume measurements derived from the MR and 3D US data for all eleven participants are presented in table 7-1.

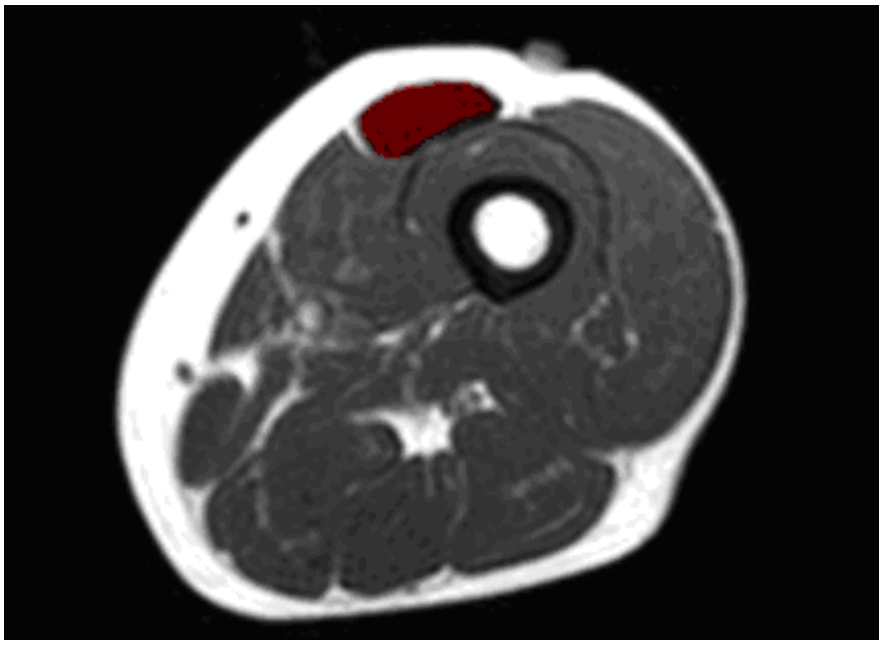

Figure 7-3: Segmentation of the rectus femoris muscle on an MR image slice.

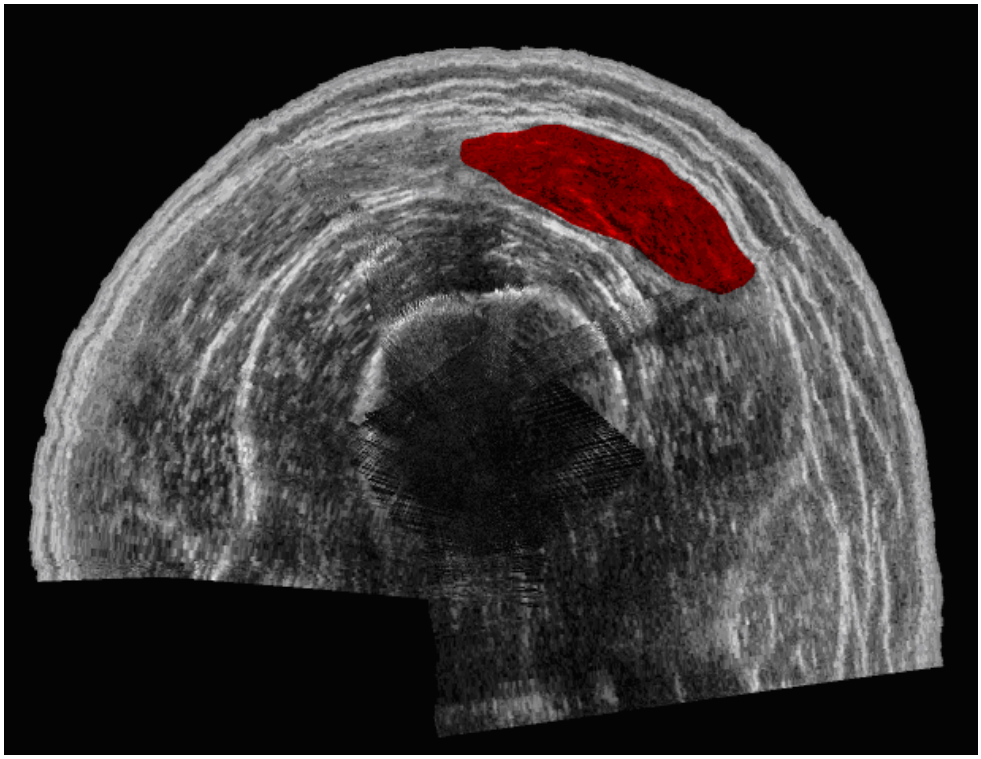

Figure 7-4: Segmentation of the rectus femoris muscle on a 3D US image.

	MR			3D Ultrasound				
	Scan 1			Scan 1			Scan 2	
	Rater a		Rater b	Rater a		Rater b	Rater a	Rater b
Participant	1st	2nd	1st	1st	2nd	1st	1st	1st
1	5.25	5	5.16	5.06	4.49	4.5	*	*
2	28.8	28.4	27.79	26.21	27.02	24.04	*	*
3	8.08	8.36	8.35	7.76	7.97	7.85	*	*
4	22.5	23.4	22.57	20.74	20.14	22.6	*	*
5	10.1	9.47	9.39	10.18	10.57	11.28	9.19	9.1
6	12.3	12	11.25	12.16	11.25	10.95	11.58	10.7
7	6.6	7.02	6.46	6.01	5.8	6.9	5.89	6.46
8	4.61	4.73	5.07	4.5	4.05	6.43	4.3	5.29
9	12.6	12.8	12.89	10.7	10.89	11.26	10.23	11.77
10	12.4	12.3	11.99	12.97	13.07	12.24	9.98	10.69
11	13.6	14.1	14.62	14.59	15.19	14.3	13.82	14.11

Table 7-1:Results of volume measurements for a 30mm long section of the rectus femoris muscle derived from MR and 3D Ultrasound data analysed by two different raters. All measurements are in cm^3

The mean difference between volume measurements derived from 3D US and MR was 0.53 cm^3 with a standard deviation (SD) of 1.09 cm^3 and 95% confidence intervals (CI) of -1.61 – 2.67 $cm^3$for rater *a*. A paired t-test was used to assess whether there was evidence of a significant difference between the two imaging techniques. This returned a value of p=0.14 indicating there was no evidence of significant difference between techniques. For rater *b* the mean difference between volume measurements derived from MR and 3D US was 0.29(1.50) cm^3, with 95% CI of -2.64 – 3.23 cm^3, returning p=0.53. The Bland-Altman plots in figures 7-5 and 7-6 show agreement between MR and 3D US volume measurements for rater *a* and rater *b* respectively. For both raters the difference in volume measurements between MR and 3D US were within ±3.75 cm^3.

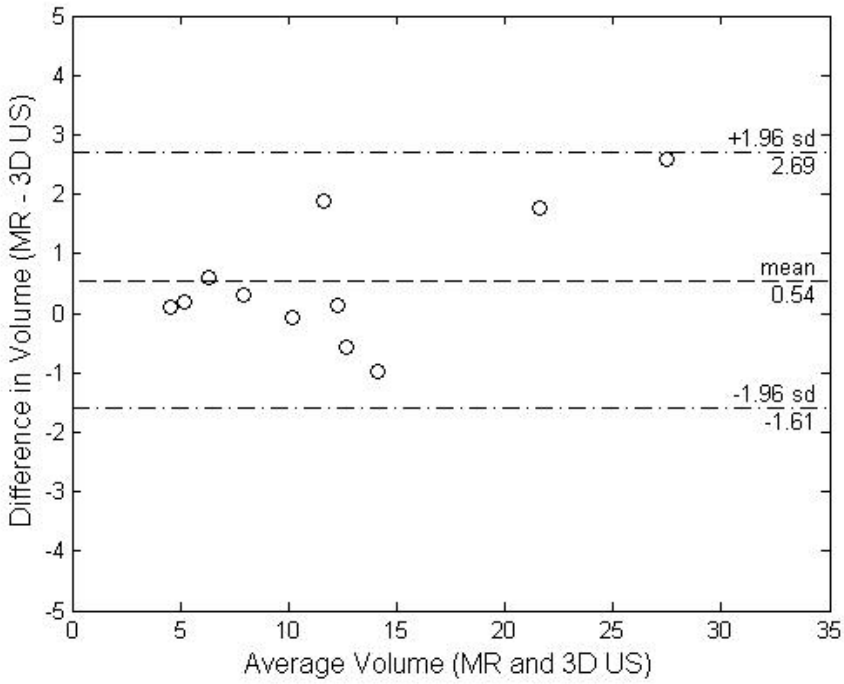

Figure 7-5: Bland-Altman plot showing the agreement between MR and 3D US derived volume measurements for rater a.

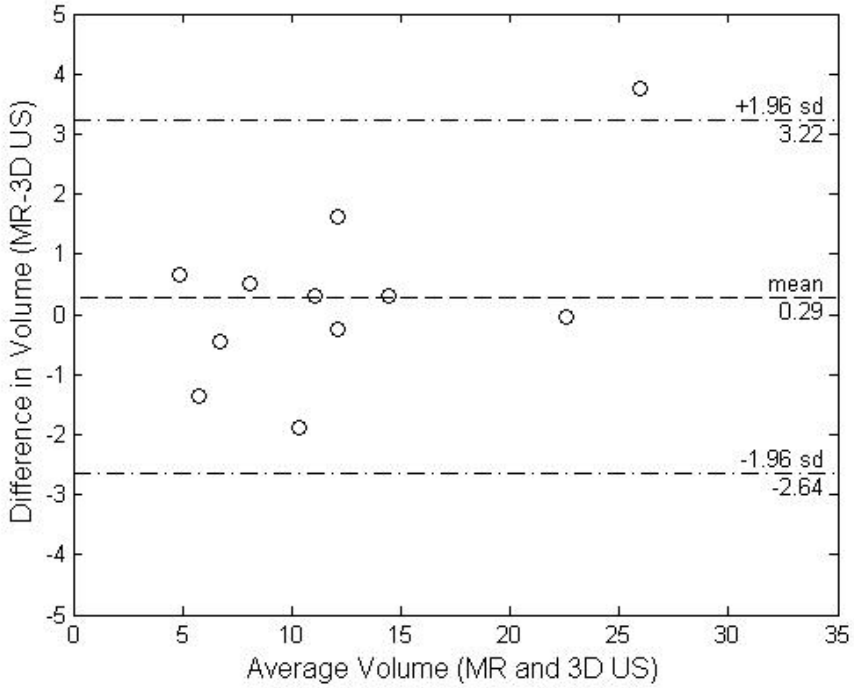

Figure 7-6: Bland-Altman plot showing the agreement between MR and 3D US derived volume measurements for rater b.

Analysis was carried out twice by rater *a* for both the MR and 3D US data to assess repeatability of the segmentation process. A paired t-test was used to assess the intra-rater difference between repeated measurements. The mean difference between repeated volume measurements from MR was -0.07(0.47) cm^3 (95% CI -0.99 – 0.83 cm^3), p=0.65. For the repeated 3D US segmentation the mean difference in volume measurements was 0.04(0.55) cm^3, (95% CI -1.04 – 1.12 cm^3) p = 0.84. Both p values showed there were no significant differences between repeated segmentations.

The inter-rater difference for the segmentation of the same set of 3D US scans gave a mean difference of -0.13(1.28) cm^3 (95% CI -2.64 – 2.38 cm^3) with p = 0.74. For MR the mean inter-rater difference for the segmentation of the same image data was 0.101(0.64) cm^3 (95% CI -1.15 – 1.36 cm^3) where p = 0.59.

For 7 of the participants a second set of 3D US scans were obtained to check repeatability of scanning. These scans were analysed by both raters and compared to the corresponding data from the original scans. For rater *a* the mean difference in volume measurements between repeated scans was 0.87(0.98) cm^3 with CI of -1.05 – 2.79 cm^3. For rater *b* the mean difference in volume measurements between repeated scans was 0.75(0.92) cm^3 with CI of -1.05 – 2.55 cm^3.

7.5. Discussion

Muscle volume measurements derived from the 3D US data were within ±16% of those derived from MR with 95% confidence intervals of ±2.14 cm^3. The differences in muscle volumes between participants varied from approximately 4.50 cm^3 to just over 28.5 cm^3, but, there was no visible trend in the size of a participants muscle compared to the volume difference found between modalities. Identification of the muscle boundaries was the biggest factor influencing the muscle volume measurements. As seen from figures 7-3 and 7-4 the muscle boundaries were easier to identify on MR than US. On the US image slices it was often the case that three

of the four muscle boundaries were reasonably easy to identify, however, the fourth boundary was difficult to depict and open to interpretation by both raters. Figure 7-7 shows a 3D US image slice from one of the participants, the muscle boundaries for the rectus femoris, identified by the two different raters, have been highlighted.

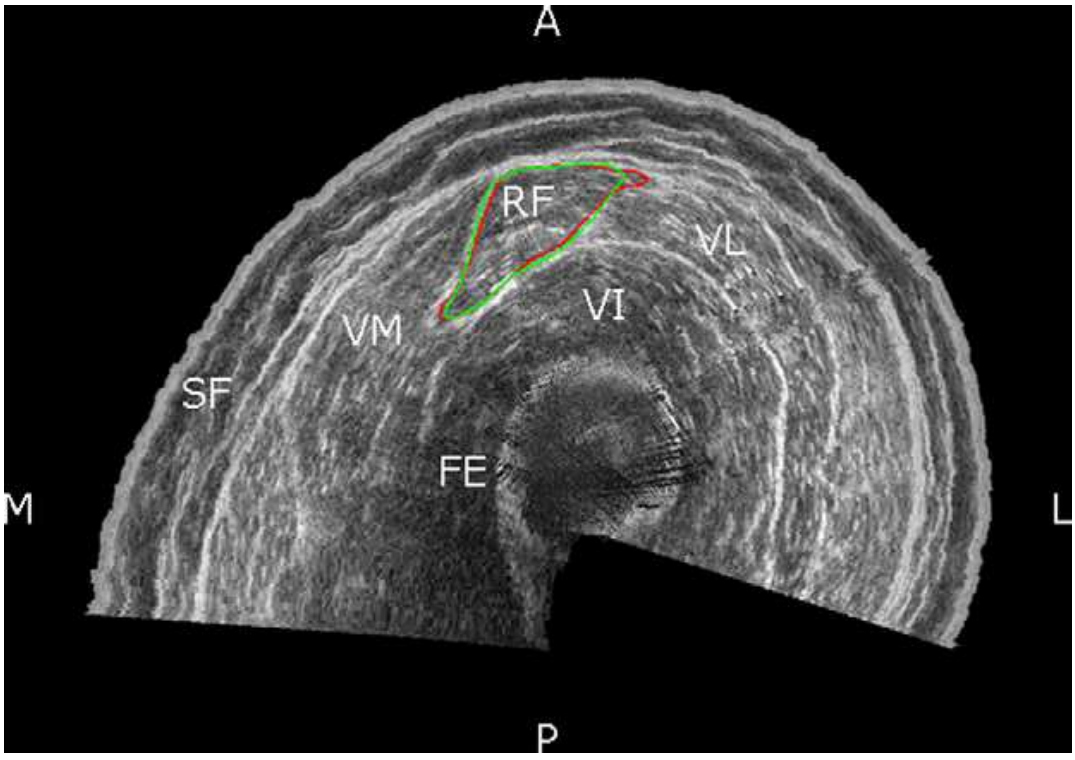

Figure 7-7: 3D Ultrasound image slice with the main features of interest labelled. (SF) subcutaneous fat. (VM) vastus medialis. (FE) femur. (VL) vastus lateralis. (VI) vastus intermedius. (RF) rectus femoris. The muscle boundaries of the RF muscle identified by the two raters are highlighted in red and green. (A) anterior, (P) posterior, (M) medial and (L) lateral.

The quality of the images obtained from the Diasus effected muscle boundary identification and this was further compounded when the data had to be put into a voxel array to be imported into ANALYZE. This additional image processing step caused a small but visible degradation of the US data. The Diasus was approximately 10 years old and a newer machine is likely to provide better image quality which would make identification of muscle boundaries easier. For comparison, figure 7-8 shows a pair of 2D US image of the rectus femoris muscle

captured using the Diasus and also a modern SONIX RP US machine (Ultrasonix, Richmond, Canada). The improvement in image quality with the SONIX RP is visible with all the boundaries of the rectus femoris muscle being easier to identify.

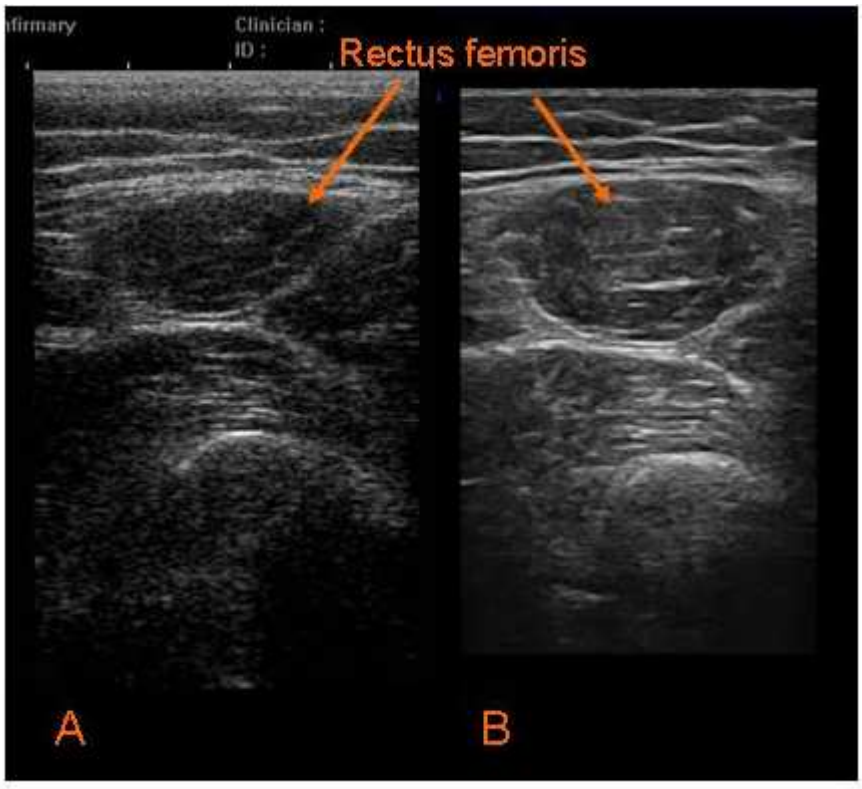

Figure 7-8: 2D Ultrasound image of the rectus femoris muscle captured just below the mid thigh point using (A) the Diasus and (B) the SONIX RP US machines.

The width of the images slices and size of the voxels in the image arrays will also have influenced the differences in volume measurements between MR and 3D US. The MR slices have a thickness of 10 mm and the size of the voxels allowed volume measurements to be made to within 0.01 cm^3. In comparison the thickness of the US slices were 1 mm and the voxel resolution allowed volume measurements to be made to within 0.01 mm^3. Therefore it was expected that the MR data would slightly overestimate the actual muscle volume. When comparing the MR and 3D US results for rater *a* in eight out of eleven cases the 3D US volumes were less than the MR volume measurements and for rater *b* it was six out of eleven cases.

A further factor affecting the volume of the muscle was the positioning of the volunteer. During the MR scan the knee was extended, whilst, during 3D US scanning the knee was flexed. As rectus femoris is a hip flexor and knee extensor muscle this difference in positioning of the participants will have had an effect on the volume of the muscle at the mid thigh point. If the whole muscle volume could have been measured then this would not have been a factor.

During the course of this investigation a study reported the use of a 3D US system, using the *StradX* software and a Flock of Birds EM tracking system, to determine muscle volumes in canines (130). 3D US was compared to MR and the mean difference between volume measurements was 3.33(4.37) cm^3 (CI -5.24-17.14 cm^3). The muscle volumes were obtained from isolated cadaver dog muscle samples scanned in a water bath. Multiple sweeps of the muscles were obtained during 3D US scanning in order to image the whole muscle rather than a short section. As the muscles were isolated identification of boundaries would not have been an issue. The accuracy of the 3D US measurements were noted as having a dependency on scanning speed, the rate at which the US frames were acquired and how frequently the object of interest was segmented within the 3D dataset. The use of the less precise EM tracking system was likely to be a source of error for the 3D US volume measurements that may have been further compounded by using multiple sweep scanning.

The optical freehand 3D US system could improve on the results of previous studies using 2D US to obtain muscle CSA and volume measurements. In the study by Reeves et al. a series of overlapping 2D US slices were captured to give a panoramic image of the quadriceps muscles which was used to measure CSA (15). The series of images were built into a panorama using a contour matching algorithm. Although the results were in good agreement with those determined from MR, within ±1.7%, the US scan time was 20 minutes compared to 6 minutes for MR. Using the 3D US system a panoramic image of the thigh could be capture in less than 5 minutes, including the time taken to position the patient. The use of 3D US would also reduce

the scan times for the study by Esformes et al. where a series of 2D US images obtained at regular intervals along the muscle belly of the tibialis anterior were used to calculate its volume (73). Scan times for 2D US were 45 minutes compared to 20 minutes for MR. The accurate volume measurements provided by the optical freehand 3D US system would also have improve upon the truncated cone approximations used to obtain the volume of the tibialis anterior muscle.

This study aimed to show 3D US is suitable for measuring muscle volumes *in vivo*. Results indicated 3D US to be able to obtain volume measurements which are comparable to MR. Although a difference between MR and 3D US of up to 16% was found it is expected that with a modern scanner and standardisation of participant positioning the mean difference would be reduced. The smaller voxel size and thinner image slices for 3D US images mean more precise volume measurements can be obtained and smaller changes in volume may be detectable. Use of the multiple sweep scanning function would allow whole muscle volumes to be captured. The 3D US system was less expensive than MR, had fewer exclusion criteria for patient scanning and provided real time data. The portability of the 3D US system would allow it to be brought into clinics or to the patient bedside as required.

8. Conclusions and Future Research

Freehand 3D US was investigated as a method of imaging the musculoskeletal system that could overcome limitations of other modalities and provide an accessible, easy to use tool for both clinical and research use. It was hypothesised that freehand 3D US could provide an alternative method to X-ray for monitoring fracture repair and also a flexible and non invasive means of obtaining accurate muscle volume measurements *in vivo*.

The systematic evaluation of two potential 3D US systems showed that the optically tracked system was the most suitable for musculoskeletal imaging. This system could reliably produce 3D datasets that were detailed and accurate. The 3D models and *Reslice* images obtained from the datasets aided interpretation of the state of healing when monitoring fracture repair. Accurate length measurements from scans allowed the changing width of the fracture gap to be measured during limb lengthening and this information was used to determine if the correct rate of distraction was applied. Novel image analysis was applied to the data captured in RF format to develop a callus density measure as well as investigate the frequency dependent appearance of fracture callus. The extended field of view images that the *Reslice* tool in *StradWin* provided were comparable to those produced during an MR scan and allowed comparable measurements of muscle volume to be made between the two modalities. Pilot studies using the optical freehand 3D US system to investigate both fracture healing and measure muscle volumes *in vivo* showed promising results.

8.1.1. Freehand Systems

2D US imaging was introduced in Chapter 2 to highlight its abilities and limitations as an imaging technique. The literature demonstrated that it had been used for a

variety of musculoskeletal imaging applications, however, operator dependency and approximations used for volume measurements meant other modalities were often favoured. The development of 3D US was covered in Chapter 3 showing how this new technique had improved upon the abilities of 2D US. The volume datasets it could provide reduced operator dependency in scan interpretation and allowed accurate length and volume measurements to be returned. Furthermore, 3D US provided the operator with additional tools for visualisation which in some cases gave views of the anatomy which would not be available with 2D US or X-ray but would require the use of MR or CT.

EM tracking offered the greatest flexibility for probe motion allowing the operator to scan the full circumference of a limb unhindered as was desirable for the intended clinical applications. A healthy volunteer study demonstrated the potential of 3D US for musculoskeletal imaging. The additional views, 3D models and length and volume measurements gave a more comprehensive means of assessing the musculoskeletal system than X-ray and in a more affordable way than MR. However, EM tracking was susceptible to other EM fields and ferromagnetic objects within or near the tracking field which made it unsuitable for the intended clinical applications. An alternative optically tracked system was sought. This provided greater positional accuracy than the EM system and was not affected by the presence of metal objects or other EM fields.

The Optical 3D US system provided an accurate and reliable means of conducting 3D US scans. The use of calibration templates that could be created in *StradWin*, allowed quick changes to be made between scan settings and US probes reducing setup times. A slow steady scanning rate used in conjunction with a frame rate of 20 fps or above was found to produce detailed datasets from which to build 3D models and make measurements and also minimised the error on separation measurements. For the calibration templates created separation measurements could be made to within a maximum error of ±0.25 mm. The Optical 3D US system was deemed suitable for use for the proposed clinical applications.

8.1.2. Fracture Repair

In Chapter 2 the fracture repair process was covered in detail introducing the limitations of using X-ray to monitor the fracture repair process. 2D US was found to be able to identify signs of healing and also the occurrence of complications before they became visible on X-ray. However, the operator dependency limitations of 2D US meant it was never adopted as a suitable alternative to X-ray. Freehand 3D US offered a comprehensive means of imaging the fracture repair process and this was trialled in Chapter 5. 3D US scanning was tolerated well by all patients. The fibrous material deposited within the fracture gap during the early stages of healing was visible using 3D US and a notable lag was detected between the amount of callus visible on X-ray compared to 3D US. The first signs of healing could be detected at approximately 2-6 weeks whereas on X-ray it was 6-19 weeks.

The 3D models and *Reslice* images allowed for easier interpretation of the shape of the fracture and developing callus as well as aided in the identification of complications. In comparison, the projection nature of X-ray meant the shape of the fracture was not always clear and it was difficult to interpret at what depth callus was forming. The change in greyscale intensity of the callus material on 3D US indicated that it was maturing and returning to a similar state as normal bone. When monitoring limb lengthening this became a limitation, the periosteal callus forming on the edges of the fracture obscured the original bone ends making it difficult to determine the rate of distraction. The use of metal marker beads which would be visible on US, placed at the edge of the osteotomy gap, was suggested to overcome this problem.

8.1.3. Callus Density Measure

Acquiring the US images in RF format rather than as processed B-scan images allowed novel image processing to be applied to the image data to try and extract additional information relating to bone density. This was covered in Chapter 6. The

Healing Index was developed as a comparative measure of the density of fracture callus compared to healthy bone on a patient specific level. The aim was to provide a means of determining when a fracture was sufficiently healed to safely allow weight bearing or removal or a fixation device without risk of re-fracture. Studies looking at the use of radiological measures and physical assessment of fracture callus strength found no agreed or validated standard. A pre-clinical trial of the *Healing Index* using sections of decalcified sheep femur showed initial promise. It was only in the later stages of the decalcification process that unexpectedly high values of the *Healing Index* were returned. It is likely these anomalous results were a product of the limited regions of interest that could be sampled as well as the variation in background speckle in the images. The effects of background speckle are a systemic limitation for the analysis of US images, however, fracture callus has a more uniform greyscale appearance than the experimentally decalcified bone so should be a lesser source of error in a clinical situation. To make the *Healing Index* applicable to patient data would require further development of the analysis technique to look at volumes of interest instead of the 2D rectangular regions which currently limit this method. Comparison of a volume of bridging callus to a volume of healthy bone would provide a more comprehensive measure of fracture callus density and a better indication of the progression of healing.

8.1.4. Muscle Volume

The need for a for an accurate, cost effective means of measuring skeletal muscle volumes *in vivo* was outlined in Chapter 2. 3D US was proposed as a suitable alternative as it could provide accurate volume measurements and image data can be viewed in a similar slice format to that of MR. The healthy volunteer study presented in Chapter 7 compared the use of MR to 3D US. The Optical freehand 3D US system was found to provide a non invasive means of measuring muscle volumes *in vivo* that was less resource intensive than MR. The current 3D US system and scanning technique provided volume measurements within ±16% of MR derived volumes. A new US machine and standardisation of patient positioning would be

required in order to improve on current results. In addition, the inclusion of the multiple sweep function into *StradWin* will now make it possible to compare whole muscle volumes. Further studies into the use of 3D US for measuring muscle volume are warranted.

8.2. Future Research

The line-of-sight restriction when using an optical tracking system limited the circumference around the limb that could be scanned. Further to this the limited mobility of some of the fracture patients also made it difficult to maintain the required line-of-sight between the tracking tool and position sensor unit. Work is being carried out by the MIG at Cambrigde to develop sensorless 3D US scanning by extracting positional data from features in the recorded US images (131). The use of fibre optics has also been discussed but this idea is in its infancy. A simple interim solution would be to look at the possibility of combining two or more Polaris sensor units and positioning these around the scanning region to allow the probe to be tracked at all times.

The fracture study showed proof of concept but a further more comprehensive trial now needs to be carried out following up greater numbers of both fracture and limb lengthening patients. It would be recommended that fracture patients be followed up at 2 weekly intervals for the first 8 weeks then at 3 months and 6 months. For limb lengthening patients follow-up should be fortnightly whilst lengthening is underway.

The callus density measure requires development in order to apply it to patient data. The rectangular regions of interest that could be selected made it impractical to apply the *Healing Index* calculation to patient data. Investigation is required into changing the regions of interest selected into volumes which can follow the contours of the callus and normal bone.

Finally, a new US machine would enable further studies using 3D US for measuring muscle volume to determine if more accurate results can be obtained. Use of multiple sweep scanning would remove the need for standardisation of patient positioning between the MR and 3D US scan. If these trials are positive 3D US should be compared to MR for measuring changes in muscle volume over a period of time due to a predetermined cause such as a set physical training regime.

Appendix A

The StradX Calibration Procedure

Temporal calibration is carried out by holding the US probe steady in the water bath near to and perpendicular to its bottom. The probe is then moved swiftly upwards to cause a significant change in both the image content and the position reading measurement. The probe must be jerked upwards at least 5 cm within a time period of 100 ms in order for the motion to be registered by *StradX*. The change in position of the line showing the bottom of the water bath and the change in the position reading for the probe are used to calculate the temporal offset between the images and positions This process should be repeated 5 times to give an averaged calibration result.

The temperature of the water in the water bath during calibration should be 48°C as this will match the average speed of US in soft tissue (1540 m/s) and is also the speed of the US pulse generated by the Diasus US machines. However, at room temperature the 48°C temperature of the water bath will cool quickly and this can cause errors in the calibration process. This can be avoided by using a 9% glycerol solution which has a propagation speed of US of 1540 m/s.

The *Spatial* calibration used in *StradX* is the single-walled method which requires a simple flat surface phantom immersed within the water bath. A set of calibration movements have been devised to ensure a sufficient range of motion of the probe is sampled for accurate calibration. Figure A shows the required probe movement (119).

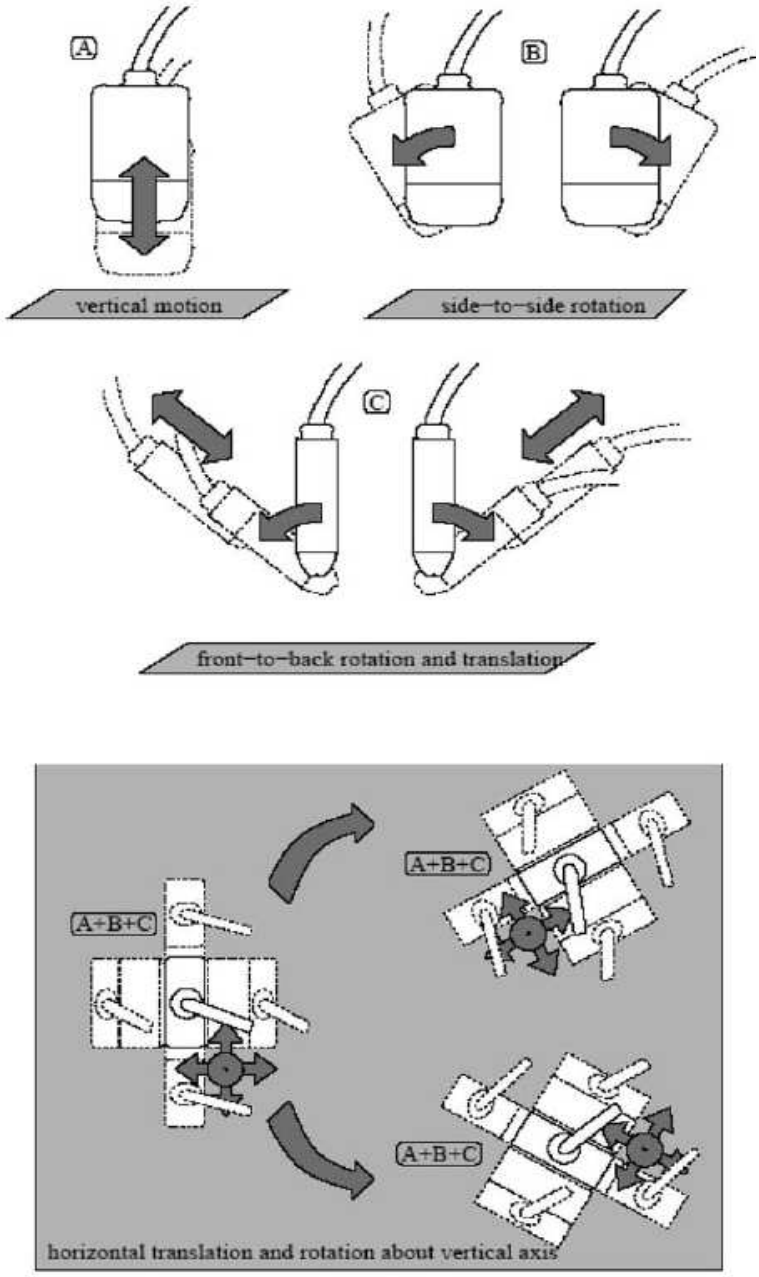

Figure A: Probe movements carried out during *Spatial* calibration. This is necessary to define both the *Spatial* calibration parameters and the location of the calibration plane (Treece, Gee et al. 2003).

The flat surface is scanned in order to obtain a series of US images that contain a single straight line. The Random Sample Consensus (RANSAC) algorithm can then be applied to the calibration images to extract information about the position of the line in each B-scan images. If a line cannot be detected by the RANSAC algorithm

due to weak image intensity or image artefacts that B-scan will be rejected by the algorithm and will play no further part in the calibration. A set of calibration parameters are then applied to the co-ordinates of several points on each line extracted from each B-scan in order to transform the lines from the co-ordinate system of the B-scan image into the real world co-ordinate system. The complete set of transformed lines should form a flat plane in real world space if the calibration parameters are correct.

The series of calibration images should be reviewed at this point to check that the positioning of the automatically detected line matches the actual position of the line in each image. This verifies that the automatic accept/reject decisions of the line detection algorithm were correct, the outcome of each decision is displayed below each image as it is reviewed in the *Spatial* calibration window. If an image has been incorrectly accepted or rejected by the algorithm the user can force the system to reject or accept the image as appropriate. The calibration solution algorithm is then applied to optimise the calibration parameters determined from the RANSAC algorithm. The residual root mean square (RMS) error from this iterative process is provided at the end of the calibration and the size of the error provides a guide as to the quality of the calibration carried out (132). An RMS error of less than 0.1 cm is deemed to be acceptable; an RMS error of less than 0.06 cm is desirable.

Verification of the quality of the calibration can also be visually assessed using the *Verify* toggle button within the *Spatial* calibration window. *Verify* mode displays a line representing the intersection of the calibrated plane superimposed on each B-scan as it is reviewed. This superimposed line should ideally match up with the position of the line showing the surface of the phantom plane. The relative position of the two lines should be checked on each image to ensure they do not vary by more than a few millimetres, this is indicative of a reliable calibration; otherwise the calibration should be carried out again.

Appendix B

The StradWin Calibration Procedure

Certain system configuration parameters must be set within *StradWin* and on the US machine before calibration can be carried out. The required depth setting and point of focus for the US probe must be first set on the US machine before initiating the live image display within *StradWin*. Live display allows the US images to be viewed as they are recorded and is displayed alongside another window that shows the position of the tracking tool within the measurement volume during scanning. The outline of the measurement volume changes colour dependent on the state of the tracking tool. If it is green the tool is within the volume, if it is yellow the tracking tool is approaching the edge of the volume and if it is red it is outside the volume or the line-of-sight between the tool and position sensor unit has been blocked.

With both live images and position tracking available the *Record* task page should be selected. Both the image source and position source configuration details should be checked to ensure they are correct for the US probe, depth and point of focus settings being used. Most of the image source configuration settings remain as default; the source of the image data should have been automatically detected. The auto image cropping function will set the height, width and offsets for the US image being recorded or they can be set manually. For RF image capture the RF image parameters need to be set, specifically the type of US probe to be used and RF signal sampling rate must be selected. Finally, the number of focal points and the position of the first focal point for the US beam must be selected. Position source configuration should automatically be detected when *StradWin* starts, however, if this has not happened details can be selected in the position source configuration menu.

On the *Record* task page the frame acquisition rate should be set to full speed and the image format should be set to Greyscale. Finally, the data format must be selected, RF or B-scan. Saving the image data in RF format gives far greater flexibility for post scan processing and analysis of US data.

Calibration is initiated on the *Probe Calib* task page. The first part of the calibration process requires the user to input the temperature of the water in the water bath. Room temperature water should be used for calibration as this avoids any change in temperature during the process which will affect the result. Previously in *StradX* water of 48°C was recommended for calibration as the speed of US in water this temperature matched the speed of sound of the US pulse produced by the Diasus. However, a new algorithm has been incorporated into *StradWin* which compensates for the affects of using lower temperature water during calibration.

Final adjustments should now be made to the US image using the Tx (Transmit gain), Rx (Received gain) and the TGC (Time Gain Compensation) controls on the US machine. The appearance of the surface of the single walled phantom, which appears as a line on the B-scan images, should be set so that it is barely visible. This helps to remove repeated surface artefacts from the image and aids the line detection process

The dimensions of the pixels which make up the US image must be determined by measuring the width and height of the image. In version 3.2 of *StradWin* and earlier only one measurement across the width of the image was made under the assumption that all US machines used square pixels. However, it has since been found that there are some US machines that use rectangular pixels in their displays and that this would affect calibration accuracy. A good image of the bottom of the water bath should be obtained and then frozen using the US machine controls this will causes the image on *StradWin* to also freeze. The measurement callipers on the US machine are used to determine the width of the image. Keeping the image frozen the image width must be measured across the same point in *StradWin* using a further set of callipers A set slider control is used to set the width of the line in *StradWin* using the

measurement obtained from the US machine callipers. This process is repeated to measure height on the US image before the image display is unfrozen. This procedure is slightly different for curvilinear probes.

The next stage in the calibration process is to collect a series of images of the phantom in the water bath that will be used in the calibration algorithm. The probe should be moved through the pre-defined set of motions shown previously in figure A for the *StradX* calibration procedure. When the probe is moved into one of the calibration positions, a good image of the bottom of the water bath should be obtained and the line detector shown on the *StradWin* live image should be checked to ensure it is correctly locked on to the line before the image is accepted for use in calibration. If the line detector is having difficulty locking onto the line a message stating 'No valid Line' will be shown. At least 40 lines should be captured using the full range or probe positions in order to give a reliable calibration. Once a set of lines has been collected, click the 'Solve for *Spatial* calibration' button to run the calibration algorithm. This algorithm uses the position information extracted from the lines to determine the co-ordinate transforms between the US probe, tracking system and the real world system. A good calibration should return an RMS error of less than 0.1 cm (109). Details of the depth setting and probe frequency need to be input before the calibration is accepted for scanning. At this point the calibration can be saved as a template to be reloaded for use at any future date. Before saving the calibration as a template ensure that the desired frame rate data format are selected on the *Record* task page.

Verification of the calibration can be carried out using a tracked pointer. The optically tracked pointer is one of the tools included with the Polaris optical system. Polaris can track two different tools simultaneously and the positions of both tools are displayed within the tracked volume. The pointer must be calibrated before verification can be carried out. The pointer tool has a small sphere at its point, to calibrate the pointer this small sphere should be kept steady in one spot or ideally the point should be located in a small hemispherical dimple to limit movement. The tracked pointer should be moved through as many degrees of freedom as is possible

over an interval of around ten seconds. With the pointer calibrated; it can be positioned within the US beam so it appears in the live image.

If the calibration of the US probe and the tracked pointer are consistent a green dot with a circle, which varies in diameter, appears around the image of the pointer tip on the US image. As the pointer is moved in and out of the US beam the green circle will decrease and increase in size. It should be smallest when the pointer reaches the mid point of the US beam, i.e. the pointer tip is brightest in appearance. If this is the case the pointer and probe are consistently calibrated and the probe calibration is reliable. The pointer check should be performed in a number of locations within the US image not just at the centre. Calibration templates can be keep long term, however, they must be periodically checked using pointer verification to ensure they are still consistent and accurate.

Appendix C

Calibration Templates

Thirty calibration templates have been created for this project, fifteen for the 5-10 MHz probe and fifteen for the 8-16 MHz probe. Tables A and B contain details of each template. The RMS errors obtained when carrying out the calibrations to create each template have not been included as they have changed each time the templates have been updated.

Template Name	Probe Frequency (MHz)	Depth of Image (mm)	Depth of Point of Focus (mm)
T8174	5-10	81	74
T8141	5-10	81	41
T6160	5-10	61	60
T6141	5-10	61	41
T6129	5-10	61	29
T6123	5-10	61	23
T4141	5-10	41	41
T4129	5-10	41	29
T4123	5-10	41	23
T4118	5-10	41	18
T4115	5-10	41	15
T3023	5-10	30	23
T3018	5-10	30	18
T3015	5-10	30	15
T3010	5-10	30	10

Table A: Details of the calibration templates created for use with the 5-10 MHz transducer

Template Name	Probe Frequency (MHz)	Depth of Image (mm)	Depth of Point of Focus (mm)
U6142	8-16	61	42
U6130	8-16	61	30
U6123	8-16	61	23
U4123	8-16	41	23
U4119	8-16	41	19
U4117	8-16	41	17
U3017	8-16	30	17
U3016	8-16	30	16
U3015	8-16	30	15
U3014	8-16	30	14
U3013	8-16	30	13
U3012	8-16	30	12
U3011	8-16	30	11
U2008	8-16	20	8
U2005	8-16	20	5

Table B: Details of the calibration templates created for use with the 8-16 MHz transducer

Appendix D

Conference Abstracts

2nd Joint Meeting of the Bone Research Society and British Orthopaedic Research Society, Manchester, June 2008

Determining Human Skeletal Muscle Volume using 3D Freehand Ultrasound

[1]E Ross*, [2]TJ MacGillivray, [1] AHRW Simpson, [3] CA Greig

1. Edinburgh Orthopaedic Engineering Centre, University of Edinburgh, Edinburgh Royal Infirmary
2. Wellcome Trust Clinical Research Facility, University of Edinburgh
3. Department of Clinical and Surgical Sciences, University of Edinburgh

Measurements of change in skeletal muscle volume can indicate response to treatment in cancer patients and also the rate of rehabilitation in the case of joint replacement. Currently, Magnetic Resonance (MR) is the favoured method for muscle volume measurements however it is resource intensive and waiting times for non urgent cases are long. 3D Ultrasound provides a non invasive method of obtaining accurate muscle volume measurements and is acquired using a standard clinical ultrasound machine and an external optical tracking devices to monitoring the position of the transducer during scanning. 3D Ultrasound is much quicker and easier to access than MR and it is also less intimidating to children, the elderly and the very ill. We have shown for the first time that 3D Freehand Ultrasound can be used to accurately determine human skeletal muscle volume in vivo. Volume measurements of the rectus femoris quadricep muscle were obtained using 3D Freehand Ultrasound from four healthy volunteers and were validated against volume measurements derived using MR. Muscle volume measurements obtained using 3D Ultrasound were within 8% of the corresponding values from MR. The mean difference was 0.22cm^3 with a standard deviation of 0.44cm^3.

European Orthopaedic Research Society Conference, Madrid, April 2008.

IMAGING OF THE MUSCULOSKELETAL SYSTEM USING 3D ULTRASOUND

E. Ross, TJ. MacGillivray, AY. Muir, AHRW. Simpson
Edinburgh Orthopaedic Engineering Centre, Chancellors Building, 49 Little France Crescent, Edinburgh, EH16 4SB U.K

X-ray is the standard method for monitoring fracture healing however it is not ideal; signs of healing are not normally visible on X-ray until around 6-8 weeks post fracture. Ultrasonography allows the detection of both the initial haematoma, usually formed immediately after fracture, and the small calcium deposits laid down between broken bone ends in the first stages of fracture healing. It has been reported that these early indicators of the healing process are visible as early as 1-2 weeks after fracture. We use Freehand 3D Ultrasound to monitor the early stages of fracture healing as both the bone surface and surrounding soft tissues can be imaged simultaneously.

The Freehand 3D Ultrasound system consists of a standard Ultrasound machine, a PC running STRADWIN (Medical Imaging Group, Cambridge University) 3D software, and an optical tracking devise (NDI Polaris) to record the position and orientation of the Ultrasound probe during scanning. Images are transferred from the Ultrasound machine to the PC using RF capture through out a scan. Calibrating the system matches up the correct image with the correct probe position to produce a 3D dataset.

We segment features of interest on the sequence of 2D images to construct a 3D model. These models are rotatable and provide views of the scanned anatomy that are not otherwise achievable using conventional Ultrasound or X-ray. The 3D data set can also be resliced through any plane to provide further views.

To conduct a 3D Ultrasound scan takes the same amount of time as a conventional 2D scan. The production of the 3D model takes between 15-60 minutes depending on the level of detail required. Distances are measurable to within ±0.4mm meaning fracture gaps of sub-millimeter width can be resolved. The system has already been evaluated on healthy volunteers and a clinical study currently underway.

British Medical Ultrasound Society, Harrogate, December 2007.

Invited to speak, no abstract submitted.

IPEM Biennial Ultrasound Meeting, Birmingham, February 2007.

IMAGING OF THE MUSCULOSKELETAL SYSTEM USING 3D ULTRASOUND

+*Ross, E; **MacGillivray, TJ; *,**McDicken, NM; * Simpson, AHRW
+*Edinburgh Orthopaedic Engineering Centre, University of Edinburgh, Edinburgh, U.K
E.Ross-4@sms.ed.ac.uk

Introduction

Imaging of the musculoskeletal system is vital for delivering optimum treatment particularly in the assessment of fracture healing. X-ray and CT are adequate imaging methods for bone but soft tissue needs other modalities such as MRI and ultrasound. We propose the use of freehand 3D ultrasound to study the early stages of fracture healing by imaging the bone surfaces at the fracture site and monitoring changes in the surrounding soft tissue.

For freehand 3D ultrasound you require a conventional ultrasound machine, a computer running Cambridge University's 3D ultrasound software, known as *Stradx*, and a tracking system to record the position and orientation of the ultrasound probe during scanning. For this work the Flock of Birds electromagnetic field tracking system was used. As each image is recorded from the ultrasound machine and sent via Ethernet link to the *Stradx* software the position of the ultrasound probe is also recorded. By ensuring the system is correctly calibrated the software is able to match up the correct image with the correct probe position to produce a complete 3D data set of the scan.

Highlighting features of interest on selected 2D images enables a 3D model to be constructed. These models are rotatable in all orientations providing views of the scanned anatomy that are not otherwise achievable using other imaging techniques.

Method

To assess the feasibility of this proposed imaging method a healthy volunteer study was conducted; approval was given for this study by the Lothian Research Ethics Committee. 15 healthy volunteers were selected, 9 male, 6 female. The anterior mid point of the lower leg was scanned in order to image the surface of the tibia. Two scans were recorded for each volunteer. All the 3D ultrasound datasets were visually reviewed after scanning to assess their suitability for 3D model reconstruction.

Results

22 of the healthy volunteer scans out of 30 were suitable for 3D reconstruction, in the remaining 8 scans artifacts present in the original 2D ultrasound images caused varying discontinuities in models constructed from that data.

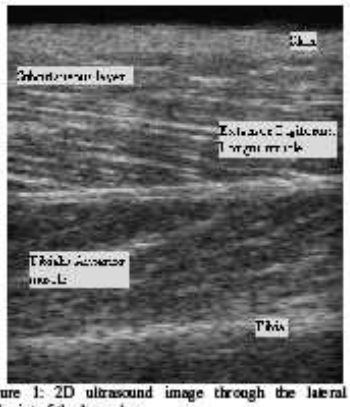

Figure 1: 2D ultrasound image through the lateral anterior midpoint of the lower leg

Figure 1 shows a typical example of a 2D ultrasound image recorded during scanning. The 3D model of the surface of the tibia is displayed in figure 2. Figure 3 shows a complete 3D model where all the soft tissues have been included. The cyan corresponds to the surface of the tibia, red to the tibialis anterior muscle, green highlights the intermuscle membrane, purple layer shows the extensor digitorum longus muscle, dark blue represents the subcutaneous layer and the skin is in yellow.

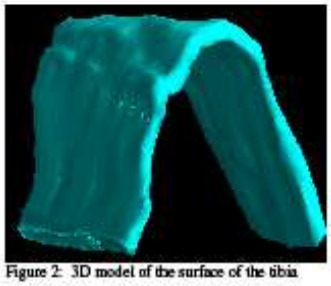

Figure 2: 3D model of the surface of the tibia

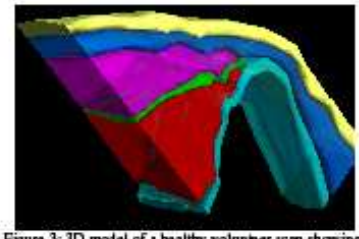

Figure 3: 3D model of a healthy volunteer scan showing both bone surface and soft tissue.

Discussion

With 3D ultrasound it is possible to image and model both the surface of the bone and the soft tissues simultaneously. The 3D models reconstructed from the scan data are fully rotatable and slices can be viewed through the 3D data sets. Both the models and *reslice* facility can provide unique views of the scanned anatomy that are not normally available with other imaging modalities.

To conduct a 3D ultrasound scan takes the same amount of time as a normal 2D scan. The production of the 3D model takes between 15-60 minutes depending on the number of images recorded and level of detail required. The quality and accuracy of the constructed model is dependent on the quality of the original ultrasound images and also on the accuracy of the tracking system being used.

Phantom work was conducted using the Flock of Birds electromagnetic field tracking system. The accuracy of the tracking system was found to depend on 3 main factors: the quality of the system calibration, the amount of ferrous metal present in the scanning environment and interference from other electromagnetic sources. The results of this phantom work have shown this tracking system not to be suitable for further clinical use. An optical tracking system is to be evaluated as a more suitable tracking system for future work using 3D ultrasound for musculoskeletal imaging. Optical tracking systems do not suffer interference from metal and electromagnetic sources; they also provide more accurate system calibration.

Affiliated Institutions for Co-Authors
** Wellcome Trust Clinical Research Facility, Western General Hospital, Edinburgh
*,** Medical Physics, University if Edinburgh, Edinburgh

British Orthopaedic Research Society, Southampton, July 2006.

IMAGING OF THE MUSCULOSKELETAL SYSTEM USING 3D ULTRASOUND

[1]E Ross*, [2]TJ MacGillivray, [1]H Simpson and [3]WN McDicken

1. Edinburgh Orthopaedic Engineering Centre, University of Edinburgh, Edinburgh Royal Infirmary
2. Wellcome Trust Clinical Research Facility, Western General Hospital, EH4 XU

3. Medical Physics, University of Edinburgh, Edinburgh Royal Infirmary

Imaging of the musculoskeletal system is vital for delivering optimum treatment particularly in the assessment of fracture healing. X-ray and CT are adequate imaging methods for bone but, soft tissue needs other modalities such as MRI and Ultrasound. We propose the use of Freehand 3D Ultrasound to study the early stages of fracture healing by imaging the bone surfaces around the fracture site and monitoring changes in the surrounding soft tissue.

Freehand 3D ultrasound is acquired by attaching a position sensor to the probe of a conventional 2D diagnostic ultrasound machine. As the probe is moved, its position and orientation are recorded along with the 2D ultrasound images. This enables slices through the body to be viewed that would be inaccessible using a normal ultrasound system. Bone surfaces around a fracture site are scanned and the data reconstructed using the Stradx and Stradwin software developed by Cambridge University, to give a 3D visualization of the area.

To assess the feasibility of this proposed method the lower limbs of healthy volunteers were scanned using a 5-10MHz ultrasound probe. The scanning resolution of the system was evaluated using a phantom to ensure millimetre detail could be detected as would be required for imaging early fracture healing. It was found that detail down to 0.8mm could easily be resolved for measurement.

The 3D system could accurately profile the different soft tissue interfaces. The visible surfaces of the tibia were reconstructed to give 3D models. Additional layers of soft tissue interfaces could easily be added to these models to provide more detail.

This imaging modality can provided detailed 3D models of bone the bone surface and surrounding soft tissue. As ultrasound is non-ionizing, rescanning can be conducted more frequently than CT or x-ray thus offering a more accurate assessment of a patient's response to healing.

Awarded the Mercia Award by the Worshipful Company of Engineers 2008

Mercia Award Abstract

Applications of 3D Freehand Ultrasound in Clinical Healthcare
Erin Ross - Edinburgh Orthopaedic Engineering Centre

3D Freehand ultrasound has the potential to revolutionise many aspects of clinical healthcare, particularly musculoskeletal examinations where X-ray is often inadequate and MR is extremely resource intensive.
Fractures are currently X-rayed however signs of healing are not normally visible until 6-8 weeks, meaning it can be months before complications are identified. This prolongs rehabilitation, causes further distress to the patient and is costly. Healing occurs initially in the soft tissues and can be imaged with 3D ultrasound after 1-2 weeks. Subsequent changes to bone surfaces can also be observed allowing much earlier detection and treatment of complications.
In addition, measurements of muscle volume can indicate a patient's response to cancer treatment as well as the rate of rehabilitation for joint replacement. We have shown that 3D freehand ultrasound can be used to measure muscle volume in humans. Scanning is much less intimidating than MR, thus well suited to children, the elderly and the very ill.

Published Paper

T.J MacGillivray, E. Ross, H. Simpson, C.A. Greig. 3D freehand Ultrasound for in vivo determination of human skeletal muscle volume. Accepted for publication in **Ultrasound in Medicine and Biology** November 35(6):2009

References

1. McArdle W, Katch F, Katch V. Exercise Physiology. Energy, Nutrition and Human Performance. Fourth ed. Baltimore: Williams & Wilkins; 1996.
2. Woo J. A short history of the development if 3D ultrasound in obstetrics and gynecology. 2001.
3. Fenster A, Downey D, Cardinal H. Three-dimensional ultrasound imaging. Physics in Medicine and Biology. 2001;46(R):R67-R99.
4. Downey D, Fenster A, Williams J. Clinical utility of three-dimensional US. Radiographics. 2000;20(2):559-71.
5. Nelson T, Pretorius D. Three-dimensional ultrasound of fetal surface imaging. Ultrasound in Obstetrics and Gynecology. 1992;2:166-74.
6. Allemand M, Tummon I, Phy J, Foong S, Dumesic D, Session D. Diagnosis of polycycstic ovaries by three-dimensional transvaginal ultrasound. Fertility and Sterility. 2006;85(1):214-9.
7. Giubilei, Ponchietti R, Biscioni S, Fanfani A, Ciatto S, Di Loro F, et al. Accuracy of prostate volume measurements using transrectal multiplanar three-dimensional sonography. International Journal of Urology. 2005;12:936-8.
8. Dekker DL, Piziali RL, Dong EJ. A system for ultrasonically imaging the human heart in three dimensions. Comput Biomed Res. 1974;7(6):544-53.
9. Gaston M, Simpson A. Inhibition of fracture healing. Journal of Bone and Joint Surgery (Br). 2007;89-B:1553-60.
10. Bhandari M, Guyatt GH, Swiontkowski MF, Tornetta P, Sprague S, Schemitsch EH. A lack of consensus in the assessment of fracture healing among Orthopaedic surgeons Journal of Orthopaedic Trauma. 2002;16(8):562-6.
11. Young J, Kostrubiak I, Resnik C, Paley D. Sonographic evaluation of bone production at the distraction site in Ilizarov limb-lengthening procedures. American Journal of Roentgenology. 1990;154:125-8.
12. Dandy D, Edwards P. Essential Orthopaedics & Trauma. 4th Edition ed. London: Churchill-Livingstone; 2003.
13. Ivey F, Tracy B, Lemmer J, NessAiver M, Metter E, Fozard J, et al. Effects of strength training and detraining on muscle quality: age and gender comparisons. Journal of Gerontology: Biological Sciences. 2000;55(A)(3):B152-7.
14. Mitsiopoulos N, Baumgartner R, Heymsfield S, Lyons W, Gallagher D, Ross R. Cadaver validation of skeletal muscle measurement by magnetic resonance imaging and computerized tomography. Journal of Applied Physiology. 1998;85:115-22.
15. Reeves N, Maganaris C, Narici M. Ultrasonographic assessment of human skeletal muscle size. European Journal of Applied Physiology. 2004 08/12/08;91:116-8.
16. Fukunaga T, Roy R, Shellock F, Hodgson J, Day M, Lee P, et al. Physiological cross-sectional area of human leg muscles based on magnetic resonance imaging. Journal of Orthopaedic Research. 1992;10:926-34.
17. Mathur S, Takai K, Macintyre D, Reid D. Estimation of thigh muscle mass with magnetic resonance imaging in older adults and people with chronic obstructive pulmonary disease. Physical Therapy. [abst]. 2008;88(2):219-30.

18. McRae R. Pocket Book of Orthopaedics & Fracture. 2nd Edition ed. Edinburgh: Churchill Livingstone; 2006.
19. McRae R, Esser M. Practical Fracture Treatment. 5th Edition ed. Edinburgh: Churchill Livingstone; 2008.
20. Solomon L, Warwick D, Nayagam S. Apley's System of Orthopaedics and Fracture. 8th Edition ed. London: Arnold; 2001.
21. Hamblen D, Simpson A. Outline of Fractures. 12th Edition ed. Edinburgh: Churchill Livingstone; 2007.
22. Paton D. Fracture and Orthopaedics. 2nd Edition ed. Edinburgh: Churchill Livingstone; 1992.
23. McKibben B. The biology of fracture healing in long bones. Journal of Bone and Joint Surgery [Br]. 1978;60(B):150-62.
24. McRae R. Pocket book of Orthopaedics and Fractures. London: Harcourt Publishers Ltd; 1999.
25. Morshed S, Corrales L, Genant H, Miclau T. Outcome assessment in clinical trials of fracture-healing. Journal of Bone and Joint Surgery (Am). 2008 25/01/09;90(Suppl 1):62-7.
26. Gokhale S. Three-dimensional sonography of muscle hernias. Journal of Ultrasound in Medicine. 2007;26(2):239-42.
27. Gaston M, Simpson A. Inhibition of fracture healing. Journal of Bone and Joint Surgery [Br]. 2007 02/02/09;89-B(12):1553-60.
28. Duckworth T. Orthopaedics and Fracture. 3rd Edition ed. Oxford: Blackwell Science Ltd; 1995.
29. Galasko C. Principles of Fracture management. Galasko C, editor. Edinburgh: Churchill Livingstone; 1984.
30. Bhandari M, Guyatt GH, Swiontkowski MF, Tornetta P, Sprague S, Schemitsch EH. A lack of consensus in the assessment of fracture healing amoung Orthopaedic surgeons. Jounral of Orthopaedic Trauma. 2002;16(8):562-6.
31. Whelan BD, Bhandari M, McKee MD, Guyatt GH, Kreder HJ, Stephen D, et al. Interobserver and intraobserver variation in the assessment of the healing of tibial fractures after intramedullary fixation. The Journal of Bone and Joint Surgery (Br). 2002;84-B(1):15-8.
32. Meire H, Farrant P. Basic Ultrasound. Chichester: John Wiley & Sons, Ltd; 1995.
33. Lerski R. Practical Ultrasound. Lerski R, editor. Oxford: IRL Press Limited; 1988.
34. Baxter G, Allan P, Morely P. Clinical Diagnostic Ultrasound. 2nd ed. Oxford: Blackwell Sciences Ltd; 1999.
35. Bushong S, Archer B. Diagnostic Ultrasound: Physics, Biology, and Instrumentation. St Louis: Mosby Year Book; 1991.
36. Hendee W, Ritenour E. Medical Imaging Physics. Fourth Edition ed. New York: Wiley-Liss; 2002.
37. Brown B, Smallwood R, Barber D, Lawford P, Hose D. Medical Physics and Biomedical Engineering. Abingdon: Taylor & Francis Group; 1999.
38. Pickuth D. Essentials of Ultrasonography: a practical guide. Berlin: Springer; 1996.

39. Breyer B, Bruguera C, Gharbi H, Goldberg B, Tan F, Wachira M, et al. Manual of Diagnostic Ultrasound. Palmer P, editor. Geneva: World Health Organisation; 1995.
40. Kaplan P, Matamoros AJ, Anderson J. Sonography of the musculoskeletal system. American Journal of Roentgenology. 1990;155:237-45.
41. Gibbon W, Long G, Barron D, O'Connor P. Complications of orthopaedic implants: sonographic evaluation. Journal of Clinical Ultrasound. 2002;30:288-99.
42. Lin J, Fressell D, Jacobson J, Weadock W, Hayes C. An illustrated tutorial of musculoskeletal sonography: Part 1, Introduction and general principles. American Journal of Roentgenology. 2000;175:637-45.
43. Cho K, Lee Y, Lee S, Shahid M, Suh K, Choi J. Sonography of bone and bone-related disease of the extremities. Journal of Clinical Ultrasound. 2004;32:511-21.
44. Howard C, Lieberman N, Mozes G, Nyaka M. Stress fracture detected sonographically. American Journal of Roentgenology. 1992;159:1350-1.
45. Mariacher-Gehler S, Michel B. Sonography: A simple way to visualise rib fractures. American Journal of Roentgenology. 1994;163:1268.
46. Hendrich C, Finkewitz U, Berner W. Diagnostic value of ultrasound and conventional radiography for the assessment of sternal fractures. Injury. 1995;26:601-4.
47. Siegel I, Anast G, Fields T. The determination of fracture healing by the measurement of sound velocity across the fracture site. Surgery, Gynecology and Obstetrics. 1958;107:327-32.
48. Riccardi L, Perissonotto A, Dabala M. Mechanical monitoring of fracture healing using ultrasound imaging. Clinical Orthopaedics and Related Research. 1993;293:71-6.
49. Maffuli N, Thorton A. Ultrasonographic appearance of external callus in long bone fractures. Injury. 1995;26:5-12.
50. Tervonen O, Junila J, Ojala R. MR imaging in tibial shaft fractures. A potential method for early visualisation of delayed union. Acta Radiologica. 1999;40(4):410-4.
51. Laasonen E, Kyro A, Korhola O, Bostman O. Magnetic resonance imaging of tibial shaft fracture repair. Archives of Orthopaedic & Trauma SUrgery. 1989;108(1):40-3.
52. Derbyshire N, Simpson A. A role for ultrasound in limb lengthening. The British Journal of Radiology. 1992;65:576-80.
53. Malde H, Hemmadi S, Chadda D, Parihar M, Bhoslae P, Kedar R. The role of skeletal sonography in limb lengthening procedures. The Journal of Postgraduate Medicine. 1993;39(3):127-9.
54. Maffuli N, Hughes T, Fixsen J. Ultrasonographic monitoring of limb lengthening. Journal of Bone and Joint Surgery [Br]. 1992;74-B:130-2.
55. Hughes T, Maffulli N, Fixsen J. Ultrasonographic appearance of regenerate bone in limb lengthening. Journal of the Royal Society of Medicine. 1993;86:18-20.
56. Eyers K, Bell M, Kanis J. Methods of assessing new bone formation during limb lengthening: Ultrasound, Dual X-ray absorptiometry and Radiography compared. Journal of Bone and Joint Surgery [Br. 1993;75(3):358-64.

57. Bouffard J, Vanderschueren G, Moed B, Goldschmit P, Craig J, Van Holsbeeck M. Sonography of healing tibial fractures. Radiology Supplement P. 1994;193(P):337.
58. Moed B, Kim E, van Holsbeeck M, Schaffler M, Subramanian S, Bouffard J, et al. Ultrasound for the early diagnosis of tibial fracture healing after static interlocked nailing without reaming: histologic correlation using a canine model. Journal of Orthopaedic Trauma. 1998;12(3):200-5.
59. Moed B, Kim E, van Holsbeeck M, Schaffler M, Subramanian S, Bouffard J, et al. Ultrasound for the early diagnosis of tibial fracture healing after static interlocked nailing without reaming: clinical results. Journal of Orthopaedic Trauma. 1998;12(3):206-13.
60. Naik K, Turner P, Gibbon W. Diagnostic ultrasound following longbone fracture fixation. The British Journal of Radiology, Proceedings of the British Medical Ultrasound Society. 1995;68:786.
61. Greig C, Young A, Skelton D, Pippet E, Butler F, Mahmud S. Exercise studies with elderly volunteers. Age and Aging. 1994;23:185-9.
62. Keynes R, Aidley D. Nerve and Muscle. Second ed. Cambridge: Cambridge University Press; 1991.
63. Bagshaw C. Muscle Contraction. Second ed. Cambridge: Chapman & Hall; 1993.
64. Wilkie D. Muscle. First ed. London: William Clowes and Sons Ltd; 1968.
65. Jones D, Round J. Skeletal muscle in health and disease. A textbook of muscle physiology. Guilford: Manchester University Press; 1999.
66. Maughan R. Basic and Applied Science for Sports Medicine. First ed. Maughan R, editor. Guilford: Butterworth-Heinemann; 1999.
67. Morse C, Tho J, Miam O, Muirhead A, Birch K, Narici M. Muslce strenght, volume and activation following 12-months resistance training in 70-year-old males. European Journal of Applied Physiology. 2005;95:197-204.
68. Lonn L, Starck G, Alpsten M, Ekholm S, Sjostrom L. Determination of tissue volumes. A comparison between CT and MR imaging. Acta Radiologica. 1999;40(3):314-21.
69. Tingart M, Apreleva M, Lethinen J, Capell B, Palmer W, Warner J. Magnetic resonance imaging in quantitative analysis of rotator cuff muscle volume. Clinical Orthopaedics and Related Research. 2003;Oct(415):104-10.
70. Juul-Kristensen B, Bojsen-Mooller F, Finsen L, Eriksson J, Johansson G, Stanhlberg F, et al. Muscle size and moment arms of rotator cuff muscles determined by magnetic resonance imaging. Cells Tissues Organs. 2000;167:214-22.
71. Tothill P, Stewart A. Estimation of thight muscle and adipose tisue volume using magnetic resonance imaging and anthropometry. Journal of Sports Science. 2002;20(7):536-76.
72. Eng C, Abrams G, Smallwood L, Lieber R, Ward S. Muscle geometry affects accuracy of forearm volume determination by magnetic resonance imaging (MRI). Journal of Biomechanics. 2007;40:3261-6.
73. Esformes J, Narici M, Maganaris C. Measurement of human muscle volume using ultrasonography. European Journal of Applied Physiology. 2002 08/12/08;87:90-2.
74. Fenster A, Downey D. 3-D ultrasound imaging: A review. IEEE Engineering in Medicine and Biology. 1996;November/December 1996:41-51.

75. Platt L. Three-dimesnional ultrasound. Ultrasound in Obstetrics and Gynecology. [Editorial]. 2000;16:295-8.
76. Fenster A, Downey D. Three-dimensional ultrasound imaging and its use in quantifying organ and pathology volumes. Anal Bioanal Chem. 2003;377:982-9.
77. Fenster A DD. Three-dimensional ultrasound imaging. Annual Reviews in Biomedical Engineering. 2000;02:457-75.
78. Prager R, Gee A, Berman L. Stradx: Real-time acquisition and visualisation of freehand 3D ultrasound Cambridge University Engineering Department Technical Report. 1998.
79. Prager R, Gee A, Berman L. Stradx: real-time acquisition and visualisation of freehand 3D ultrasound. Medical Image Analysis. 1999;3(2):129-40.
80. Rohling R, Gee A. Issues in 3-D free-hand medical ultrasound imaging. Cambridge University Engineering Department, Medical Imaging Technical Report. 1996:1-28.
81. Prager R, Rohling R, Gee A, Berman L. Automatic calibration for 3-D free-hand ultrasound. Cambridge University Engineering Department Technical Report. 1997:1-27.
82. Rosseau F, Hellier P, Barillot P. Confhusius: A robust and fully automatic calibration method for 3D freehand ultrasound. Medical Image Analysis. 2005;9:25-38.
83. Brinkley J, Muramatsu S, McCallum W, Popp R. In vitro evaluation of an ultrasonic three-dimensional imaging and volume system. Ultrasonic Imaging. 1982;4:126-39.
84. Treece G, Prager R, Gee A, Berman L. Fast surface and volume estimation for non-parallel cross-sections, for freehand three-dimensional ultrasound. Medical Image Analysis. 1999;3(2):141-73.
85. Treece G, Prager R, Gee A, Berman L. Surface interpolation from sparse cross sections using regional correspondence. IEEE Transactions on Medical Imaging. 2000;19(11):1106-14.
86. King D. Errors as a result of metal in the near field environment when using an electromagnetic locator with freehand three-dimensional echocardiography. American Society of Echocardiography. 2002;15(7):731-5.
87. Detmer P, Bashein G, Hodges T, Beach K, Filer E, Burns D, et al. 3D ultrasonic image feature localization based on magnetic scanhead tracking: in vitro calibration and validation. Ultrasound in Medicine & Biology. 1994;20(9):923-36.
88. Nelson N, Pretorius D. Three-dimensional ultrasound imaging. Ultrasound in Medicine & Biology. 1998;24(9):1243-70.
89. Dekker DL, Piziali RL, Dong E, Jr. A system for ultrasonically imaging the human heart in three dimensions. Comput Biomed Res. 1974 Dec;7(6):544-53.
90. Yanagihara T, Hata T. Three-dimensional sonographic visualisation of the fetal skeleton in the second trimester of pregnency. Gynecological and Obstetric Investigation. 1999;49:12-6.
91. Benoit B. The value of three-dimensional ultrasonography in the screening of the foetal skeleton. Childrens Nervous System. 2003;19:403-9.
92. Faro C, Benoit B, Wegrzyn P, Chaouri R, Nicolaides K. Three-dimensional sonographic description of the fetal frontal bones and metopic suture. Ultrasound in Obstetrics and Gynecology. 2005;26(6):618-21.

93. Ruano R, Martinovic J, Dommergues M, Aubry M, Dumez Y, Benachi A. Accuracy of fetal lung volume assessed by three-dimensional sonography. Ultrasound in Obstetrics and Gynecology. 2005;26(7):725-30.
94. Avni F, Cos T, Cassart M, Donner C, Ismaili K, Hall M. Evolution of fetal ultrasonography. European Radiology. 2006;April.
95. Gerards F, Twisk J, Bakker M, Barkhof F, Van Vugt J. Fetal lung volume: three-dimensional ultrasonography compared with magnetic resonance imaging. Ultrasound in Obstetrics and Gynaecology. 2007;29(5):533-6.
96. Peralta C, Cavoretto P, Csapo B, Falcon O, Nicolaides K. Lung and heart volumes by threee-dimensional ultrasound in normal fetuses at 12-32 weeks' gestation. Ultrasound in Obstetrics and Gynaecology. 2006;27:128-33.
97. Pilu G, Segata M. A novel technique for visualization of the normal and cleft fetal secondary palate: angled insonation and three-dimensional ultrasound. Ultrasound in Obstetrics and Gynaecology. 2007;29(2):166-9.
98. Treece G, Prager R, Gee A, Berman L. 3D Ultrasound examination of large organs. Cambridge University Engineering Department Technical Report. 1999:1-27.
99. Fenster A, Surry K, Mills G, Downey D. 3D Ultrasound guided breast biopsy system. Ultrasonics. 2004;42:769-74.
100. Watermann D, Foldi M, Hanjalic-Beck A, Hasenburg A, Lughausen A, Prompeler H, et al. Three-dimensional ultrasound for the assessment of breast lesions. Ultrasound in Obstetrics and Gynaecology. 2005;25(6):592-8.
101. Shipley J, Duck F, Hillman M, Halliwell M, Jones M, Thomas B. Automated quantitative volumetric breast ultrasound data-acquisition system. Ultrasound in Medicine and Biology. 2005;31(7):905-17.
102. Gooding M, Mellor M, Shipley J, Broadbent K, Goddard D. Automatic mammary duct detection in 3D ultrasound. Ultrasound in Medicine and Biology. 2005;31(7):905-17.
103. Serafin-Krol M, Krol R, Ziolkowski M, Jedrzejczyk M, Marianowska A, Mlosek R, et al. Potential value of three-dimensional ultrasonography in diagnosing muscle injuries in comparison to two-dimensional examination--preliminary results. Orthopedia, Traumatologia, Rehabilitacja. 2008;10(2):137-45.
104. Cash C, Sardesai A, Berman L, Herrick M, Treece G, Prager R, et al. Spatial mapping of the brachial plexus using three-dimensional ultrasound. The British Journal of Radiology. 2005;78:1086-94.
105. Cash C, Treece G, Berman L, Gee A, Prager R. 3D reconstruction of the skeletal anatomy of the normal neonatal foot using 3D ultrasound. The British Journal of Radiology. 2005;78:587-95.
106. Ju J, Kim J, Yoon J, Park S. Three-dimensional ultrasonographic application for analyzing synovial hypertophy of the knee in patients with osteoarthritis. Journal of Ultrasound in Medicine. 2008;27(5):729-36.
107. Gerscovich E, Greenspan A, Cronan M, Karol L, McGahan J. Three-dimensional sonographic evaluation of developmental dysplasia of the hip: preliminary findings. Radiology Supplement P. 1994;190:407-10.
108. Hunerbein M, Raschke M, Hass N, Schlag P. Three-dimensional ultrasonography: new prospects for ultrasound imaging of bone. The Lancet. 2000;355:116-7.
109. Hsu P, Prager R, Gee A, Treece G. Rapid, easy and reliable calibration for freehand 3D ultrasound. Ultrasound in Medicine & Biology. 2006;32(6):823-35.

110. Treece G, Gee A, Prager R. RF and amplitude-based probe pressure correction for 3D ultrasound. Ultrasound in Medicine and Biology. 2004;31(4):493-503.
111. Gee A, Prager R, Treece G, Berman L. Engineering a freehand 3D ultrasound system. Pattern Recognition Letters 2003;24:757-77.
112. Hastenteufel M, Vetter M, Meinzer H, Wolf I. Effect of 3D ultrasound probes in the accuracy of electromagnetic tracking systems. Ultrasound in Medicine & Biology. 2006;32(9):1359-68.
113. Gee A, Prager R, Treece G. Sequential 3D Diagnositc Ultrasound using the Stradx System. Cambridge University Engineering Department Technical Report. 2001.
114. Ascension Technology Corporation. The Flock of Birds position and orientation measurement system. Installation and operation guide. 1998. p. 1-143.
115. Huang Q, Zheng Y, Lu M, Chi Z. Development of a portable 3D ultrasound imaging system for musculoskeletal tissues. Ultrasonics. 2005;43:153-63.
116. Hodges T, Detmer P, Burns D, Beach K, Strandness DJ. Ultrasonic three-dimensional reconstruction: in vitro and in vivo volume and area measurements. Ultrasound in Medicine & Biology. 1994;20(8):719-29.
117. Gee A, Housden R, Hassenpflug P, Treece G, Prager R. Sensorless freehand 3D ultrasound in real tissue: speckle decorrelation without fully developed speckle. Cambridge University Engineering Department Technical Report. 2005.
118. Treece G, Prager R, Gee A. Ultrasound attenuation measurement in the presence of scatter variation for reduction of shadowing and enhancement. IEEE Transactions on Ultrasounics, Ferroelectrics & Frequency Control. 2005;52(12):2346-60.
119. Treece G, Gee A, Prager R, Cash C, Berman L. High definition freehand 3-D ultrasound. Ultrasound in Medicine & Biology. 2003;29(4):529-46.
120. Mc Rae R, Esser M. Practical Fracture Treatment. 5th Edition ed. Edinburgh: Churchill Livingstone; 2008.
121. Marsh D. Concepts of fracture union, delayed union and nonunion. Clinical Orthopaedics and Related Research. 1998;355S:S22-S30.
122. Abendschein W, Hyatt G. Ultrasonics and physical properties of healing bone. The Journal of Trauma. 1972;12(4):297-301.
123. Gill P, Kernohan G, Mawhinney I, Mollan R, McIllhagger R. Investigation of the mechanical properties of bone using ultrasound. Proceedings of the Institute of Mechanical Engineers, Part H Journal of Engineering in Medicine. 1989;203:61-3.
124. Simpson A, Gardner T, Evans M, Kenwright J. Stiffness, strength and healing assessment in different bone fractures - a simple mathematical model. Injury. 2000;31:777-81.
125. Webb G, Herling G, Gardner T, Kenwright J, Simpson A. Manual assessment of fracture stiffness. Injury. 1996;27(5):319-20.
126. Oni O, Dunning J, Mobbs R, Gregg P. Clinical factors and the size of the external callus in tibial shaft fractures. Clinical Orthopaedics and Related Research. 1991;273:278-82.
127. Shah K, Goh J, Karunanithy R, Low S, Das De S, Bose K. Effects of decalcification on bone mineral content and bending stiffness of feline femur. Calcified Tissue International. 1995;56:78-82.

128. MacGillivray TJ, Ross E, Simpson A, Greig CA. 3D freehand Ultrasound for in vivo determination of human skeletal muscle volume. Ultrasound in Medicine & Biology. 2009;35(6):928-35.
129. Bland M. An introduction to medical statistics. 3rd Edition ed. Oxford: Oxford University Press; 2000.
130. Weller R, Pfau T, Ferrari M, Griffith R, Bradford T, Wilson A. The determination of muscle volume with a freehand Ultrasonography system. Ultrasound in Medicine & Biology. 2007 13/10/08;33(3):402-7.
131. Housden R, Gee A, Treece G, Prager R. Sensorless reconstruction of unconstrained freehand 3D ultrasound data. Cambridge University Engineering Department Technical Report. 2006.
132. Hsu P, Prager R, Gee A, Treece G. Rapid, easy and reliable calibration for freehand 3D ultrasound; 2005 Contract No.: Document Number|.